Study of Transport Phenomena for Parallel Flow in Microfluidic Channels

Sudha, A.

DOI
10.4233/uuid:f2ac1125-ec30-46b6-b5cd-8e0b7c91b475

Publication date
2025

Document Version
Final published version

Citation (APA)
Sudha, A. (2025). *Study of Transport Phenomena for Parallel Flow in Microfluidic Channels*. [Dissertation (TU Delft), Delft University of Technology]. https://doi.org/10.4233/uuid:f2ac1125-ec30-46b6-b5cd-8e0b7c91b475

Study of Transport Phenomena for Parallel Flow in Microfluidic Channels

Study of Transport Phenomena for Parallel Flow in Microfluidic Channels

Dissertation

for the purpose of obtaining the degree of doctor
at Delft University of Technology
by the authority of the Rector Magnificus Prof. Dr. Ir. T. H. J. J. van der Hagen,
chair of the Board for Doctorates,
to be defended publicly on 24th April 2025 at 15:00 o'clock

by

Anand Sudha

Master of Science in Mechanical Engineering, Delft University of Technology, Delft, Netherlands
born in Chennai, India.

This dissertation has been approved by the promotors

promotor: Dr. M. Rohde
promotor: Prof. dr. ir. J. L. Kloosterman

Composition of the Doctoral Committee:

Rector Magnificus,	chairperson
Dr. M. Rohde,	TU Delft, NL, promotor
Prof. dr. ir. J. L. Kloosterman,	TU Delft, NL, promotor

Independent members:

Prof. dr. ir. J. R. van Ommen	TU Delft, NL
Dr. B. Bera	TU Delft, NL
Dr. D. C. Visser	NRG, NL
Prof. dr. C. J. M. van Rijn	University van Amsterdam, NL
Prof. dr. ir. J. J. Derksen	University of Abderdeen, UK
Prof. dr. ir. C. R. Kleijn	TU Delft, NL, Reserve

Keywords: microfluidics, transport phenomena, multiphase flow, lattice boltzmann, mass transfer, parallel flow

Printed by:

ISBN 000-00-0000-000-0

An electronic version of this dissertation is available at
http://repository.tudelft.nl/.

Contents

Summary

Microfluidic two-phase flows are increasingly being used in many mass transfer applications because of the numerous advantages of operating in the microscale such as stability of the interface and low cost. Such two-phase flows have multiple applications in various fields such as medicine, metal extraction, chemistry, oil and gas, and handling of industrial effluents. It is particularly important in both the transport and extraction of substances from one fluid to another fluid. The main reasons for this are the short diffusion distances and large surface-volume ratios when using multiple chips in parallel.

Among the various flow regimes, parallel flow in the microscale is considered to be advantageous for extraction applications, especially radioisotope transfer. In this regime, the two fluids move parallel to each other in a microfluidic channel. If the fluid-fluid interface remains stable throughout, efficient transfer is possible without necessitating a step to separate the two fluids. This benefit offered by microfluidics is very important for radioisotopes with short half-lives, as the absence of a separation step ensures that radioisotopes can be transferred efficiently in a quick time, thereby maximizing their utility for different applications such as pharmaceuticals.

However, stable parallel flow is hard to achieve as it is contingent on several factors. In a microfluidic channel with two inlets, a rectangular main channel and outlets, the ideal scenario for efficient mass transfer involves a stable fluid-fluid interface to be located exactly in the middle of the rectangular channel, followed by the two fluids flowing to their respective outlets without any fluid leaking to another outlet. Considering the utility of such a regime, it is important to study the underlying flow phenomena which govern the regime and leakage. This thesis, therefore, focuses on using simulations and experiments to study parallel flow in microfluidic channels, followed by an analysis of the mass transfer when using such a regime for radioisotope extraction.

The flow phenomena are studied numerically using the Lattice Boltzmann Method (LBM), specifically the Rothman-Keller (RK) model. The LBM is based on the numerical modelling of the Boltzmann equation which is then related to the Navier-Stokes equations for fluid mechanics. A probabilistic particle distribution function is tracked across a discrete lattice mesh, and using such a mesh makes the model more efficient compared to other simulation techniques for fluid flow, while also resulting in a localized approach. The LBM is extended for multiphase flows using the RK model, where each fluid is allocated a separate particle distribution function. This model provides greater flexibility and accuracy than other models while retaining

the simplicity of the LBM.

Before the relevant transport phenomena are studied, the validity of the model for such flows needs to be established first. In microfluidics, low flow rates are very common because high residence times enhance extraction efficiency. At such flow rates, just like some simulation techniques, the RK model generates numerical or spurious velocities which can have a significant influence on the results. These spurious velocities are related to the implementation of the surface tension in the RK model. Such an implementation approximates the pressure balance at the fluid-fluid interface, which is fine as long as the Capillary number (ratio of inertial and interfacial forces) is below 10^{-3}. Below this value, however, spurious velocities are generated. In this work, the RK model is modified for such flows at low Capillary numbers by modifying the surface tension term. This modified RK model is used for simulating multiphase flows in a Y-Y microfluidic channels and compared with experiments and other simulation techniques. The modification certainly resulted in an improvement, as the RK model was able to successfully capture most of the flow regimes observed in the experiments. It proved particularly effective in capturing leakage, which wasn't the case with other simulation techniques.

Leakage was observed for all fluid flow rates in the experiments. One solution to minimize leakage is to apply hydrophilic and hydrophobic coatings to the channels. Though this method is effective, it is less flexible as different coatings might be needed for different fluids. One key factor which influences leakage is the channel geometry. This thesis focuses on developing modified geometries to minimize leakage while also understanding how the channel geometry plays a role in influencing leakage. One possible option is to modify the outlet geometry to help guide the fluids to their respective outlets. Adding a third outlet helps in this regard, as a third outlet ensures that pure fluid is obtained in the remaining two outlets. However, this results in a loss of fluid, so the third outlet was slightly modified by adding a circular head. The modified RK model was used for simulating fluid flow in these channels, and the model was validated using experiments. The modified triple outlet design proved to be very successful in minimizing leakage for a wide range of flow rates, and the amount of fluid lost to the third outlet can be reduced by altering the dimensions of the circular head or the ratio of flow rates of the aqueous and organic phases (ϕ).

An alternative to using the third outlet would be to add a circular reservoir in such a way that the two outlets do not lie in a straight line, but are displaced from each other at a distance equal to the radius of the reservoir. Such a design slows the fluids down because of the enlarged area of the reservoir, but does not prevent leakage entirely as the fluids slowly leak into the outlets. To prevent this leakage, a circular pillar is added at the centre of the reservoir. The diameter of this circular pillar is crucial to control leakage, with leakage being observed at smaller ϕ for smaller diameters and larger ϕ for larger diameters. The pillar has an associated capillary pressure, and it is this pressure which is responsible for preventing leakage.

Instead of modifying the outlet, the entire channel geometry can be modified as well. One such idea which has been used in extraction studies is the 'step' channel, which is basically an asymmetric channel where the two halves of the channel have different depths. However, the impact such an asymmetry has on fluid behaviour has been less studied. A combination of experiments and simulations are used to study such channels by developing flow maps based on the Capillary number. Parallel flow is observed at low Capillary numbers in contrast to a symmetric channel, where parallel flow is observed at higher Capillary numbers. Additionally, no leakage is observed at low Capillary numbers in step channels. Experiments are performed on 'step' channels of varying widths and degrees of asymmetry to obtain a broader understanding of how this asymmetry influences flow behaviour. In all step channels, stable parallel flow without leakage at lower Capillary numbers and at higher Capillary numbers, leakage was observed. Stable parallel flow was observed at a broader range of Capillary numbers for step channels with higher degrees of asymmetry. Volume-of-fluid simulations were also performed to compare step and symmetric channels at low Capillary numbers and they revealed that the surface tension helps in stabilizing parallel flow in a step channel while forming slugs or droplets in a symmetric channel.

In the case of mass transfer for parallel flow, a common mechanism for extraction involves chemical reactions taking place close to the liquid-liquid interface. For such a reaction mechanism, three dimensionless numbers are important - the Biot number (reaction to diffusion forces), the Peclet number (convection to diffusion forces) and the Damkohler number (reaction to convection forces). To understand the influence of these dimensionless numbers, a finite difference code was developed to solve the convection-diffusion equations for mass transfer. The velocity profile is obtained from the modified RK model. The finite difference code is validated using experimental data from two different sources.

For channels with smaller cross-sections, a high Biot and a lower Peclet number are preferred for large extraction efficiencies. However, if the Damkohler number remains constant, the extraction efficiency remains approximately the same. In the case of channels with larger cross-sections, the Peclet number is very important as the isotope needs time to diffuse to the interface before it is extracted. This implies that the flow rates of the fluids have to be very small as the convective forces are small. Thus, the step channel can be used for this purpose to ensure small flow rates and large interfacial areas while maintaining stable parallel flow. Based on the application and nature of the study, the channel geometry can be modified accordingly for stable parallel flow.

Overall, channel geometry is one of the most important factors determining the transport phenomena in the microscale. Simulation techniques need to be further modified to obtain a broader understanding of the transport phenomena in the microscale and to further characterize the role played by channel geometry.

Samenvatting

Microfluïdische tweefasestroming wordt steeds vaker gebruikt in toepassingen waarin stoftransport de hoofdrol speelt. Redenen hiervoor zijn de voordelen van het werken op microschaal, zoals de stabiliteit van het contactoppervlak tussen beide fasen en de lage kosten. Dit type stroming wordt toegepast in bijvoorbeeld de geneeskunde, metaalwinning, chemie, olie- en gaswining, en de verwerking van industriële afvalstoffen, en is bijzonder belangrijk voor zowel het transport als de extractie van stoffen van de ene vloeistof naar de andere. De voornaamste voordelen zijn de korte diffusieafstanden en de grote oppervlak-volumeverhoudingen bij het gebruik van meerdere parallel-geschakelde microchips.

Parallelle stroming op microschaal is vooral wenselijk tijdens de extractie van radioisotopen. In dit stromingsregime bewegen de twee vloeistoffen parallel naast elkaar in een microfluïdisch kanaal. Als het vloeistof-vloeistofcontactoppervlak in het gehele kanaal stabiel blijft, is efficiënte overdracht mogelijk zonder dat er een extra stap nodig is om de twee vloeistoffen te scheiden van elkaar. Dit voordeel is met name wenselijk voor radio-isotopen met een korte halveringstijd, aangezien de afwezigheid van een extra scheidingsstap zorgt voor een snelle extractie. Op deze wijze wordt met name de bruikbaarheid van isotopen in geneeskundige toepassingen gemaximaliseerd.

Stabiele parallelle stroming is echter moeilijk te bewerkstelligen, omdat het afhankelijk is van verschillende factoren. In het ideale geval zou zich een stabiel contactoppervlak instellen dat zich precies in het midden bevindt van een microkanaal, en zouden beide fasen perfect gescheiden worden van elkaar door elk in een apart uitstroomkanaal te stromen. Gezien de bruikbaarheid van parallelle stroming is het dus van belang om de onderliggende stromingsfenomenen te bestuderen die het regime en scheiding van beide fasen bepalen. Dit proefschrift richt zich daarom op het gebruik van simulaties en experimenten om parallelle stroming in microfluïdische kanalen te bestuderen, gevolgd door een analyse van stofoverdracht in het geval van parallelle stroming voor de extractie van radioisotopen.

De stromingsverschijnselen worden numeriek bestudeerd met behulp van de Lattice Boltzmann Methode (LBM), waarbij het Rothman-Keller (RK) model wordt gebruikt. De LBM is de numerieke versie van de Boltzmann-vergelijking, en wordt gebruikt om de Navier-Stokes-vergelijkingen voor vloeistofdynamica op te lossen. In LBM wordt een deeltjesverdelingsfunctie beschouwd op een numeriek rooster. Voor een aantal toepassingen kan LBM efficiënter zijn dan andere simulatietechnieken voor het berekenen van stroming, bijvoorbeeld omdat de vergelijkingen lokaal opgelost kunnen worden. De LBM kan wroden uitgebreid voor meerfase-

stromen met behulp van het RK-model, waarbij elke vloeistof een aparte deeltjesverdelingsfunctie krijgt toegewezen. Dit model biedt meer flexibiliteit en nauwkeurigheid dan andere modellen, terwijl het de eenvoud van de LBM behoudt.

Voordat de relevante verschijnselen worden bestudeerd, moet de geldigheid van het model voor dergelijke stromen eerst worden vastgesteld. In microfluïdische stroming zijn lage stroomsnelheden heel gebruikelijk, omdat lange verblijftijden de extractie-efficiëntie verhogen. Bij dergelijke stroomsnelheden genereert het RK-model, net als sommige andere simulatie-technieken, artificiële ("spurious") snelheden die een significante invloed op de resultaten kunnen hebben. Deze artificiële snelheden zijn gerelateerd aan de implementatie van de oppervlaktespanning in het RK-model. Een dergelijke implementatie benadert de drukbalans bij het contactoppervlak, wat goed is zolang het Capillaire getal (de verhouding van traagheidskrachten en oppervlaktespanning) kleiner dan 10^{-3} blijft. Beneden deze waarde worden artificiële snelheden gegenereerd. In dit onderzoek wordt het RK-model aangepast voor een laag Capillair getal door de oppervlaktespanningsterm aan te passen. Dit gewijzigde RK-model wordt gebruikt voor het simuleren van meerfase-stromen in zogenaamde Y-Y microfluïdische kanalen, en wordt vergeleken met experimenten en andere simulatie-technieken. De aanpassing van het model resulteerde in een grotere overeenkomst met de stromingsregimes die in de experimenten werden waargenomen. Het model bleek bovendien bijzonder effectief in het simleren van lekkage (= een deel van één van de fasen stroomt via het uitstroomkanaal van de andere fase mee naar buiten) aan het uiteinde van het microkanaal, wat niet het geval was bij andere simulatie-technieken.

Lekkage vond tijdens de experimenten altijd plaats. Eén van de oplossingen om lekkage te minimaliseren is het toepassen van hydrofiele en hydrofobe coatings op de kanalen. Hoewel deze methode effectief kan zijn, is het minder flexibel inzetbaar omdat verschillende coatings nodig kunnen zijn voor verschillende vloeistoffen. Een andere belangrijke factor die lekkage beïnvloedt, is de kanaalgeometrie. Dit proefschrift richt zich op het ontwikkelen van gemodificeerde geometrieën om lekkage te minimaliseren, en het begrijpen van de invloed van dergelijke modificaties op eventuele lekkage. Het toevoegen van een derde uitlaat kan hierbij helpen, aangezien een derde uitlaat ervoor zorgt dat door de resterende twee uitstroomkanalen alleen één enkele fase kan stromen. Dit resulteert echter in een verlies van product. Om deze reden werd daarom de derde uitlaat gemodificeerd door een ronde kop toe te voegen. Het gewijzigde RK-model werd gebruikt voor het simuleren van vloeistofstroming in deze kanalen, en het model werd gevalideerd met behulp van experimenten. Het gewijzigde ontwerp met drie uitlaten bleek zeer succesvol te zijn in het minimaliseren van lekkage voor een groot bereik van volumedebieten. De hoeveelheid vloeistof die in de derde uitlaat verloren gaat, kan bovendien worden verminderd door de afmetingen van de ronde kop of de verhouding van volumedebieten van de water- en organische fasen (ϕ) te veranderen.

Een alternatief voor het gebruik van de derde uitlaat zou zijn om een rond reservoir toe te voegen, en wel op zo'n manier dat de twee uitstroomkanalen niet

in een rechte lijn liggen, maar op een afstand van elkaar zijn geplaatst die gelijk is aan de straal van het reservoir. Een dergelijk ontwerp vertraagt de vloeistoffen vanwege het vergrote oppervlak van het reservoir, maar kan lekkage niet volledig voorkomen omdat de vloeistoffen langzaam in de uitstroomkanalen lekken. Om deze lekkage te voorkomen, wordt daarom een ronde pilaar in het midden van het reservoir geplaatst. De pilaar bewerkstelligt een zekere capillaire druk die hiervoor verantwoordelijk is. De diameter van deze ronde pilaar blijkt een sterke invloed te hebben op lekkage: lekkage treedt op bij kleinere ϕ voor kleinere diameters en bij grotere ϕ voor grotere diameters. Door de juiste combinatie te kiezen kan lekkage voorkomen worden.

In plaats van de uitlaat te modificeren, kan ook de gehele kanaalgeometrie worden aangepast. Eén van de mogelijkheden is het zogenaamde 'stap'-kanaal, wat in wezen een asymmetrisch kanaal is waarbij de twee helften van het kanaal verschillende dieptes hebben. De invloed van zo'n asymmetrie in de geometrie op het vloeistofgedrag is tot nu toe nauwelijks bestudeerd. In dit onderzoek worden daarom experimenten en simulaties gebruikt om flowcharts te ontwikkelen op basis van het Capillaire getal Ca. Parallelle stroming werd waargenomen bij lage Capillaire getallen, in tegenstelling tot een symmetrisch kanaal, waar juist parallelle stroming wordt waargenomen bij een hoog Capillaire getal. Bovendien wordt er bij een laag Capillaire getal in stapkanalen geen lekkage waargenomen. In dit onderzoek werden verscheidene experimenten uitgevoerd waarbij verschillende kanaalbreedtes en mate van asymmetrie gevarieerd om een beter begrip te verkrijgen hoe dergelijke stap-kanalen het vloeistofgedrag beïnvloeden. In alle stapkanalen werd stabiele parallelle stroming zonder lekkage waargenomen bij een laag Capillaire getal, en bij een hoog Capillaire getal werd juist wel lekkage waargenomen. Voor kanalen die meer asymmetrisch waren werd voor een groot bereik van het Capillaire getal een stabiele, parallelle stroming waargenomen. Volume-of-fluid simulaties werden uitgevoerd om stap- en symmetrische kanalen bij lage Capillaire nummers te vergelijken. Deze berekeningen toonden aan dat de oppervlaktespanning helpt bij het stabiliseren van parallelle stroming in een stapkanaal terwijl het druppels in een symmetrisch kanaal vormt.

In het geval van extractie in parallelle stroming worden chemische reacties dicht bij het contactoppervlak gebruikt om de extractie te bevorderen. Voor een dergelijk reactiemechanisme zijn drie dimensieloze getallen belangrijk - het Biot-getal (reactietijden versus diffusietijden), het Peclet-getal (convectie versus diffusie) en het Damkohler-getal (reactietijdebn versus convectietijden). Om de invloed van deze dimensieloze getallen te begrijpen, werd een Finite Difference schema ontwikkeld om de convectie-diffusievergelijkingen voor massatransfer op te kunnen lossen. Het snelheidsprofiel werd verkregen uit de stromingsberekeningen waarbij het gewijzigde RK-model werd gebruikt. Het Finite Difference schama werd gevalideerd met behulp van experimentele gegevens uit twee verschillende bronnen uit de literatuur.

Voor kanalen met een kleiner doorstroomd oppervlak leveren een hogere Biot-

getal en een lagere Peclet-getal een grotere extractie-efficiëntie. Echter, als het Damkohler-getal constant blijft, blijft de extractie-efficiëntie ongeveer gelijk. In het geval van kanalen met groter doorstroomd oppervlak is het Peclet-getal zeer belangrijk, aangezien het isotoop tijd nodig heeft om naar de interface te diffunderen voordat het kan worden geëxtraheerd. Dit impliceert dat de stroomsnelheden van de vloeistoffen zeer klein moeten zijn, aangezien de convectieve krachten klein zijn. Daarom kan het stapkanaal voor dit doel worden gebruikt om kleine stroomsnelheden en grote interfaciale gebieden te bewerkstelligen, terwijl stabiele parallelle stroming wordt behouden. Op basis van de toepassing en de aard van de studie kan de kanaalgeometrie dienovereenkomstig worden aangepast voor stabiele parallelle stroming.

In het algemeen kan geconcludeerd worden dat de kanaalgeometrie één van de belangrijkste factoren is die transportverschijnselene (impuls, stof) op microschaal bepalen. Simulatietechnieken zullen verder moeten worden aangepast om een nog beter begrip te kunnen verkrijgen van de deze verschijnselen en de invloed van de geometrie op deze verschijnselen.

1

Introduction

1

Radioisotopes have become increasingly important in the past few decades because of their vast capabilities in medical applications [1], particularly in the diagnosis [2, 3], imaging [4, 5] and treatment of cancer and other diseases [6, 7]. They are generated either in nuclear reactors, cyclotrons or accelerators [8]. In the case of a reactor, radioisotopes are produced either as fission products [9] or from neutron capture [10]. These radioisotopes generally have longer half-lives than those generated in a cyclotron, where the radionuclides are generated by the bombardment of accelerated protons on a material [11]. Linear electron accelerators offer another alternative, though they are less used commercially [8].

For these applications, the radioisotopes have to be highly pure in accordance with the medical standards [12]. Here, the purity is defined as the percentage of radioactivity in a product/material resulting from the radioisotope [12]. However, they are normally present in a mixture of oxides along with fission products generated from the nuclear reaction [13]. Pure radioisotopes are not easy to obtain because of the presence of various chemical products in the nuclear fuel. Some of these fission products are extremely reactive and react with the isotope to form new compounds, such as transuranium radionuclides in Uranium fuels [13]. In order to extract the maximum utility from a radioisotope, it is necessary to separate them from the fuel to render them safe for medical application. Thus, the desired radioisotope needs to be extracted from the product at high purity as impurities reduce the efficacy of the drug or diagnosing technique [14].

Methods such as ion exchange chromatography [15, 16], electromagnetic isotope separation [17, 18] and electrochemical separation [19, 20] are used to separate and purify the radioisotopes for external use. An important factor to keep in mind is the short half-life of some of these radioisotopes, so a longer separation step can lead to a reduced quantity of isotopes available for use [21, 9]. This needs to be considered along with the efficiency of the respective techniques. One method which is gaining increased traction is Liquid-Liquid Extraction (LLE) [22, 14].

1.1. Liquid-Liquid Extraction

Liquid-Liquid Extraction (LLE) is the process of material transfer between two immiscible fluids accomplished by their mixing and subsequent separation [14]. This is generally applied to a two-phase system consisting of a continuous phase, where the solutes are dissolved, and a dispersed phase, where the solutes are transferred. This transfer is governed by the composition of two phases, chemical affinity of the solute for the dispersed phases and reaction kinetics [23], along with the nature of the flow regime [24]. Additionally, changes to the fluids' chemical properties such as pH also influence the extraction process.

LLE has been used in a variety of applications in the chemical, food, nuclear, petrochemical and pharmaceutical industries for separation [22, 25, 14]. It was first applied for separating radionuclides in the 1940s industrially [26, 23]. This is tra-

ditionally carried out on a batch scale, where the multiphase mixture is agitated in large-scale containers or columns followed by gravity-based separation of the two phases. The dispersed phase containing the isotope is then selectively removed and used for medical applications [27, 28]. Since the two liquids are immiscible, vigorous agitation is necessary to provide a suitable contact area for mass transfer to take place and prevent the chemicals from travelling long distances across the liquid-liquid interface. However, this is not very favourable for isotope extraction because large volumes of fluids are required, thus leading to a low surface-volume ratio, which in turn increases the time required for successful mass transfer [29, 14]. The necessity of a separation step can be extremely detrimental when transferring radioisotopes with short half-lives since the time required for an extra step might lead to a significant decay in isotope concentration [14]. If the concentration of the solute is low, batch extraction is very difficult as small concentrations of solutes have to cover large distances to diffuse through the interface [30].

These limitations can be overcome by shifting the process to the microscale. This involves the transfer of isotopes across the liquid-liquid interface in small channels with transverse dimensions in micrometres. In addition to using far smaller liquid volumes, this form of extraction largely increases the surface-to-volume ratio [29], with some microfluidic devices showing an almost tenfold increase [31, 32]. This also has the effect of decreasing the diffusion distances the isotope has to traverse while also stabilizing the liquid-liquid interface. The microchannel can be modified geometrically to enhance mass transfer and is amenable to automation, thus allowing greater control over the transport phenomena [33, 34].

1.2. Microfluidic LLE

Microfluidics is the science of fluid behaviour in the small scale, where the transverse lengths associated with fluid flow are usually in the order of a few hundred micrometres [35]. Microfluidic multiphase flow finds applications in a wide range of fields, be it in biology [36], pharmaceuticals [37], chemistry [38] and radioisotope extraction [22] because of the aforementioned advantages.

In the microscale, both viscous and inertial forces compete with each other, and the domination of one force over the other results in different flow patterns [39]. When multiphase microfluidics is considered, the interfacial forces acquire a special importance. This interfacial force is governed by a property called surface tension, which represents the cohesive forces between two liquids. The surface tension allows the liquid interface to assume a position of minimum surface area under the action of external forces [40]. Based on the interaction of inertial, viscous and interfacial forces, the two liquids assume different configurations as shown in Figure 1.1. These interactions are represented using three dimensionless numbers - the Reynolds, Capillary and Weber numbers.

1

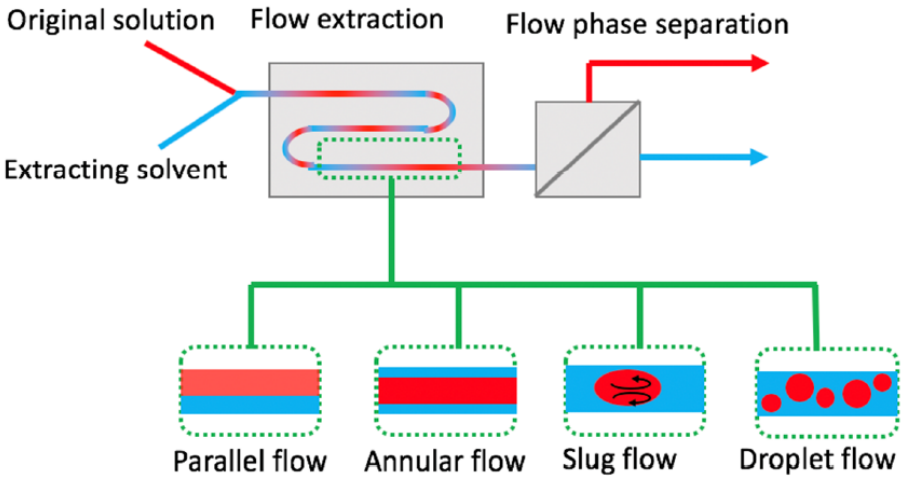

Figure 1.1: Flow setup showing LLE and separation in the microscale along with the different flow regimes. [14].

$$Re = \frac{\text{Inertial Forces}}{\text{Viscous Forces}} = \frac{uL}{\nu} \tag{1.1}$$

$$Ca = \frac{\text{Viscous Forces}}{\text{Interfacial Forces}} = \frac{u\mu}{\sigma} \tag{1.2}$$

$$We = \frac{\text{Inertial Forces}}{\text{Interfacial Forces}} = \frac{\rho u^2 L}{\sigma} \tag{1.3}$$

$$\tag{1.4}$$

where u is the fluid velocity, L is the characteristic length of the fluid, ρ is the density of the fluid, μ is the dynamic viscosity, $\nu = \frac{\mu}{\rho}$ the kinematic viscosity and σ is the surface tension of the two fluids.

Similar to batch-wise LLE, the two fluids are mixed in a channel and then subsequently separated. Figure 1.1 shows four different flow regimes - parallel, annular, slug and droplet flow. These flow patterns have been extensively studied for microchannels of various geometries and different fluids, along with the mass transfer at such dimensions. The surface-to-volume ratio is the largest in slug flow, which makes it particularly suited for mass transfer. Additionally, the circulation that takes place inside the slugs in the form of Taylor vortices caused by the friction at the wall increases the extraction efficiency [41]. The mass transfer can be enhanced by adding an inert gas to the channel as a third phase which results in an increased interfacial area [14]. This is why many studies have been devoted to slug flow [42, 43, 44]. However, slug flow is not advantageous when extracting radioisotopes because it necessitates a separation step which usually involves membranes

[28] or complex geometries to selectively trap droplets of one phase [45]. If the radioisotopes have short half-lives, the separation step could significantly limit the viable amount of radioisotope [25].

The short half-life of radioisotopes is the reason why microfluidic LLE is geared towards parallel flow even though the mass transfer rate can be lower than slug flow. Parallel flow extraction has been performed for radi2oactive Copper from an acidic solution [25], Calcium isotope from ultrapure water [46], Cadmium (II) from nitrate medium [47] and Uranium from acidic media [48]. Theoretically, parallel flow should lead to the complete separation of the two phases in two outlet channels as shown in Figure 1.2a. However, separation is highly contingent on factors such as flow rates, channel width, wall wettability and physical properties such as viscosity and density [24]. More often than not, patterns like that shown in Figure 1.2b emerge, where one phase leaks into the outlet of the other. Leakage reduces the purity of the radioisotope and might even necessitate a separation step, thus rendering the advantages of parallel flow less useful. Therefore, it is imperative to examine the factors governing the flow patterns in a microchannel and obtain an understanding of the phenomena involved.

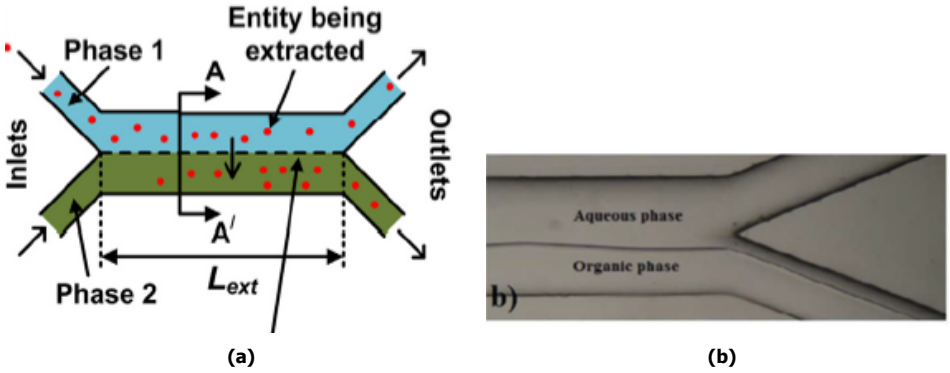

Figure 1.2: a) LLE using parallel flow with a stable interface at the middle of the channel [25] b) Instance of aqueous phase leaking into the outlet of the organic phase from Jahromi *et al.* [46]

1.3. Flow Patterns and Flow Maps

1.3.1. Flow Patterns in Literature

Flow patterns have been extensively studied in microchannels of various geometries such as Y-Y channels [49, 47, 24, 50], T-T channels [24, 50, 51, 52]and cross-junction channels [53, 54, 55]. These channels are shown in Figure 1.3. The flow patterns commonly observed in the literature are slug and parallel flow [56]. In the case of slug flow, droplets of the dispersed phase form in the continuous phase, and parallel flow is defined as the regime where the continuous and dispersed phases

flow parallel to each other in a microchannel. Slug flow generally occurs when interfacial forces are dominant, and parallel flow when inertial or viscous forces are dominant. Both these regimes are illustrated in Figure 1.4.

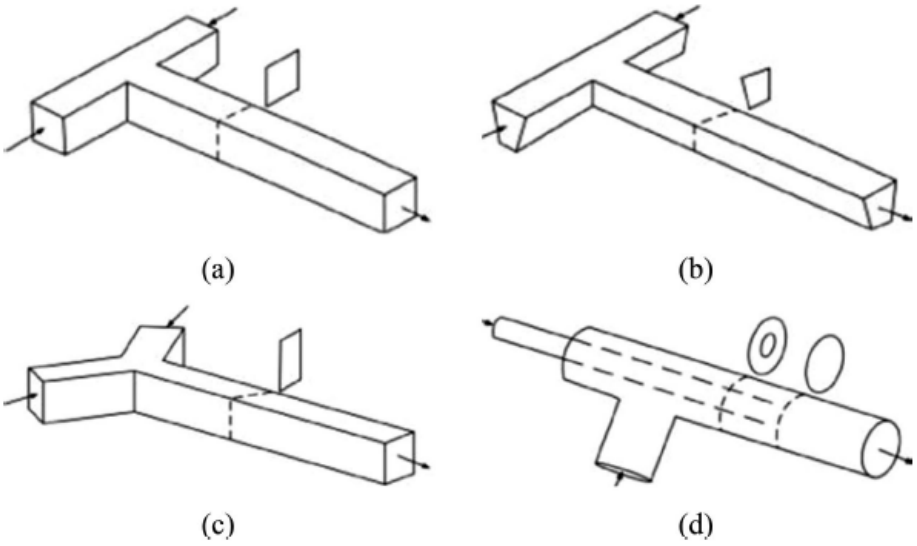

Figure 1.3: Various channels used by Kashid *et al.* [24] - a) T channel with a square cross-section, b) T- trapezoidal c) Y-rectangular d) Cross junction channel with concentric cross section

In addition to these, many flow patterns intermediate to slug and parallel flow have been observed. These patterns vary for different geometries, wettabilities and fluids. The nature of these intermediate regimes is governed by various factors - fluid properties, channel geometry and affinity of the fluids to the channel material (wettability). In some cases, the intermediate regimes include slugs of varying lengths [49], parallel flow with deformed interface [24] or rivulet flow, where the fluid interface is warped and one fluid wets the channel [57]. Generally, in these intermediate regimes, parallel flow is observed for a certain length of the channel after which the interface deforms to form droplets [56, 58].

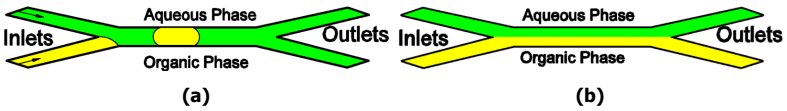

Figure 1.4: a) Slug Flow b) Parallel Flow

The factors determining the various patterns are studied and plotted in flow maps which show the various regimes observed. One way of representing the flow patterns is through the flow rates of the respective phases as was done by Darekar

et al. [49] in their studies on a Y-shaped microchannel. They found that lower flow rates lead to slug flow while high flow rates resulted in parallel flow. However, the results from such maps cannot be extended to other fluids since the impact of the other forces such as viscous and interfacial forces are neglected. Darekar *et al.* themselves realized this, so they shifted to a more general approach to study the flow phenomena in their paper.

1.3.2. Influence of Dimensionless Numbers

Dimensionless numbers are very useful in classifying flow regimes precisely because they can indicate the impact of competing forces while providing a more universal picture. In the case of the water-butanol mixture in Darekar *et al.*, for example, the Capillary number of the aqueous phase plays a very important role in the flow pattern observed. Parallel flow is observed only after a certain value of the continuous Capillary number is reached, regardless of the value of the dispersed phase [49].

However, this does not paint the full picture of the flow phenomena observed as inertial forces are not taken into account when merely the Capillary number is used. Zhao *et al.* [59] showcased their flow maps through the Weber numbers of the two fluids for a water-kerosene system in a T-T channel. Contrary to the Capillary number flow map of Darekar *et al.*, the Weber numbers of both the fluids were found to be equally important here, with higher Weber numbers resulting in parallel flow. Cao *et al.* [53] went a step further and conducted a dimensional analysis to understand the dimensionless numbers which govern the flow transition. They performed experiments on a cross-junction channel for water-butanol and water-toluene, and they developed the following relation to predict the flow transition:

$$c_0 Re_c^{c_1} We_c^{c_2} = Re_d^{c_3} We_d^{c_4} \tag{1.5}$$

where the subscripts c and d correspond to the continuous and dispersed phases respectively, and c_0, c_1, c_2, c_3, c_4 are constants whose values depend on whether the flow pattern is in the annular-slug transition regime or the slug-droplet regime. They observed that 3 different liquid mixtures satisfied this equation. However, Equation 1.5 does not indicate the effects of viscous forces, so it doesn't give the full picture even if it can be extended for different liquid-liquid combinations. To show the impact and interaction of three forces, Dessimoz *et al.* [50] plotted flow maps for their water-toluene system using the mean Capillary and Reynolds number. This allowed good visualization of the flow phenomena involved while segregating the patterns into regimes - parallel, transition and slug - effectively. From these papers, it can be concluded that higher interfacial forces lead to slug flow, while higher inertial forces lead to parallel flow, with the viscous forces contributing to both transition and parallel flow regimes.

1

1.3.3. Impact of Geometry

Dessimoz *et al.* [50] also studied the influence of geometry on the flow patterns by classifying their regimes for both T-T and Y-Y microchannels. The geometry of the channel was found to play a considerable role in the flow patterns, with the propensity for parallel flow being much higher in the Y-Y as compared to the T-T channel, where slug flow was more common. Kashid *et al.* [24] performed experiments on a water-toluene mixture for three different channels- T-T, Y-Y and cross junction microchannels with a concentric cross-section. In addition to this, they worked with two cross-sections in the T-T channel - square and trapezoidal. The cross-section was not found to have a prominent impact on the flow patterns. They initially plotted their flow maps based on flow rates, and contrary to Dessimoz *et al.* [50], the T-T and Y-Y channels gave similar flow patterns. The concentric channel, however, showed a much greater tendency for slug flow.

Darekar *et al.* [49] varied the widths of their Y-Y channels and observed that channels with smaller widths showed regime transitions at lower flower rates as compared to channels with larger widths. In order to further understand the effect of channel width, Kashid *et al.* [60] developed a new parameter based on the hydraulic diameter of the channel (d_h), the Reynolds number of the dispersed phase and the volumetric flow fraction of the dispersed phase (ϵ_d) -$Re_D d d_h/\epsilon_d$. To show the effects of viscous and interfacial forces, they plotted this parameter against the Re_c/Ca_c for three different channels. Here, the influence of geometry was more clearly observed, with the T-T channel requiring a higher Re_c/Ca_c for flow transition as compared to the Y-Y channel. They even plotted the results of other papers - Zhao *et al.* [59] and Salim *et al.* [52] in a similar manner, and observed that they fit very well with the universal trend as shown in Figure 1.5a.

There's much debate, however, on what combination of dimensionless numbers is ideal for representing flow patterns. We already discussed how Cao *et al.* [62] and Kashid *et al.* [24] came up with different combinations for their flow maps. Asadi-Sanghadi *et al.* [61] studied the flow patterns in a Y-Y serpentine channel and neither of these dimensionless number combinations proved to be the ideal fit for their results. Instead, they came up with 5 different combinations, the result from one of which is shown in Figure 1.5b.

1.3.4. Influence of Wettability

Another important parameter which determines the flow patterns is the affinity of the liquid for the solid surface - their wettability. Among the two liquids, one might show a greater affinity for the solid as compared to the other. Most papers neglect this parameter when plotting their generalized flow maps, and this explains the difficulty of coming up with a universal dimensionless number to predict flow phenomena. In the paper of Darekar *et al.* [49], glass microchannels were used, which showed greater affinity for water as compared to the organic fluid, i.e., the channel is hydrophilic ("water-loving"). To test the influence of wettability, they coated the

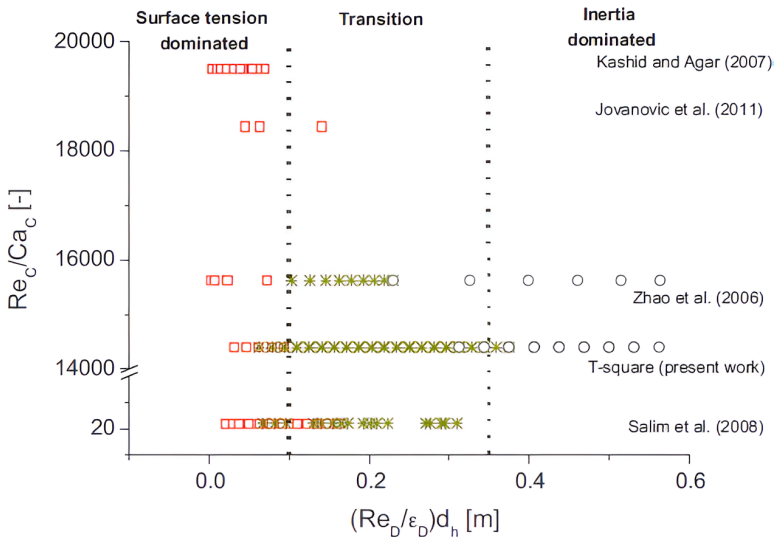

(a)

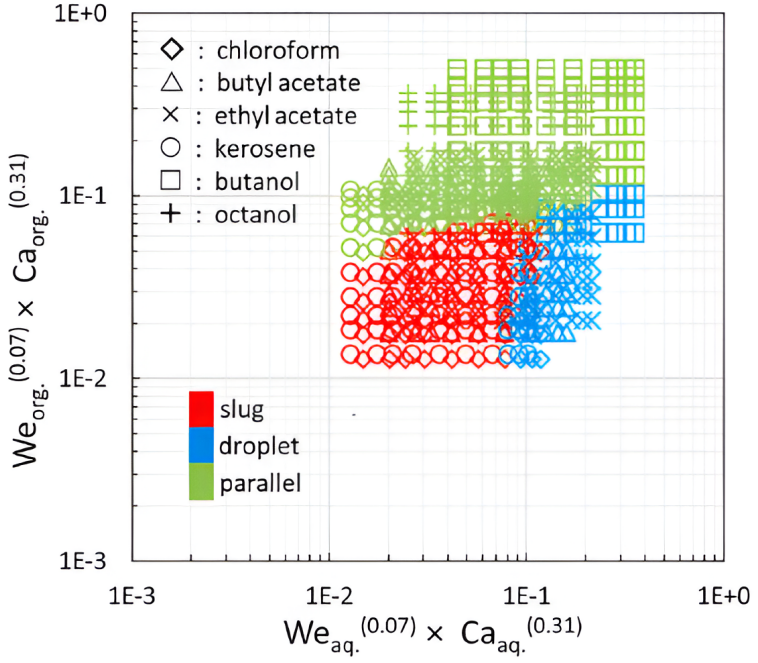

(b)

Figure 1.5: a) Flow Maps showing Re_c/Ca_c as a function of $Re_d d_h/\epsilon_d$ for different studies [24] b) Flow patterns observed by Asadi-Sanghadi *et al.* [61] for various fluids using a combination of Ca and We

walls of the channel to make it more hydrophobic ("water-hating"). Here, water is the dispersed phase as compared to the hydrophilic channel, where it's the continuous phase. Slug flow was observed to be more prominent in hydrophobic channels as compared to the hydrophilic ones, with parallel flow being a lot less common.

1.3.5. Slug Flow and Leakage

While all the aforementioned papers have studied the flow maps, among the individual regimes, only slug flow has been studied in great detail. Many papers have studied slug formation [63, 64, 65, 66] in different geometries. Some papers have looked into the length of each slug and the factors which influence it [58, 64, 67]. Generalized formulae for predicting the slug length have been developed, but similar to the flow patterns [68, 64, 62], these are successful only in some cases.

In the case of parallel flow, there are papers like Li *et al.*. [69] and Guillot *et al.*. [70] who observe the stability of parallel flow by examining the factors which lead to deformed interfaces. Parallel flow in this case is closer to annular flow, where the dispersed phase is flanked by the continuous phase on either side as it flows parallel. Other papers focus on the flow phenomena that develop at the outlet. Pohar *et al.*. [71] studied the interface positions in parallel flow and developed a correlation to predict when the interface will be exactly at the middle for a particular set of flow rates. They found that the viscosity ratio was the main parameter in preventing leakage, but as the results of Zheng Liu showed [58], this correlation doesn't give the full picture as Liu observed leakage for all his flow rates.

Aota *et al.*. [72] found that leakage was related to the balancing of the pressure loss due to viscosity difference and Laplace pressure due to the interfacial tension. No leakage was observed when these pressures were balanced. They also developed a design of asymmetric cross-section which ensured that the two pressures were balanced for a broader range of flow rates, subsequently leading to stable parallel flow without leakage [73]. This design was also used by Hibara *et al.*. [74] and Smirnova *et al.*. [75]. Some setups used ridges [76] or guiding structures [77] to minimize leakage. Alternatively, one can modify the wettability of the channel through coatings, and this is among the most common methods to prevent leakage [78, 74, 34], though this limits the applicability to a particular set of fluids and channel materials.

1.4. Mass Transfer

Two parameters which assume great importance in LLE papers are the volumetric mass transfer coefficient and the extraction efficiency. The volumetric mass transfer coefficient is defined as the rate of mass transfer per unit fluid volume [79]. The extraction efficiency is the percentage of solute transferred to the extracting phase

and is given by [46] :

$$EE = \frac{C_{org,out} \times Q_{org}}{C_{aq,in} \times Q_{aq}} \tag{1.6}$$

where C refers to the concentration of the solute,Q is the volumetric flow rate and the subscripts org, out and aq, in refer to the organic phase at the outlet and aqueous phase at the inlet respectively.

Both the geometry and flow regime have a considerable influence on mass transfer, and many papers have studied the effects of these factors on extraction efficiency. The extraction efficiency of vanillin was determined for two different channel geometries by Fries *et al..* [80] as shown in Figure 1.6a. In the T-T channel, experiments were performed with slug flow while parallel flow was tested for the Y-Y channel. Slug flow indeed showed 15 % greater extraction efficiency as mentioned by Kashid *et al..* [24] and Martini *et al..*[14] due to internal circulation, but parallel flow showed an increased extraction efficiency comparable to slug flow when the width of the channel was decreased. The values were observed to be comparable to that of the T-T channel with a width of 300 μm (Figure 1.6a).

The effect of geometry was expanded for T-T and cross-junction channels by Zhao *et al..* [81] using the Lattice Boltzmann Method (LBM). Though they only considered slug flow, the influence of geometry can be clearly discerned from the higher mass transfer rate in cross channels. Further, they modified the shape of the T-T channel with a venturi-shaped junction after the T-inlets. The modified structures led to the squeezing of the droplet near the venturi, while increasing the mass transfer efficiency.

The absence of a separation step makes parallel flow particularly attractive, which is why many LLE investigations of radioisotopes seek to optimize the mass transfer rate for parallel flow and, at the same time, try to maintain the stability of the interface. Y-Y channels are mainly used to accomplish this since they show a greater tendency for parallel flow. Both Mariet *et al..* [48] and Jahromi *et al..* [46] focused their attention on the flow inlet conditions for interface stability, and both observed stable interfaces located at the middle of the Y-shaped channel. Jahromi *et al..* also extended their study to improve the extraction efficiency by adding reagents such as calcium chloride and picric acid to aid in the extraction of calcium isotope. They concluded that low concentrations of calcium chloride and relatively high concentrations of picric acid led to the best extraction efficiencies of 50 %.

Farahani *et al..* [47] studied the importance of geometry in the extraction of a cadmium isotope in a Y-Y channel as shown in Figure 1.6b. They found that the mass transfer coefficients improved with decreasing widths as observed in the literature, but they couldn't achieve large residence times with small channel widths. At residence times greater than 8 s, the extraction efficiency is slightly reduced for small widths, indicating a possible back-extraction. The effect of channel length on mass transfer was also studied, with longer channels improving the extraction

efficiency.

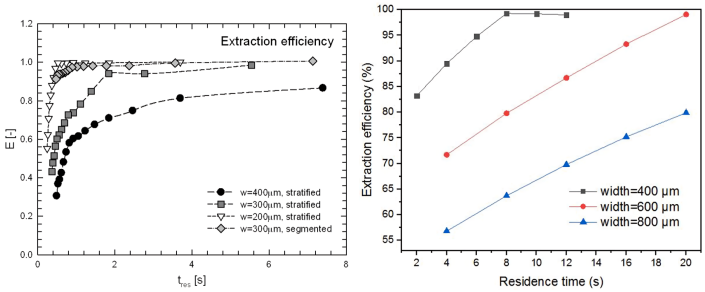

(a) (b)

Figure 1.6: a) Extraction efficiency of vanillin as a function of residence time for slug (segmented) and parallel (stratified) flow in channels of different widths [80] b)Extraction efficiency of Cadmium as a function of residence time for three channel widths [82]

In addition to studying the effect of geometry on extraction efficiency, Goyal *et al.*. [78] also developed an analytical model based on their results to predict the optimal width and the maximum length of the channel for which the interface is still stable for Cu-64 extraction. However, they applied hydrophobic surface coatings to their channels to ensure a broader range of flow rates for stable parallel flow without leakage.

Most of these aforementioned papers involve mass transfer across the entire area occupied by the fluid in parallel flow. Depending on the isotope being transferred and the substance used for initiating the reaction (chelator) and subsequent mass transfer, the mass transfer can be solely restricted to regions close to the liquid-liquid interface. Such a system was studied both experimentally and numerically by Ciceri *et al.*. [83] who investigated whether the mass transfer is diffusion-limited or reaction-limited. They studied the extraction kinetics of cobalt ions in a Y-Y channel with parallel flow and observed the mass transfer to be dependent on both diffusion and reaction kinetics. A combination of a numerical model and experiments was employed for this purpose. Similar studies have also focussed on the role of reaction and diffusion in interfacial mass transfer for Uranium extraction [84, 85]. Helle *et al.*. [84] also plotted the concentration profiles obtained from simulations for this as shown in Figure 1.7.

1.5. Motivation, Approach and Outline

1.5.1. Motivation

The literature on microchannels and LLE is growing, especially because of the potential applications. However, it is first important to obtain an overall understanding of the flow phenomena and the multitude of factors which play a role in influencing

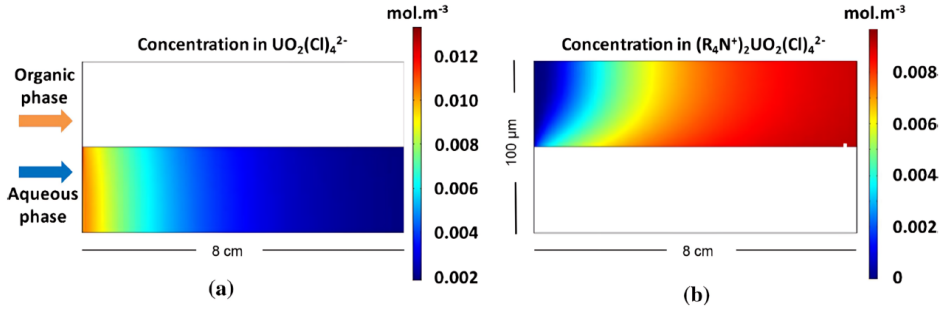

Figure 1.7: Concentration profile of Uranium in a) Aqueous phase, which the Uranium isotope is originally dissolved, and b) Organic phase, to which the Uranium isotope is transferred, for interfacial mass transfer [84]

them. Though flow patterns in microchannels have been extensively studied, there are still quite a few areas which can be delved into a bit deeper. Considering the utility of microchannels in radioisotope transfer, it is imperative to obtain a clearer understanding of the flow dynamics and mass transfer involved, especially on the phenomena of parallel flow and leakage. To have a greater understanding of the underlying flow phenomena, both experiments and numerical simulations are necessary.

The Lattice Boltzmann Method (LBM) has been gaining ground in microfluidic multiphase simulations [86, 87, 88] because of its high degree of localization, lack of interface tracking and faster simulation times [89, 90]. This thesis, thus, employs the LBM, specifically the Rothman-Keller (RK) model to study flow phenomena in a Y-Y channel.

Many LBM papers study multiphase flows at relatively high Capillary numbers ranging from 10^{-3} to 1 [91, 92, 86, 93], while some applications require lower Capillary numbers [58, 49, 50] ($Ca<10^{-3}$). The LBM, specifically the RK model, is not free from problems at these Capillary numbers, with spurious velocities being observed at the liquid-liquid interface. These spurious velocities result from the implementation of the surface tension term [94, 95]. Therefore, it is essential to study the capability of the RK model to capture flow phenomena at such Capillary numbers and adapt the model where necessary.

When it comes to the phenomenon of leakage, there have been many papers on interface position and stability, though a significant number of these have only commented on leakage from the practical perspective of leakage avoidance [25, 48, 46]. Pohar *et al.*. [71], however, studied phase separation and leakage in greater detail, and observed that the interface position is related to the viscosity ratio of the two fluids. Aota *et al.*. [96] went further in this direction by theorizing that leakage was related to the balancing of the viscous pressure loss and the Laplace pressure

due to surface tension. They confirmed this theory with experiments. Liu [58], however, observed leakage for all flow rates and his experiments could not validate the relations proposed by Pohar *et al..* [71] and Aota *et al..* [58]. Additionally, he couldn't successfully capture leakage in simulations using the phase-field method. His results underscore the necessity of studying leakage in greater detail both experimentally and numerically.

One factor which has a considerable influence on leakage is the channel geometry. Lu *et al..* [97] employed a third outlet in his T-channel and minimized leakage for a large number of flow rates. They also created leakage maps and obtained a range of flow rates for which stable parallel flow was observed. Another option to minimize leakage is by using phaseguides - guiding structures in the channel geometry which result in an abrupt change in capillary pressure [77, 98]. A problem with such structures is that the liquids eventually leak into the outlets once the pressure of the fluid exceeds the pressure associated with the geometry [98].

For this reason, modifying the outlet seems a better option. The triple outlet proposed by Lu *et al..* [99] is an effective solution to the problem of leakage, but it does result in a loss of fluid. Recycling the fluids can be very beneficial in applications such as radiopharmaceuticals [100], so the loss associated with such a design also needs to be studied and quantified. Additionally, the triple outlet constitutes only one design, and a broader study of the influence of the outlet geometry on leakage and the flow fields will help understand how the fluids interact with the outlet geometry.

Instead of modifying only a part of the geometry, the whole geometry can be modified to aid parallel flow. One such design is that used by Aota *et al..* [73], where a Y-Y channel is modified to have an asymmetric cross-section. The channel is divided into two halves, with each half having a different height, giving the cross-section the shape of a staircase step. This design has been shown to be effective in pinning the liquid-liquid interface and minimizing leakage [73]. Though this design has been used in multiple papers [101, 84, 102], no fundamental study exists, to this author's knowledge, where the influence of such a modification on the flow patterns and leakage is thoroughly investigated.

Most of the papers dealing with LLE have not discussed the transport phenomena in terms of dimensionless numbers, and this is especially the case for mass transfer. While Fries *et al..* [103] and Farahani *et al..* [82] have looked at the influence of various factors such as width, flow rate and flow regime on extraction efficiency, the absence of dimensionless numbers in their discussions makes it difficult to understand the interplay of competing forces involved in the transport phenomena.

1.5.2. Research Questions

Based on the literature review, the following research questions were formulated:

1. How capable is the Lattice-Boltzmann method, specifically the Rothman-Keller (RK) model, of capturing multiphase flow phenomena and flow patterns in a microchannel at low Capillary numbers? What modifications are necessary to improve its capability and how does the methodology compare to the phase-field method and other techniques in simulating leakage?
2. How does the outlet geometry influence the flow profile and leakage in the case of parallel flow? How can the outlet be modified to minimize leakage?
3. What role does an asymmetric cross-section play in influencing the flow phenomena? Does modifying the entire geometry lead to a significant alteration in the observed flow and leakage regimes, and if yes, what new flow regime can be observed?
4. What dimensionless numbers can be used to describe interfacial mass transfer in microchannels and how do these influence the extraction efficiency?

1.5.3. Outline

The thesis outline is as follows:

Chapter 2 outlines the theory behind multiphase flows, contact angles and the numerical techniques used to study the transport phenomena.

Chapter 3 discusses the capability of the LBM model in capturing flow phenomena in microchannels at low Capillary numbers. The flow map, slug lengths and leakage regimes from the simulations are compared with Liu's [58] experiments, and a modification to the model is proposed to reduce the spurious velocities. The capability of the model is further examined by comparing the results with two other numerical techniques - Volume of Fluid (VOF) and phase-field.

The impact of the outlet geometry on leakage is studied in **Chapter 4**. Multiple outlet geometries are proposed and their leakage regimes are studied using the Lattice Boltzmann model discussed in **Chapter 3**. The effect of outlet dimensions on leakage is considered in particular and velocity contours are plotted to understand how the fluids respond to this change in outlet geometry. One of the proposed designs is tested using experiments, thus further validating the Lattice Boltzmann model as well.

Chapter 5 considers a geometry of asymmetric cross-section and discusses the influence this geometry has on flow patterns and leakage. This geometry has been used appreciably in literature for LLE applications, though it has been less studied from a fluid mechanics perspective. The flow patterns are studied experimentally

in this case as the Capillary numbers used are quite low ($<10^{-5}$) and they are compared with a channel of symmetric cross-section to understand how this design influences fluid flow. VOF simulations are then employed to supplement these experiments to study the flow profile and pressure plots.

The dimensionless numbers used for describing interfacial mass transfer are elucidated in **Chapter 6**, along with the finite-difference model used to simulate the mass transfer. Lattice-Boltzmann simulations are used to provide this model with the velocity profile, and various flow and geometrical parameters are varied to understand the factors which influence extraction efficiency. This is further extended by performing a kinetic study of the Gallium-isotope using both experiments and the finite-difference model to shed light on the mass-transfer mechanism of Gallium.

Finally, conclusions and recommendations are provided in **Chapter 7**.

Bibliography

[1] Johannes Czernin, Ida Sonni, Aria Razmaria, and Jeremie Calais. The future of nuclear medicine as an independent specialty. *Journal of Nuclear Medicine*, 60(Supplement 2):3S–12S, 2019.

[2] Norman Veall, Herbert Vetter, et al. Radioisotope techniques in clinical research and diagnosis. *Radioisotope techniques in clinical research and diagnosis.*, 1958.

[3] Brahm Shapiro, Milton D Gross, and Barry Shulkin. Radioisotope diagnosis and therapy of malignant pheochromocytoma. *Trends in Endocrinology & Metabolism*, 12(10):469–475, 2001.

[4] Rui Huang, Mingwei Wang, Yizhou Zhu, Peter S Conti, and Kai Chen. Development of pet probes for cancer imaging. *Current Topics in Medicinal Chemistry*, 15(8):795–819, 2015.

[5] Kristina Søborg Pedersen, Joseph Imbrogno, Jesper Fonslet, Marcella Lusardi, Klavs F Jensen, and Fedor Zhuravlev. Liquid–liquid extraction in flow of the radioisotope titanium-45 for positron emission tomography applications. *Reaction Chemistry & Engineering*, 3(6):898–904, 2018.

[6] George Sgouros, Lisa Bodei, Michael R McDevitt, and Jessie R Nedrow. Radiopharmaceutical therapy in cancer: clinical advances and challenges. *Nature reviews Drug discovery*, 19(9):589–608, 2020.

[7] William A Vandergrift and Sunil J Patel. Convection-enhanced delivery of immunotoxins and radioisotopes for treatment of malignant gliomas. *Neurosurgical Focus*, 20(4):E13, 2006.

[8] Valeriia N. Starovoitova, Lali Tchelidze, and Douglas P. Wells. Production of medical radioisotopes with linear accelerators. *Applied Radiation and Isotopes*, 85:39–44, February 2014. ISSN 09698043. doi: 10.1016/j.apradiso.2013.11.122. URL https://linkinghub.elsevier.com/retrieve/pii/S096980431300571X.

[9] Bert Wolterbeek, Jan Leen Kloosterman, Danny Lathouwers, Martin Rohde, August Winkelman, Lodewijk Frima, and Frank Wols. What is wise in the production of 99 mo? a comparison of eight possible production routes. *Journal of Radioanalytical and Nuclear Chemistry*, 302:773–779, 2014.

[10] Tanveer Bokhari, A Mushtaq, and Islam Khan. Production of low and high specific activity 64 cu in a reactor. *Journal of radioanalytical and nuclear chemistry*, 284(2):265–271, 2010.

[11] Paul Schmor. Review of cyclotrons for the production of radioactive isotopes for medical and industrial applications. *Reviews of accelerator science and technology*, 4(01):103–116, 2011.

[12] V Shivarudrappa and KV Vimalnath. High purity materials as targets for radioisotope production: Needs and challenges. *Bulletin of Materials Science*, 28:325–330, 2005.

[13] Clarisse Mariet, Axel Vansteene, Marion Losno, Julien Pellé, Jean-Philippe Jasmin, Anthony Bruchet, and Gwendolyne Hellé. Microfluidics devices applied to radionuclides separation in acidic media for the nuclear fuel cycle. *Micro and Nano Engineering*, 3:7–14, May 2019. ISSN 25900072. doi: 10.1016/j.mne.2019.02.006. URL https://linkinghub.elsevier.com/retrieve/pii/S2590007219300115.

[14] Petra Martini, Andrea Adamo, Neilesh Syna, Alessandra Boschi, Licia Uccelli, Nopphon Weeranoppanant, Jack Markham, and Giancarlo Pascali. Perspectives on the use of liquid extraction for radioisotope purification. *Molecules*, 24(2):1–17, 2019. ISSN 14203049. doi: 10.3390/molecules24020334.

[15] S Umehara, T Kishimoto, H Kakubata, M Nomura, T Kaneshiki, T Suzuki, Y Fujii, and S Nemoto. A basic study on the production of enriched isotope ca-48 by using crown-ether resin. *Progress of Theoretical and Experimental Physics*, 2015(5), 2015.

[16] J.D. Navratil. Ion exchange technology in spent fuel reprocessing. *Journal of Nuclear Science and Technology*, 26(8):735–743, 1989. doi: 10.1080/18811248.1989.9734377. URL https://doi.org/10.1080/18811248.1989.9734377.

[17] A Hanser. Routine production of high purity 81rb by means of electromagnetic isotope separation. *International Journal of Radiation Applications and Instrumentation. Part A. Applied Radiation and Isotopes*, 40(4):309–314, 1989.

[18] GJ Beyer, E Herrmann, F Molnar, VI Raiko, and H Tyrroff. Highly-effective method for the separation of actinide isotopes. Technical report, Joint Inst. for Nuclear Research, Dubna, USSR, 1972.

[19] Ashutosh Dash and F. F. Knapp. An overview of radioisotope separation technologies for development of 188W/188Re radionuclide generators providing 188Re to meet future research and clinical demands. *RSC Advances*, 5(49): 39012–39036, 2015. ISSN 20462069. doi: 10.1039/c5ra03890a.

[20] Rubel Chakravarty, Ashutosh Dash, and M RA Pillai. Electrochemical separation is an attractive strategy for development of radionuclide generators for medical applications. *Current radiopharmaceuticals*, 5(3):271–287, 2012.

[21] Deborah W McCarthy, Laura A Bass, P Duffy Cutler, Ruth E Shefer, Robert E Klinkowstein, Pilar Herrero, Jason S Lewis, Cathy S Cutler, Carolyn J Anderson, and Michael J Welch. High purity production and potential applications of copper-60 and copper-61. *Nuclear medicine and biology*, 26(4):351–358, 1999.

[22] N. Assmann, A. Ladosz, and P. Rudolf von Rohr. Continuous Micro Liquid-Liquid Extraction. *Chemical Engineering and Technology*, 36(6):921–936, 2013. ISSN 09307516. doi: 10.1002/ceat.201200557.

[23] Gordon M Ritcey and AW Ashbrook. Solvent extraction. principles and applications to process metallurgy. part i. 1984.

[24] Madhvanand Kashid and Lioubov Kiwi-Minsker. Quantitative prediction of flow patterns in liquid-liquid flow in micro-capillaries. *Chemical Engineering and Processing: Process Intensification*, 50(10):972–978, 2011. ISSN 02552701. doi: 10.1016/j.cep.2011.07.003. URL http://dx.doi.org/10.1016/j.cep.2011.07.003.

[25] Sachit Goyal, Amit V. Desai, Robert W. Lewis, David R. Ranganathan, Hairong Li, Dexing Zeng, David E. Reichert, and Paul J.A. Kenis. Thiolene and SIFEL-based microfluidic platforms for liquid-liquid extraction. *Sensors and Actuators, B: Chemical*, 190:634–644, 2014. ISSN 09254005. doi: 10.1016/j.snb.2013.09.065.

[26] Donald W Bridges and Joe B Rosenbaum. *Metallurgical application of solvent extraction: Fundamentals of the process*, volume 8139. US Department of the Interior, Bureau of Mines, 1962.

[27] C Bauer, P Bauduin, Jean-François Dufrêche, Thomas Zemb, and Olivier Diat. Liquid/liquid metal extraction: Phase diagram topology resulting from molecular interactions between extractant, ion, oil and water. *The European Physical Journal Special Topics*, 213(1):225–241, 2012.

[28] Jason G Kralj, Hemantkumar R Sahoo, and Klavs F Jensen. Integrated continuous microfluidic liquid–liquid extraction. *Lab on a Chip*, 7(2):256–263, 2007.

[29] Yuanhai Su, Yuchao Zhao, Guangwen Chen, and Quan Yuan. Liquid–liquid two-phase flow and mass transfer characteristics in packed microchannels. *Chemical Engineering Science*, 65(13):3947–3956, 2010.

[30] Kevin P Nichols, Rebecca R Pompano, Liang Li, Artem V Gelis, and Rustem F Ismagilov. Toward mechanistic understanding of nuclear reprocessing chemistries by quantifying lanthanide solvent extraction kinetics via microfluidics with constant interfacial area and rapid mixing. *Journal of the American Chemical Society*, 133(39):15721–15729, 2011.

[31] A Ghaini, MN Kashid, and DW Agar. Effective interfacial area for mass transfer in the liquid–liquid slug flow capillary microreactors. *Chemical Engineering and Processing: Process Intensification*, 49(4):358–366, 2010.

[32] Alexander Holbach and Norbert Kockmann. Counter-current arrangement of microfluidic liquid-liquid droplet flow contactors. *Green Processing and Synthesis*, 2(2):157–167, 2013.

[33] Akihide Hibara, Manabu Tokeshi, Kenji Uchiyama, Hideaki Hisamoto, and Takehiko Kitamori. Integrated multilayer flow system on a microchip. *Analytical sciences*, 17(1):89–93, 2001.

[34] Manabu Tokeshi, Tomoko Minagawa, Kenji Uchiyama, Akihide Hibara, Kiichi Sato, Hideaki Hisamoto, and Takehiko Kitamori. Continuous-Flow Chemical Processing on a Microchip by Combining Microunit Operations and a Multiphase Flow Network. *Analytical Chemistry*, 74(7):1565–1571, April 2002. ISSN 0003-2700, 1520-6882. doi: 10.1021/ac011111z. URL https://pubs.acs.org/doi/10.1021/ac011111z.

[35] Nam-Trung Nguyen, Steven T Wereley, and Seyed Ali Mousavi Shaegh. *Fundamentals and applications of microfluidics*. Artech house, 2019.

[36] Jérôme Charmet, Paolo Arosio, and Tuomas PJ Knowles. Microfluidics for protein biophysics. *Journal of molecular biology*, 430(5):565–580, 2018.

[37] Rui Ran, Qi Sun, Thejus Baby, David Wibowo, Anton PJ Middelberg, and Chun-Xia Zhao. Multiphase microfluidic synthesis of micro-and nanostructures for pharmaceutical applications. *Chemical Engineering Science*, 169: 78–96, 2017.

[38] Axel Günther and Klavs F. Jensen. Multiphase microfluidics: from flow characteristics to chemical and materials synthesis. *Lab Chip*, 6(12):1487–1503, 2006. ISSN 1473-0197, 1473-0189. doi: 10.1039/B609851G. URL http://xlink.rsc.org/?DOI=B609851G.

[39] Patrick Tabeling. *Introduction to microfluidics*. OUP Oxford, 2005.

[40] Christopher Earls Brennen and Christopher E Brennen. Fundamentals of multiphase flow. 2005.

[41] MN Kashid, I Gerlach, S Goetz, J Franzke, JF Acker, F Platte, DW Agar, and S1 Turek. Internal circulation within the liquid slugs of a liquid- liquid slug-flow capillary microreactor. *Industrial & engineering chemistry research*, 44 (14):5003–5010, 2005.

[42] Ying Zhang, Xubin Zhang, Bujian Xu, Wangfeng Cai, and Fumin Wang. CFD simulation of mass transfer intensified by chemical reactions in slug flow microchannels. *Canadian Journal of Chemical Engineering*, 93(12):2307–2314, 2015. ISSN 1939019X. doi: 10.1002/cjce.22360.

[43] Gim Yau Soh, Guan Heng Yeoh, and Victoria Timchenko. A CFD model for the coupling of multiphase, multicomponent and mass transfer physics for micro-scale simulations. *International Journal of Heat and Mass Transfer*, 113:922–934, 2017. ISSN 00179310. doi: 10.1016/j.ijheatmasstransfer.2017.06.001. URL http://dx.doi.org/10.1016/j.ijheatmasstransfer.2017.06.001.

[44] Nathalie Di Miceli Raimondi and Laurent Prat. Numerical study of the coupling between reaction and mass transfer for liquid-liquid slug flow in square microchannels. *AIChE journal*, 57(7):1719–1732, 2011.

[45] Hong Shen, Qun Fang, and Zhao-Lun Fang. A microfluidic chip based sequential injection system with trapped droplet liquid–liquid extraction and chemiluminescence detection. *Lab on a Chip*, 6(10):1387–1389, 2006.

[46] Peyman Foroozan Jahromi, Javad Karimi-Sabet, and Younes Amini. Ion-pair extraction-reaction of calcium using Y-shaped microfluidic junctions: An optimized separation approach. *Chemical Engineering Journal*, 334(November): 2603–2615, 2018. ISSN 13858947. doi: 10.1016/j.cej.2017.11.129. URL https://doi.org/10.1016/j.cej.2017.11.129.

[47] Amin Farahani, Ahmad Rahbar-Kelishami, and Hadi Shayesteh. Microfluidic solvent extraction of Cd(II) in parallel flow pattern: Optimization, ion exchange, and mass transfer study. *Separation and Purification Technology*, 258(P2):118031, 2021. ISSN 18733794. doi: 10.1016/j.seppur.2020.118031. URL https://doi.org/10.1016/j.seppur.2020.118031.

[48] Clarisse Mariet, Axel Vansteene, Marion Losno, Julien Pellé, Jean Philippe Jasmin, Anthony Bruchet, and Gwendolyne Hellé. Microfluidics devices applied to radionuclides separation in acidic media for the nuclear fuel cycle. *Micro and Nano Engineering*, 3(February):7–14, 2019. ISSN 25900072. doi: 10.1016/j.mne.2019.02.006. URL https://doi.org/10.1016/j.mne.2019.02.006.

[49] Mayur Darekar, Krishna Kumar Singh, Sulekha Mukhopadhyay, and Kalsanka Trivikram Shenoy. Liquid-Liquid Two-Phase Flow Patterns in Y-Junction Microchannels. *Industrial and Engineering Chemistry Research*, 56(42):12215–12226, 2017. ISSN 15205045. doi: 10.1021/acs.iecr.7b03164.

[50] Anne Laure Dessimoz, Laurent Cavin, Albert Renken, and Lioubov Kiwi-Minsker. Liquid-liquid two-phase flow patterns and mass transfer characteristics in rectangular glass microreactors. *Chemical Engineering Science*, 63 (16):4035–4044, 2008. ISSN 00092509. doi: 10.1016/j.ces.2008.05.005.

[51] Yumei Yong, Chao Yang, Yi Jiang, Ameya Joshi, Youchun Shi, and Xiaolong Yin. Numerical simulation of immiscible liquid-liquid flow in microchannels using lattice Boltzmann method. *Science China Chemistry*, 54(1):244–256, 2011. ISSN 16747291. doi: 10.1007/s11426-010-4164-z.

[52] Abdelkader Salim, Mostafa Fourar, Jacques Pironon, and Judith Sausse. Oil-water two-phase flow in microchannels: FLow patterns and pressure drop measurements. *Canadian Journal of Chemical Engineering*, 86(6):978–988, 2008. ISSN 00084034. doi: 10.1002/cjce.20108.

[53] Zhen Cao, Zan Wu, and Bengt Sundén. Dimensionless analysis on liquid-liquid flow patterns and scaling law on slug hydrodynamics in cross-junction microchannels. *Chemical Engineering Journal*, 344:604–615, 2018.

[54] Zan Wu, Zhen Cao, and Bengt Sundén. Liquid-liquid flow patterns and slug hydrodynamics in square microchannels of cross-shaped junctions. *Chemical Engineering Science*, 174:56–66, 2017.

[55] Ich-Long Ngo, Sang Woo Joo, and Chan Byon. Effects of junction angle and viscosity ratio on droplet formation in microfluidic cross-junction. *Journal of Fluids Engineering*, 138(5), 2016.

[56] Madhvanand N. Kashid and David W. Agar. Hydrodynamics of liquid–liquid slug flow capillary microreactor: Flow regimes, slug size and pressure drop. *Chemical Engineering Journal*, 131(1-3):1–13, July 2007. ISSN 13858947. doi: 10.1016/j.cej.2006.11.020. URL https://linkinghub.elsevier.com/retrieve/pii/S1385894706005092.

[57] Anna A. Yagodnitsyna, Alexander V. Kovalev, and Artur V. Bilsky. Flow patterns of immiscible liquid-liquid flow in a rectangular microchannel with T-junction. *Chemical Engineering Journal*, 303:547–554, 2016. ISSN 13858947. doi: 10.1016/j.cej.2016.06.023. URL http://dx.doi.org/10.1016/j.cej.2016.06.023.

[58] Z. Liu. *Purifying Radionuclides with Microfluidic Technology for Medical Purpose: Simulating multiphase flows inside a microfluidic channel with the phase field method*. PhD thesis, Delft University of Technology, 2022. URL http://resolver.tudelft.nl/uuid:e1bebcdd-185a-4515-b352-76d68f65ace8.

[59] Yuchao Zhao, Guangwen Chen, and Quan Yuan. Liquid-liquid two-phase flow patterns in a rectangular microchannel. *AIChE journal*, 52(12):4052–4060, 2006.

[60] Madhvanand Kashid and Lioubov Kiwi-Minsker. Quantitative prediction of flow patterns in liquid–liquid flow in micro-capillaries. *Chemical Engineering and Processing: Process Intensification*, 50(10):972–978, October 2011. ISSN 02552701. doi: 10.1016/j.cep.2011.07.003. URL https://linkinghub.elsevier.com/retrieve/pii/S0255270111001553.

[61] Hamid Asadi-Saghandi, Javad Karimi-Sabet, Sohrabali Ghorbanian, and Seyed Mohammad Ali Moosavian. Dimensionless analysis on liquid–liquid two-phase flow patterns in a numbered-up microfluidic device. *Chemical Engineering Journal*, 429:132428, February 2022. ISSN 13858947. doi:

10.1016/j.cej.2021.132428. URL https://linkinghub.elsevier.com/retrieve/pii/S1385894721040067.

[62] Zhen Cao, Zan Wu, and Bengt Sundén. Dimensionless analysis on liquid-liquid flow patterns and scaling law on slug hydrodynamics in cross-junction microchannels. *Chemical Engineering Journal*, 344:604–615, July 2018. ISSN 13858947. doi: 10.1016/j.cej.2018.03.119. URL https://linkinghub.elsevier.com/retrieve/pii/S1385894718304789.

[63] M.N. Kashid, A. Renken, and L. Kiwi-Minsker. CFD modelling of liquid–liquid multiphase microstructured reactor: Slug flow generation. *Chemical Engineering Research and Design*, 88(3):362–368, March 2010. ISSN 02638762. doi: 10.1016/j.cherd.2009.11.017. URL https://linkinghub.elsevier.com/retrieve/pii/S0263876209003104.

[64] Li Lei, Yuting Zhao, Xinyu Wang, Gongming Xin, and Jingzhi Zhang. Experimental and numerical studies of liquid-liquid slug flows in micro channels with Y-junction inlets. *Chemical Engineering Science*, 252:117289, April 2022. ISSN 00092509. doi: 10.1016/j.ces.2021.117289. URL https://linkinghub.elsevier.com/retrieve/pii/S000925092100854X.

[65] Siva Kumar Reddy Cherlo, Sreenath Kariveti, and S. Pushpavanam. Experimental and Numerical Investigations of Two-Phase (Liquid−Liquid) Flow Behavior in Rectangular Microchannels. *Industrial & Engineering Chemistry Research*, 49(2):893–899, January 2010. ISSN 0888-5885, 1520-5045. doi: 10.1021/ie900555e. URL https://pubs.acs.org/doi/10.1021/ie900555e.

[66] Piyush Kumar and Manabendra Pathak. Dynamic wetting characteristics during droplet formation in a microfluidic T-junction. *International Journal of Multiphase Flow*, 156:104203, November 2022. ISSN 03019322. doi: 10.1016/j.ijmultiphaseflow.2022.104203. URL https://linkinghub.elsevier.com/retrieve/pii/S0301932222001823.

[67] Yuehao Li, Rupesh K. Reddy, Challa S. S. R. Kumar, and Krishnaswamy Nandakumar. Computational investigations of the mixing performance inside liquid slugs generated by a microfluidic T-junction. *Biomicrofluidics*, 8(5):054125, September 2014. ISSN 1932-1058. doi: 10.1063/1.4900939. URL https://pubs.aip.org/bmf/article/8/5/054125/386245/Computational-investigations-of-the-mixing.

[68] Yu Han, Xiaofei Xu, Fengxia Liu, Wei Wei, and Zhijun Liu. Dimensionless Analysis of the Effects of Junction Angle on the Gas-Liquid Two-Phase Flow Transition and the Scaling Law of the Microbubble Generation Characteristics in Y-Junctions. *Sustainability*, 14(14):8592, July 2022. ISSN 2071-1050. doi: 10.3390/su14148592. URL https://www.mdpi.com/2071-1050/14/14/8592.

[69] Yujie Li, Jie Wang, Di Li, and Ronggang Liu. Flow pattern diagrams of oil-water two-phase microflows and stable parallel flows obtained at low Reynolds numbers. *International Journal of Multiphase Flow*, 98:139–146, January 2018. ISSN 03019322. doi: 10.1016/j.ijmultiphaseflow.2017.09.008. URL https://linkinghub.elsevier.com/retrieve/pii/S0301932217302252.

[70] Pierre Guillot and Annie Colin. Stability of parallel flows in a microchannel after a T junction. *Physical Review E*, 72(6):066301, December 2005. ISSN 1539-3755, 1550-2376. doi: 10.1103/PhysRevE.72.066301. URL https://link.aps.org/doi/10.1103/PhysRevE.72.066301.

[71] Andrej Pohar, Mitja Lakner, and Igor Plazl. Parallel flow of immiscible liquids in a microreactor: modeling and experimental study. *Microfluidics and Nanofluidics*, 12(1-4):307–316, January 2012. ISSN 1613-4982, 1613-4990. doi: 10.1007/s10404-011-0873-7. URL http://link.springer.com/10.1007/s10404-011-0873-7.

[72] Arata Aota, Kazuma Mawatari, Susumu Takahashi, Teruki Matsumoto, Kazuteru Kanda, Ryo Anraku, Akihide Hibara, Manabu Tokeshi, and Takehiko Kitamori. Phase separation of gas–liquid and liquid–liquid microflows in microchips. *Microchimica Acta*, 164(3-4):249–255, March 2009. ISSN 0026-3672, 1436-5073. doi: 10.1007/s00604-008-0085-3. URL http://link.springer.com/10.1007/s00604-008-0085-3.

[73] Arata Aota, Akihide Hibara, and Takehiko Kitamori. Pressure Balance at the Liquid−Liquid Interface of Micro Countercurrent Flows in Microchips. *Analytical Chemistry*, 79(10):3919–3924, May 2007. ISSN 0003-2700, 1520-6882. doi: 10.1021/ac070031d. URL https://pubs.acs.org/doi/10.1021/ac070031d.

[74] Akihide Hibara, Shinobu Iwayama, Shinya Matsuoka, Masaharu Ueno, Yoshikuni Kikutani, Manabu Tokeshi, and Takehiko Kitamori. Surface Modification Method of Microchannels for Gas−Liquid Two-Phase Flow in Microchips. *Analytical Chemistry*, 77(3):943–947, February 2005. ISSN 0003-2700, 1520-6882. doi: 10.1021/ac0490088. URL https://pubs.acs.org/doi/10.1021/ac0490088.

[75] Adelina Smirnova, Kazuma Mawatari, Akihide Hibara, Mikhail A. Proskurnin, and Takehiko Kitamori. Micro-multiphase laminar flows for the extraction and detection of carbaryl derivative. *Analytica Chimica Acta*, 558(1-2):69–74, February 2006. ISSN 00032670. doi: 10.1016/j.aca.2005.10.073. URL https://linkinghub.elsevier.com/retrieve/pii/S0003267005018519.

[76] Tatsuo Maruyama, Tomoaki Kaji, Tomohiro Ohkawa, Ken-ichiro Sotowa, Hironari Matsushita, Fukiko Kubota, Noriho Kamiya, Katsuki Kusakabe, and Masahiro Goto. Intermittent partition walls promote solvent extraction of

metal ions in a microfluidic device. *The Analyst*, 129(11):1008, 2004. ISSN 0003-2654, 1364-5528. doi: 10.1039/b411630p. URL http://xlink.rsc.org/?DOI=b411630p.

[77] Paul Vulto, Susann Podszun, Philipp Meyer, Carsten Hermann, Andreas Manz, and Gerald A. Urban. Phaseguides: a paradigm shift in microfluidic priming and emptying. *Lab on a Chip*, 11(9):1596, 2011. ISSN 1473-0197, 1473-0189. doi: 10.1039/c0lc00643b. URL http://xlink.rsc.org/?DOI=c0lc00643b.

[78] Sachit Goyal, Amit V. Desai, Robert W. Lewis, David R. Ranganathan, Hairong Li, Dexing Zeng, David E. Reichert, and Paul J.A. Kenis. Thiolene and SIFEL-based microfluidic platforms for liquid–liquid extraction. *Sensors and Actuators B: Chemical*, 190:634–644, January 2014. ISSN 09254005. doi: 10.1016/j.snb.2013.09.065. URL https://linkinghub.elsevier.com/retrieve/pii/S0925400513011064.

[79] Junior D Seader, Ernest J Henley, and D Keith Roper. *Separation process principles*, volume 25. wiley New York, 1998.

[80] Donata Maria Fries, Tobias Voitl, and Philipp Rudolf von Rohr. Liquid extraction of vanillin in rectangular microreactors. *Chemical Engineering and Technology*, 31(8):1182–1187, 2008. ISSN 09307516. doi: 10.1002/ceat.200800169.

[81] Shufang Zhao, Wentan Wang, Mengxue Zhang, Ting Shao, Yong Jin, and Yi Cheng. Three-dimensional simulation of mixing performance inside droplets in micro-channels by Lattice Boltzmann method. *Chemical Engineering Journal*, 207-208:267–277, 2012. ISSN 13858947. doi: 10.1016/j.cej.2012.06.098. URL http://dx.doi.org/10.1016/j.cej.2012.06.098.

[82] Amin Farahani, Ahmad Rahbar-Kelishami, and Hadi Shayesteh. Microfluidic solvent extraction of Cd(II) in parallel flow pattern: Optimization, ion exchange, and mass transfer study. *Separation and Purification Technology*, 258:118031, March 2021. ISSN 13835866. doi: 10.1016/j.seppur.2020.118031. URL https://linkinghub.elsevier.com/retrieve/pii/S1383586620325041.

[83] Davide Ciceri, Lachlan R. Mason, Dalton J. E. Harvie, Jilska M. Perera, and Geoffrey W. Stevens. Modelling of interfacial mass transfer in microfluidic solvent extraction: part II. Heterogeneous transport with chemical reaction. *Microfluidics and Nanofluidics*, 14(1-2):213–224, January 2013. ISSN 1613-4982, 1613-4990. doi: 10.1007/s10404-012-1039-y. URL http://link.springer.com/10.1007/s10404-012-1039-y.

[84] Gwendolyne Hellé, Sean Roberston, Siméon Cavadias, Clarisse Mariet, and Gérard Cote. Toward numerical prototyping of labs-on-chip: modeling for

liquid–liquid microfluidic devices for radionuclide extraction. *Microfluidics and Nanofluidics*, 19(5):1245–1257, November 2015. ISSN 1613-4982, 1613-4990. doi: 10.1007/s10404-015-1643-8. URL http://link.springer.com/10.1007/s10404-015-1643-8.

[85] H. Karim, C. Castel, A. Lélias, A. Magnaldo, and P. Sarrat. Kinetic study of uranium (VI) extraction with tributyl-phosphate in a stratified flow microchannel. *Separation and Purification Technology*, 314:123489, June 2023. ISSN 13835866. doi: 10.1016/j.seppur.2023.123489. URL https://linkinghub.elsevier.com/retrieve/pii/S1383586623003970.

[86] Haihu Liu and Yonghao Zhang. Droplet formation in microfluidic cross-junctions. *Physics of Fluids*, 23(8), 2011. ISSN 10706631. doi: 10.1063/1.3615643.

[87] S. Van Der Graaf, T. Nisisako, C. G.P.H. Schroën, R. G.M. Van Der Sman, and R. M. Boom. Lattice Boltzmann simulations of droplet formation in a T-shaped microchannel. *Langmuir*, 22(9):4144–4152, 2006. ISSN 07437463. doi: 10.1021/la052682f.

[88] Feng Bai, Xiaoming He, Xiaofeng Yang, Ran Zhou, and Cheng Wang. Three dimensional phase-field investigation of droplet formation in microfluidic flow focusing devices with experimental validation. *International Journal of Multiphase Flow*, 93:130–141, 2017.

[89] Sauro Succi. Mesoscopic Modeling of Slip Motion at Fluid-Solid Interfaces with Heterogeneous Catalysis. *Physical Review Letters*, 89(6):064502, July 2002. ISSN 0031-9007, 1079-7114. doi: 10.1103/PhysRevLett.89.064502. URL https://link.aps.org/doi/10.1103/PhysRevLett.89.064502.

[90] Timm Krüger, Halim Kusumaatmaja, Alexandr Kuzmin, Orest Shardt, Goncalo Silva, and Erlend Magnus Viggen. *The Lattice Boltzmann Method: Principles and Practice*. Graduate Texts in Physics. Springer International Publishing, Cham, 2017. ISBN 978-3-319-44647-9 978-3-319-44649-3. doi: 10.1007/978-3-319-44649-3. URL http://link.springer.com/10.1007/978-3-319-44649-3.

[91] R. G.M. Van Der Sman. Galilean invariant lattice Boltzmann scheme for natural convection on square and rectangular lattices. *Physical Review E - Statistical, Nonlinear, and Soft Matter Physics*, 74(2), 2006. ISSN 15393755. doi: 10.1103/PhysRevE.74.026705.

[92] Yuhang Fu, Lin Bai, Kexin Bi, Shufang Zhao, Yong Jin, and Yi Cheng. Numerical study of Janus droplet formation in microchannels by a lattice Boltzmann method. *Chemical Engineering and Processing: Process Intensification*, 119:34–43, September 2017. ISSN 02552701. doi: 10.1016/j.cep.2017.05.019. URL https://linkinghub.elsevier.com/retrieve/pii/S0255270116306572.

[93] Zhao Yu, Orin Hemminger, and Liang Shih Fan. Experiment and lattice Boltzmann simulation of two-phase gas-liquid flows in microchannels. *Chemical Engineering Science*, 62(24):7172–7183, 2007. ISSN 00092509. doi: 10.1016/j.ces.2007.08.075.

[94] Stéphane Popinet. Numerical Models of Surface Tension. *Annual Review of Fluid Mechanics*, 50(1):49–75, January 2018. ISSN 0066-4189, 1545-4479. doi: 10.1146/annurev-fluid-122316-045034. URL https://www.annualreviews.org/doi/10.1146/annurev-fluid-122316-045034.

[95] I. Halliday, R. Law, C. M. Care, and A. Hollis. Improved simulation of drop dynamics in a shear flow at low Reynolds and capillary number. *Physical Review E - Statistical, Nonlinear, and Soft Matter Physics*, 73(5):1–11, 2006. ISSN 15393755. doi: 10.1103/PhysRevE.73.056708.

[96] Arata Aota, Kazuma Mawatari, and Takehiko Kitamori. Parallel multiphase microflows: fundamental physics, stabilization methods and applications. *Lab on a Chip*, 9(17):2470, 2009. ISSN 1473-0197, 1473-0189. doi: 10.1039/b904430m. URL http://xlink.rsc.org/?DOI=b904430m.

[97] Yangcheng Lu, Yang Xia, and Guangsheng Luo. Phase separation of parallel laminar flow for aqueous two phase systems in branched microchannel. *Microfluidics and Nanofluidics*, 10(5):1079–1086, May 2011. ISSN 1613-4982, 1613-4990. doi: 10.1007/s10404-010-0736-7. URL http://link.springer.com/10.1007/s10404-010-0736-7.

[98] Francesca Garbarino, Kasper Kistrup, Giovanni Rizzi, and Mikkel Fougt Hansen. Burst pressure of phaseguide structures of different heights in all-polymer microfluidic channels. *Journal of Micromechanics and Microengineering*, 27(12):125015, December 2017. ISSN 0960-1317, 1361-6439. doi: 10.1088/1361-6439/aa97b7. URL https://iopscience.iop.org/article/10.1088/1361-6439/aa97b7.

[99] J. H. Lu, H. Y. Lei, and C. S. Dai. Lattice Boltzmann equation for mass transfer in multi solvent systems. *International Journal of Heat and Mass Transfer*, 132(April):519–528, 2019. ISSN 00179310. doi: 10.1016/j.ijheatmasstransfer.2018.12.010.

[100] Giancarlo Pascali, Paul Watts, and Piero A Salvadori. Microfluidics in radiopharmaceutical chemistry. *Nuclear medicine and biology*, 40(6):776–787, 2013.

[101] Yasutoshi Ban, Yoshikuni Kikutani, Manabu Tokeshi, and Yasuji Morita. Extraction of Am(III) at the Interface of Organic-Aqueous Two-Layer Flow in a Microchannel. *Journal of Nuclear Science and Technology*, 48(10):1313–1318, October 2011. ISSN 0022-3131, 1881-1248. doi: 10.1080/18811248.2011.9711821. URL http://www.tandfonline.com/doi/abs/10.1080/18811248.2011.9711821.

[102] Akihide Hibara, Mao Fukuyama, Myungwha Chung, Craig Priest, and Mikhail A. Proskurnin. Interfacial Phenomena and Fluid Control in Micro/Nanofluidics. *Analytical Sciences*, 32(1):11–21, January 2016. ISSN 0910-6340, 1348-2246. doi: 10.2116/analsci.32.11. URL https://link.springer.com/10.2116/analsci.32.11.

[103] D. Maria Fries, T. Voitl, and P. Rudolf von Rohr. Liquid Extraction of Vanillin in Rectangular Microreactors. *Chemical Engineering & Technology*, 31(8):1182–1187, August 2008. ISSN 09307516, 15214125. doi: 10.1002/ceat.200800169. URL https://onlinelibrary.wiley.com/doi/10.1002/ceat.200800169.

2

Theory

In this chapter, the theory behind the transport phenomena observed in the subsequent chapters will be discussed. First, a basic overview of the fluid mechanics and multiphase flow will be provided, followed by an introduction to wetting and contact angle hysteresis. We mentioned that the Lattice Boltzmann Method (LBM) will be used to simulate flow phenomena in chapter 1, and the theory behind that will also be laid out. Finally, the equations for mass transfer are provided along with the underlying theory, followed by a description of the Finite Difference Method (FDM).

2.1. Fluid Dynamics

A fluid (liquid or gas) is a substance that deforms or moves continuously under the action of external forces, and fluid mechanics is the study of fluids at rest or motion [1]. This section describes some of the concepts used in fluid mechanics.

2.1.1. Navier-Stokes Equation

The Navier-Stokes equation is used to describe fluid flow and behaviour by expressing the momentum balance. These equations are also coupled with the mass conservation (continuity equation), and both these equations are given by [1]:

$$\begin{cases} \frac{\partial \rho}{\partial t} + \nabla \cdot (\rho \mathbf{u}) = 0 \\ \frac{\partial \rho \mathbf{u}}{\partial t} + \nabla \cdot (\rho \mathbf{u}.\nabla \mathbf{u}) = -\nabla p + \nabla \cdot \boldsymbol{\tau} + \rho \mathbf{g} \end{cases} \tag{2.1}$$

where ρ refers to the density of the fluid, u the characteristic fluid velocity, p the pressure, $\boldsymbol{\tau}$ the shear stress and $\mathbf{g}$ the body force term, which usually corresponds to gravity. However, for the case of incompressible flow (density or volume doesn't change with pressure), the above equations simplify to the following form:

$$\begin{cases} \nabla \cdot \mathbf{u} = 0 \\ \rho \frac{D\mathbf{u}}{Dt} = -\nabla p + \mu \nabla^2 \mathbf{u} + \rho \mathbf{g} \end{cases} \tag{2.2}$$

where $\frac{D}{Dt} = \frac{\partial}{\partial t} + \mathbf{u} \cdot \nabla$ is the material derivative and μ is the shear viscosity of the fluid.

2.1.2. Contact Angle

Multiphase flow refers to the simultaneous flow of two or more phases [2]. These phases can constitute the same fluid (like water and water vapour) or different fluids. When one is dealing with multiphase flows enclosed by a solid boundary, there are two forces to consider in addition to the inertial and viscous forces present in single-phase flows. These are the cohesive forces, which are the forces between liquid molecules (described by the interfacial tension discussed in Chapter 1), and the adhesive forces, the forces between liquid and solid molecules [3].

The interaction of these two forces has a considerable influence on the behaviour of a fluid near a solid boundary, with the effects sometimes extending to the bulk as well. This interaction is visualized as the angle made by the two interfaces – liquid-liquid and liquid-solid interfaces. This angle is termed the contact angle, and its value is indicative of how wettable the surface is [3].

As shown in Figure 2.1a, a smaller contact angle (θ_c) implies that the liquid has a greater affinity for the surface and a contact angle of 0 ° implies that the liquid spreads evenly on the surface. On the other hand, surfaces with a contact angle greater than 90 ° are called non-wetting as the liquid tries to detach from the surface [4] (Figure 2.1b. A contact angle of 90 ° corresponds to a neutrally wetting surface.

The formula for the contact angle in a homogeneous surface was developed by Thomas Young in 1805 [5], based on the balance of the interfacial forces as shown in Figure 2.1a. The formula is given by:

$$cos(\theta_c) = \frac{\sigma_{SG} - \sigma_{SL}}{\sigma_{LG}} \tag{2.3}$$

where θ_c is the contact angle, σ is the surface tension, and the subscripts S, L, and G correspond to solid, liquid and gas respectively. Note that the gas phase can be a liquid as well.

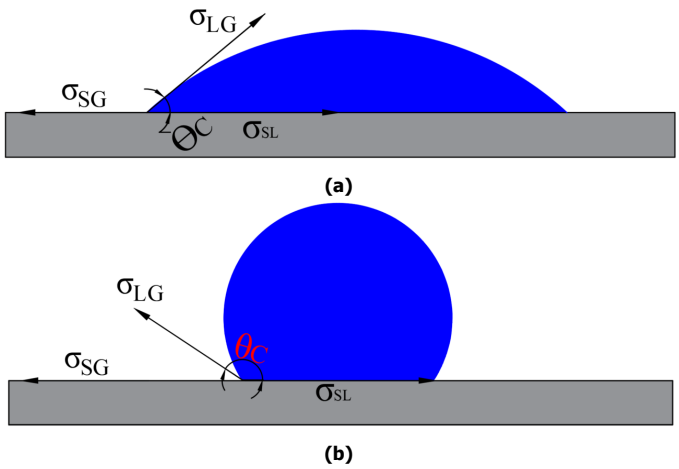

Figure 2.1: a) An example of a wetting surface. In such a surface, the droplet tries to spread over the surface. b)An example of a non-wetting surface. The droplet tries to detach from the surface in this case.

The above definition of the contact angle is valid only for a homogeneous and chemically smooth surface. In reality, such surfaces are almost impossible to find. The roughness of the surface introduces a range of contact angles instead of one metastable value as defined by Equation 2.3 [6]. The angle defined by Young's

equation is called the equilibrium/static contact angle, i.e., the contact angle of the surface, if it's perfectly homogeneous [7].

Generally, the contact angle θ varies in the range denoted by $\theta_r < \theta < \theta_a$. θ_r, the receding contact angle, is defined as the angle with which the droplet recedes with respect to the surface if some liquid is removed, and θ_a, the advancing contact angle, is defined as the angle by which the droplet advances if some liquid is added to the droplet [8].

The advancing and receding angles depend on the physical and chemical properties of the surface and fluids, and history effects. The difference between these two angles is called hysteresis. The presence of surface heterogeneities makes it difficult for the fluid to maintain the same contact angle throughout, as some configurations might lead to an increased interfacial area. To avoid this energy cost, the contact angle on the surface keeps varying. In the presence of bulk fluid velocity, contact line motion is also possible. Contact line motion only occurs when the advancing angle is exceeded or the contact angle is below the receding angle. This is because there is an energy cost associated with the contact line motion, and it is thus resisted until the hysteresis limits are reached, after which it is no longer energetically viable for the droplet to maintain its original configuration [8].

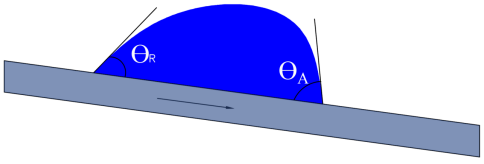

Figure 2.2: Illustration of contact angle hysteresis. A droplet is sliding on an inclined plane under the action of gravitational forces. The droplet shape deforms, with the contact angle at the front being the advancing contact angle (subscript 'A') and the contact angle at the rear being the receding contact angle (subscript 'R').

Contact angle hysteresis is illustrated in Figure 2.2. The motion of a droplet along an inclined plane is considered. Under the action of gravitational forces, the droplet starts sliding downward. This can occur only if the droplet simultaneously advances on the downhill side and recedes on the uphill side. The same applies to droplet motion even in a horizontal plane, where the droplet moves along the direction of bulk velocity. However, the droplet's shape needs to be changed before it can move for a hysteresis greater than zero [8]. Therefore, there is an activation energy necessary for motion and subsequent un-pinning of the contact line [8].

2.2. Computational Fluid Dynamics (CFD)

Computational Fluid Dynamics (CFD) refers to the simulation of the fluid flow field by obtaining a numerical description of the fluid flow using approximations of the gov-

erning Navier-Stokes equations (Equation 2.1) [9]. The choice of the CFD method is contingent on several factors such as flow regime, number of phases and the scale of the problem.

In the case of multiphase microfluidic flow, the fluids mostly flow in the laminar regime, which is indicated by a lower value of Reynold's number [10]. The commonly used techniques for simulating two-phase flow at the microscale include Level Set [11, 12], Volume of Fluid (VOF) [13, 14] and phase field method [15, 16]. One method which is increasingly gaining traction in the field of multiphase microfluidics is the LBM, and that will be the focus of the next section.

2.3. Lattice Boltzmann Method (LBM)

The LBM is essentially an extension of the Cellular Automata (CA) technique invented by John Von Neumann in the 1950s [17]. In order to understand the mechanisms leading to self-replication in biological organisms, Neumann devised a fully discrete system made up of cells. All these cells have a characteristic internal state which consists of a finite number of information bits [18]. The system evolves via discrete steps in time and space by programming the fundamental "rules" determining the evolution of the system into each cell. The evolution of each cell is a function of the states of the neighbouring cells. Though this system appears to be simple, it has been used to successfully capture a range of phenomena such as pattern formation, transport phenomena and laminar flow [18].

However, the deficiencies associated with its discrete nature naturally led to inaccuracies when dealing with more complex problems. There are also issues related to the flexibility of the parameters when describing a wider range of physical phenomena [18]. Thus, it would be better to describe the problem using real-valued states that correspond to probabilities rather than discrete deterministic states. McNamara and Zanetti [19] extended the Boolean framework of (CA) to describe real values by calculating the probability of a cell having a given state. Though this improved the applicability of the method, the neglect of many-body correlations and interaction among the cells from different directions led to numerical instabilities and didn't provide the whole picture of the phenomenon. This was remedied by Higuera *et al* [20], who set the foundations for LBM as it is known today.

The LBM is based on the numerical modelling of the Boltzmann equation [21]. Though the Boltzmann equation describes the dynamics of a gas in the mesoscale, it can be easily related and extended to the macroscale, thereby broadening the scope of the method to include heat and mass transfer, chemical kinetics, fluid mechanics and more.

The LBM tracks the variability of the probabilistic particle distribution function $f(\mathbf{x}, \boldsymbol{\varepsilon}, t)$ across a discrete lattice mesh. Here, $\mathbf{x}, \boldsymbol{\varepsilon}, t$ correspond to the position vector, microscopic velocity vector and time respectively. Since the method uses a discrete lattice mesh, the simplicity of CA is retained while allowing more complex

scenarios to be modelled.

2.3.1. LBM for single-phase flow

As mentioned in the previous section, the LBM can be numerically related to the Navier-Stokes equation through the Boltzmann equation. There are numerous advantages in simulating fluid flow using the LBM, and many of them stem from the inherent simplicity of the model through its usage of discrete lattice sites and the Boltzmann equation. The Navier-Stokes equation need not be solved and this saves a considerable amount of time and effort. This also has a strong physical basis because of the well-established Boltzmann equation [21, 18]. LBM was found to be second-order accurate for the weakly compressible Navier-Stoke equation.

In traditional methods, the non-linear advection term $u \cdot \nabla u$ is difficult to discretize as these derivative approximations need to be determined non-linearly. In LBM, however, the non-linearity is located in a local collision process within each node, thereby ensuring that the particle description is local and within the node themselves [21]. Therefore, its localised approach makes the LBM very amenable to parallelization.

Even though the method uses a simple lattice mesh, it can be easily extended to complex geometries and also conserves mass in such flows [22]. Moving boundaries can be implemented in a such manner that the mass is conserved [23]. The mesoscale nature of LBM makes it very suitable for microfluidics [10, 24]. Thermal fluctuations and aeroacoustics can also be simulated by LBM [21].

Since the LBM models the fluid in terms of particle distributions, the particle motions need to be accordingly related to the macroscopic fluid motions. These distribution functions at a particular node can be easily correlated to the fluid properties through the weighted sum of the Particle Distribution Functions (PDF) in each direction:

$$\begin{aligned} \rho(\mathbf{x}, t) &= \sum_i f_i(\mathbf{x}, t) \\ \rho\mathbf{u}(\mathbf{x}, t) &= \sum_i \mathbf{e}_i f_i(\mathbf{x}, t) \end{aligned} \tag{2.4}$$

Here, i refers to the direction of the discrete PDF and e_i is the discrete velocity along the ith direction. Discrete velocity models are specified as $\mathrm{D}_n\mathrm{Q}_m$, where n is the dimension and m represents the number of possible directions [21, 25]. Commonly used models include D2Q7, D2Q9, D3Q15 and D3Q15, all of which are illustrated in Figure 2.3. For the D2Q9 model, the discrete velocities are given by:

$$\begin{bmatrix} \mathbf{e}_0 & \mathbf{e}_1 & \mathbf{e}_2 & \mathbf{e}_3 & \mathbf{e}_4 & \mathbf{e}_5 & \mathbf{e}_6 & \mathbf{e}_7 & \mathbf{e}_8 \end{bmatrix} = c \begin{bmatrix} 0 & 1 & 0 & -1 & 0 & 1 & -1 & -1 & 1 \\ 0 & 0 & 1 & 0 & -1 & 1 & 1 & -1 & -1 \end{bmatrix}$$

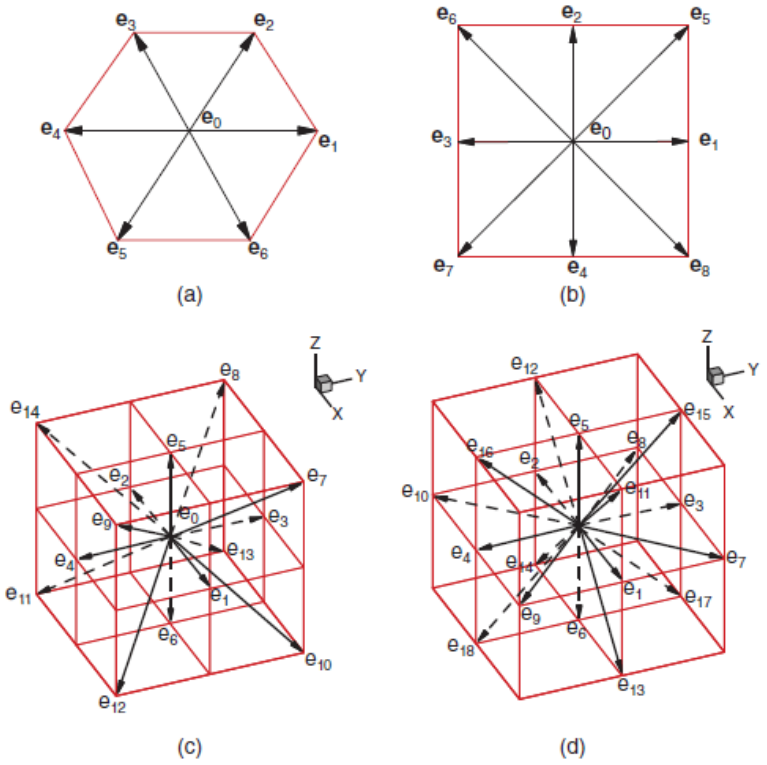

Figure 2.3: Discrete velocity models [25] a) D2Q7 b)D2Q9 c) D3Q15 d) D3Q19

Here $c = \frac{\Delta x}{\Delta t}$ is the lattice speed, where Δx is defined as 1 lattice unit and Δt is the time step. The PDFs are streamed or propagated to the neighbouring nodes. This is akin to the fluid flowing across the domain and this streaming step at each time step is given by the following equation [21]:

$$f_i(\mathbf{x} + \mathbf{e}_i \Delta t, t + \Delta t) = f_i^{'}(\mathbf{x}, t) \tag{2.5}$$

$f_i^{'}(\mathbf{x}, t)$ corresponds to the post-collision distribution function of the previous iteration. The collision or relaxation step basically represents the gas particles colliding with each other, and this can be likened to any form of resistance to the flow. The viscosity of the fluid manifests in this term in the form of relaxation time. Generally, the collision step is derived from the Bhatnagar-Gross-Kook (BGK) approximation of the Boltzmann equation [26] :

$$f_i(\mathbf{x} + \mathbf{e}_i \Delta t, t + \Delta t) = f_i(\mathbf{x}, t) - \frac{\Delta t}{\tau}(f_i(\mathbf{x}, t) - f_i^{eq}(\mathbf{x}, t)) + S_i(\mathbf{x}, t) \tag{2.6}$$

where $S_i(\mathbf{x}, t)$ is the source term added to the LBM equation, and this could be used to implement forces such as gravity. τ is the relaxation time and is related to the kinematic viscosity of the fluid by the following equation:

$$\nu = c_s^2(\tau - 0.5\Delta t) \tag{2.7}$$

c_s^2 is the speed of sound and is linked to the lattice speed by $c_s^2 = c^2/3$. The equilibrium distribution function is generally calculated as [21]:

$$f_i^{eq}(\mathbf{x}, t) = w_i \rho \left[1 + \frac{\mathbf{e}_i \cdot \mathbf{u}}{c_s^2} + \frac{(\mathbf{e}_i \cdot \mathbf{u})^2}{2c_s^4} - \frac{\mathbf{u}^2}{2c_s^2}\right] \tag{2.8}$$

w_i are the weights accorded to each direction, and for the D2Q9 model, the weights are given by :

$$\mathbf{w} = \begin{cases} w_0 = \frac{4}{9} \\ w_{1-4} = \frac{1}{9} \\ w_{5-8} = \frac{1}{36} \end{cases} \tag{2.9}$$

2.3.2. LBM for Multiphase Flow

The LBM has quickly developed into a very useful tool for simulating multiphase flows. In addition to the advantages when simulating single-phase flows, many multiphase LBM methods do not involve an explicit interface tracking step, thereby significantly reducing the computational load [25]. Since this is a fairly new simulation technique for multiphase flows, a wide range of models have been developed for different cases and are still undergoing amendments today. All the deficiencies associated with the multiphase LB models, such as the development of spurious currents at the interface [27, 28] and problems when simulating fluids of high density/viscosity ratio [25], are slowly being corrected to expand the range of LBM.

As mentioned before, there are a variety of Lattice Boltzmann models to choose from for multiphase flow. Among these, the most common are the Shan-Chen (SC) model developed by Shan and Chen [29], the colour-gradient or Rothman-Keller (RK) model developed by Gunstensen *et al* [30] and the free-energy model developed by Swift *et al* [31]. Modifications have been made to these basic models to broaden their application.

In the SC model, a forcing term is incorporated into the Lattice Boltzmann equation, replacing the ideal gas equation in single-phase LBM with a non-ideal, non-monotonic equation of state. It can be implemented in the form of a single component, where both fluids are represented by a single PDF, or by multiple components, where each fluid has its own PDF [25]. The forcing term in the model can be related to the surface tension of the fluids, and the adhesive forces between the solid surface and the liquid.

The SC model is the most intuitive of the options and the least time-consuming. It also allows density ratios of O(10), which can go up to O(100) with modifications. The surface tension depends on the density and viscosity ratios, though, and this makes the model a lot less flexible. Additionally, the accuracy of the model is limited as spurious currents are generated at the interface [25, 27].

The RK model represents each fluid using different "colours", where one component is a red-coloured fluid and the other is a blue-coloured fluid. The collision step in this case is modified to include a perturbation step, where the surface tension of the two fluids is applied. In addition to this, there is a redistribution step which ensures that the two fluids remain immiscible. One major advantage of this method is that surface tension and density ratios can be adjusted independently, unlike the other multiphase LBM methods. This makes the RK model a lot more flexible. The accuracy of the method is also very high, though it is very difficult for it to be implemented for fluids with high density and viscosity ratios [32, 25], although improvements are being made in this direction [33]. Spurious velocities are also observed at low Capillary numbers [33, 34], similar to methods such as Volume of Fluid [35].

To ensure thermodynamic consistency, Swift *et al* [31] incorporated the thermodynamic free energy into the pressure tensor in the Navier-Stokes equation, thus revising the equilibrium distribution function. A non-ideal equation of state is used for the free-energy density which in turn is used to determine the pressure. This model is similar to the phase-field method in its implementation of surface tension [36] which improves the accuracy of the model as it tracks changes in the diffuse interface through the order parameter. Higher density and viscosity ratios can also be simulated. The issue of Gallilean invariance is present in this model, though some papers have rectified that issue [37].

There are other models which are gaining ground, such as the one developed by Inamuro *et al* [38], He *et al* [39] and Santos *et al* [40]. However, these models either involve the solving of the Poisson equation for pressure or tracking the interface through a separate equation, thus overriding the advantages of LBM by making it more computationally expensive.

For our case of liquid-liquid flow in a Y-shaped channel, the RK model is chosen. Since we are dealing with liquids here, high density and viscosity ratios aren't necessary. Even if that is the case, modifications have been made to the equations by Ba *et al* [41] and Leclaire *et al* [33]. Leclaire *et al* [42] compared the RK and SC models for shear deformation of a droplet and terminal velocity of a rising bubble, and observed that though both models captured the flow phenomena, the RK model was more accurate. Additionally, the numerical parameters in the RK model were easier to adjust, whereas the SC required a new set of parameters for each case, and there is no direct method to determine the appropriate value of these parameters.

Though the problem associated with numerical parameters isn't as pronounced in the free-energy model as it is in the SC model, numerical parameters such as mobility and chemical potential aren't independent of fluid parameters, and these introduce numerical dimensionless numbers. Komrakova *et al* [36] identified these dimensionless numbers as the Peclet and Cahn numbers and studied the limits of stability for droplet deformation and breakup in shear flow. Though they narrowed down the ranges of these dimensionless numbers, the flexibility of the model is still limited as some reference data is needed to confirm the choice of Cahn and Peclet numbers. Additionally, the free-energy model is similar to the phase-field method, and the phase-field method was found to be less successful by Zheng Liu [43] in capturing leakage. Thus, the simplicity, flexibility and ease of application for liquid-liquid flows makes the RK model an attractive choice.

2.3.3. RK Model for Two-Phase Flow

The RK model used in this paper is similar to the one used by Ba *et al* [44] and Halliday *et al* [34]. The two immiscible fluids are represented as "colours", with each of these fluids has its own distribution function represented by f_i^k, where i is the lattice velocity direction and k corresponds to the kth fluid. The total distribution is the sum of these two distributions. The evolution of the distribution function is given by :

$$f_i^k(\mathbf{x} + \mathbf{e}_i\Delta t, t + \Delta t) = f_i^k(\mathbf{x}, t) + \Omega_i^k(f_i^k(\mathbf{x}, t)), \tag{2.10}$$

where $\mathbf{x}$ and t are the position and time, $\mathbf{e}_i$ is the lattice velocity in the ith direction, Δt is the time step and Ω_i^k is the collision operator. The collision operator consists of three parts :

$$\Omega_i^k = (\Omega_i^k)^{(3)}[(\Omega_i^k)^{(1)} + (\Omega_i^k)^{(2)}]. \tag{2.11}$$

$(\Omega_i^k)^{(1)}$ is the standard single-phase collision operator, $(\Omega_i^k)^{(2)}$ is the Pertubation Operator (PO) responsible for the interfacial tension and $(\Omega_i^k)^{(3)}$ is the redistribution operator which ensures that the two phases remain separated and the interface is maintained.

The Bhatnagar-Gross-Krook (BGK) operator for single-phase collision is similar to that described in Equation 2.12.

$$f_i^k(\mathbf{x} + \mathbf{e}_i\Delta t, t + \Delta t) = f_i^k(\mathbf{x}, t) - \frac{\Delta t}{\tau}(f_i^k(\mathbf{x}, t) - f_i^{k,eq}(\mathbf{x}, t)), \tag{2.12}$$

The macroscopic parameters for the individual fluids can be obtained from the distribution functions:

$$\begin{aligned} \rho^k &= \sum_i f_i^k \\ \rho\mathbf{u} &= \sum_i \sum_k \mathbf{e}_i f_i^k, \end{aligned} \tag{2.13}$$

where $\rho = \sum_k \rho^k$ is the density of the fluid mixture and $\mathbf{u}$ is the fluid velocity. We use the modified equilibrium distribution function proposed by Ba *et al* [44] to account for the error terms in the Chapman-Enskog expansion of the RK model [32].

$$f_i^{k,eq}(\rho^k, \mathbf{u}) = \rho^k \left(\phi_i^k + w_i \left[\frac{\mathbf{e}_i \cdot \mathbf{u}}{c_s^2} \left\{ 1 + 0.5 \left(\frac{(c_s^k)^2}{c_s^2} - 1 \right) \left(\frac{\mathbf{e}_i^2}{c_s^2} - 4 \right) \right\} + \frac{(\mathbf{e}_i \cdot \mathbf{u})^2}{2c_s^4} - \frac{\mathbf{u}^2}{2c_s^2} \right] \right).$$

Here, ϕ_i^k is a parameter related to the density ratio of the fluid and is defined as:

$$\phi_i^k = \begin{cases} \alpha^k, & i = 0 \\ (1 - \alpha^k)/5, & i = 1, 2, 3, 4 \\ (1 - \alpha^k)/20, & i = 5, 6, 7, 8. \end{cases} \tag{2.14}$$

α^k is a free parameter related to the speed of sound in each fluid by $(c_s^k)^2 = \frac{3c^2}{5}(1 - \alpha^k)$, and to the pressure in each phase through the equation of state, $p^k = \rho^k (c_s^k)^2$ [32]. The density ratio is therefore related to α by :

$$\frac{\rho^{\mathrm{R}}}{\rho^{\mathrm{B}}} = \frac{1 - \alpha^{\mathrm{B}}}{1 - \alpha^{\mathrm{R}}}. \tag{2.15}$$

Since we are concerned with the two fluids of different viscosity, the relaxation times at the diffuse interface should be defined accordingly. We adopt the following scheme defined by Huang *et al* [32].

$$\tau(\mathbf{x}) = \begin{cases} \tau^{\mathrm{R}}, & \rho^{\mathrm{N}} > \delta \\ s_1 + s_2 \rho^{\mathrm{N}} + s_3 (\rho^{\mathrm{N}})^2, & \delta \geq \rho^{\mathrm{N}} > 0 \\ t_1 + t_2 \rho^{\mathrm{N}} + s_3 (\rho^{\mathrm{N}})^2, & 0 \geq \rho^{\mathrm{N}} \geq -\delta \\ \tau^{\mathrm{B}}, & \rho^{\mathrm{N}} < -\delta, \end{cases} \tag{2.16}$$

where $s_1 = t_1 = 2\frac{\tau^{\mathrm{B}}\tau^{\mathrm{R}}}{\tau^{\mathrm{B}}+\tau^{\mathrm{R}}}$, $s_2 = 2\frac{\tau^{\mathrm{R}}-s_1}{\delta}$, $s_3 = \frac{-s_2}{\delta}$, $t_2 = 2\frac{\tau^{\mathrm{B}}+s_1}{\delta}$, $t_3 = \frac{-t_2}{\delta}$. $\delta \leq 1$ is a free and positive parameter that affects the interface thickness, and is normally taken to be 0.98. ρ^{N} is the phase field/colour function indicating how much each fluid is located at a given node. It is defined as :

$$\rho^{\mathrm{N}}(\mathbf{x}, t) = \frac{\rho^{\mathrm{R}}(\mathbf{x}, t) - \rho^{\mathrm{B}}(\mathbf{x}, t)}{\rho^{\mathrm{R}}(\mathbf{x}, t) + \rho^{\mathrm{B}}(\mathbf{x}, t)}, \quad -1 \leq \rho^{\mathrm{N}} \leq 1. \tag{2.17}$$

The PO is similar to the one defined by Guo *et al*[45] and reads as follows:

$$(\Omega_i^k)^{(2)} = A^k w_i \left(1 - \frac{1}{2\tau^k} \right) \left[\frac{\mathbf{e}_i - \mathbf{u}}{c_s^2} + \frac{(\mathbf{e}_i \cdot \mathbf{u})\mathbf{e}_i}{c_s^2} \right] \cdot \mathbf{F}_s \Delta t \tag{2.18}$$

where A^k is the fraction of the interfacial tension contributed by the fluid k, and $\sum_k A^k = 1$. $\mathbf{F}_s$ is the body force term which is used to implement the interfacial

tension. Using the Continuum Surface Force (CSF) model of Brackbill *et al* [46], this term can be expressed as :

$$\mathbf{F}_s = \frac{1}{2}\sigma K \nabla \rho^{\mathrm{N}}. \tag{2.19}$$

Here, σ is the surface tension coefficient which can be directly implemented in the model, and K is the local curvature of the interface $K = -\nabla_{\mathrm{S}} \cdot \mathbf{n}$, with $\nabla_{\mathrm{S}} = (\mathbf{I} - \mathbf{nn}) \cdot \nabla$ being the surface gradient operator and $\mathbf{n}$ the outward-pointing unit normal vector of the interface which is given by:

$$\mathbf{n} = \frac{\nabla \rho^{\mathrm{N}}}{|\nabla \rho^{\mathrm{N}}|} \tag{2.20}$$

The curvature of the interface in 2D is given by:

$$K = n_x n_y \left(\frac{\partial}{\partial y} n_x + \frac{\partial}{\partial x} n_y \right) - n_x^2 \frac{\partial}{\partial y} n_y - n_y^2 \frac{\partial}{\partial x} n_x \tag{2.21}$$

The local fluid velocity needs to be modified to accommodate the spatially varying body force [45].

$$\rho \mathbf{u} = \sum_i \sum_k \mathbf{e}_i f_i^k(\mathbf{x}, t) + 0.5 \mathbf{F}_s \Delta t \tag{2.22}$$

Finally, we have the redistribution step, $(\Omega_i^k)^{(3)}$, which is applied to enhance phase separation of the two fluids [47].

$$\begin{aligned} f_i^{\mathbf{R}} &= \frac{\rho^{\mathrm{R}}}{\rho} f_i'(\mathbf{x}, t) + \beta \frac{\rho^{\mathrm{R}} \rho^{\mathrm{B}}}{\rho^2} \cos(\varphi_i) |\mathbf{e}_i| \sum_k f_i^{k,eq}(\rho^k, \alpha^k, \mathbf{u} = 0) \\ f_i^{\mathbf{B}} &= \frac{\rho^{\mathrm{B}}}{\rho} f_i'(\mathbf{x}, t) - \beta \frac{\rho^{\mathrm{R}} \rho^{\mathrm{B}}}{\rho^2} \cos(\varphi_i) |\mathbf{e}_i| \sum_k f_i^{k,eq}(\rho^k, \alpha^k, \mathbf{u} = 0), \end{aligned} \tag{2.23}$$

where β is a numerical parameter which influences numerical stability and interface thickness. A value of 0.7 is used for β, which is the most common value mentioned in literature as it provides the best balance between accuracy, stability and spurious velocities [41, 48]. φ_i is the angle between the phase field gradient and the lattice direction, and it is given by:

$$\cos(\varphi_i) = \frac{\mathbf{e}_i \cdot \nabla \rho^{\mathrm{N}}}{|\mathbf{e}_i||\nabla \rho^{\mathrm{N}}|} \tag{2.24}$$

The partial derivatives for the phase-field gradient and curvature are calculated using a 9-point finite different stencil as evaluated for any variable ψ by Liu *et al* [49].

$$\frac{\partial \psi(\mathbf{x})}{\partial x_\gamma} = \frac{1}{c_s^2} \sum_i w_i \psi(\mathbf{x} + \mathbf{e}_i \Delta t) e_{i\gamma}. \tag{2.25}$$

2.3.4. Boundary Conditions

In a discrete lattice mesh, three kinds of nodes are possible as depicted in Figure 2.4 [21]. The fluid nodes refer to the bulk where the Lattice Boltzmann equation is applied. At the solid nodes, no equation is solved. The boundary nodes provide the link between the fluid and solid nodes, and these require some special steps to apply the no-slip Boundary Condition (BC) or an inlet/outlet BC.

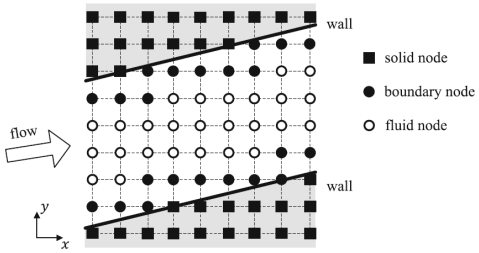

Figure 2.4: Various nodes in a lattice mesh [21]

At the boundary nodes, the PDF in some directions are unknown because there is no streaming from the solid node to the fluid node. In the case of stationary walls, the no-slip and no-penetration BCs are applied through the mid-way bounce-back method [21, 22]. The populations striking a rigid wall are reflected back to their original positions, thereby determining the unknown distribution functions in those directions. This process is illustrated in Figure 2.5 for a population moving along the positive x-axis towards a wall. The standard streaming step is replaced by the following formula:

$$f_{\bar{i}}(\mathbf{x}_b, t + \Delta t) = f_i^{'}(\mathbf{x}_b, t) \tag{2.26}$$

where x_b is the location of the boundary node, $\bar{i}$ corresponds to the direction opposite to i, and $f_i^{'}$ is the post-collision distribution function before the streaming step. From this equation, we can see that the populations are reflected back with the same velocity but in the opposite direction. For straight and flat boundaries, the bounceback method is second-order accurate.

However, this method presupposes the position of the wall to be located exactly halfway between two nodes. This is not the case for inclined walls and curved boundaries. For those cases, a staircasing technique is used to represent the non-flat boundary [22]. Naturally, this reduces to accuracy of the method to first-order for non-flat boundaries [21].

Numerous alternatives for non-flat boundaries have been proposed, such those by Guo *et al* [45], Bouzidi *et al* [50], Rohde *et al* [51], Mei *et al* [52] and Chun and Ladd [53]. However, few of these methods have been used for multiphase flow, and these introduce deficiencies such as larger spurious velocities when dealing with

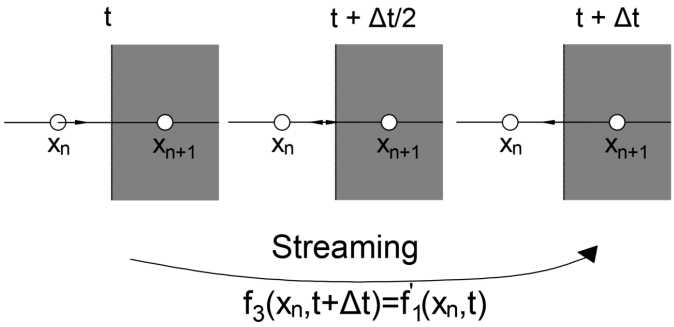

Figure 2.5: Illustration of the midway bounceback method [21]

multiphase flow. Most multiphase papers dealing with curved or inclined boundaries have therefore only used the midway bounceback method [54, 55, 56, 57].

For velocity inlets, the method described by Ladd [23] is used, which is an extension of the bounceback method. This implies that the particles gain a given amount of momentum after getting reflected. The PDFs are thus described near the inlet boundary as follows:

$$f_{\bar{i}}(\mathbf{x}_b, t + \Delta t) = f_i^{'}(\mathbf{x}_b, t) - 2w_i\rho_{\mathrm{w}}\frac{\mathbf{e}_i \cdot \mathbf{u}_{\mathrm{w}}}{c_s^2} \tag{2.27}$$

The subscript w indicates the inlet location, with $\mathbf{u}_{\mathrm{w}}$ being the inlet velocity. The density ρ_{w} is generally taken as the local density at the boundary node [21]. In the case of the outlet BC, a pressure BC is normally used for single-phase flow. However, since the pressure is linked to density, this is difficult to apply for multiphase flow. Huang *et al* [58] developed a method to apply the pressure BC based on the wet node bounceback technique of Zou and He [59]. They applied this method only for fluids of the same density, however, and large-amplitude oscillations are observed at the outlet when a fluid of different density passes through it [60].

A better outlet BC for multiphase flows is the application of the fully developed condition at the outlet. Lou *et al* [61] investigated the performances of three different outlet BCs - the Neumann, convective and extrapolation BC - in multiphase flow for various cases such as a moving droplet in a long channel and the same droplet in a channel with an obstacle. They observed that the convective BC gave the best results in terms of accuracy and stability, and that's what we have used for our outlet BC. The formulation of the convective BC at x=N, with N being the outlet location, is given by:

$$\frac{\partial \chi}{\partial t} + U\frac{\partial \chi}{\partial x} = 0 \tag{2.28}$$

χ refers to any quantity such as f, and U is the velocity normal to the boundary whose value can be either the maximum velocity of the nodes closest to the

boundary, the local velocity of the boundary node or the average velocity of (N-1)th layer near the boundary. Lou *et al* [61] compared these three schemes as well, and found that the averaging scheme gave the most accurate results, which is exactly what we have used as well. In the mesoscale, this equation can be written for x=N as:

$$f_i(N, t + \Delta t) = \frac{f_i(N, t) + \lambda f_i(N - 1, t + \Delta t)}{1 + \lambda}/, \tag{2.29}$$

with $\lambda = U(t + \Delta t)\Delta t/\Delta x$.

2.3.5. Contact Angle at an Inclined Plane

This subsection details the contact angle implementation at the boundary. Generally, the contact angle is applied by specifying a fictitious density at the boundary that is related to the contact angle [62]. However, this method is not only inaccurate, but it also induces spurious velocities [63]. A better approach was developed by Liu *et al* [64] based on a geometric formulation proposed by Ding and Spelt [65]. The method was found to conserve mass and give accurate results. However, this method is applicable only for flat boundaries.

A recent approach for applying contact angle in non-flat or inclined boundaries was developed by Leclaire *et al* [28] and later modified by Xu *et al* [48] for greater accuracy and stability. According to this approach, the lattice nodes are divided into 4 categories (shown in Figure 2.6):

- C_{FB}: the nodes which are located in the fluid domain and in contact with at least one node in the solid domain
- C_{FL}: the nodes which are located in the fluid domain and not in contact with any node in the solid domain
- C_{SB}: the nodes which are located in the solid domain and in contact with at least one node in the fluid domain
- C_{SL}: the nodes which are located in the solid domain and not in contact with any node in the fluid domain

The color gradient $\nabla\rho^{\mathrm{N}}$ for the points at C_{FB} requires the phase field at C_{SB} according to the 9-point stencil in Equation 2.25. The contact angle is implemented at C_{FB} through the modification of the colour gradient. The colour gradient is modified in such a way that the interface normal is at an angle θ as shown in Figure 2.7. The value of the phase field at C_{SB} is first obtained through a weighted average of its nearest fluid node neighbours.

$$\rho^{\mathrm{N}}_{SB} = \frac{\sum_{(i:\mathbf{x}+\mathbf{e}_i\Delta t\ \in C_{\mathrm{FB}})}\ w_i\rho^{\mathrm{N}}(\mathbf{x} + \mathbf{e}_i\Delta t)}{\sum_{(i:\mathbf{x}+\mathbf{e}_i\Delta t\ \in C_{\mathrm{FB}})}\ w_i} \tag{2.30}$$

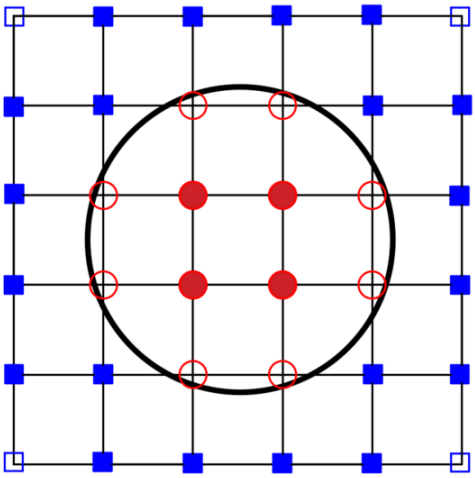

Figure 2.6: Representation of the lattice nodes used in implementing the contact angle in a lattice grid. The fluid is encased within a circular boundary in this case for the sake of representation. Red circles point to the fluid nodes, with the filled nodes corresponding to C_{FL} and the open circles corresponding to C_{FB}. The blue triangles represent the solid nodes, with the filled nodes corresponding to C_{SB} and open nodes corresponding to C_{SL}.

The colour gradient at C_{FB} can now be determined using Equation 2.25. Since the phase field determined at C_{SB} is an estimate, the colour gradient at C_{FB} is also an estimate. Thus, the normal at the interface is also an estimate. $\nabla\rho^{\mathrm{N}^*}$ (Figure 2.7). The predicted unit normal at the interface is given by:

$$\mathbf{n}^* = \frac{\nabla\rho^{\mathrm{N}^*}}{|\nabla\rho^{\mathrm{N}^*}|} \tag{2.31}$$

This predicted normal is compared to the two interface normals, $\mathbf{n_1}$ and $\mathbf{n_2}$. The interface normals are determined from the normal perpendicular to the surface $\mathbf{n_s}$ and contact angle. The surface normal is given by :

$$\mathbf{n_s} = \frac{\sum_l w\left(|c_l|^2\right) s(\mathbf{x}+c_l\Delta t)c_l}{\left|\sum_l w\left(|c_l|^2\right) s(\mathbf{x}+c_l\Delta t)c_l\right|}\ ,\ \mathbf{x}\in C_{\mathrm{FB}} \tag{2.32}$$

where c_l is the lth mescoscopic velocity associated with the isotropic discretization, $s(\mathbf{x})$ is an indicator function that equals 1 for $\mathbf{x}\in C_{\mathrm{S}}$ and 0 elsewhere, and $w\left(|c_l|^2\right)$ is the weight function associated with the discretization . An eight-order discretization is used to minimize spurious velocities. The weights associated with these discretizations are the same as those specified in Sbragaglia *et al* [66]. Two interface normal vectors are possible for a given contact angle, and these can be determined from the surface normal.

$$\begin{aligned}\mathbf{n_1} &= \left(n_{s,x}\cos\theta - n_{s,y}\sin\theta, n_{s,y}\cos\theta + n_{s,x}\sin\theta\right)\\ \mathbf{n_2} &= \left(n_{s,x}\cos\theta + n_{s,y}\sin\theta, n_{s,y}\cos\theta - n_{s,x}\sin\theta\right)\end{aligned} \tag{2.33}$$

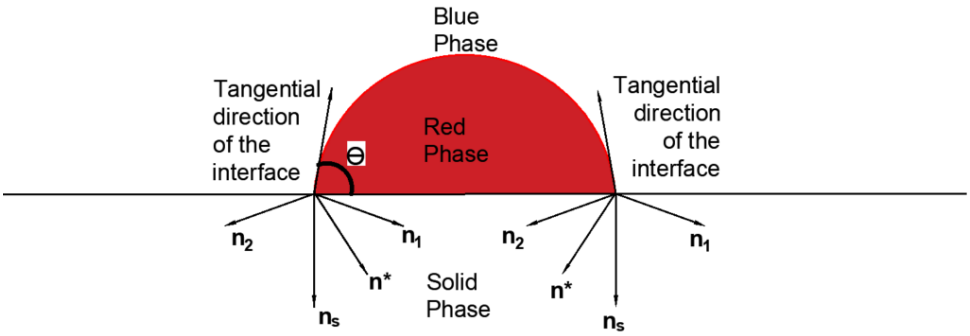

Figure 2.7: Image of the wetting boundary condition. $\mathbf{n_s}$ is the unit vector normal to the wall, $\mathbf{n_1}$ and $\mathbf{n_2}$ are the two interface normals, $\mathbf{n}^*$ is the predicted normal and θ is the contact angle.

The appropriate unit normal vector is chosen by calculating the Euclidean distances D_1 and D_2 from the predicted normal, and then selecting the correct interface normal.

$$\mathbf{n} = \begin{cases} \mathbf{n_1}, & D_1 < D_2 \\ \mathbf{n_2}, & D_1 > D_2 \\ \mathbf{n_s}, & D_1 = D_2 \end{cases} \tag{2.34}$$

The modified colour gradient is obtained by $\nabla\rho^{\mathrm{N}} = \left|\nabla\rho^{\mathrm{N}*}\right|\mathbf{n}$. The results from the RK model and the modifications made to it will be further discussed in Chapter 3.

2.4. Mass Transfer in Multiphase Flow

The transport of species in multiphase flow is governed by the Convection-Diffusion Equation (CDE) [67, 68]. The conservative form of the CDE describing the concentration of species i is given by:

$$\underbrace{\frac{\partial c_i}{\partial t}}_{\text{Transient term}} = \nabla \cdot \Big(\underbrace{D\nabla c_i}_{\text{Diffusive}} - \underbrace{\mathbf{u}c_i}_{\text{Convective}} \Big) + \underbrace{S_i}_{\text{Source / Sink}} \tag{2.35}$$

where c_i is the concentration of the species i, D is the diffusion coefficient, u is the velocity of the fluid and S_i is the source/sink term which corresponds to the generation/destruction of the species. Both the convective and diffusive terms compete with one another, and a measure of the dominant phenomenon is given by the Peclet number, which is the ratio of convective and diffusive mass transfer [69].

$$Pe = \frac{uL}{D} \tag{2.36}$$

where L is the characteristic length of the flow. Like the Navier-Stokes equations, Equation 2.35 is solved based on the approximations and boundary conditions

prescribed for a given problem. This thesis studies parallel flow, so the mass transfer equations described in the following section will correspond to parallel flow as well.

2.4.1. Mass Transfer for Parallel Flow

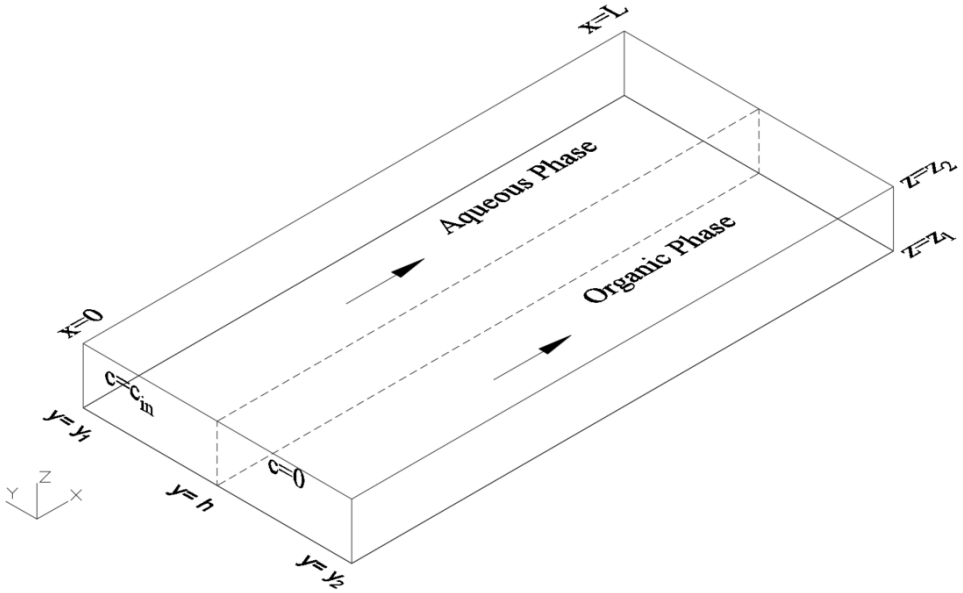

Figure 2.8: Mass transfer for parallel flow along the x direction. The interface is located at y=h. The species is located in the aqueous phase and will be transferred to the organic phase.

Figure 2.8 illustrates the mass transfer case for 3D parallel flow. The species is located in the aqueous phase and it will be extracted to the organic phase. To solve Equation 2.35 for parallel flow, the following assumptions and approximations are made:

1. Flow is laminar and fully developed.
2. Flow is steady.
3. The diffusion along the x direction can be neglected. This is because the Pe is of O (10^4), which indicates that convective transport dominates over diffusive transport.
4. Convection along the y and z directions can be neglected, as the velocity along the lateral directions is negligible in the case of parallel flow.
5. The interface is assumed to be straight even though it is curved in reality

Based on the figure and these assumptions, Equation 2.35 can be simplified to the following form:

$$\mathbf{u}\frac{\partial c}{\partial x} = D\left(\frac{\partial^2 c}{\partial y^2} + \frac{\partial^2 c}{\partial z^2}\right) \tag{2.37}$$

In 2D, the equation is further simplified to:

$$\mathbf{u}\frac{\partial c}{\partial x} = D\frac{\partial^2 c}{\partial y^2} \tag{2.38}$$

The boundary conditions (BC) applied are no species penetration at the adiabatic walls and an initial boundary condition at the inlet. The no-penetration BC ensures that there is no diffusion across the wall and is given by:

$$\begin{aligned} \frac{\partial c}{\partial y} &= 0, \quad \text{at } y = y_1 \ \& \ y = y_2 \\ \frac{\partial c}{\partial z} &= 0, \quad \text{at } z = z_1 \ \& \ z = z_2 \end{aligned} \tag{2.39}$$

At the inlet, the following boundary condition is applied:

$$\begin{aligned} c &= c_{\text{in}}, \quad x = 0,\ y_1 \le y \le h,\ z_1 \le z \le z_2 \\ c &= 0, \quad x = 0,\ h \le y \le y_2,,\ z_1 \le z \le z_2 \end{aligned} \tag{2.40}$$

For the problem to be fully bounded, a boundary condition at the interface needs to be defined. If there's no chemical reaction taking place at the interface, then the discontinuity at the interface is resolved by using the distribution ratio. This is nothing but a relative measure of the affinity of the species for the fluids. In this case, the interfacial BC is given by [69]:

$$\begin{aligned} c_{\text{aq}} &= K c_{\text{org}} \\ -D_{\text{aq}}\frac{\partial c_{\text{aq}}}{\partial y} &= -D_{\text{org}}\frac{\partial c_{\text{org}}}{\partial y} \end{aligned} \tag{2.41}$$

where K is the distribution ratio, and the subscripts 'aq' and 'org' correspond to the aqueous and organic phases respectively. This condition is applied even when there's a chemical reaction taking place in one of the phases [67]. However, when the chemical reaction takes place only at the interface and does not extend to the individual phases, the interfacial BC has to be modified [70, 71]. The interfacial reaction and boundary condition will be discussed in Chapter 6.

2.5. Finite Difference Method

Equations 2.37 and 2.38 are solved using the Finite Difference Method (FDM). FDM is a numerical technique that solves differential or partial differential equations by approximating derivatives using finite differences [72]. These finite differences are

usually evaluated using Taylor's series expansion at the point of consideration. The physical space is first discretized into nodes in a grid. If we consider the simplest 1D case in a grid with the distance between each node being Δx, the forward finite difference (FD) of the quantity f at the node j is given by [72]:

$$\frac{\partial f}{\partial x_j} = \frac{f(x_{j+1}) - f(x_j)}{\Delta x} \tag{2.42}$$

where the subscripts denote the location where the quantity is being evaluated. Similarly, the backward FD is given by:

$$\frac{\partial f}{\partial x_j} = \frac{f(x_j) - f(x_{j-1})}{\Delta x} \tag{2.43}$$

Both these approximations have truncation errors of order Δx, which implies that the error scales linearly with the grid refinement. The central FD approximation has a higher order of accuracy (Δx^2), so it is more frequently used than the forward and backward FDs [72].

$$\frac{\partial f}{\partial x_j} = \frac{f(x_{j+1}) - f(x_{j-1})}{2\Delta x} \tag{2.44}$$

For solving equations 2.38 and 2.37, the backward FD is applied along the x direction and central FD is applied for all the other derivatives, similar to the method used by Malengier *et al* [69]. Since the inlet condition is applied at $x = 0$, it was more convenient to apply backward FD along the x direction instead of defining a ghost node for central FD. If we consider the 2D case, Equation 2.35 is discretized as follows:

$$u_{i+1,j}\frac{c_{i+1,j} - c_{i,j}}{\Delta x} = D\frac{c_{i+1,j+1} - 2c_{i+1,j} + c_{i+1,j-1}}{\Delta y^2} \tag{2.45}$$

Here, i corresponds to the nodes along the x direction and j corresponds to the nodes along the y direction. This method is used in Chapter 6 and the validation will be discussed in further detail in the same chapter.

Bibliography

[1] Frank M White, CO Ng, and S Saimek. *Fluid mechanics*. McGraw-Hill, cop., 2011.

[2] Christopher Earls Brennen and Christopher E Brennen. Fundamentals of multiphase flow. 2005.

[3] Robert J Good. Contact angle, wetting, and adhesion: a critical review. *Journal of adhesion science and technology*, 6(12):1269–1302, 1992.

[4] Yuehua Yuan and T Randall Lee. Contact angle and wetting properties. In *Surface science techniques*, pages 3–34. Springer, 2013.

[5] Thomas Young. Iii. an essay on the cohesion of fluids. *Philosophical transactions of the royal society of London*, (95):65–87, 1805.

[6] Robert N Wenzel. Surface roughness and contact angle. *The Journal of Physical Chemistry*, 53(9):1466–1467, 1949.

[7] CW Extrand. Contact angles and hysteresis on surfaces with chemically heterogeneous islands. *Langmuir*, 19(9):3793–3796, 2003.

[8] Lichao Gao and Thomas J. McCarthy. Contact angle hysteresis explained. *Langmuir*, 22(14):6234–6237, 2006. ISSN 07437463. doi: 10.1021/la060254j.

[9] John David Anderson and J Wendt. *Computational fluid dynamics*, volume 206. Springer, 1995.

[10] Martin Wörner. Numerical modeling of multiphase flows in microfluidics and micro process engineering: A review of methods and applications. *Microfluidics and Nanofluidics*, 12(6):841–886, 2012. ISSN 16134982. doi: 10.1007/s10404-012-0940-8.

[11] Shazia Bashir, Julia M Rees, and William B Zimmerman. Simulations of microfluidic droplet formation using the two-phase level set method. *Chemical Engineering Science*, 66(20):4733–4741, 2011.

[12] Voon-Loong Wong, Katerina Loizou, Phei-Li Lau, Richard S Graham, and Buddhika N Hewakandamby. Numerical studies of shear-thinning droplet formation in a microfluidic t-junction using two-phase level-set method. *Chemical Engineering Science*, 174:157–173, 2017.

[13] Auro Ashish Saha and Sushanta K Mitra. Effect of dynamic contact angle in a volume of fluid (vof) model for a microfluidic capillary flow. *Journal of colloid and interface science*, 339(2):461–480, 2009.

[14] Mehdi Nekouei and Siva A Vanapalli. Volume-of-fluid simulations in microfluidic t-junction devices: Influence of viscosity ratio on droplet size. *Physics of Fluids*, 29(3):032007, 2017.

[15] Mario De Menech. Modeling of droplet breakup in a microfluidic t-shaped junction with a phase-field model. *Physical Review E*, 73(3):031505, 2006.

[16] Feng Bai, Xiaoming He, Xiaofeng Yang, Ran Zhou, and Cheng Wang. Three dimensional phase-field investigation of droplet formation in microfluidic flow focusing devices with experimental validation. *International Journal of Multiphase Flow*, 93:130–141, 2017.

[17] Christopher G Langton. Self-reproduction in cellular automata. *Physica D: Nonlinear Phenomena*, 10(1-2):135–144, 1984.

[18] Bastien Chopard, Alexandre Dupuis, Alexandre Masselot, and Pascal Luthi. Cellular automata and lattice boltzmann techniques: An approach to model and simulate complex systems. *Advances in complex systems*, 5(02n03):103–246, 2002.

[19] Guy R McNamara and Gianluigi Zanetti. Use of the boltzmann equation to simulate lattice-gas automata. *Physical review letters*, 61(20):2332, 1988.

[20] FJ Higuera, S Succi, and R Benzi. Lattice gas dynamics with enhanced collisions. *EPL (Europhysics Letters)*, 9(4):345, 1989.

[21] Timm Kr ”u ger, Halim Kusumaatmaja, Alexandr Kuzmin, Orest Shardt, Goncalo Silva, and Erlend Magnus Viggen. The lattice boltzmann method. *Springer International Publishing*, 10(978-3):4–15, 2017.

[22] Sauro Succi. *The lattice Boltzmann equation: for fluid dynamics and beyond*. Oxford university press, 2001.

[23] Anthony J. Ladd. Numerical Simulations of Particulate Suspensions Via a Discretized Boltzmann Equation. Part 1. Theoretical Foundation. *Journal of Fluid Mechanics*, 271:285–309, 1994. ISSN 14697645. doi: 10.1017/S0022112094001771.

[24] Junfeng Zhang. Lattice Boltzmann method for microfluidics: Models and applications. *Microfluidics and Nanofluidics*, 10(1):1–28, 2011. ISSN 16134990. doi: 10.1007/s10404-010-0624-1.

[25] Haibo Huang, Michael Sukop, and Xiyun Lu. Multiphase lattice boltzmann methods: Theory and application. 2015.

[26] Xiaoyi He and Li-Shi Luo. Theory of the lattice boltzmann method: From the boltzmann equation to the lattice boltzmann equation. *Physical review E*, 56 (6):6811, 1997.

[27] Li Chen, Qinjun Kang, Yutong Mu, Ya Ling He, and Wen Quan Tao. A critical review of the pseudopotential multiphase lattice Boltzmann model: Methods and applications. *International Journal of Heat and Mass Transfer*, 76:210–236, 2014. ISSN 00179310. doi: 10.1016/j.ijheatmasstransfer.2014.04.032. URL http://dx.doi.org/10.1016/j.ijheatmasstransfer.2014.04.032.

[28] Sébastien Leclaire, Nicolas Pellerin, Marcelo Reggio, and Jean Yves Trépanier. A multiphase lattice Boltzmann method for simulating immiscible liquid-liquid interface dynamics. *Applied Mathematical Modelling*, 40(13-14):6376–6394, 2016. ISSN 0307904X. doi: 10.1016/j.apm.2016.01.049.

[29] Xiaowen Shan and Hudong Chen. Lattice boltzmann model for simulating flows with multiple phases and components. *Physical review E*, 47(3):1815, 1993.

[30] Andrew K. Gunstensen, Daniel H. Rothman, Stéphane Zaleski, and Gianluigi Zanetti. Lattice Boltzmann model of immiscible fluids. *Physical Review A*, 43 (8):4320–4327, 1991. ISSN 10502947. doi: 10.1103/PhysRevA.43.4320.

[31] Michael R. Swift, E. Orlandini, W. R. Osborn, and J. M. Yeomans. Lattice Boltzmann simulations of liquid-gas and binary fluid systems. *Physical Review E - Statistical Physics, Plasmas, Fluids, and Related Interdisciplinary Topics*, 54 (5):5041–5052, 1996. ISSN 1063651X. doi: 10.1103/PhysRevE.54.5041.

[32] Haibo Huang, Jun Jie Huang, Xi Yun Lu, and Michael C. Sukop. On simulations of high-density ratio flows using color-gradient multiphase lattice boltzmann models. *International Journal of Modern Physics C*, 24(4):1–19, 2013. ISSN 01291831. doi: 10.1142/S0129183113500216.

[33] Sébastien Leclaire, Marcelo Reggio, and Jean Yves Trépanier. Isotropic color gradient for simulating very high-density ratios with a two-phase flow lattice Boltzmann model. *Computers and Fluids*, 48(1):98–112, 2011. ISSN 00457930. doi: 10.1016/j.compfluid.2011.04.001.

[34] I. Halliday, R. Law, C. M. Care, and A. Hollis. Improved simulation of drop dynamics in a shear flow at low Reynolds and capillary number. *Physical Review E - Statistical, Nonlinear, and Soft Matter Physics*, 73(5):1–11, 2006. ISSN 15393755. doi: 10.1103/PhysRevE.73.056708.

[35] Stéphane Popinet. Numerical Models of Surface Tension. *Annual Review of Fluid Mechanics*, 50(1):49–75, January 2018. ISSN 0066-4189, 1545-4479. doi: 10.1146/annurev-fluid-122316-045034. URL https://www.annualreviews.org/doi/10.1146/annurev-fluid-122316-045034.

[36] A. E. Komrakova, Orest Shardt, D. Eskin, and J. J. Derksen. Lattice Boltzmann simulations of drop deformation and breakup in shear flow. *International Journal of Multiphase Flow*, 59:24–43, 2014. ISSN 03019322. doi: 10.1016/j.ijmultiphaseflow.2013.10.009. URL http://dx.doi.org/10.1016/j.ijmultiphaseflow.2013.10.009.

[37] H. W. Zheng, C. Shu, and Y. T. Chew. A lattice Boltzmann model for multiphase flows with large density ratio. *Journal of Computational Physics*, 218(1):353–371, 2006. ISSN 10902716. doi: 10.1016/j.jcp.2006.02.015.

[38] Takaji Inamuro, Tajima Ogata, S Tajima, and N Konishi. A lattice boltzmann method for incompressible two-phase flows with large density differences. *Journal of Computational physics*, 198(2):628–644, 2004.

[39] Xiaoyi He, Shiyi Chen, and Raoyang Zhang. A lattice boltzmann scheme for incompressible multiphase flow and its application in simulation of rayleigh–taylor instability. *Journal of computational physics*, 152(2):642–663, 1999.

[40] L. O.E. Santos, P. C. Facin, and P. C. Philippi. Lattice-Boltzmann model based on field mediators for immiscible fluids. *Physical Review E - Statistical Physics, Plasmas, Fluids, and Related Interdisciplinary Topics*, 68(5), 2003. ISSN 1063651X. doi: 10.1103/PhysRevE.68.056302.

[41] Yan Ba, Haihu Liu, Qing Li, Qinjun Kang, and Jinju Sun. Multiple-relaxation-time color-gradient lattice boltzmann model for simulating two-phase flows with high density ratio. *Physical Review E*, 94(2):023310, 2016.

[42] Sébastien Leclaire, Andrea Parmigiani, Bastien Chopard, and Jonas Latt. Three-dimensional lattice Boltzmann method benchmarks between color-gradient and pseudo-potential immiscible multi-component models. *International Journal of Modern Physics C*, 28(7):1–30, 2017. ISSN 01291831. doi: 10.1142/S0129183117500851.

[43] Z. Liu. *Purifying Radionuclides with Microfluidic Technology for Medical Purpose: Simulating multiphase flows inside a microfluidic channel with the phase field method*. PhD thesis, Delft University of Technology, 2022. URL http://resolver.tudelft.nl/uuid:e1bebcdd-185a-4515-b352-76d68f65ace8.

[44] Yan Ba, Haihu Liu, Qing Li, Qinjun Kang, and Jinju Sun. Multiple-relaxation-time color-gradient lattice Boltzmann model for simulating two-phase flows with high density ratio. *Physical Review E*, 94(2):023310, August 2016. ISSN 2470-0045, 2470-0053. doi: 10.1103/PhysRevE.94.023310. URL https://link.aps.org/doi/10.1103/PhysRevE.94.023310.

[45] Zhaoli Guo, Chuguang Zheng, and Baochang Shi. An extrapolation method for boundary conditions in lattice Boltzmann method. *Physics of Fluids*, 14(6):2007–2010, 2002. ISSN 10706631. doi: 10.1063/1.1471914.

[46] Jeremiah U Brackbill, Douglas B Kothe, and Charles Zemach. A continuum method for modeling surface tension. *Journal of computational physics*, 100 (2):335–354, 1992.

[47] M. Latva-Kokko and Daniel H. Rothman. Static contact angle in lattice Boltzmann models of immiscible fluids. *Physical Review E - Statistical, Nonlinear, and Soft Matter Physics*, 72(4):1–7, 2005. ISSN 15393755. doi: 10.1103/PhysRevE.72.046701.

[48] Zhiyuan Xu, Haihu Liu, and Albert J. Valocchi. Lattice Boltzmann simulation of immiscible two-phase flow with capillary valve effect in porous media: CAPILLARY VALVE EFFECT IN POROUS MEDIA. *Water Resources Research*, 53(5): 3770–3790, May 2017. ISSN 00431397. doi: 10.1002/2017WR020373. URL http://doi.wiley.com/10.1002/2017WR020373.

[49] Haihu Liu, Albert J. Valocchi, and Qinjun Kang. Three-dimensional lattice Boltzmann model for immiscible two-phase flow simulations. *Physical Review E - Statistical, Nonlinear, and Soft Matter Physics*, 85(4):1–14, 2012. ISSN 15393755. doi: 10.1103/PhysRevE.85.046309.

[50] M'hamed Bouzidi, Mouaouia Firdaouss, and Pierre Lallemand. Momentum transfer of a Boltzmann-lattice fluid with boundaries. *Physics of Fluids*, 13 (11):3452–3459, 2001. ISSN 10706631. doi: 10.1063/1.1399290.

[51] M. Rohde, D. Kandhai, J. J. Derksen, and H. E.A. Van den Akker. Improved bounce-back methods for no-slip walls in lattice-Boltzmann schemes: Theory and simulations. *Physical Review E - Statistical Physics, Plasmas, Fluids, and Related Interdisciplinary Topics*, 67(6):10, 2003. ISSN 1063651X. doi: 10.1103/PhysRevE.67.066703.

[52] Renwei Mei, Li-shi Luo, and Wei Shyy. an accurate curved boundary treatment in the LBM.pdf. *Journal of Computational Physics*, 330:307–330, 1999.

[53] B. Chun and A. J.C. Ladd. Interpolated boundary condition for lattice Boltzmann simulations of flows in narrow gaps. *Physical Review E - Statistical, Nonlinear, and Soft Matter Physics*, 75(6):1–12, 2007. ISSN 15393755. doi: 10.1103/PhysRevE.75.066705.

[54] Takashi Akai, Branko Bijeljic, and Martin J. Blunt. Wetting boundary condition for the color-gradient lattice Boltzmann method: Validation with analytical and experimental data. *Advances in Water Resources*, 116(April):56–66, 2018. ISSN 03091708. doi: 10.1016/j.advwatres.2018.03.014. URL https://doi.org/10.1016/j.advwatres.2018.03.014.

[55] Abbas Fakhari and Diogo Bolster. Diffuse interface modeling of three-phase contact line dynamics on curved boundaries: A lattice Boltzmann model for large density and viscosity ratios. *Journal of Computational Physics*, 334: 620–638, 2017. ISSN 10902716. doi: 10.1016/j.jcp.2017.01.025. URL http://dx.doi.org/10.1016/j.jcp.2017.01.025.

[56] K. C. Sahu and S. P. Vanka. A multiphase lattice Boltzmann study of buoyancy-induced mixing in a tilted channel. *Computers and Fluids*, 50(1):199–215, 2011. ISSN 00457930. doi: 10.1016/j.compfluid.2011.07.012.

[57] Sébastien Leclaire, Kamilia Abahri, Rafik Belarbi, and Rachid Bennacer. Modeling of static contact angles with curved boundaries using a multiphase lattice boltzmann method with variable density and viscosity ratios. *International Journal for Numerical Methods in Fluids*, 82(8):451–470, 2016.

[58] Jingwei Huang, Feng Xiao, and Xiaolong Yin. Lattice Boltzmann simulation of pressure-driven two-phase flows in capillary tube and porous medium. *Computers and Fluids*, 155:134–145, 2017. ISSN 00457930. doi: 10.1016/j.compfluid.2017.05.027. URL http://dx.doi.org/10.1016/j.compfluid.2017.05.027.

[59] Qisu Zou and Xiaoyi He. On pressure and velocity boundary conditions for the lattice Boltzmann BGK model. *Physics of Fluids*, 9(6):1591–1596, 1997. ISSN 10706631. doi: 10.1063/1.869307.

[60] Yi Zong, Min Li, and Kai Wang. Outflow boundary condition of multiphase microfluidic flow based on phase ratio equation in lattice Boltzmann method. *Physics of Fluids*, 33(7):073304, July 2021. ISSN 1070-6631, 1089-7666. doi: 10.1063/5.0058045. URL https://pubs.aip.org/aip/pof/article/1060984.

[61] Qin Lou, Zhaoli Guo, and Baochang Shi. Evaluation of outflow boundary conditions for two-phase lattice Boltzmann equation. *Physical Review E - Statistical, Nonlinear, and Soft Matter Physics*, 87(6):1–16, 2013. ISSN 15393755. doi: 10.1103/PhysRevE.87.063301.

[62] Jun Jie Huang, Haibo Huang, and Xinzhu Wang. Numerical study of drop motion on a surface with stepwise wettability gradient and contact angle hysteresis. *Physics of Fluids*, 26(6), 2014. ISSN 10897666. doi: 10.1063/1.4880656. URL http://dx.doi.org/10.1063/1.4880656.

[63] Takashi Akai, Branko Bijeljic, and Martin J. Blunt. Wetting boundary condition for the color-gradient lattice Boltzmann method: Validation with analytical and experimental data. *Advances in Water Resources*, 116:56–66, June 2018. ISSN 03091708. doi: 10.1016/j.advwatres.2018.03.014. URL https://linkinghub.elsevier.com/retrieve/pii/S030917081731028X.

[64] Haihu Liu, Yaping Ju, Ningning Wang, Guang Xi, and Yonghao Zhang. Lattice Boltzmann modeling of contact angle and its hysteresis in two-phase flow with large viscosity difference. *Physical Review E*, 92(3):033306, September 2015. ISSN 1539-3755, 1550-2376. doi: 10.1103/PhysRevE.92.033306. URL https://link.aps.org/doi/10.1103/PhysRevE.92.033306.

[65] Hang Ding and Peter D.M. Spelt. Wetting condition in diffuse interface simulations of contact line motion. *Physical Review E - Statistical, Nonlinear, and Soft Matter Physics*, 75(4):1–18, 2007. ISSN 15393755. doi: 10.1103/PhysRevE.75.046708.

[66] M. Sbragaglia, R. Benzi, L. Biferale, S. Succi, K. Sugiyama, and F. Toschi. Generalized lattice Boltzmann method with multirange pseudopotential. *Physical Review E*, 75(2):026702, February 2007. ISSN 1539-3755, 1550-2376. doi: 10.1103/PhysRevE.75.026702. URL https://link.aps.org/doi/10.1103/PhysRevE.75.026702.

[67] Y. Haroun, D. Legendre, and L. Raynal. Volume of fluid method for interfacial reactive mass transfer: Application to stable liquid film. *Chemical Engineering Science*, 65(10):2896–2909, May 2010. ISSN 00092509. doi: 10.1016/j.ces.2010.01.012. URL https://linkinghub.elsevier.com/retrieve/pii/S0009250910000291.

[68] Dmitri Kuzmin. A guide to numerical methods for transport equations, 2010.

[69] B. Malengier, S. Pushpavanam, and S. D'Haeyer. Optimizing performance of liquid-liquid extraction in stratified flow in micro-channels. *Journal of Micromechanics and Microengineering*, 21(11), 2011. ISSN 09601317. doi: 10.1088/0960-1317/21/11/115030.

[70] Gwendolyne Hellé, Sean Roberston, Siméon Cavadias, Clarisse Mariet, and Gérard Cote. Toward numerical prototyping of labs-on-chip: modeling for liquid–liquid microfluidic devices for radionuclide extraction. *Microfluidics and Nanofluidics*, 19(5):1245–1257, November 2015. ISSN 1613-4982, 1613-4990. doi: 10.1007/s10404-015-1643-8. URL http://link.springer.com/10.1007/s10404-015-1643-8.

[71] Davide Ciceri, Lachlan R. Mason, Dalton J.E. Harvie, Jilska M. Perera, and Geoffrey W. Stevens. Extraction kinetics of Fe(III) by di-(2-ethylhexyl) phosphoric acid using a Y–Y shaped microfluidic device. *Chemical Engineering Research and Design*, 92(3):571–580, March 2014. ISSN 02638762. doi: 10.1016/j.cherd.2013.08.033. URL https://linkinghub.elsevier.com/retrieve/pii/S0263876213003626.

[72] William F Ames. *Numerical methods for partial differential equations*. Academic press, 2014.

3

Rothman-Keller Simulations of Flow Phenomena in a Y-Y microfluidic channel at Low Capillary Numbers

The common flow phenomena observed in microchannels were discussed in Chapter 1. To have a greater understanding of these flow phenomena, besides experimental evidence, numerical simulations are necessary. Numerous numerical studies have been conducted on microchannels to supplement the results obtained from the experiments. Some of the methods used for simulation include Volume of Fluid (VOF) [1], Level-Set (LS) [2], Phase-Field [3] and Lattice Boltzmann methods (LBM) [4]. Generally, these studies see if the overall flow map can be reproduced, with some studying slug flow in more detail [5, 6, 7]. However, there are very few studies which numerically simulate the phenomenon of leakage, and the phase-field simulations of Liu [3] were unsuccessful in completely capturing the phenomenon.

Two key advantages of the LBM which accounts for its increased usage in multiphase simulations [4, 8, 9] are its high degree of localization and lack of interfacial tracking[10]. Its localization makes it easily amenable to parallelization [11]. The lattice mesh can be extended to complex geometries and the mesoscale nature of LBM makes it very suitable for micro-fluidics [12]. Since the phase-field method was unable to capture leakage successfully, the LBM is thus adopted for this study. Specifically, the RK model is used, the reasons for which are already elucidated in Chapter 2.

Multiphase channel flow simulations have been performed using the LBM for T channels [13, 8] and cross junction channels [4, 14]. Most of these papers have

considered mainly the case of droplet generation and development in a channel, with few like the paper by Liu *et al* [4] showing parallel flow as a proof-of-concept, but not exploring further. The geometries considered in LB simulations are generally rectangular, and the outlet section of the channels is rarely modelled. The outlet sections of the channels are especially important when studying parallel flow, as leakage of one fluid into the outlet of another should be avoided in extraction applications. Some papers, like the one by Yu *et al* [15], modified the cross channel inlets to make it inclined, but they simulated only droplet flow and operated at higher Capillary numbers.

Considering the use of Y-Y micro-channels in a large number of micro-fluidic studies, especially those involving radioisotope extraction [16, 17, 18], it is imperative to study the factors affecting the flow phenomena in a Y-Y channel numerically. Most LBM papers study such flows at higher Capillary numbers ranging from 0.001 to 1 [19, 20, 4, 15], while many flows occur at lower Capillary numbers [3, 21, 22]. Thus, this chapter studies the capability of the LBM, specifically the RK model, to simulate the flow phenomena, especially *parallel flow and leakage*, across a range of low Capillary numbers. The implementation of surface tension will be looked into to understand the workings of the model when dealing with such geometries and Capillary numbers, and a solution is proposed to enhance the effectiveness of the RK model at such Capillary numbers. VOF and Phase-Field method will be compared with the RK model to examine the capabilities of the simulation methods in each flow regime.

The R-K model was previously discussed in Chapter 2. In this chapter, the surface tension implementation is modified to improve the model's ability to capture flow phenomena at low Capillary numbers. This modification, along with the VOF model, will be discussed in the next section. Then, the utility of this model is discussed by comparing it with the experiments of Graaf *et al* [8]. Finally, the older RK model, modified RK model, VOF and phase-field method are compared based on their accuracy in reproducing the flow maps and individual flow regimes observed in the experiments of Liu [3].

3.1. Methodology

3.1.1. RK model

The RK model used in this chapter is mostly the same as that discussed in Chapter 2. The difference lies in the perturbation operator, especially in Equation 2.22, where the velocity is modified. Here, we propose a different velocity modification as follows:

$$\rho \mathbf{u} = \sum_i \sum_k \mathbf{e}_i f_i^k(\mathbf{x}, t) + m\mathbf{F}_s \Delta t, \quad m = \begin{cases} \frac{1}{2}, \text{Guo approach} \\ 0, \text{Current approach} \end{cases} \tag{3.1}$$

Guo *et al* [23] mentions that both the equilibrium (u^*) and local fluid velocities (u) need to be modified (Equation 2.22) for the model to correctly capture the Navier-Stokes equations and accommodate for spatial and temporal variations of the momentum with the CSF term (Equation 2.19). However, this modification, along with the CSF term, introduces spurious currents [24]. These spurious velocities aren't a problem at higher Capillary numbers but could significantly influence the result for cases when surface tension forces are dominant. The CSF term has been known to introduce spurious velocities not only for LBM, but also for Volume-of-Fluid and Level-Set methods [25, 26].

To accommodate lower Capillary flows, we propose to neglect the velocity modification for u^* and apply it only for u, i.e, $m = 0$ for u^* (Equation 3.1) This approach was used by Ladd and Verberg [27] for their forcing term. Their forcing term was shown to introduce additional terms in the momentum equation by Guo *et al* [23]. In summary, we apply Ladd and Verberg's velocity modification to the forcing term by Guo *et al* [23] described in Equation 2.18(Current approach, $m = 0$) and compare it with the standard approach proposed by Guo (Guo approach, $m = 0.5$).

Barring this modification, the rest of the RK model is the same as in Chapter 2.

3.1.2. Volume of Fluid

Ansys FLUENT 2022 R2 is used to simulate VOF. The Navier-Stokes equations for the individual fluids (Equations 2.1) are simulated in VOF [1]. The position of the interface is tracked using the volume fraction continuity equation and the density and viscosity of the two-phase mixture are described by:

$$\begin{aligned} \rho &= \alpha\rho_1 + (1-\alpha)\rho_2 \\ \mu &= \alpha\mu_1 + (1-\alpha)\mu_2 \end{aligned} \tag{3.2}$$

where ρ and μ are the density and viscosity of the mixture respectively, α is the volume fraction of liquid 1. To include the surface tension, a source term is added to the Navier-Stokes equation based on the CSF model described by Brackbill et al [28]. This is given by:

$$F = \frac{2\sigma\rho\kappa\nabla\alpha}{\rho_1 + \rho_2} \tag{3.3}$$

where σ is the surface tension and κ is the curvature. Equation 3.3 has a similar form to Equation 2.19, and this is expected as both are based on the CSF model. As mentioned earlier, the CSF term is known to induce spurious currents in VOF [25, 29]. The main reason for this is because the Laplace relation of surface tension and pressure difference is not exactly satisfied [25]. For higher Capillary numbers, this inaccuracy doesn't have a big impact on the solution, but for low Capillary numbers, large spurious velocities are developed. Besides, the same gradient operator is used to calculate the smooth pressure term and the discontinuous

surface tension term, which leads to an inaccurate estimation of gradients and curvature [25]. One solution for this is to combine VOF with LS, as LS involves a continuous function for implementing surface tension [30]. Instead of a volume fraction equation, an equation for the Level-Set function is solved. This option is available in FLUENT and the model is the same as that in the FLUENT theory guide [31]. We run simulations with both methods for the Y-Y channel to understand the impact of the forcing term on simulations of low Capillary number flows and leakage.

3.2. Code Validation

The model is first validated by running static contact angle simulations as described in the paper of Xu *et al* [32]. Both the Guo and Current approaches are applied (Equation 2.22), and the same results are obtained. To validate a more dynamic case, the T-channel experiments of Graaf *et al* [8] are simulated in 2D and the droplet diameters are compared for both approaches. The T-channel has two inlet junctions perpendicular to each other and an outlet located along the inlet of the continuous phase (Figure 3.1).

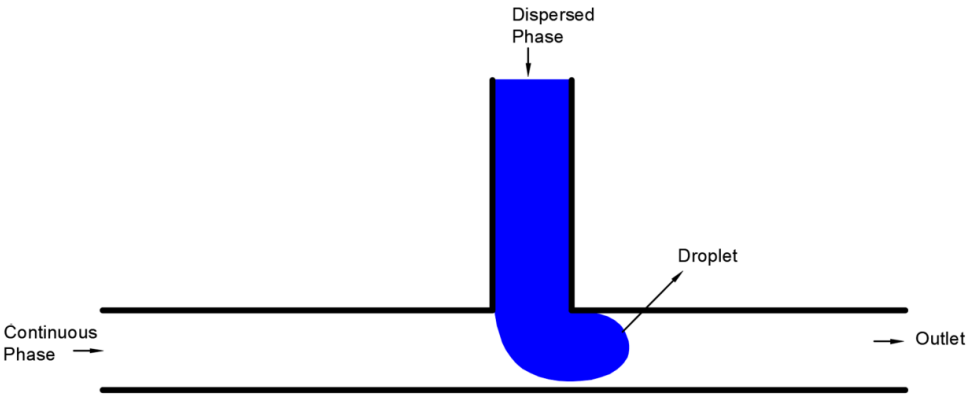

Figure 3.1: T channel setup for droplet simulations [8]

The width of the channel is 100 μm. The densities of the continuous and dispersed phases are taken as $\rho_c = 1000 \mathrm{kg/m^3}$ and $\rho_d = 1000 \mathrm{kg/m^3}$. The densities of the fluids used by Graaf *et al* [8] are very similar to each other, so they are made equal in the simulation for convenience. The dynamic viscosities are the same as those of the experiments, with $\mu_c = 1.95 \times 10^{-3}$Pa s and $\mu_d = 6.71 \times 10^{-3}$Pa s. A contact angle of 45 $^\circ$ with respect to the continuous phase is implemented and the surface tension is $\sigma = 5.0 \times 10^{-3}$ N/m. The Capillary number of the dispersed phase is kept constant at $Ca_d = 0.011$ while the continuous phase Ca_c is varied from 0.0033 to 0.066.

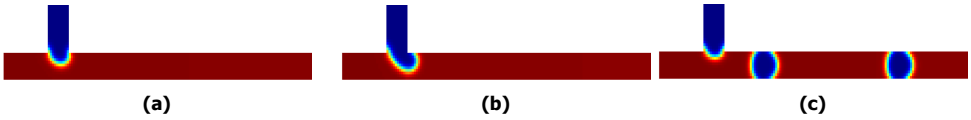

Figure 3.2: Droplet formation and development in a T channel at Ca_c = 0.016. The red fluid is the continuous phase and the blue fluid is the dispersed phase, with the diffuse interface represented by the transitioning of colours from blue to red. The droplet develops in three stages - a)expansion, b)necking c)detachment [8].

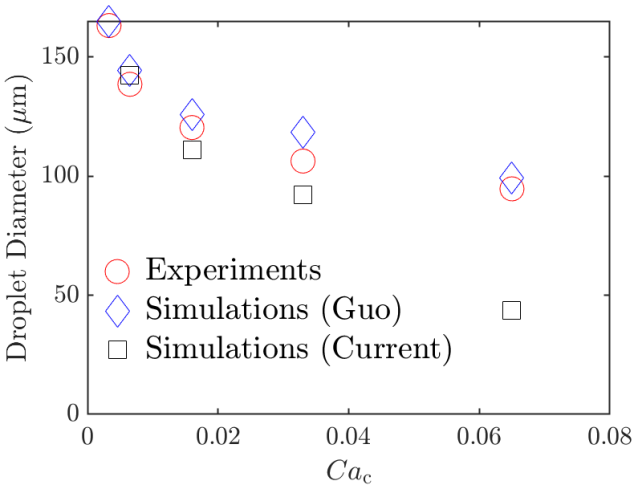

Figure 3.3: Comparison of droplet diameters obtained from the simulations using Guo (blue diamonds) and Current (black squares) approaches with the experiments (red circles) of Graaf *et al* [8] for varying Ca_C at a constant Ca_D

As shown in Figure 3.2, the droplet forms the expected shape and follows the expected steps of expansion and necking during formation [8]. The droplet diameters of the experiments and simulations are plotted in Figure 3.3. We observe an interface thickness of around 3-4 lu, and this is the expected thickness for β =0.7 [33]. Since the experiments are in 3D, Graaf *et al* [8] calculated an equivalent spherical diameter from the volume of the droplets. Following their procedure, we, therefore, calculate the equivalent circular diameter from the droplet *area* in our 2D simulations. In order to make a valid comparison, the Strouhal numbers (St) are equalized in 2D and 3D as this number is a measure independent of the dimensions and reflects the dynamics of droplet breakup. Hence,

$$\begin{aligned} St_{2D} &= St_{3D} \\ \Rightarrow \frac{f_{2D}L}{U_{2D}} &= \frac{f_{3D}L}{U_{3D}} \end{aligned} \tag{3.4}$$

where f is the droplet frequency, L is the characteristic length of the flow (hydraulic diameter) and U is the flow velocity. The characteristic lengths in 2D and 3D are the

same as the width and height are equal. The fluids flow only along the x direction in the main channel, so the velocities are also equal in both dimensions. This implies

$$\begin{aligned} f_{2D} &= f_{3D} \\ \Rightarrow \frac{Q_{2D}}{A} &= \frac{Q_{3D}}{V} \\ Q_{3D} &= Q_{2D} L \end{aligned} \tag{3.5}$$

where Q is the flow rate, A is the area of the slug and V is the volume of the slug. Let d_{2D} be the equivalent circular diameter of the 2D slug and d_{3D} the equivalent spherical diameter of the 3D slug. Therefore, a 3D diameter is calculated from the 2D results using the results from Equation 3.5 :

$$\begin{aligned} A &= \frac{\pi}{4} d_{2D}^2 \\ V_{3D} &= \frac{\pi}{6} d_{3D}^3 \\ \Rightarrow d_{3D} &= \left(\frac{3}{2} d_{2D}^2 H \right)^{\frac{1}{2}} \end{aligned} \tag{3.6}$$

From Figure 3.3, we can see that the droplet diameters closely match the experiments for the Guo approach for a wide range of Ca numbers, whereas the current approach is accurate for low Ca numbers ($Ca < 0.016$). Since the focus of this chapter is flows at low Ca ($Ca < 10^{-3}$), the current approach is considered sufficient for this study.

3.3. Numerical Setup

The simulations are conducted in 2D and compared to experimental studies on the Y-Y channel by Liu [3]. Liu used a glass microchip manufactured by the Institute of Micro-chemical Technology (IMT) as shown in Figure 3.4. The channel dimensions and the corresponding lattice dimensions are shown in Table 5.2. Water and toluene are the two fluids used for comparing parallel flow with Liu's results. The properties of these fluids are described in Table 5.1, along with the inlet velocities (u_{in}) at $Ca = 10^{-4}$, as this would provide the reader with an idea of the velocity magnitude when talking about spurious velocities. The advancing and receding angles are unknown in the experiments and the implementation of the contact angle as described in Section 2.3.5 also doesn't allow for hysteresis, so hysteresis will not be included in this study. This table also shows the values of α^k (Equation 2.15) and β, the parameter related to interface thickness in Equation 2.23. The chosen relaxation time is close to the stability limit of 0.5 [11]. Such a low relaxation time is chosen so that the computational load is smaller, as a larger relaxation time would necessitate very large domains for the same Capillary numbers.

The flow is initialized in the simulation domain as shown in Figure 5.1.4. The red fluid corresponds to the aqueous phase and the blue fluid is the organic phase.

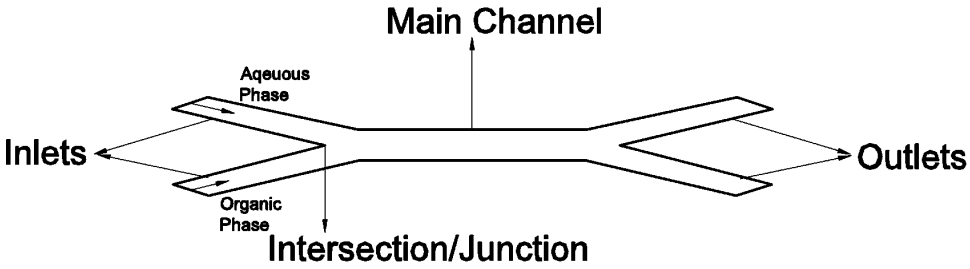

Figure 3.4: Y-Y microchannel used by Liu [3], with two inlets and outlets

Fully developed laminar flow is assumed at the inlet, so a shorter inlet length of 500 microns can be used. A channel length of 2 mm is used instead of the actual length of 2 cm. This assumption was justified by running the simulations for both channel lengths, 2 mm and 2 cm, with no difference in the results.

Figure 3.5: Flow Initialization in all simulations. The red fluid is the aqueous phase and the blue fluid is the organic phase.

Table 3.1: Channel and domain dimensions in physical and lattice units

Material	**Length** (cm / l.u)	**Width** (μm / l.u)	**Depth** (μm/ l.u)	**Angle Between Inlets** ($^\circ$)
Borosilicate glass	2	100 $\pm$ 0.2	40 $\pm$ 0.1	26
Lattice Mesh	2400 (240)	20		26

3.4. Results

We first simulate the flow map obtained by Zheng Liu [3] for a water-toluene mixture. The Capillary numbers applied are in the range of 3 $\times 10^{-5}$ to 2 $\times 10^{-3}$. These values are relatively low compared to those used in literature, the lowest Capillary number used in the literature for the RK model being 10^{-3} by Wu *et al* [14] and Liu *et al* [34], both of whom simulated fluid flow in a cross junction channel. Both these papers compared their results with experiments, and in these experiments, the lowest Capillary number was 10^{-3}. The results, consisting of the flow pattern and leakage, are compared for both VOF and RK models with the experiments and phase-field simulations of Liu [3], who observed three regimes - slug, transition

Table 3.2: Properties of the fluids used in the simulations

Fluid	**Viscosity** (mPa · s)	**Density** (g/cm^3)	**Coefficient of Interfacial Tension** (mN/m)	**Contact Angle** (°)	**Relaxation Time** (l.s)	α	β	u_{in} (lu/lt) at $Ca = 10^{-4}$
Water	1.00	1.00		46.6	0.529	5/9	0.7	0.000409
n-heptane	0.386	0.680	50.1		0.517	3/9	0.7	0.00108
Water	1.00	1.00		49.1	0.533	4/9	0.7	
Toluene	0.583	0.867	36.1		0.522	3.25/9	0.7	

and parallel flow.

The flow pattern map obtained from the experiments and simulations for water-toluene mixtures is shown in Figure 5.5. The Current approach and VOF are able to capture parallel and slug flow at the respective Capillary numbers, but not the relatively narrow region of transition flow. The phase-field method, however, is able to successfully capture all the flow regimes - slug, parallel and transition flow. However, the benefits of the Current approach compared to the phase-field method is made clear when simulating leakage, and this will be discussed in Section 3.4.2.

In the case of the Guo approach, it was difficult to observe grid-independent results, especially when simulating parallel flow, but slug flow was successfully captured. Grid convergence could not be obtained for parallel flow at all the expected Capillary numbers and this will be further discussed in Section 3.5.2. For this reason, the regimes obtained from the Guo approach are not plotted in Figure 5.5.

3.4.1. Slug Length

In this subsection, we look at the capabilities of each technique to accurately capture the slug length at various low Capillary numbers. We once again use the experimental results of Liu [3], but this time for water-heptane instead of water-toluene as no data on the slug length is available for the water-toluene system. The flow map of water-heptane is not presented in Figure 5.5 for clarity, as the same findings were also observed here. The slug lengths of all the techniques (VOF, Phase-Field, Guo and Current approaches) are compared with the experiments in Figure 3.7.

The slug lengths remain more or less constant in the case of the Guo approach and VOF with varying Capillary numbers. The current approach, on the other hand, shows the right trend of slug lengths decreasing with increasing Capillary number, but the lengths differ from the experiments by around 30 %. The phase-field method is the only technique which is able to both capture the right trend and show

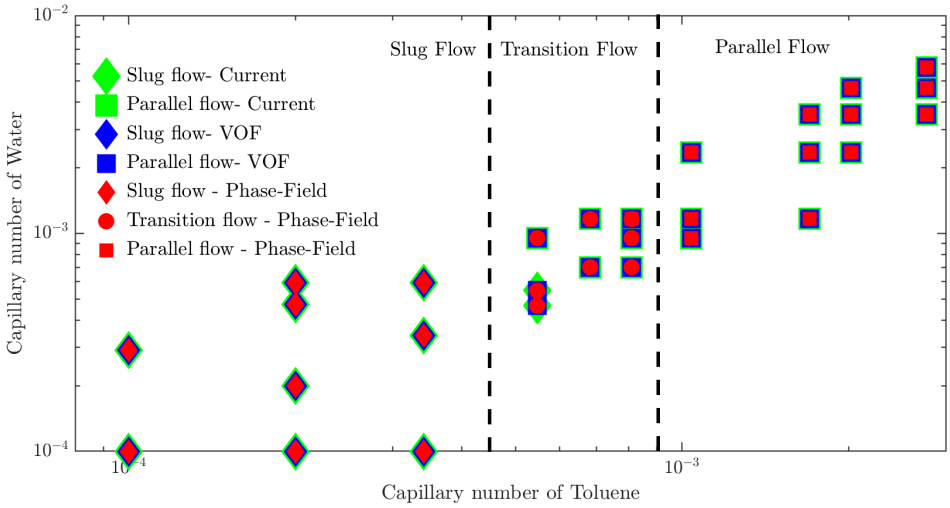

Figure 3.6: Flow patterns of water-toluene mixtures for various Capillary numbers - simulations (Current approach- green symbols, VOF - blue symbols and Phase-field [3] - red symbols). The dashed lines indicate the patterns found in the experiments.

accurate slug lengths, with the maximum error observed being around 10 %.

3.4.2. Leakage

The outlet section of the Y-Y channel is now modelled in the case of parallel flow because we want to observe the phenomenon of leakage, where one fluid leaks into the outlet of the other [3]. Perfect flow separation and stability are important when we consider the transfer of species from one fluid to another [17], so it is imperative that simulation techniques (Current approach, VOF and Phase Field) are able to capture this phenomenon accurately. The Guo approach is not considered here as we couldn't obtain grid-independent results for parallel flow. The simulations are compared with the experiments of Liu [3].

Three different leakage regimes are observed when using the Current approach - leakage to the toluene outlet, leakage to the water outlet and leakage to both outlets. These regimes are shown in Figure 3.8. Only two leakage regimes are observed in the experiments, however, leakage to the toluene outlet and leakage to the water outlet, and the experimental regimes are shown in Figure 3.9.

Liu did not discuss the nature of the leakage regime near the outlet, i.e., whether the fluid leaks in the form of droplets or parallel flow, so we restrict our discussions regarding the nature of the leakage regime to the simulations. In the case of leakage to the toluene outlet, the flow of water in the LBM simulations is always parallel. In the case of leakage to the water outlet, leakage occurs either in the

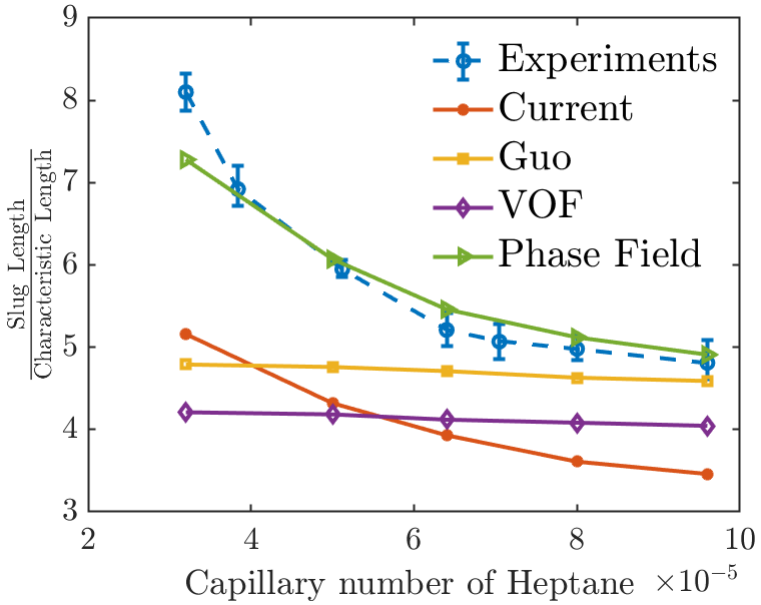

Figure 3.7: Slug lengths obtained using VOF (diamonds), Phase-Field (right triangles, [3]), Guo (squares) and Current approaches (closed circles), and from the experiments (open circles, [3]). The characteristic length is the width of the channel. The velocity of water is the same as that of Heptane.

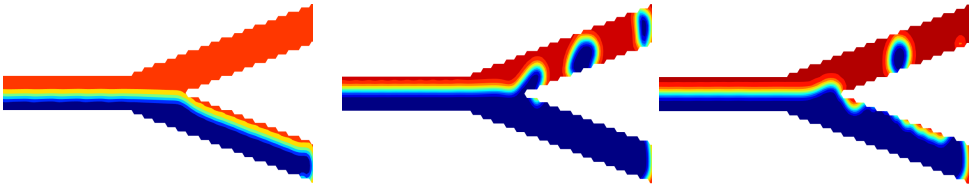

Figure 3.8: Leakage regimes observed in LBM simulations of Water (red)-toluene (blue) mixture. a) Leakage to toluene outlet, b) Leakage to water outlet, c) Leakage to both outlets. The Capillary number of toluene is fixed at 2 $\times 10^{-3}$ and the flow rate of water is varied to obtain different regimes Flow rate ratio is 1, 0.6 and 0.8 for a),b) and c) respectively.

form of droplets of toluene or as parallel flow. Droplets are observed in the case of leakage to both outlets.

The leakage regimes are plotted in Figure 3.10, where the Capillary number of toluene and the ratio of flow rates have been varied. The figure shows that, while increasing the flow rate ratio, the leakage regime goes from leakage to the water outlet in the shape of droplets, to leakage to the water outlet as parallel flow, to leakage to both outlets and finally to leakage to the toluene outlet as parallel flow.

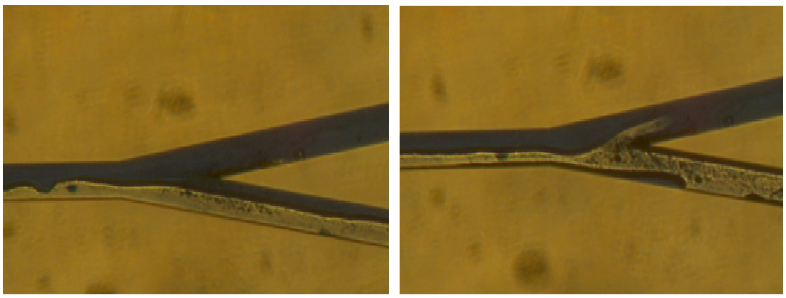

(a) (b)

Figure 3.9: Leakage regimes as observed in the experiments [3] for Water (dark)-toluene (light) mixture. a) Leakage to toluene outlet b) Leakage to water outlet

When comparing the results of the current approach with the experimental results of Liu [3] in Figure 3.10, the same trend is roughly visible, i.e. leakage to the water outlet at low flow rate ratios and leakage to the toluene outlet at high ratios. The numerical simulations, however, show a transition regime with leakage to both outlets at flow rate ratios between 0.8-1, whereas the experiments don't.

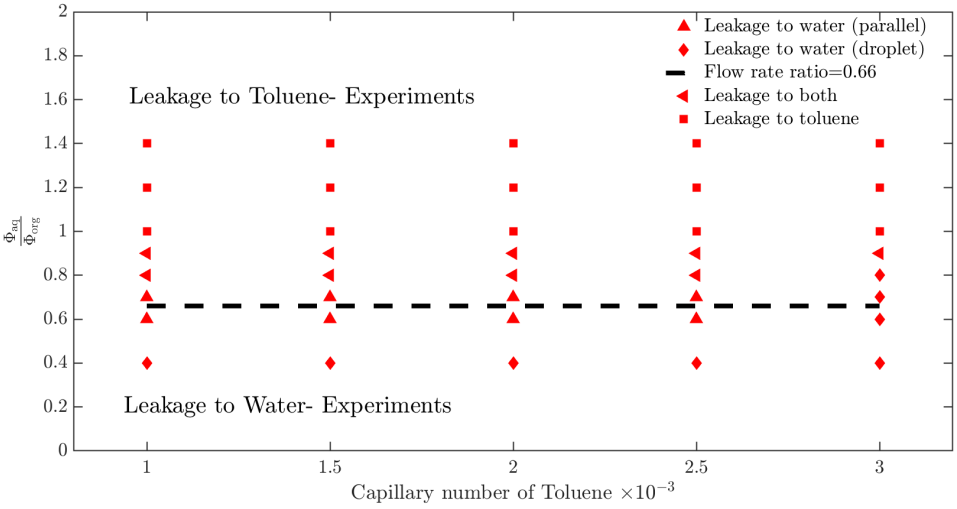

Figure 3.10: Comparison of leakage regimes of LBM simulations (current approach, black symbols) with experiments (regions above and below the horizontal line). The vertical axis corresponds to the ratio of the aqueous to the organic flow rate. A flow rate ratio of 0.66 (black horizontal line) points to the region where leakage switches from the water outlet to the toluene outlet [3].

In the case of VOF and VOF-LS, we observe droplets being generated near the intersection for all Capillary numbers (Figure 3.11). Though leakage is observed, these results do not match the experiments of Liu. The phase-field simulations of

Liu were also unable to capture leakage correctly, with the results showing either no leakage at all or leakage similar to that observed in VOF.

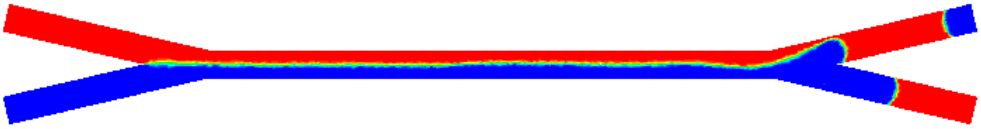

Figure 3.11: Parallel flow for water-toluene mixture simulated using VOF and VOF-LS. The red fluid is water and the blue fluid is toluene.

The Current approach, thus, produces the most accurate results when it comes to leakage compared to both VOF and phase-field. A possible explanation for the results observed using the Current approach can be gleaned from the findings of Latva-Kokko and Rohtman [35]. They observed that the implementation of the RK model generates an artificial slip velocity, leading to a dynamic contact angle even though it wasn't specified. The role played by dynamic contact angles in leakage is less known, though it must be mentioned that Liu observed leakage, albeit inaccurately, in his simulations when he included an expression for a non-equilibrium dynamic contact angle, and no leakage when this expression was not included [3]. Even when we consider the Guo approach at Capillary numbers larger than 2×10^{-3}, leakage was accurately captured for most flow rate ratios, except for 0.8-1 where no leakage was obtained.

Obviously, more study is needed to see how dynamic contact angle and slip are related to leakage. However, this section clearly shows the ability of the Current approach to capture leakage.

3.5. Discussion

To understand the reasons for the results shown in Section 5.2, we dive a little deeper into the numerical aspects of each technique in this section, with a particular emphasis on spurious velocities. The current and Guo approaches, VOF and VOF-LS are looked into in the following subsections. The deficiencies of the phase field method are discussed in detail by Liu [3], so we won't be discussing them here.

3.5.1. Spurious Velocities

Current vs Guo

Figure 3.12 shows the capability of the Guo and Current approaches in capturing parallel flow in the microchannel. At a Toluene Capillary number of 10^{-3}, the flow is parallel when using the Current approach (Figure 3.12c) which is the expected experimental result, whereas slug flow is obtained when applying the Guo approach

(Figure 3.12a). A possible explanation for this difference can be found in the magnitude of the spurious velocities, which are created by the CSF term. Figure 3.13 shows the contours of the u_x/u_{max} (u_{max} being the maximum expected fluid velocity at the centre of the main channel) for both cases at Ca=10^{-3}. While the Current approach shows the correct velocity profile and maximum velocity (Figure 3.13b), Figure 3.13a points to larger velocities at the interface when using the Guo approach (u_x/u_{max}=1.4), especially near the intersection of both inlets. These large spurious velocities are in line with the results of Xu et al [32], where the largest velocities were observed at the contact points of the fluid-fluid and fluid-solid interfaces, especially at corners.

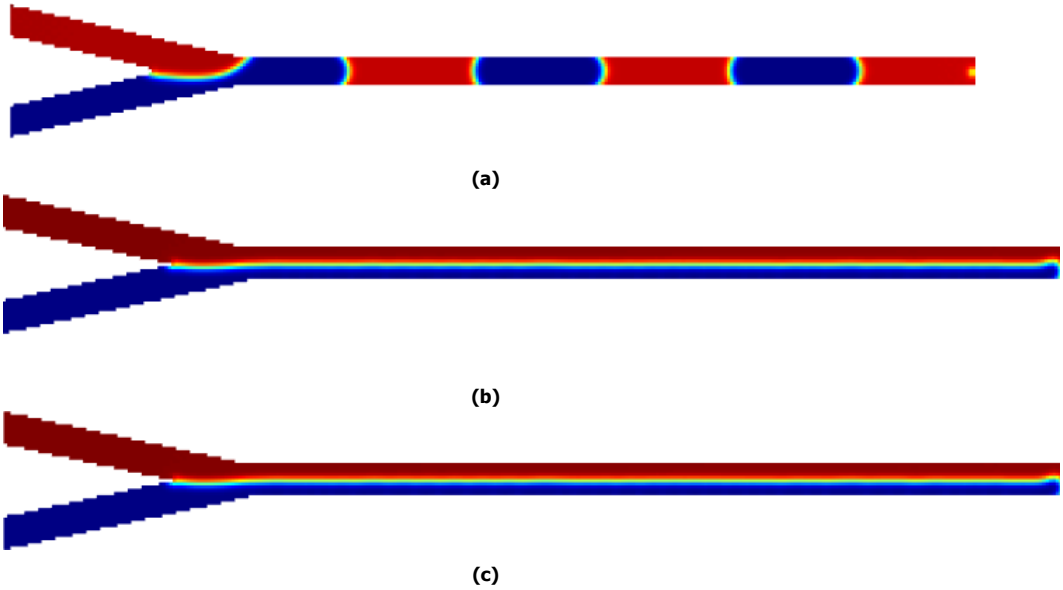

Figure 3.12: Flow pattern of Water (red)-Toluene (blue) system observed for the a) Guo approach, $Ca = 10^{-3}$, b) Guo approach, $Ca = 2 \times 10^{-3}$ and c) Current approach, $Ca = 10^{-3}$.

The spurious velocities can be more prominently visualized at a lower Capillary number of 10^{-4}, as shown in Figures 3.14 and 3.15. At this range, we can see from Figure 3.14b that the velocities at the interface using the Current approach are only a little larger than the maximum fluid velocity (the ratio is around 1.2). On the other hand, the spurious velocities observed in the Guo approach are nearly an order of magnitude larger than the expected fluid u_{max} (Figure 3.15b).

At a Capillary number of 10^{-3}, the maximum fluid velocity is lesser than the interfacial velocities in the Guo approach, so these spurious velocities compete with the expected flow phenomena. If we operate at a higher Capillary number, where the fluid velocity is larger than the spurious velocities, we should obtain parallel flow. At a Capillary number of 2×10^{-3}, the maximum fluid velocity is larger than

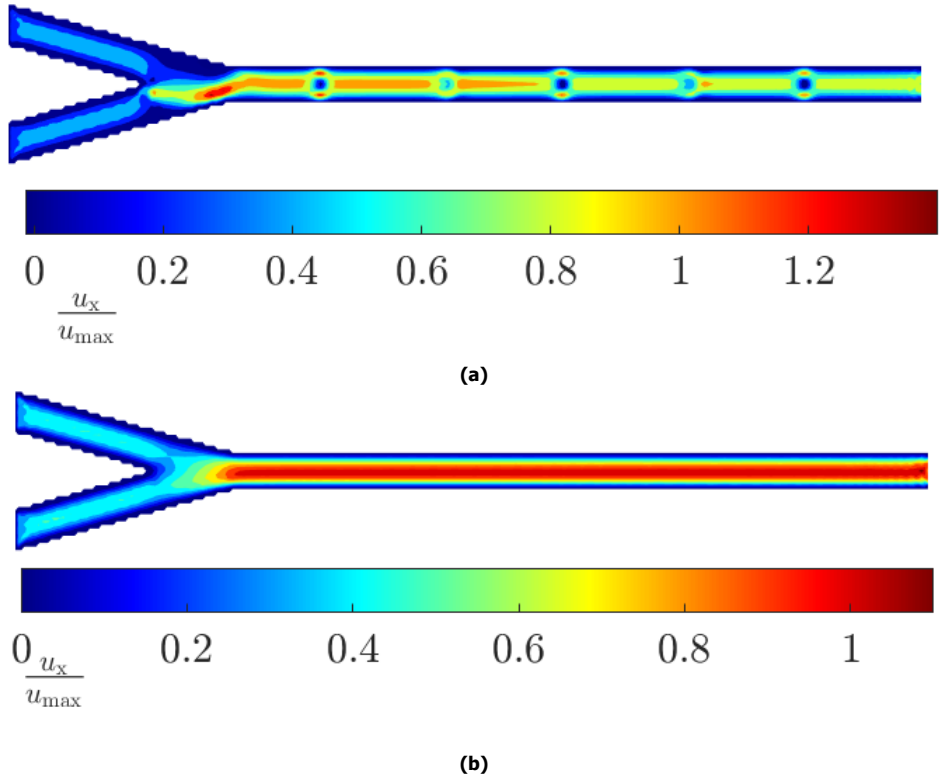

Figure 3.13: Normalized u_x contour for the a) Guo and b) Current approaches at a Capillary number of 10^{-3}.

the interfacial velocity of around 0.04, and, as seen in Figure 3.12b, parallel flow is indeed obtained.

To conclude, in LBM, the Current approach is more practical in predicting parallel flow in microchannel than the Guo approach at low Capillary numbers (Ca<10^{-3}).

VOF

Since the VOF method uses the CSF term for implementing surface tension, one would expect similar problems as observed for the Guo approach. If we look at the u_x contours at $Ca = 10^{-4}$, we can see that the spurious velocities are very high for VOF (Figure 3.16b), and lower for VOF-LS (Figure 3.16c). The velocities are observed to be the largest at the intersection, with the spurious velocities being an order of magnitude larger for VOF and nearly 6 times larger for VOF-LS.

Note that though the VOF-LS approach does reduce the spurious velocities present in VOF, it still requires more modifications to operate at very low Capillary

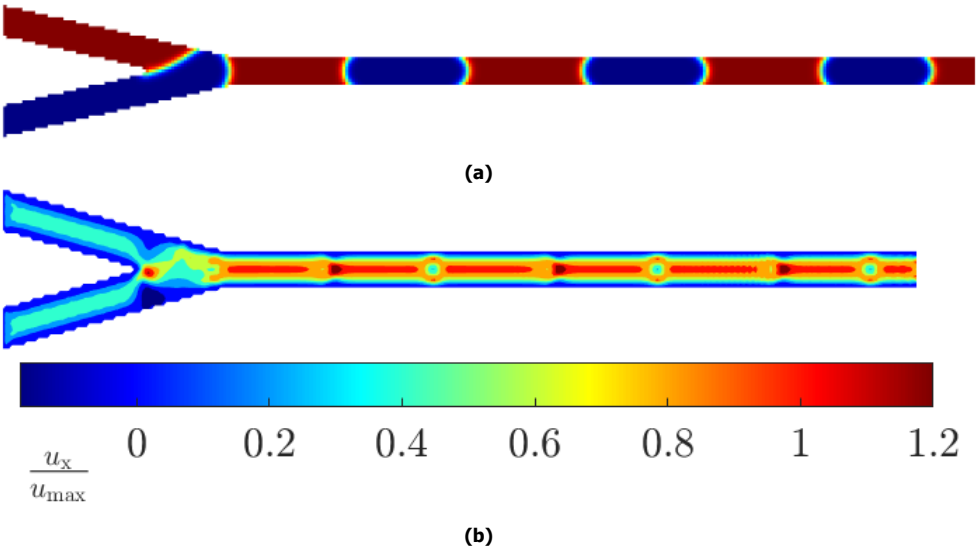

Figure 3.14: Slug flow for a Capillary number of 10^{-4} using the Current approach, with the same velocities for both fluids. a) Density contour, b) Normalized u_x contour. The red fluid is water and the blue fluid is toluene, with the diffuse interface represented by the transitioning of colours from blue to red.

numbers. In summary, looking at Figures 3.13a, 3.16b and 3.16c, we can clearly see that the CSF term introduces large interfacial velocities regardless of whether we use VOF or LBM. This could be a possible reason why we observe constant slug lengths for VOF and the Guo approach in Figure 3.7, and why we observe the expected trend once we reduce the spurious velocities using the Current approach.

3.5.2. Grid Convergence

One way of checking for grid independence is by plotting the slug lengths across different grid resolutions and observing the point of convergence [3, 5, 8], i.e., when the slug length remains constant with further refinement. It has been found that both the VOF and RK models show converged slug lengths at a mesh size of 8 μm.

A more strict criterion for grid convergence is proposed here, which is based on the ability of the scheme to capture parallel flow. Figure 3.17 shows the results for VOF as well as the RK approaches. This figure covers Ca numbers where parallel flow is to be expected (see Figure 5.5).

In Figure 3.17, we can see that the Current approach converges the quickest. Even for large mesh sizes, parallel flow is predicted for most Ca numbers. In the case of VOF and the Guo approach, however, the presence of large spurious velocities considerably influences the flow regime as indicated by Figure 3.12a, favouring

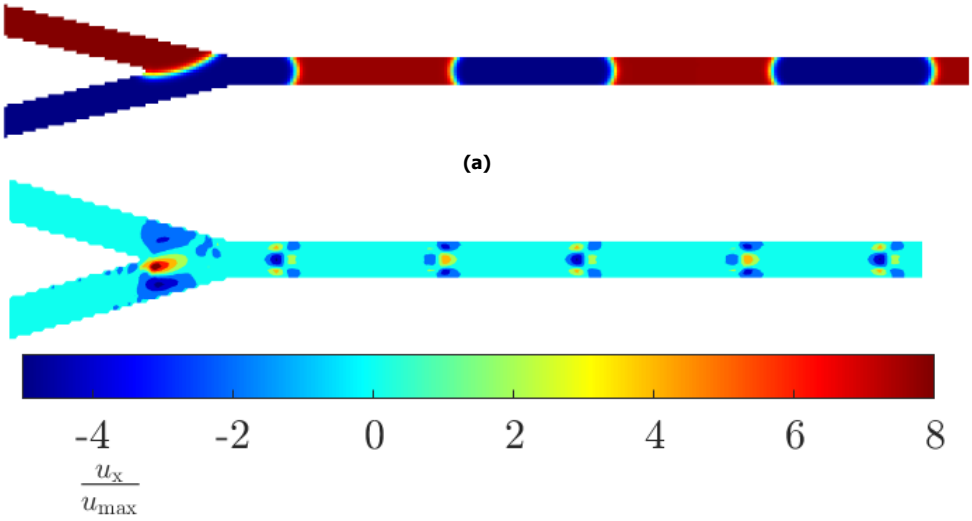

Figure 3.15: Slug flow for a Capillary number of 10^{-4} using the Guo approach, with the same velocities for both fluids. a) Density contour, b) Normalized u_x contour. The red fluid is water and the blue fluid is toluene.

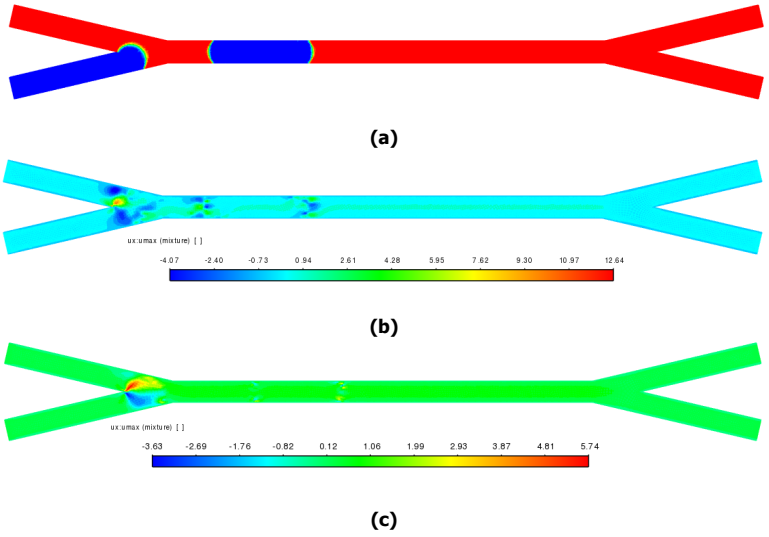

Figure 3.16: Slug flow for a Capillary number of 10^{-4} using VOF and VOF-LS, with the same velocities for both fluids. a) Density contour of VOF and VOF-LS, b) Normalized u_x contour using VOF c) Normalized u_x contour using VOF-LS. The red fluid is water and the blue fluid is toluene, with the diffuse interface represented by the transitioning of colours from blue to red.

slug instead of parallel flow. The Guo approach doesn't converge even at a reso-

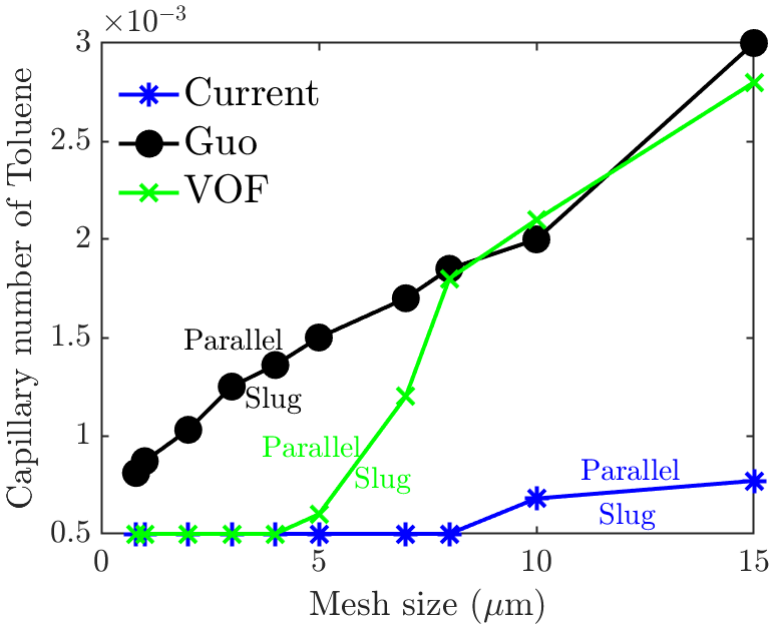

Figure 3.17: Grid convergence for the Current (circles) and Guo approaches (asterisks), and VOF (crosses). The vertical axis corresponds to the Capillary number of Toluene at which parallel flow is first observed in the simulation and the horizontal axis is the mesh size. Slug flow is observed for all the Capillary numbers below the respective lines and parallel flow is above the lines.

lution as low as 0.8 μm, hence finer domains are required for convergence. Both the VOF and VOF-LS models show slug flow in coarse grids, and capture parallel flow at a mesh size of $5\ \mu m$(Figure 3.11) after grid refinement, despite the large spurious velocities.

In conclusion, the Current approach predicts the transition from parallel flow to slug flow at relatively coarse meshes, which is favourable in terms of calculation time.

3.5.3. Comparison of the Simulation Techniques

The capabilities of the different approaches in capturing the flow phenomena at relatively low Ca numbers in a Y-Y channel are summarized in Table 3.3.

We can clearly see that no technique is able to successfully and accurately capture all the flow phenomena, but overall, the Phase-Field and Current approaches are the most successful. The current approach is a better option when simulating parallel flow and leakage, while the phase-field approach is a good choice for capturing slug lengths and the overall flow map. It must be mentioned that considerable care has to be exercised in choosing the numerical parameters in the Phase-Field method, especially the numerical Peclet and Cahn numbers. Different Peclet numbers lead to changes in the observed simulation results when it comes to

Table 3.3: Table comparing the capabilities of simulation techniques in capturing flow phenomena at low Capillary numbers. Based on the simulation results, each technique is accorded a value for each category. X corresponds to not capturing the phenomenon at all, 0 to qualitatively capturing the overall phenomenon but unable to capture the finer details (E.g VOF showing constant slug lengths with varying Capillary numbers and not the expected trend), + to successfully capturing the finer details, although inaccurately (E.g inaccurate leakage regimes) and ++ to accurately capturing all the details.

Technique	Slug Flow	Transition Flow	Parallel Flow	Leakage	Grid Convergence	Flexibility
Current	+	X	++	++	++	++
Guo	0	X	0	++	X	++
Phase Field	++	++	++	0	++	0
VOF	0	X	++	+	+	++

slug lengths and leakage [3], and this limits the flexibility of the Phase-Field method. The current approach, on the other hand, doesn't have as stringent a requirement on the value of its numerical parameters, thus providing an added advantage when simulating multiphase flows at low Capillary numbers.

3.6. Conclusion

This chapter examines the RK-LBM model's capability and accuracy in simulating flow regimes in a complex geometry - a Y-Y channel - under convective conditions and at low Capillary numbers. The approach proposed by Xu *et al* [32] was used for implementing the contact angle. The forcing term proposed by Guo [23] was modified to reduce the magnitude of the spurious velocities and extend the application of the RK model to lower Capillary numbers.

The current approach is clearly an improvement over the existing Guo approach at low Capillary numbers, showing quick grid convergence and successfully capturing leakage. Additionally, it also shows the expected trend of slug lengths decreasing with Capillary number as opposed to VOF and the Guo approach. More accurate slug lengths are observed in the phase-field method, but the Phase-Field method isn't able to capture leakage accurately. Thus, the current approach is a viable option at lower Capillary numbers especially when it comes to simulating parallel flow and leakage.

More studies are needed to come up with better solutions to capture intermediate phenomena such as transition and deformed interface flows. Modifications to the CSF term have been done in Volume-of-Fluid methods [36, 29], but these modifications have not been applied to complex cases such as micro-channel flows. Future models would have to work along the lines of accurate determination of the curvature (Equation 2.21) for improved results.

Bibliography

[1] Xiao-Bin Li, Feng-Chen Li, Juan-Cheng Yang, Haruyuki Kinoshita, Masamichi Oishi, and Marie Oshima. Study on the mechanism of droplet formation in t-junction microchannel. *Chemical engineering science*, 69(1):340–351, 2012.

[2] Vinesh H Gada and Atul Sharma. Analytical and level-set method based numerical study on oil–water smooth/wavy stratified-flow in an inclined plane-channel. *International journal of Multiphase flow*, 38(1):99–117, 2012.

[3] Z Liu. Purifying radionuclides with microfluidic technology for medical purpose: Simulating multiphase flows inside a microfluidic channel with the phase field method. 2022.

[4] Haihu Liu and Yonghao Zhang. Droplet formation in microfluidic cross-junctions. *Physics of Fluids*, 23(8), 2011. ISSN 10706631. doi: 10.1063/1.3615643.

[5] Li Lei, Yuting Zhao, Xinyu Wang, Gongming Xin, and Jingzhi Zhang. Experimental and numerical studies of liquid-liquid slug flows in micro channels with Y-junction inlets. *Chemical Engineering Science*, 252:117289, 2022. ISSN 00092509. doi: 10.1016/j.ces.2021.117289. URL https://doi.org/10.1016/j.ces.2021.117289.

[6] M. N. Kashid, A. Renken, and L. Kiwi-Minsker. CFD modelling of liquid-liquid multiphase microstructured reactor: Slug flow generation. *Chemical Engineering Research and Design*, 88(3):362–368, 2010. ISSN 02638762. doi: 10.1016/j.cherd.2009.11.017. URL http://dx.doi.org/10.1016/j.cherd.2009.11.017.

[7] Piotr Garstecki, Michael J. Fuerstman, Howard A. Stone, and George M. Whitesides. Formation of droplets and bubbles in a microfluidic T-junction - Scaling and mechanism of break-up. *Lab on a Chip*, 6(3):437–446, 2006. ISSN 14730189. doi: 10.1039/b510841a.

[8] S. Van Der Graaf, T. Nisisako, C. G.P.H. Schroën, R. G.M. Van Der Sman, and R. M. Boom. Lattice Boltzmann simulations of droplet formation in a T-shaped microchannel. *Langmuir*, 22(9):4144–4152, 2006. ISSN 07437463. doi: 10.1021/la052682f.

[9] Yan Ba, Haihu Liu, Jinju Sun, and Rongye Zheng. Three dimensional simulations of droplet formation in symmetric and asymmetric t-junctions using the color-gradient lattice boltzmann model. *International Journal of Heat and Mass Transfer*, 90:931–947, 2015.

[10] Timm Krüger, Halim Kusumaatmaja, Alexandr Kuzmin, Orest Shardt, Goncalo Silva, and Erlend Magnus Viggen. The lattice boltzmann method. *Springer International Publishing*, 10(978-3):4–15, 2017.

[11] Sauro Succi. Mesoscopic Modeling of Slip Motion at Fluid-Solid Interfaces with Heterogeneous Catalysis. *Physical Review Letters*, 89(6):1–4, 2002. ISSN 10797114. doi: 10.1103/PhysRevLett.89.064502.

[12] Martin Wörner. Numerical modeling of multiphase flows in microfluidics and micro process engineering: A review of methods and applications. *Microfluidics and Nanofluidics*, 12(6):841–886, 2012. ISSN 16134982. doi: 10.1007/s10404-012-0940-8.

[13] Haihu Liu, Yaping Ju, Ningning Wang, Guang Xi, and Yonghao Zhang. Lattice Boltzmann modeling of contact angle and its hysteresis in two-phase flow with large viscosity difference. *Physical Review E - Statistical, Nonlinear, and Soft Matter Physics*, 92(3), 2015. ISSN 15502376. doi: 10.1103/PhysRevE.92.033306.

[14] Long Wu, Michihisa Tsutahara, Lae Sung Kim, and Man Yeong Ha. Three-dimensional lattice Boltzmann simulations of droplet formation in a cross-junction microchannel. *International Journal of Multiphase Flow*, 34(9):852–864, 2008. ISSN 03019322. doi: 10.1016/j.ijmultiphaseflow.2008.02.009.

[15] Zhao Yu, Orin Hemminger, and Liang Shih Fan. Experiment and lattice Boltzmann simulation of two-phase gas-liquid flows in microchannels. *Chemical Engineering Science*, 62(24):7172–7183, 2007. ISSN 00092509. doi: 10.1016/j.ces.2007.08.075.

[16] Sachit Goyal, Amit V. Desai, Robert W. Lewis, David R. Ranganathan, Hairong Li, Dexing Zeng, David E. Reichert, and Paul J.A. Kenis. Thiolene and SIFEL-based microfluidic platforms for liquid-liquid extraction. *Sensors and Actuators, B: Chemical*, 190:634–644, 2014. ISSN 09254005. doi: 10.1016/j.snb.2013.09.065.

[17] Peyman Foroozan Jahromi, Javad Karimi-Sabet, and Younes Amini. Ion-pair extraction-reaction of calcium using Y-shaped microfluidic junctions: An optimized separation approach. *Chemical Engineering Journal*, 334(November):2603–2615, 2018. ISSN 13858947. doi: 10.1016/j.cej.2017.11.129. URL https://doi.org/10.1016/j.cej.2017.11.129.

[18] N. Assmann, A. Ladosz, and P. Rudolf von Rohr. Continuous Micro Liquid-Liquid Extraction. *Chemical Engineering and Technology*, 36(6):921–936, 2013. ISSN 09307516. doi: 10.1002/ceat.201200557.

[19] R. G.M. Van Der Sman. Galilean invariant lattice Boltzmann scheme for natural convection on square and rectangular lattices. *Physical Review E - Statistical,*

Nonlinear, and Soft Matter Physics, 74(2), 2006. ISSN 15393755. doi: 10.1103/PhysRevE.74.026705.

[20] Yuhang Fu, Lin Bai, Kexin Bi, Shufang Zhao, Yong Jin, and Yi Cheng. Numerical study of Janus droplet formation in microchannels by a lattice Boltzmann method. *Chemical Engineering and Processing: Process Intensification*, 119 (May):34–43, 2017. ISSN 02552701. doi: 10.1016/j.cep.2017.05.019. URL http://dx.doi.org/10.1016/j.cep.2017.05.019.

[21] Mayur Darekar, Krishna Kumar Singh, Sulekha Mukhopadhyay, and Kalsanka Trivikram Shenoy. Liquid-Liquid Two-Phase Flow Patterns in Y-Junction Microchannels. *Industrial and Engineering Chemistry Research*, 56(42):12215–12226, 2017. ISSN 15205045. doi: 10.1021/acs.iecr.7b03164.

[22] Anne Laure Dessimoz, Laurent Cavin, Albert Renken, and Lioubov Kiwi-Minsker. Liquid-liquid two-phase flow patterns and mass transfer characteristics in rectangular glass microreactors. *Chemical Engineering Science*, 63(16): 4035–4044, 2008. ISSN 00092509. doi: 10.1016/j.ces.2008.05.005.

[23] Zhaoli Guo, Chuguang Zheng, and Baochang Shi. An extrapolation method for boundary conditions in lattice Boltzmann method. *Physics of Fluids*, 14(6): 2007–2010, 2002. ISSN 10706631. doi: 10.1063/1.1471914.

[24] I. Halliday, R. Law, C. M. Care, and A. Hollis. Improved simulation of drop dynamics in a shear flow at low Reynolds and capillary number. *Physical Review E - Statistical, Nonlinear, and Soft Matter Physics*, 73(5):1–11, 2006. ISSN 15393755. doi: 10.1103/PhysRevE.73.056708.

[25] Stéphane Popinet. Numerical models of surface tension. *Annual Review of Fluid Mechanics*, 50:49–75, 2018.

[26] Markus Meier, George Yadigaroglu, and Brian L Smith. A novel technique for including surface tension in plic-vof methods. *European Journal of Mechanics-B/Fluids*, 21(1):61–73, 2002.

[27] A J C Ladd and R Verberg. Lattice-Boltzmann Simulations of Particle-Fluid Suspensions. 104(September):1191–1251, 2001.

[28] Jeremiah U Brackbill, Douglas B Kothe, and Charles Zemach. A continuum method for modeling surface tension. *Journal of computational physics*, 100 (2):335–354, 1992.

[29] Ali Q Raeini, Martin J Blunt, and Branko Bijeljic. Modelling two-phase flow in porous media at the pore scale using the volume-of-fluid method. *Journal of Computational Physics*, 231(17):5653–5668, 2012.

[30] Mark Sussman and Elbridge Gerry Puckett. A coupled level set and volume-of-fluid method for computing 3d and axisymmetric incompressible two-phase flows. *Journal of computational physics*, 162(2):301–337, 2000.

[31] J Abrahamson. Fluent Theory Guide. 2022.

[32] Zhiyuan Xu, Haihu Liu, and Albert J Valocchi. Lattice b oltzmann simulation of immiscible two-phase flow with capillary valve effect in porous media. *Water Resources Research*, 53(5):3770–3790, 2017.

[33] Jun Jie Huang, Haibo Huang, and Xinzhu Wang. Numerical study of drop motion on a surface with stepwise wettability gradient and contact angle hysteresis. *Physics of Fluids*, 26(6):1–34, 2014. ISSN 10897666. doi: 10.1063/1.4880656.

[34] Haihu Liu, Albert J. Valocchi, and Qinjun Kang. Three-dimensional lattice Boltzmann model for immiscible two-phase flow simulations. *Physical Review E - Statistical, Nonlinear, and Soft Matter Physics*, 85(4):1–14, 2012. ISSN 15393755. doi: 10.1103/PhysRevE.85.046309.

[35] M. Latva-Kokko and Daniel H. Rothman. Scaling of dynamic contact angles in a Lattice-Boltzmann model. *Physical Review Letters*, 98(25):98–101, 2007. ISSN 00319007. doi: 10.1103/PhysRevLett.98.254503.

[36] C Ierardi, A Della Torre, G Montenegro, A Onorati, Francesco Radaelli, Luca Visconti, and Marco Miarelli. Modeling of two-phase flows at low capillary number with vof method. *Computers & Fluids*, 252:105772, 2023.

4

Influence of the Outlet Geometry on Leakage

Sections 1.3.5 and 1.5 elucidated the different methods which can be applied to the channel geometry to eliminate leakage. Some studies have dedicated their efforts towards phaseguides [1, 2] and the use of external coatings to minimize leakage [3, 4]. A phaseguide is basically an obstacle in a microfluidic channel where a change in geometry results in a change in capillary pressure applied to the fluids. Generally, such modifications are located inside the main channel. Modifications in the main channel affect the surface area available for mass transfer and extraction. Coatings, on the other hand, are very limited in their flexibility as different coatings are required for different fluids and channel materials. An alternative option to both of these would be to modify the channel outlet alone to prevent leakage. This has the advantage of not affecting the surface area for mass transfer while offering greater flexibility. Thus, this chapter focuses on the influence of the outlet geometry on fluid behaviour and leakage.

One modification to the outlet which has proven to be successful was the addition of a third outlet to a T-T microfluidic channel used by Lu *et al* [5]. Though this design is very effective, a problem with the third outlet, as mentioned in Section 1.5, is the loss of fluid. It could be very beneficial for applications involving radioisotopes to recycle fluids [6], and this is especially so for radioisotopes with short half-lives and rarer elements. Thus, a broader study of this design should also aim to chronicle the percentage of fluid lost.

In this chapter, different outlet modifications are proposed and their leakage regimes are subsequently observed. Additionally, the flow profiles are also plotted to obtain a broader understanding of fluid behaviour at the outlet. The RK model is first validated by comparing simulations with experiments done using the triple outlet. Next, the triple outlet design proposed by Lu *et al* [7] is studied, with the

third outlet being slightly modified to minimize loss and leakage. Both the loss of fluid and leakage are considered.

We then shift our attention to newly proposed designs that do not involve fluid loss at the outlet. In these designs, an additional reservoir is included at the outlet to minimize leakage, and this is further modified to incorporate the principle of phaseguides proposed by Vulto *et al* [1].

4.1. Code Validation for Modified Outlet

Chapter 3 established that the modified RK model simulates leakage and parallel flow better than other simulation techniques (Table 3.3). Thus, we will be using the modified RK model for our leakage simulations in these new designs. All the simulations are performed in 2D. To further validate the RK model, we run experiments for Water-Novec (HydroFluoroEther, HFE, 3M™ Novec™ 7500 Engineered Fluid) in a modified triple outlet design. The experimental methodology and the validation results are described in the next subsections.

4.1.1. PDMS Microfluidic Chip Fabrication

Microfluidic chips could be fabricated using different materials. As it is important to modify the geometry of the chips, polydimethylsiloxane (PDMS) is used because the chips can be easily manufactured. PDMS is an organosilicon polymer that stays in liquid form upon mixing the elastomers with the curing agent. As a result, the mixture can be poured into a petri dish with a patterned mould master, where it takes the shape of the pattern printed on the mould master. The petri dish can be set in an oven to speed up the hardening process.

The mould master is first fabricated using the soft lithography technique. On top of a cleaned 4 inch silicon wafer, a negative photoresist (SU8-2050, micro resist technology GmbH) at 2000 rpm is spin-coated for 30 s to obtain a layer of 50 µm thickness. The wafer was then baked at 100°C for 15 min and loaded onto a Laser-Writer (Heidelberg, 1 µm laser beam at 365 nm). The pattern was then written on the wafer. Afterwards, the wafer was soft-baked at 100°C for 5 min. The wafer was then developed using Propylene glycol methyl ether acetate (> 99.5%, Merck Sigma) for 10 min, and post-baked at 200°C for 30 min.

The PDMS microfluidic chip was fabricated by mixing the elastomer (Sylgard 184 Elastomer Kit, Dow Corning Comp.) and the curing agent with a mass ratio of 10:1. The mixture was then degassed, poured over the patterned master mould on a petri dish, and cured at 70°C for 10 h. The hardened PDMS chips were gently removed from the mould master and cut to size. The inlets and outlets were punched using a 1.5 mm biopsy puncher, before being cleaned using ethanol. On the other hand, a glass slide was spin-coated with 20 µm PDMS (2000 rpm for 2 min, Laurell

WS-650-23B). Both the chips and the coated glass slides were bonded together using oxygen plasma treatment (Harrick PDC-002) at 0.2-0.4 mbar for 140 s. The preparation of the mould master and fabrication of the chips was done by Albert Santoso, while the chips were cut from the mould master by the author himself.

4.1.2. Flow Setup

To conduct the flow experiments, we used two syringe pumps (Pump 11 Pico Plus Elite). On each of the syringe pumps, a 10 mL syringe (Beckton-Dickinson, Discardit II) was mounted. One of the syringes contained demineralized water with 10 mg/L brilliant blue dye while the other syringe contained an immiscible fluorinated oil (HydroFluoroEther, HFE, 3M™ Novec™ 7500 Engineered Fluid). The syringes were connected with PEEK tubes (0.5 mm ID, 1.59 mm OD, 300 mm in length) to the inlets of the microfluidic chips. The outlets were connected to other PEEK tubes, leading to a disposal container.

4.1.3. Fluid Properties

Water-Novec mixtures are used in the experiments and the experimental results are also validated using the simulations. After validation, Water-toluene mixtures are used in the simulations with the same properties as described in Chapter 3. The channel for water-toluene also has the same wettability as that was used in the Y-Y channel simulations. The fluid properties are described in Table 5.1.

Table 4.1: Properties of the fluids used in the simulations

Fluid	**Viscosity** (mPa · s)	**Density** (g/cm^3)	**Coefficient of Interfacial Tension** (mN/m)	**Contact Angle** (°)
Water	1.00	1.00		49.1
Toluene	0.583	0.867	36.1	
Novec™ 7500	1.24	1.614	43.8	39.7

4.1.4. Numerical Validation

The purpose of the experiments is to provide further validation of the modified RK model in capturing leakage. The PDMS chip described in Section 4.1.1 is used here and the properties of the Water-Novec mixture are described in Table 5.1. The dimensions of the T-T channel are the same as that mentioned in Section 4.2, with $D_1 = 70\mu$m, $D_2 = 140\mu$m and $D_3 = 100\mu$m and the channel depth being 40 μm.

Figure 4.1a shows the experimental result when ϕ=0.6. ϕ is defined as

$$\phi = \frac{Q_{\text{aq}}}{Q_{\text{org}}} = \frac{u_{\text{aq}}}{u_{\text{org}}} \tag{4.1}$$

where Q and u correspond to the flow rate and velocity respectively, with the subscripts aq and org corresponding to the aqueous and organic phases respectively. The simulation result is also shown for comparison (Figure 4.1b), and it can be clearly seen that the simulation successfully captures the experimental flow and leakage regime. Further, Table 4.2 shows the range of ϕ that shows stable parallel flow for the Water-Novec mixture in this channel. The simulations appear to differ slightly from the experiments here, but this could arise from the fluctuations observed in syringe pumps [8, 9]. Regardless, the modified RK model has been sufficiently validated as a reliable tool for capturing leakage.

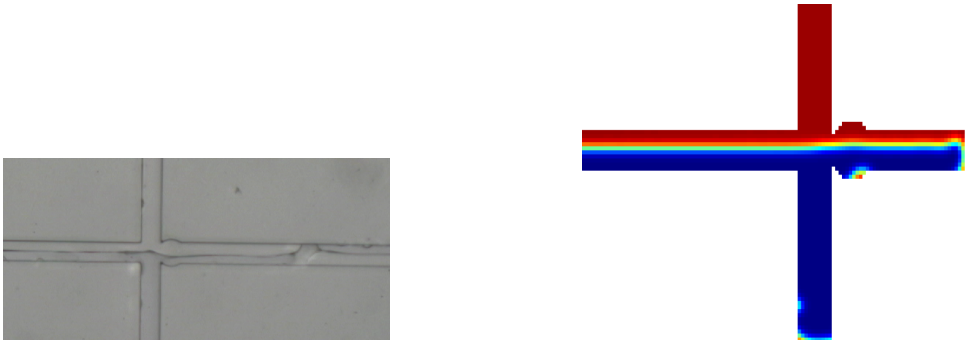

(a) (b)

Figure 4.1: a) Experimental result showing stable parallel flow for the Water-Novec mixture in a PDMS T-T channel with the modified triple outlet design at ϕ=0.6. $D_1 = 70\mu$m, $D_2 = 140\mu$m and $D_3 = 100\mu$m. b)Simulations for the same flow configuration using the modified RK model. The blue fluid is Novec and the red fluid is water

Table 4.2: Comparison of experiments and simulations regarding the range of ϕ showing stable parallel flow in the PDMS chip for a Water-Novec mixture

Method	Range of ϕ
Experiments	0.5-1.9
Simulations	0.5-2.1

4.2. Channel Designs

T-T channels are adopted for this study instead of Y-Y channels. The reason for this is that Lu *et al's* [5] used a T-T channel in their triple outlet design (Figure 4.2a), so using a T-T channel will be easier for comparison. However, the results observed in the chapter can easily be extended to a Y-Y channel as a T-T channel is nothing but a Y-Y channel with an angle of 180 ° between the inlets.

The T-T channel has the same dimensions for all the designs, with a width of 100 μm and a length of 1 cm. Four different designs are employed in this chapter

and each of them is described in the following subsections.

4.2.1. Modified Triple Outlet Design

The triple outlet design used in this chapter is a slight modification of the design proposed by Lu *et al* [5]. Here, a circular head is added at the start of the third outlet as shown in Figure 4.2b. This circular head is added to minimize the loss of fluid and also to study the influence of the geometry of the third outlet on leakage. In the case of Lu *et al*, the third outlet has the same dimensions and shape as the other two outlets (Figure 4.2a). The dimensions of the third outlet in the modified design are governed by three measures - D_1, D_2, D_3. There are, thus, three different parameters to control as opposed to a simple rectangular outlet, where the only parameter of importance is the width of the outlet. Therefore, this design may offer more flexibility to control loss and leakage.

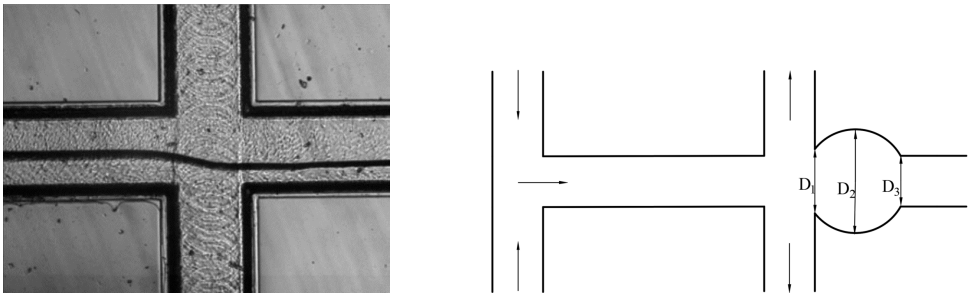

(a) (b)

Figure 4.2: a) The triple outlet design used by Lu *et al* [5] b) Modified triple outlet design used in this chapter

As discussed in many papers [10, 11], leakage is governed by the balance of the pressure loss due to viscosity and the Laplace pressure. Both the viscous pressure and capillary pressure experienced by the non-wetting fluid, which in our case, is the organic phase, is inversely proportional to the hydraulic diameter [10, 12]. While the hydraulic diameter can be difficult to estimate for the third outlet as there is variability in the outlet geometry, the loss of organic fluid to the third outlet should generally decrease with a decrease in either D_1, D_2 or D_3 as the non-wetting fluid experiences a higher capillary pressure at the third outlet, which means that it will have less preference for entering the third outlet. This is the main rationale for adding a circular head to the third outlet and the simulations are run to test that.

4.2.2. Circular Head Design

In this design, a closed semi-circular head is added in the space between the two outlets as shown in Figure 4.3. The idea behind this design is to minimize leakage

by pinning the three-phase point on the circular head.

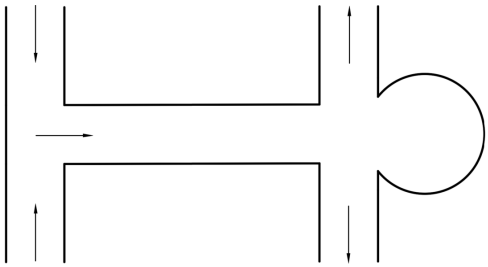

Figure 4.3: A T-T channel with a semi-circular head located between the outlets

4.2.3. Displaced Outlets with Circular Reservoir

Here, the outlets no longer lie in a straight line as in other designs, but the upper outlet is displaced from the lower outlet by a certain distance. This distance is given by the radius of the circular reservoir which connects the two outlets (Figure 4.4). The larger area of the circular reservoir should result in a significant slowdown in the fluid velocity, and this could help to prevent the leakage of the non-wetting fluid to the upper outlet. Because of the slow down in fluid velocity, the non-wetting fluid would ideally remain inside the circular reservoir as it would not have sufficient momentum to leak to the upper outlet.

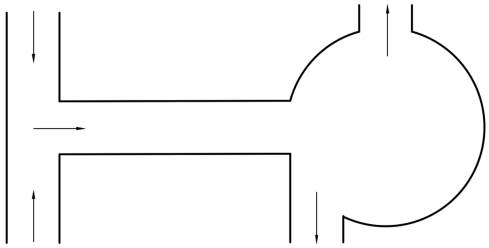

Figure 4.4: T-T channel with the upper outlet displaced horizontally from the lower outlet at a distance of the radius of the circular reservoir

However, there is a possibility for the non-wetting fluid to gradually accumulate in the reservoir and then leak into the upper outlet. To improve the design, there must be a means to pin the non-wetting fluid inside the reservoir. One technique which has been used in microchannels is the implementation of phaseguides. A phaseguide is defined as a change in geometry that spans the complete length of the liquid-liquid interface [1, 2]. This abrupt change in geometry results in an abrupt change in capillary pressure. An example of such a phaseguide is a small rectangular pillar located in the main rectangular channel. This property of the phaseguide ensures that the liquid is pinned, even though it is only temporary in

many cases [2]. Generally, phaseguides are located in the main channel as their application in previous studies has generally been restricted to controlling the filling of fluids in the channel rather than avoiding leakage altogether [1, 2].

Garbarino *et al* [2] studied the phenomena of pinning and filling in a channel with a ridge located inside the main channel to control the flow. They observed that the phaseguide geometry has an associated capillary pressure, which they termed *burst pressure*. Once the fluid pressure exceeds this burst pressure, it will flow over the ridge and into the outlet. The non-wetting fluid will especially experience a higher capillary pressure on this phase guide. Their experiments showed that the non-wetting fluid remains completely pinned if the burst pressure is too large for the fluid to overcome.

To extend the application of these phaseguides even further, we incorporate them in the outlet of the channel. The goal here is to not just control leakage, but to stop it altogether. Therefore, we combine the idea of a phaseguide with the circular reservoir. Since the circular reservoir slows down the velocity of the fluids significantly, a phaseguide located inside the reservoir will serve to stall fluid motion altogether, as the non-wetting will not have the sufficient momentum to overcome the burst pressure associated with the phaseguide when they are inside the reservoir.

To accomplish this, we propose the inclusion of pillars inside the circular reservoir. These pillars can be small obstacles blocking fluid flow, like the circular and rectangular pillar shown in Figure 4.5a. Alternatively, a large pillar can be placed at the centre of the circular reservoir, thereby altering the flow path. This can take the form of the pillar shown in Figure 4.5b, where a large circular pillar concentric to the reservoir is located.

Garbarino *et al* [2] observed that this burst pressure is contingent on the phaseguide geometry and channel wettability. Though their ridges were located along the depth of the channel, the principle of an abrupt change in geometry pinning the fluids can be extended to our 2D case as well. In the case of the concentric pillar, the burst pressure inside the circular reservoir can be approximated as:

$$P_{\text{burst}} = \frac{4\sigma\cos\theta}{(\text{O.D} - \text{I.D})}, \tag{4.2}$$

where P_{burst} is the burst pressure experienced by the non-wetting fluid in the reservoir, σ is the interfacial tension, θ is the contact angle, O.D is the diameter of the reservoir and I.D is the diameter of the pillar. From equation 4.2, we can see that a larger pillar diameter leads to a larger P_{burst}, which subsequently makes it more difficult for the non-wetting fluid to leak to the upper outlet. Naturally, this expression isn't entirely accurate, as the burst pressure will keep varying in the circular reservoir because the interface normals (fluid-fluid and fluid-solid) vary locally in a circular geometry. This expression, however, gives an idea of how the

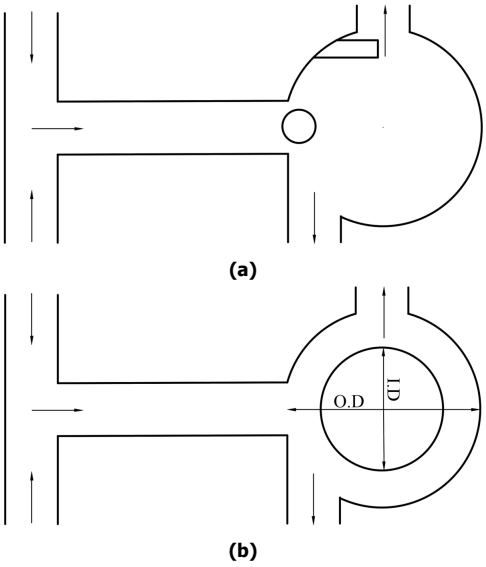

Figure 4.5: T channel with circular reservoir and a) Two pillars b) Concentric pillar

diameter of the pillar influences the pressure experienced by the non-wetting fluid.

4.3. Results

4.3.1. Modified Triple Outlet Design

The simulations are performed for water-toluene and the leakage regimes are observed. One of the measures (Figure 4.2b) is varied while the other two are fixed, and ϕ is varied for that particular geometrical configuration. ϕ is varied by varying the water flow rate while the flow rate of toluene is fixed.

Figure 4.6a shows the flow and leakage regime for a particular geometric configuration, where no leakage occurs as the water and toluene are perfectly separated. This illustrates the proof-of-concept, with the excess of both fluids being pushed to the third outlet as pure fluid is obtained in the top and bottom outlets. The velocity at the third outlet changes with the change in outlet dimensions.

First, D_1 is varied while D_2 and D_3 are fixed. Table 4.3 shows the range of ϕ for which stable parallel flow is observed without leakage to the upper or lower outlet. The broadest range of ϕ for which leakage is not observed is obtained for $D_1 = 70\mu$m, and a smaller range of ϕ is obtained for the other values. The desired range of ϕ depends on the nature of the application and a lower loss of organic fluid at the outlet is generally preferred. Based on the application, the measures can be varied accordingly.

The percentage of toluene lost to the third outlet is also calculated for various D_1

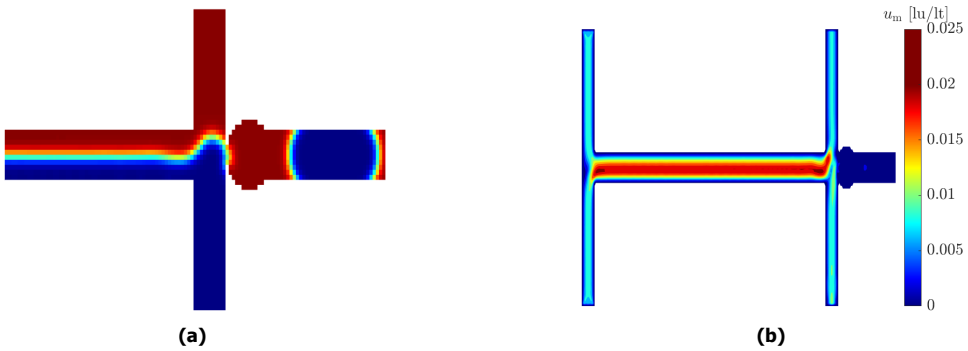

Figure 4.6: a) Simulations of a T-T channel with $D_1 = 50\mu$m, $D_2 = 140\mu$m and $D_3 = 100\mu$m. The Capillary number of toluene is 10^{-3} and ϕ=1. The blue fluid is toluene and the red fluid is water. b)Velocity magnitude contour for the same simulation with the units in lattice unit/lattice time (lu/lt).

Table 4.3: Range of ϕ showing stable parallel flow and loss of fluid when D_1 is varied

D_1 (μm)	D_2 (μm)	D_3 (μm)	Range of ϕ	% Loss when ϕ=1
50	140	100	0.5-1.35	6.94
70	140	100	0.45-2.2	37.75
90	140	100	0.5-2.1	47.39

when $\phi = 1$. This value is determined from the average velocity of toluene at the bottom and third outlet, and the area occupied by toluene in the respective outlets. The loss of toluene is considered important as extraction applications generally involve the transfer of solutes from an aqueous to an organic fluid [13, 14, 15]. The formula for the loss of toluene is given by:

$$\%Loss = \frac{u_{3,o}h_1}{(u_{3,o}h_1 + u_{1,o}H)} \tag{4.3}$$

where u corresponds to the average toluene velocity, the subscripts o correspond to the outlet, with 1 being the lower outlet and 3 being the outlet with the circular head, H is the width of the main channel/outlet/inlet and h_1 is the total surface occupied by toluene in the third outlet, which in the 2D case, is nothing but the width of the toluene in the third outlet. For an outlet of given length L, h_1 is given by:

$$h_1 = \frac{\text{Total surface occupied by Toluene in the third Outlet}}{L} \tag{4.4}$$

From Table 4.3, it can be seen that a smaller D_1, as expected, leads to a smaller loss of fluid.

Figures 4.6a and 4.6b clearly show why a small D_1 leads to a smaller loss of fluid while showing a reduced range of ϕ for which stable parallel flow is observed.

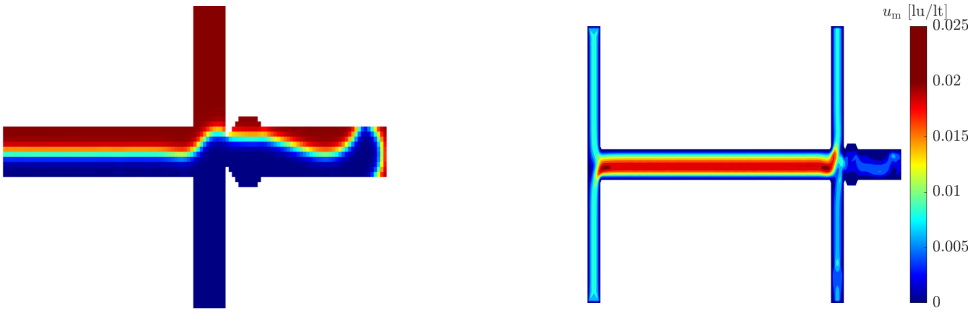

Figure 4.7: a) Simulations of a T-T channel with $D_1 = 70\mu$m, $D_2 = 140\mu$m and $D_3 = 100\mu$m. The Capillary number of toluene is 10^{-3} and ϕ=1. The blue fluid is toluene and the red fluid is water. b)Velocity magnitude contour for the same simulation in lu/lt.

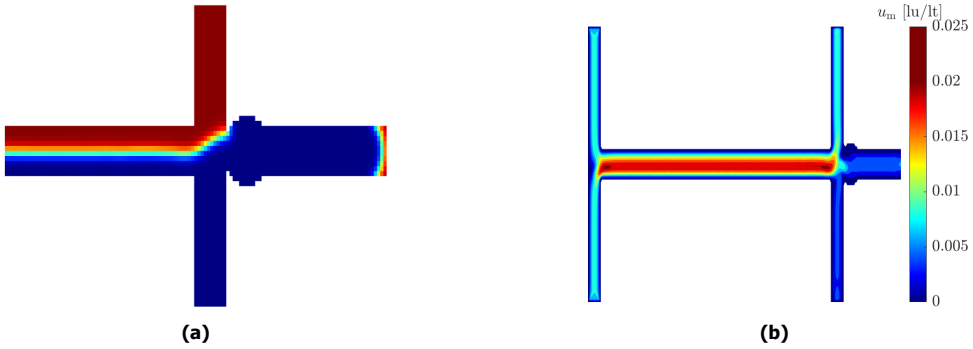

Figure 4.8: a) Simulations of a T-T channel with $D_1 = 90\mu$m, $D_2 = 140\mu$m and $D_3 = 100\mu$m. The Capillary number of toluene is 10^{-3} and ϕ=1. The blue fluid is toluene and the red fluid is water. b)Velocity magnitude contour for the same simulation in lu/lt.

The velocity at the third outlet (Figure 4.6b) is nearly an order of magnitude lower compared to the other two outlets, which shows that the liquids have a preference for the other two outlets. From equation 4.3, we can see that a smaller velocity at the third outlet results in a smaller loss of fluid. This confirms our hypothesis discussed in Section 4.2.1. However, a smaller D_1 also reduces the range of ϕ for which stable parallel flow is observed. As $D_1 \to 0$ the outlet geometry approaches a standard T-T channel, where leakage is commonly observed and stable parallel flow is hard to achieve.

When D_1 is relatively high, however, a parallel or wavy interface, is observed at the third outlet (Figure 4.7a) or toluene occupies the entire outlet (Figure 4.8a). The velocity at the third outlet increases with an increase in D_1 (Figures 4.7b and 4.8b), and this results in a parallel or wavy regime being observed at the third outlet. A larger velocity, however, also increases the loss of toluene as Table 4.3 shows.

The influence of D_2 on leakage and loss of fluid is studied next. From Table 4.4, we can see that D_2 has a minimal effect on leakage and stable parallel flow. This is because, at $\phi > 2.2$, droplets and slugs are observed in the main channel, not parallel flow. The overall flow regime (slug or parallel flow) observed is unrelated to the outlet geometry, and is an inlet phenomenon, as droplet flow is observed for a simple T-T channel at this ϕ without a third outlet. The loss, increases with an increase in D_2, confirming our expectations as discussed in Section 4.3. This can be seen when we compare the velocity contours in Figures 4.7b and 4.9b, where a larger velocity is observed in the third outlet for a larger D_2.

Table 4.4: Range of ϕ showing stable parallel flow and loss of fluid when D_2 is varied

D_1 (μm)	D_2 (μm)	D_3 (μm)	Range of ϕ	% Loss when ϕ=1 (%)
70	120	100	0.45-2.1	30.89
70	140	100	0.45-2.2	37.75
70	160	100	0.45-2.2	43.56
70	180	100	0.45-2.2	55.27

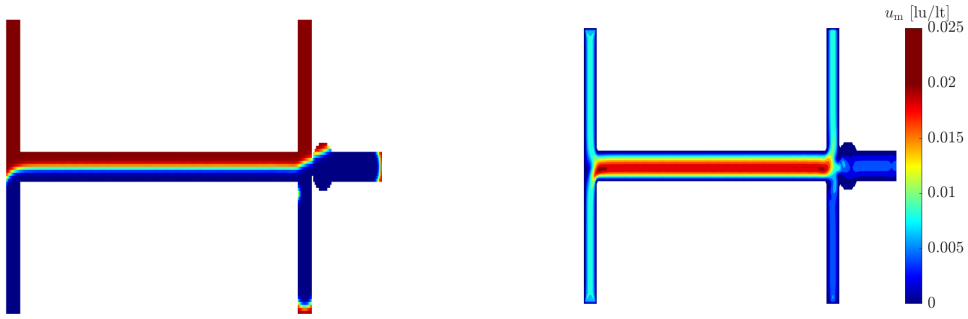

(a) (b)

Figure 4.9: a) Simulations of a T-T channel with $D_1 = 70\mu$m, $D_2 = 160\mu$m and $D_3 = 100\mu$m. The Capillary number of toluene is 10^{-3} and ϕ=1. The blue fluid is toluene and the red fluid is water. b)Velocity magnitude contour for the same simulation in lu/lt.

Finally, D_3 is varied while the other two diameters are fixed. A larger D_3 shows a broader range of flow rates where stable parallel flow is observed (Table 4.5). However, this also comes with a greater loss of fluid, similar to the trends observed for D_1 and D_2.

Tables 4.3,4.4 and 4.5 show the loss of toluene only at ϕ=1. Now, the ϕ is varied while $D_1 = 70\mu$m, $D_2 = 140\mu$m and $D_3 = 100\mu$m are kept constant. The Capillary number of toluene is fixed at 10^{-3} while the flow rate of water is varied. These results are plotted in Figure 4.10, where it can be seen that a larger ϕ reduces the amount of organic fluid lost to the third outlet, with the percentage lost

Table 4.5: Range of ϕ showing stable parallel flow and loss of fluid when D_3 is varied

D_1 (μm)	D_2 (μm)	D_3 (μm)	Range of ϕ	% Loss when ϕ=1 (%)
70	140	60	0.7-1.05	6.74
70	140	80	0.6-1.45	25.23
70	140	100	0.45-2.1	37.75
70	140	120	0.4-2.2	54.45

being as low as 2 % when ϕ= 2.1. At larger ϕ, water occupies the bulk of the third outlet as the water velocity is much larger (Figures 4.11a and 4.11b), thereby reducing the amount of toluene lost to the third outlet. Toluene only occupies the third outlet in the form of droplets at such ϕ, and the frequency of droplets reduces with an increase in ϕ.

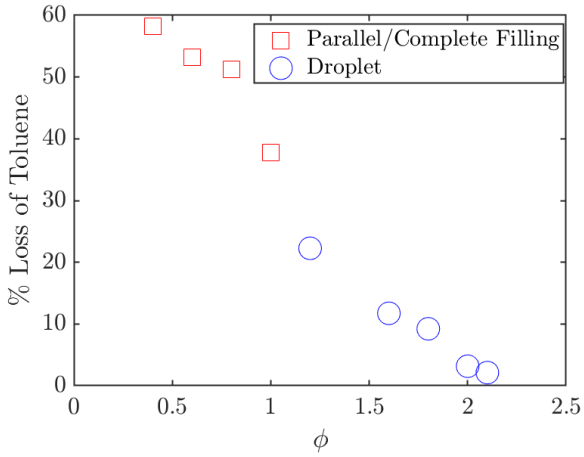

Figure 4.10: % loss of toluene as a function of ϕ. The Capillary number of toluene is fixed and is 10^{-3} as the velocity of water is varied. The red squares correspond to parallel flow or complete filling of toluene in the third outlet and the blue circles point to toluene as droplets in the third outlet.

Finally, this modified design is compared to the standard triple outlet design proposed by Lu *et al* [5]. Here, the third outlet has the same width as the rest of the outlets. The simulated result for this design at ϕ=1 is shown in Figure 4.12a. The velocity of toluene in the third outlet is even larger than the velocity in the lower outlet (Figure 4.12b), thus leading to a greater loss of fluid (60.39 %) compared to any of our designs, even the ones with high D_1, D_2 and D_3. The range of ϕ for which no leakage is observed, however, is quite broad (0.45-2.1). Thus, adding the circular head reduces loss but does not increase the range of ϕ.

To summarize, adding a third outlet clearly minimizes leakage, though it comes at the cost of losing some fluid to the third outlet. A circular head is added to the

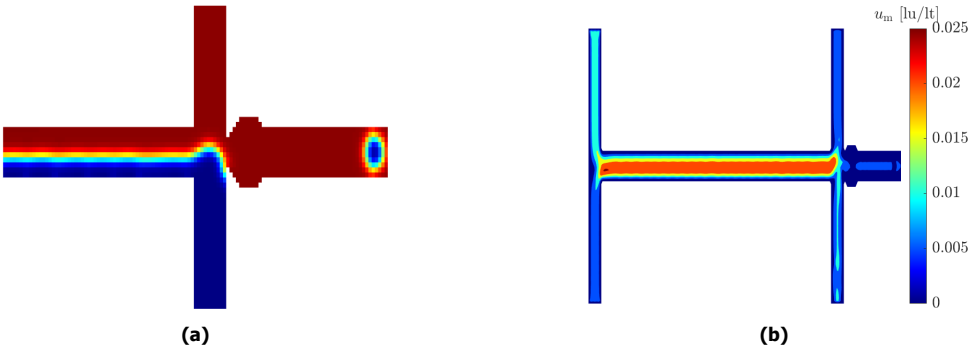

Figure 4.11: a) Simulations of a T-T channel with $D_1 = 70\mu$m, $D_2 = 140\mu$m and $D_3 = 100\mu$m. The Capillary number of toluene is 10^{-3} and ϕ=1. The blue fluid is toluene and the red fluid is water. b)Velocity magnitude contour for the same simulation in lu/lt.

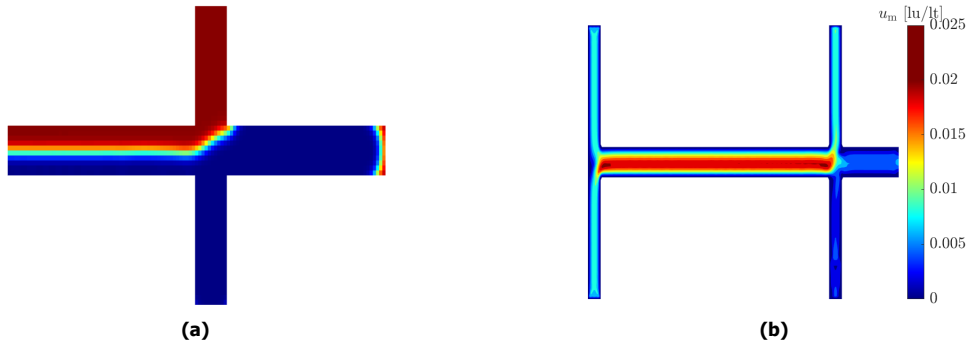

Figure 4.12: a) Simulations of a T-T channel with a third outlet similar to the design shown in Figure 4.2a [5]. The Capillary number of toluene is 10^{-3} and ϕ=1. The blue fluid is toluene and the red fluid is water. b)Velocity magnitude contour for the same simulation in lu/lt.

third outlet to minimize that loss. Smaller diameters result in lower loss and range of ϕ for which no leakage is observed, while larger diameters broaden the range of ϕ while increasing the amount of toluene lost to the third outlet. The choice of diameters naturally depends on the application, though a choice of $D_1 = 70\mu$m, $D_2 = 140\mu$m and $D_3 = 100\mu$m is a very good option as it allows for a broad range of ϕ and loss can be minimized by operating at a large ϕ.

4.3.2. Circular Head Design

Similar to the previous section, the Capillary number of toluene is fixed at 10^{-3} and the leakage regimes are observed. Figure 4.13a shows the flow and leakage regime when ϕ =1. Leakage is observed for this ϕ and it appears that organic fluid has not entered into the circular head. To understand the fluid behaviour at the outlet better, the velocity magnitude is plotted in Figure 4.13b. This figure clearly shows that

the velocity inside the circular head is negligible compared to the rest of the channel.

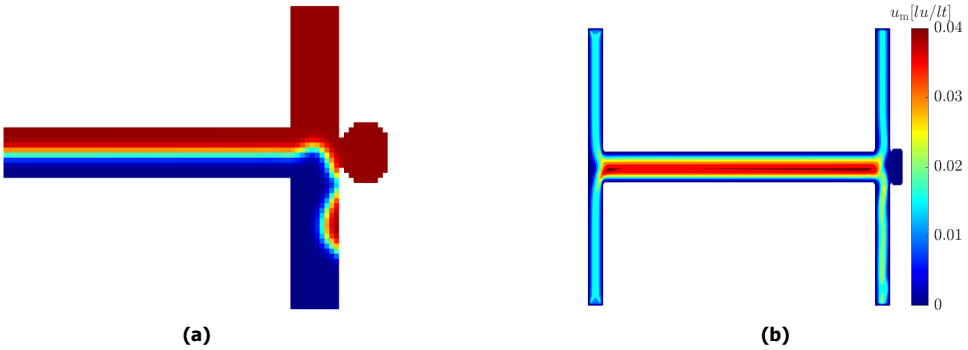

Figure 4.13: a)Leakage in a T-T channel with a circular head at the outlet. The Capillary number of toluene is 2×10^{-3} and ϕ =1. The blue fluid is toluene and the red fluid is water. b) Velocity magnitude for the same simulation with the units in lattice unit/lattice time (lu/lt).

As the circular reservoir is fully closed and doesn't have an outlet, the fluid velocities are significantly reduced. This design is similar to that shown in Figure 4.2b except that $D_3 = 0$. Table 4.5 shows that the range of ϕ considerably decreases with a decrease in D_3. So at $D_3 = 0$, toluene doesn't even enter the circular head, and this is the case even if the diameter of the circular head is changed.

4.3.3. Displaced Outlets with Circular Reservoir

The problem associated with the previous design is circumvented by connecting a circular reservoir to the two outlets, thereby ensuring that the two liquids will enter and accumulate in the circular reservoir (Figure 4.14a). The enlarged area of the reservoir ensures that the fluids slow down while in the reservoir (Figure 4.14b).

However, toluene gradually accumulates inside the reservoir until it finally acquires enough momentum to eventually leak into the other outlet as shown in Figure 4.14c. This is especially the case when toluene has a larger or comparable velocity to water (ϕ<1). Figure 4.14c shows significant velocities at the centre of the reservoir, and this eventually results in toluene leaking to the upper outlet. Thus, for a large range of ϕ, the leakage is controlled but never fully stopped.

Though the above paragraph describes the dominant trend, stable parallel flow is observed for a small range of ϕ (1.2-1.3). When the water velocity is larger than that of toluene, toluene doesn't have the required inertial forces to push the water upwards. However, at ϕ>1.3, water leaks to the lower outlet. This will be discussed in greater detail in Section 4.3.5.

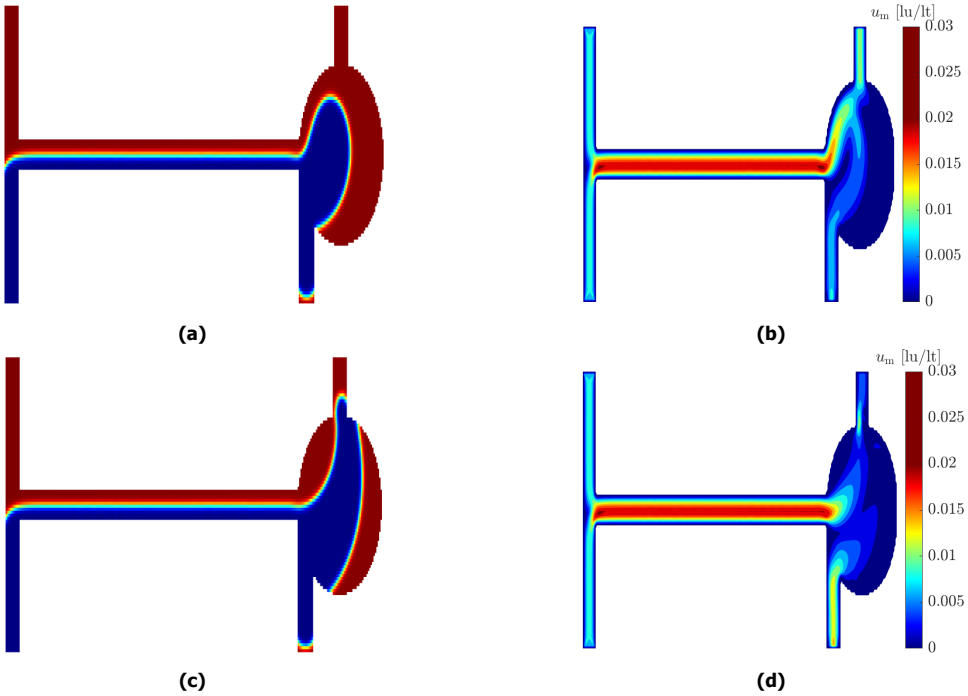

Figure 4.14: a)Gradual accumulation of toluene in the circular reservoir at t= 6.5 ms. The Capillary number of toluene is 10^{-3} and ϕ =1. The blue fluid is toluene and the red fluid is water. b) Velocity magnitude in lu/lt for the same simulation at t=6 ms. c) Leakage observed at t=17.1 ms. d) Velocity magnitude at t=17.1 ms

4.3.4. Circular Reservoir with Two Pillars

We first focus on the design shown in Figure 4.5a. Here, a circular pillar with a diameter of around 60 μm is located at the entrance of the reservoir and a rectangular pillar is located near the upper outlet. Figures 4.16a and 4.16b show the functioning of these two pillars. The velocity contour shows a significant drop in velocity in the circular reservoir, the velocity being larger than the one seen in Figure 4.14b. The circular pillar forces the two fluids to go around it which reduces the flow velocity, after which the rectangular pillar works to further hinder toluene from reaching the upper outlet.

However, like the results generally observed with phaseguides, toluene eventually leaks into the upper outlet when ϕ<1 as shown in Figures 4.15a and 4.15b, though this process takes a lot longer than that observed for the circular reservoir without pillars. For ϕ >1, the toluene doesn't flow upwards, though water gradually leaks to the bottom outlet at higher ϕ. Stable parallel flow is observed for ϕ=0.9-1.2 (Figure 4.16a), and the larger range points to a larger burst pressure applied on the fluids by the pillars.

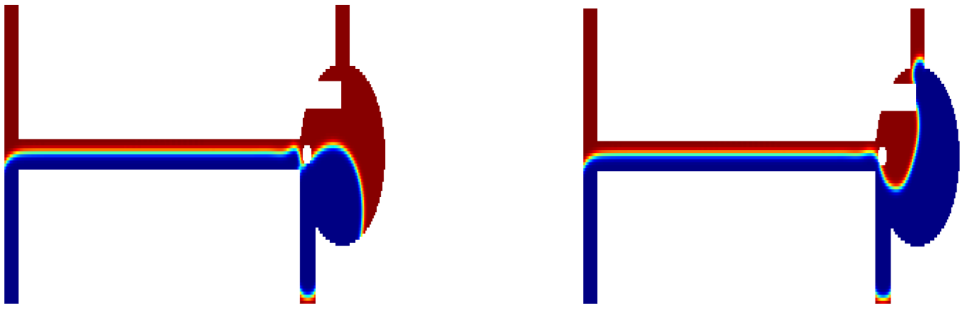

(a) (b)

Figure 4.15: Stages of accumulation leakage in a circular reservoir with two pillars at a)t= 7 ms and b)t =20 ms. The blue fluid is toluene and the red fluid is water, with the Capillary number of toluene being 10^{-3} and $\phi = 0.6$.

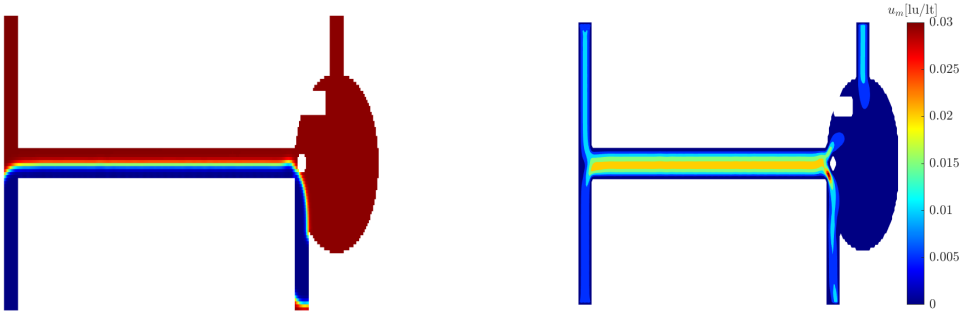

(a) (b)

Figure 4.16: a)Stable parallel flow in the T-T channel at ϕ=1.2 when the circular reservoir contains two pillars. The blue fluid is toluene and the red fluid is water, with the Capillary number of toluene being 10^{-3}. b) Velocity magnitude for the same simulation with the units in lattice unit/lattice time (lu/lt).

4.3.5. Circular reservoir with Concentric Pillar

The inclusion of pillars clearly improves the effectiveness of the circular reservoir by significantly reducing the fluid velocity and hindering fluid flow. However, the range of ϕ for which no leakage is observed is small, and when ϕ<1, toluene is still able to flow upwards along the circular reservoir. To effectively hinder this motion at ϕ<1, a circular pillar concentric to the reservoir is used as shown in Figure 4.5b. The idea behind this design is that toluene will have a larger distance to cover before it reaches the upper outlet.

Figures 4.17a and 4.17b demonstrate the utility of the concentric pillar in pinning the water-toluene interface. The flow velocity is large near the entrance of the outlet, and it is close to negligible on the other side of the concentric pillar. Toluene does not have sufficient velocity to overcome the burst pressure imposed by the pillar, and this pins the fluid.

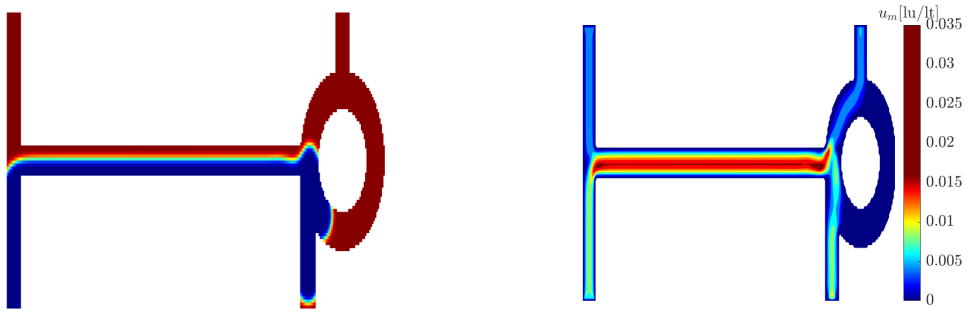

Figure 4.17: a)Stable parallel flow in the circular reservoir (600 μm diameter) with a concentric pillar (300 μm diameter). The Capillary number of toluene is 10^{-3} and ϕ =0.6. The blue fluid is toluene and the red fluid is water. b) Velocity magnitude for the same simulation with the units in lattice unit/lattice time (lu/lt).

Influence of the Pillar Diameter

The diameter (I.D) of the concentric pillar and the diameter (O.D) of the reservoir influence leakage and flow stability as variations in the geometry alter the burst pressure [2]. First, the O.D is fixed at 600 μm as the I.D is varied. The case without any concentric pillar discussed in the previous section is also considered here, as the I.D can be taken to be 0 in this particular case. As usual, the range of ϕ for which stable parallel flow is studied and the results are tabulated in Table 4.6 along with the burst pressure calculated using Equation 4.2.

Table 4.6: Range of ϕ for which stable parallel flow is observed as the I.D of the concentric pillar is varied. The O.D is fixed at 600 μm and the Capillary number of toluene is 10^{-3}.

I.D (μm)	Range of ϕ	P_{burst} (Pa)
0	1.2-1.3	-
100	1-1.3	198.43
200	0.55-1.2	248.04
300	0.45-1.1	310.71
400	0.4-0.95	496.08
500	-	992.16

A clear trend can be discerned from Table 4.6. In the case of smaller I.Ds, no leakage is observed for higher ϕ and, lower ϕ for larger I.Ds. The range of ϕ increases until an I.D of 200 μm, after which it is more or less constant until an I.D of 500 μm. As discussed earlier in Section 4.2.3, the burst pressure is larger for large I.Ds. This means that toluene has to overcome a larger pressure if it has to leak into the upper outlet, and this explains why no leakage is observed even for low ϕ at larger I.Ds. However, this does not explain why no leakage is observed

at smaller I.Ds for high ϕ. To understand the reasons for this trend, a qualitative pressure balance analysis is performed at the circular pillar.

Since the pillar has a circular geometry, the velocity keeps varying inside the reservoir, and thus the pressure also keeps varying. It is, thus, very difficult to apply an accurate pressure balance at every point to predict the range of ϕ analytically. Instead, we qualitatively apply a pressure balance at the outlet to understand which parameters have an influence on leakage.

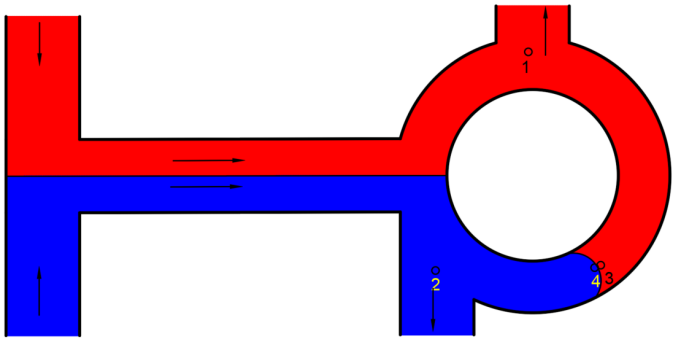

Figure 4.18: Illustration of pinning in a T-T channel with a circular reservoir and concentric pillar at the outlet, along with the 6 points used for a pressure analysis. The blue fluid is the organic phase and the red fluid is the aqueous phase.

Consider the illustration shown in Figure 4.18 of pinning in such a channel. Here, the organic fluid is pinned in the reservoir. To obtain an understanding of the forces involved, we use a combination of the Bernoulli theorem and Young-Laplace equation at points 1,2,3 and 4. Points 1 and 2 are located at the upper and lower outlets, while points 3 and 4 are located inside the reservoir on either side of the interface. Applying the Bernoulli principle at points 1 and 3 in the aqueous phase, we get:

$$p_1 + \frac{1}{2}\rho u_1^2 = p_3 \tag{4.5}$$

where p is the pressure, ρ is the density and u is the velocity, with the subscripts corresponding to the points shown in Figure 4.18. The velocity at points 3 and 4 is taken to be 0 as the interface does not travel further in the reservoir. Similarly, for the organic phase at points 2 and 4, we get:

$$p_2 + \frac{1}{2}\rho u_2^2 = p_4 \tag{4.6}$$

The density of the aqueous and organic phases are assumed to be equal for simplification. From Table 5.1, we can also see that the densities of water and toluene are similar. Points 3 and 4 are very close to the fluid interface. Thus,

according to the Young-Laplace equation, we get [16]:

$$p_4 - p_3 = \frac{4\sigma\cos\theta}{\delta} \tag{4.7}$$

where δ is (O.D-I.D). The Laplace pressure in this case is nothing but the burst pressure. Combining Equations 4.5,4.6 and applying in it Equation 4.7, we get:

$$p_2 - p_1 = \frac{1}{2}\rho(u_1^2 - u_2^2) + \frac{4\sigma\cos\theta}{\delta} \tag{4.8}$$

The Laplace pressure in the rectangular channel is given by :

$$p_{\text{Lap,rect}} = \frac{2\sigma\cos\theta}{d} \tag{4.9}$$

where d is the depth of the channel. Since our simulations are in 2D, there is no depth in our channel. The curvature across the width of the channel is zero. Therefore, in our 2D case, the pressure of the individual fluids are equal across the entire channel except inside the reservoir. Therefore, $p_1 = p_2$. Equation 4.8, thus, further simplifies to:

$$\frac{1}{2}\rho(u_2^2 - u_1^2) = \frac{4\sigma\cos\theta}{\delta} \tag{4.10}$$

The velocities at the outlet can be considered equal to the inlet velocities if no leakage takes place. Therefore, they can be related to ϕ in the same manner.

$$\phi = \frac{u_{\text{aq}}}{u_{\text{org}}} = \frac{u_1}{u_2} \tag{4.11}$$

where the subscripts aq and org correspond to the velocities at the aqueous and organic inlets respectively. Rearranging Equation 4.10 in terms of ϕ, we get:

$$\rho u_1^2\left(\frac{1}{\phi^2} - 1\right) = \frac{4\sigma\cos\theta}{\delta} \tag{4.12}$$

Rewriting the above equation in terms of the aqueous Weber number inside the reservoir - $We_1 = \frac{\rho u_1^2 \delta}{\sigma}$ - we get:

$$\phi^2 = \frac{1}{1 + \frac{4\cos\theta}{We_1^2}} \tag{4.13}$$

If we include the laplace pressure in our analysis for the 3D case, the above relation is modified to the following form:

$$\phi^2 = \frac{1}{1 - \frac{4\cos\theta\left(2\frac{d}{\delta} - 1\right)}{We_d}} \tag{4.14}$$

where $We_d = \frac{\rho u_1^2 d}{\sigma}$ is the Weber number of the aqueous phase across the depth of the channel.

Clearly, both expressions are a major approximation of the actual pressure balances. From Equation 4.10, we can see that Equations 4.13 and 4.14 are valid only when $u_2 > u_1$, otherwise we obtain an imaginary ϕ. However, Table 4.6 shows stable parallel flow in pillars with smaller IDs for $\phi > 1$. Using the Bernoulli equation, as we have done in our analysis, completely neglects the viscous pressure drop, which can be significant at the entrance of the reservoir where the interface is curved as shown in Figure 4.17a. Including the viscous pressure to drop to Equation 4.10 allows for ϕ to be greater than 1. This pressure balance thus takes the following form [17]:

$$p_2 - p_1 = \frac{1}{2}\rho(u_1^2 - u_2^2) + \frac{4\sigma\cos\theta}{\delta} + \frac{2f\rho(u_1^2 - u_2^2)L}{\delta} \tag{4.15}$$

where f is the friction factor, which is unknown for the reservoir, L is the length of the reservoir (O.D). Even if the friction factor is known, the above expression is still not entirely accurately because the burst pressure inside the reservoir is not constant as the interface normals keep changing across the reservoir. Equation 4.13, however, is formulated to qualitatively understand the influence of the I.D on leakage and despite all the approximations, this equation can explain some of the results observed in Table 4.6. Φ and δ are inversely related in this expression, which means that for a larger I.D, i.e., smaller δ, a smaller ϕ is sufficient to balance the pressures. Conversely, for a smaller I.D, a larger ϕ is required to balance the pressures. Even though the range of ϕ can't be predicted, Equation 4.13 provides the trend between I.D and leakage.

In addition to Equation 4.13, the flow regimes and velocity contours are looked into for I.Ds of 200 and 400 μm . The idea is to observe the influence of the I.D at higher and lower ϕ and explain the results from Table 4.6 better by visualizing the flow phenomena. We first consider the contour plots at ϕ=1. Figures 4.19a and 4.19b show the regime and velocity contour for a concentric pillar with I.D= 200 μm. Similar to Figure 4.17b, the velocity contour shows that the larger velocities are concentrated in the region between the entrance of the outlet and the concentric pillar, while the velocities on the other side of the pillar are much smaller.

On the other hand, the velocity contour for a concentric pillar with a larger I.D of 400 μm at ϕ=1 shows significant velocities on the right side of the concentric pillar as well (Figure 4.20b). Consequently, leakage is observed in the toluene outlet as shown in Figure 4.20a. These results observed in Figures 4.19a and 4.20a cannot be explained by the burst pressure alone, which is why the qualitative expression in Equation 4.14 helps in making sense of these results. At this I.D, the pressures are not balanced which is why larger velocities are observed inside the reservoir.

Now we consider the case of a lower ϕ of 0.45. Figures 4.21a and 4.21b show

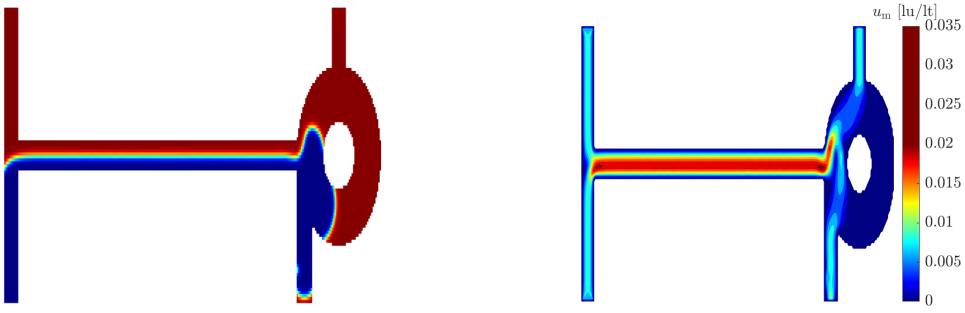

Figure 4.19: a)Stable parallel flow in the circular reservoir (600 μm diameter) with a concentric pillar (200 μm diameter). The Capillary number of toluene is 10^{-3} and ϕ =1. The blue fluid is toluene and the red fluid is water. b) Velocity magnitude for the same simulation with the units in lattice unit/lattice time (lu/lt).

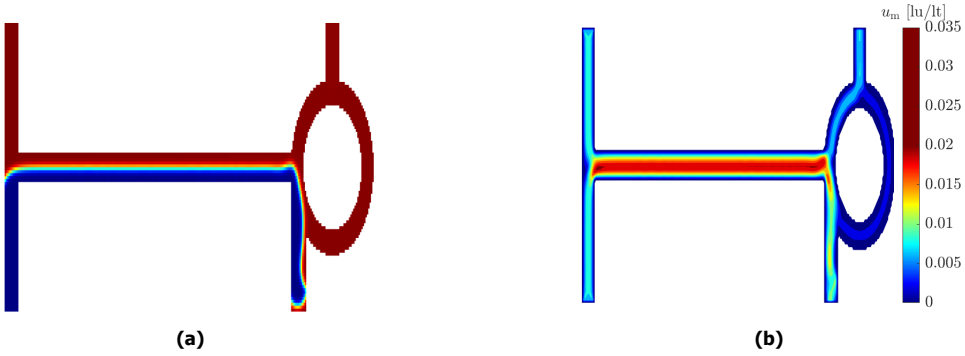

Figure 4.20: a)Leakage in the circular reservoir design (600 μm diameter) with a concentric pillar of 400 μm diameter. The Capillary number of toluene is 10^{-3} and ϕ =1. The blue fluid is toluene and the red fluid is water. b) Velocity magnitude for the same simulation with the units in lattice unit/lattice time (lu/lt).

the flow regime and profile for an I.D of 200μm. Leakage is observed here as toluene has circumnavigated the entire I.D of the pillar. The velocity contour shows that the velocity at the bottom outlet is considerably larger than the rest at the outlet and reservoir. The velocity at the upper outlet, though still larger than the velocities inside the reservoir, is much lower than the water velocity at the water inlet. Clearly, the lower burst pressure results in the leakage of toluene.

In contrast, the velocity near the upper outlet of the concentric pillar is much larger when the ID is 400 μm (Figure 4.22b). Stable parallel flow is consequently observed at this ϕ as shown in Figure 4.22a as the burst pressure associated with the pillar is too high.

Finally, we look at the contour plots for an I.D of 500 μm where stable parallel

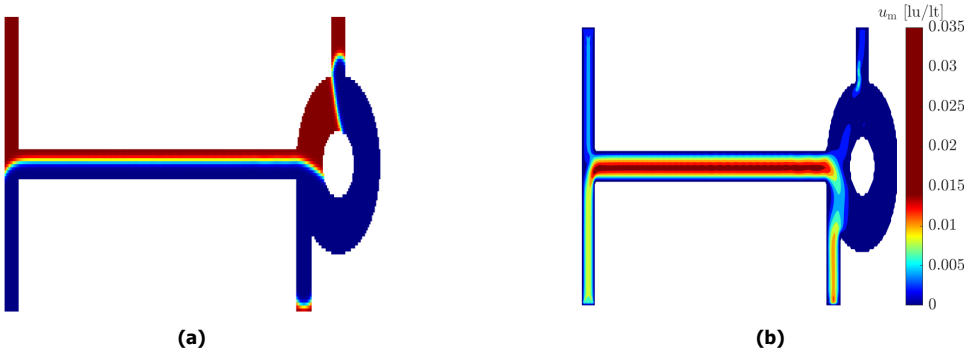

Figure 4.21: a)Leakage in the circular reservoir design (600 μm diameter) with a concentric pillar of 200 μm diameter. The Capillary number of toluene is 10^{-3} and ϕ =0.45. The blue fluid is toluene and the red fluid is water. b) Velocity magnitude for the same simulation with the units in lattice unit/lattice time (lu/lt).

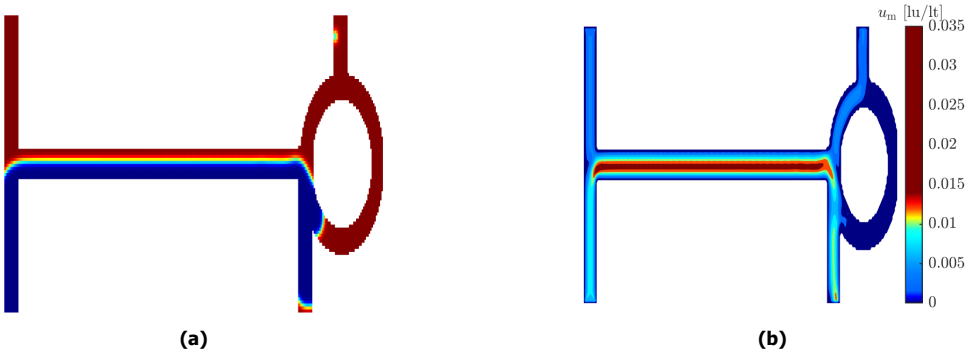

Figure 4.22: a)Stable parallel flow in the circular reservoir design (600 μm diameter) with a concentric pillar of 400 μm diameter. The Capillary number of toluene is 10^{-3} and ϕ =0.45. The blue fluid is toluene and the red fluid is water. b) Velocity magnitude for the same simulation with the units in lattice unit/lattice time (lu/lt).

flow is not observed. At an I.D of 500 μm, P_{burst} is the largest, but the area occupied by toluene is very small as (O.D-I.D) is small. Figure 4.23a shows toluene breaking into droplets once it reaches the outlet because of the small area. The velocity is at its largest at the entrance of the outlet (Figure 4.23b), where the toluene is sheared to form droplets because of the large burst pressure. This is observed for all ϕ.

4.3.6. Influence of Dimensionless numbers

The influence of the dimensionless numbers - Capillary, Weber and Reynolds - is studied in this section. From Equation 4.13, it appears that the Weber number is the most important dimensionless number that describes the leakage at the outlets, with the ϕ expected to decrease with an increase in Weber number. To test if

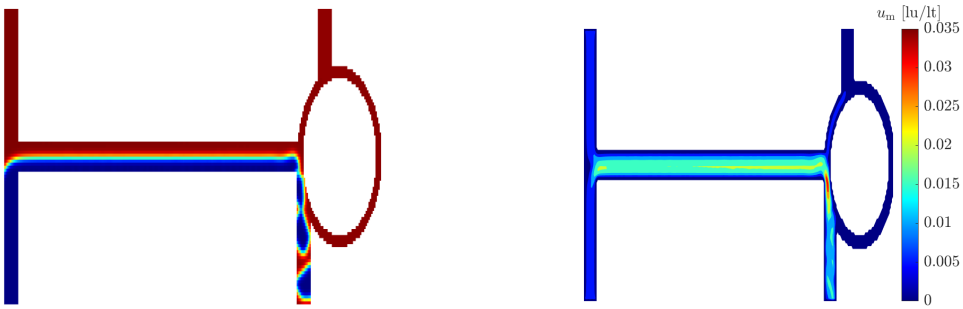

Figure 4.23: a)Droplets were observed in the toluene outlet in the circular reservoir design (600 μm diameter) with a concentric pillar of 500 μm diameter. The Capillary number of toluene is 10^{-3} and ϕ =1. The blue fluid is toluene and the red fluid is water. b) Velocity magnitude for the same simulation with the units in lattice unit/lattice time (lu/lt).

this is indeed the case, we vary the flow parameters individually and observe their influence on leakage.

First, the fluid inlet velocity is varied. From Equation 1.4, we can see that changing the velocity influences all the dimensionless numbers. All the previous simulations were conducted at a Toluene Capillary number of 10^{-3}. Now, the range of ϕ is studied for different toluene velocities in Table 4.7.

Table 4.7: Range of ϕ for which stable parallel flow is observed as the velocity of toluene is varied. The O.D is fixed at 600 μm and the I.D is 300 μm.

Toluene Velocity(m/s)	Ca_{org}	We_{org}	Re_{org}	Range of ϕ
0.062	10^{-3}	9.2×10^{-3}	9.2	0.45-1.1
0.093	1.5×10^{-3}	2.07×10^{-2}	13.8	0.55-0.9
0.124	2×10^{-3}	3.68×10^{-2}	18.4	0.65-0.75

Leakage is observed for a smaller range of ϕ at larger velocities. Larger velocities imply that We_1 is larger and the dynamic pressure is larger (Equations 4.14 and 4.8), and this reduces the average ϕ for which stable parallel flow is observed. Consequently, the range of ϕ for which stable parallel flow is observed is also limited, as can be seen in Table 4.7.

To visualize the influence of velocity better, we plot contour plots for two different toluene velocities at $\phi = 0.45$ and $\phi = 1$. Figure 4.24a shows the leakage of toluene to the water outlet at $\phi = 0.45$ and a toluene velocity of 0.124 m/s. The velocities of the fluids are large enough to break the toluene-water interface near the concentric pillar (Figure 4.24b), ultimately resulting in the leakage of the broken toluene fragment. At ϕ=1, the water velocity is large enough to leak into the lower

outlet from the corner as shown in Figures 4.25a and 4.25b. Even though the velocity on the right side of the concentric pillar is small for both ϕ compared to the outlet velocities, the larger overall fluid velocities result in leakage.

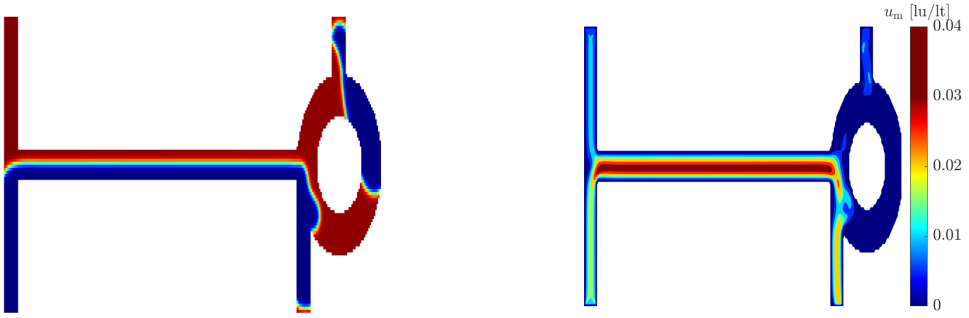

Figure 4.24: a)Leakage to the upper outlet in the circular reservoir design (600 μm diameter) with a concentric pillar of 300 μm diameter. The Capillary number of toluene is 2×10^{-3} and ϕ =0.45, with a toluene velocity of 0.124 m/s. The blue fluid is toluene and the red fluid is water. b) Velocity magnitude for the same simulation with the units in lattice unit/lattice time (lu/lt).

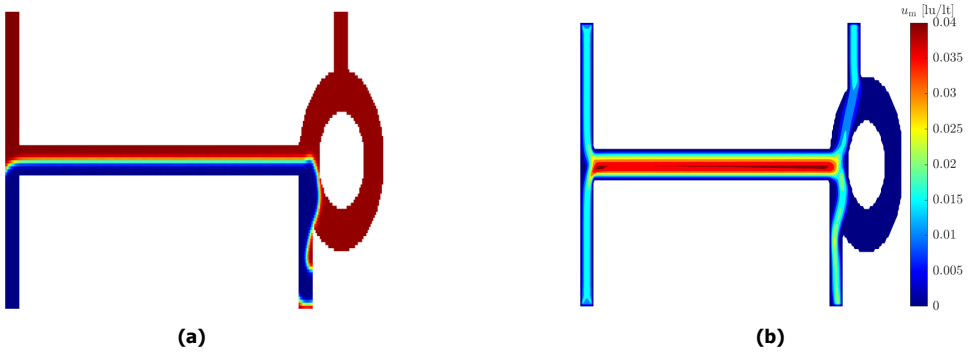

Figure 4.25: a)Leakage to the lower outlet in the circular reservoir design (600 μm diameter) with a concentric pillar of 300 μm diameter. The Capillary number of toluene is 2×10^{-3} and ϕ =1, with a toluene velocity of 0.124 m/s. The blue fluid is toluene and the red fluid is water. b) Velocity magnitude for the same simulation with the units in lattice unit/lattice time (lu/lt).

Now the viscosity of both fluids is varied such that the viscosity ratio is the same as that described in Table 5.1. The velocity of toluene is once again fixed at 0.062 m/s, as ϕ is varied by changing the water velocity. Changing the viscosity changes both the Reynolds and Capillary numbers, but not the Weber number, so the impact on ϕ should be minimal (Equation 4.13). The range of ϕ where no leakage is observed for different fluid viscosities is tabulated in Table 4.8.

Table 4.8 shows that viscosity has little impact on leakage, which points to the

Table 4.8: Range of ϕ for which stable parallel flow is observed as the viscosities of toluene and water are varied. The viscosity ratio is the same as that in Table 5.1. The O.D is fixed at 600 μm and the I.D is 300 μm.

Toluene Viscosity (mPas)	Ca_{org}	We_{org}	Re_{org}	Range of ϕ
0.583	10^{-3}	9.2×10^{-3}	9.2	0.45-1.1
0.875	1.5×10^{-3}	9.2×10^{-3}	6.13	0.5-1.2
1.17	2×10^{-3}	9.2×10^{-2}	4.6	0.5-1.2

importance of the Weber number. To further check if this is indeed the case, we vary the density and tabulate the range of ϕ for which no leakage is obtained in Table 4.9.

Table 4.9: Range of ϕ for which stable parallel flow is observed as the densities of toluene and water are varied. The density ratio is the same as that in Table 5.1. The O.D is fixed at 600 μm and the I.D is 300 μm.

Toluene Density (kg/m^3)	Ca_{org}	We_{org}	Re_{org}	Range of ϕ
867	10^{-3}	9.2×10^{-3}	9.2	0.45-1.1
1300.5	10^{-3}	1.38×10^{-2}	13.8	0.5-0.95
1734	10^{-3}	1.84×10^{-2}	18.4	0.6-0.85

Changing the density changes the Reynolds and Weber number, but not the Capillary number. Consequently, a change in the range of ϕ is seen. The results from Tables 4.7, 4.8 and 4.9 show the importance of the Weber number in such a design. Generally, an increase in Weber number leads to more leakage. By changing the Weber number, we can accordingly control the leakage according to our desired application.

In the case of the RK model, the pressure is coupled with the density [18, 19], so a pressure plot is not very useful to understand the flow phenomena. Therefore, to understand the pressure balances better, it will be useful to study this setup experimentally to develop pressure plots.

4.4. Conclusion

The influence of outlet geometry on leakage is studied in this chapter. Four different designs are proposed, each involving the modification of the outlet geometry in a T-T channel. The principle behind each of the designs is to either include an additional outlet as proposed by Lu *et al* [5] or to incorporate a phaseguide (Vulto *et al* [1]) at the outlet.

The triple outlet design successfully ensures pure fluid at the upper and lower outlets, but there is a loss of fluid to the third outlet. To minimize the loss, the triple outlet design is slightly modified by including a circular head at the start of the outlet. The influence of these diameters on leakage and loss was subsequently studied and validated experimentally. Generally, smaller diameters are preferred for reducing the loss of toluene, and larger diameters for a broader range of ϕ at which stable parallel flow is observed. Alternatively, the loss can also be minimized by operating at a large ϕ.

When it comes to the reservoir designs, the displaced outlet design with a concentric pillar proved to be the most successful in stemming leakage. However, the effectiveness of the design is governed by several factors, such as the diameter of the pillar and the Weber number of the fluids. Stable parallel flow is generally observed for lower ϕ at higher I.D and higher ϕ at lower I.D. At higher Weber numbers, the effectiveness of the design is much reduced, as the fluids have enough momentum to overcome the burst pressure of the pillar and leak into the upper or lower outlets.

Bibliography

[1] Paul Vulto, Susann Podszun, Philipp Meyer, Carsten Hermann, Andreas Manz, and Gerald A. Urban. Phaseguides: a paradigm shift in microfluidic priming and emptying. *Lab on a Chip*, 11(9):1596, 2011. ISSN 1473-0197, 1473-0189. doi: 10.1039/c0lc00643b. URL http://xlink.rsc.org/?DOI=c0lc00643b.

[2] Francesca Garbarino, Kasper Kistrup, Giovanni Rizzi, and Mikkel Fougt Hansen. Burst pressure of phaseguide structures of different heights in all-polymer microfluidic channels. *Journal of Micromechanics and Microengineering*, 27 (12):125015, December 2017. ISSN 0960-1317, 1361-6439. doi: 10.1088/1361-6439/aa97b7. URL https://iopscience.iop.org/article/10.1088/1361-6439/aa97b7.

[3] Sachit Goyal, Amit V. Desai, Robert W. Lewis, David R. Ranganathan, Hairong Li, Dexing Zeng, David E. Reichert, and Paul J.A. Kenis. Thiolene and SIFEL-based microfluidic platforms for liquid-liquid extraction. *Sensors and Actuators, B: Chemical*, 190:634–644, 2014. ISSN 09254005. doi: 10.1016/j.snb.2013.09.065.

[4] Madhvanand N. Kashid and David W. Agar. Hydrodynamics of liquid–liquid slug flow capillary microreactor: Flow regimes, slug size and pressure drop. *Chemical Engineering Journal*, 131(1-3):1–13, July 2007. ISSN 13858947. doi: 10.1016/j.cej.2006.11.020. URL https://linkinghub.elsevier.com/retrieve/pii/S1385894706005092.

[5] Yangcheng Lu, Yang Xia, and Guangsheng Luo. Phase separation of parallel laminar flow for aqueous two phase systems in branched microchannel. *Microfluidics and Nanofluidics*, 10(5):1079–1086, May 2011. ISSN 1613-4982, 1613-4990. doi: 10.1007/s10404-010-0736-7. URL http://link.springer.com/10.1007/s10404-010-0736-7.

[6] Giancarlo Pascali, Paul Watts, and Piero A Salvadori. Microfluidics in radiopharmaceutical chemistry. *Nuclear medicine and biology*, 40(6):776–787, 2013.

[7] J. H. Lu, H. Y. Lei, and C. S. Dai. Lattice Boltzmann equation for mass transfer in multi solvent systems. *International Journal of Heat and Mass Transfer*, 132(April):519–528, 2019. ISSN 00179310. doi: 10.1016/j.ijheatmasstransfer.2018.12.010.

[8] Zida Li, Sze Yi Mak, Alban Sauret, and Ho Cheung Shum. Syringe-pump-induced fluctuation in all-aqueous microfluidic system implications for flow rate accuracy. *Lab on a Chip*, 14(4):744–749, 2014.

[9] Martina Baeckert, Martin Batliner, Beate Grass, Philipp K Buehler, Marianne Schmid Daners, Mirko Meboldt, and Markus Weiss. Performance of modern syringe infusion pump assemblies at low infusion rates in the perioperative setting. *British journal of anaesthesia*, 124(2):173–182, 2020.

[10] Arata Aota, Kazuma Mawatari, Susumu Takahashi, Teruki Matsumoto, Kazuteru Kanda, Ryo Anraku, Akihide Hibara, Manabu Tokeshi, and Takehiko Kitamori. Phase separation of gas–liquid and liquid–liquid microflows in microchips. *Microchimica Acta*, 164(3-4):249–255, March 2009. ISSN 0026-3672, 1436-5073. doi: 10.1007/s00604-008-0085-3. URL http://link.springer.com/10.1007/s00604-008-0085-3.

[11] Akihide Hibara, Mao Fukuyama, Myungwha Chung, Craig Priest, and Mikhail A. Proskurnin. Interfacial Phenomena and Fluid Control in Micro/Nanofluidics. *Analytical Sciences*, 32(1):11–21, January 2016. ISSN 0910-6340, 1348-2246. doi: 10.2116/analsci.32.11. URL https://link.springer.com/10.2116/analsci.32.11.

[12] Bastian E Rapp. *Microfluidics: modeling, mechanics and mathematics*. Elsevier, 2022.

[13] Amin Farahani, Ahmad Rahbar-Kelishami, and Hadi Shayesteh. Microfluidic solvent extraction of Cd(II) in parallel flow pattern: Optimization, ion exchange, and mass transfer study. *Separation and Purification Technology*, 258:118031, March 2021. ISSN 13835866. doi: 10.1016/j.seppur.2020.118031. URL https://linkinghub.elsevier.com/retrieve/pii/S1383586620325041.

[14] Gwendolyne Hellé, Clarisse Mariet, and Gérard Cote. Liquid–liquid microflow patterns and mass transfer of radionuclides in the systems Eu(III)/HNO3/DMDBTDMA and U(VI)/HCl/Aliquat® 336. *Microfluidics and Nanofluidics*, 17(6):1113–1128, December 2014. ISSN 1613-4982, 1613-4990. doi: 10.1007/s10404-014-1403-1. URL http://link.springer.com/10.1007/s10404-014-1403-1.

[15] Sachit Goyal, Amit V. Desai, Robert W. Lewis, David R. Ranganathan, Hairong Li, Dexing Zeng, David E. Reichert, and Paul J.A. Kenis. Thiolene and SIFEL-based microfluidic platforms for liquid–liquid extraction. *Sensors and Actuators B: Chemical*, 190:634–644, January 2014. ISSN 09254005. doi: 10.1016/j.snb.2013.09.065. URL https://linkinghub.elsevier.com/retrieve/pii/S0925400513011064.

[16] Christopher Earls Brennen and Christopher E Brennen. Fundamentals of multiphase flow. 2005.

[17] Arata Aota, Akihide Hibara, and Takehiko Kitamori. Pressure Balance at the Liquid−Liquid Interface of Micro Countercurrent Flows in Microchips. *Analytical Chemistry*, 79(10):3919–3924, May 2007. ISSN 0003-2700, 1520-

6882. doi: 10.1021/ac070031d. URL https://pubs.acs.org/doi/10.1021/ac070031d.

[18] Timm Kr ”u ger, Halim Kusumaatmaja, Alexandr Kuzmin, Orest Shardt, Goncalo Silva, and Erlend Magnus Viggen. The lattice boltzmann method. *Springer International Publishing*, 10(978-3):4–15, 2017.

[19] Haibo Huang. Multiphase Lattice Boltzmann Methods.

5

Influence of a 'Step' on the Liquid-Liquid Flow Patterns and Flow Phenomena in a Microfluidic Y-Y channel

In Chapter 4, we looked at the influence of the outlet on leakage and observed that leakage can be effectively minimized once the outlet geometry is accordingly modified. An alternative to this option is to modify the overall geometry of the channel, and a design that has been used in literature for LLE purposes is an asymmetric microchannel with different depths for the two fluids[1, 2, 3]. We call this design the 'step' design as the presence of a shallow and deep part resembles a step (Figure 5.1b). This channel has been found to be particularly effective in obtaining stable, parallel flow [4].

Flow patterns have been extensively studied in microchannels of various geometries such as Y-shaped channel [5, 6, 7, 8], T-shaped channel [7, 8, 9, 10] and cross-junction channel [11, 12, 13]. Generally, these studies observed the effect of the dimensionless numbers mentioned in Equation 1.4 on the flow regimes. Some papers, like those of Kashid *et al* [7] and Asadi-Sanghandi *et al* [14], tried developing generalized flow maps to describe flow regimes for all possible fluids and geometries.

However, all these studies have been conducted on channels of symmetric cross-section (standard design). Papers which have studied the influence of channel geometry have limited their research to channel dimensions and inlet geometry [7, 8]. To this author's knowledge, no studies have been conducted on this geometric modification's effect on the flow patterns, let alone flow maps. The influence

of dimensionless numbers on the various flow regimes has not been documented in flow maps. Considering the utility of the step channel in multiple LLE applications [1, 2, 3], it is imperative to understand the effect such a modification might have on the flow phenomena. Studying the flow patterns for such a step channel and comparing it to a channel with a symmetric cross section will, therefore, not only expand the application of such microfluidic channels in LLE, but also enhance our understanding of the influence of channel geometry on fluid flow. This is especially important when we consider the use of such channels in radioisotope extraction studies.

Therefore, this chapter focuses on understanding the nature of the flow phenomena in such a step design and, the influence of channel dimensions and geometry on two-phase flow. The flow patterns obtained from this design will be compared experimentally with the corresponding results obtained from the commonly used channel with a symmetric cross-section. Further, the effect of the channel dimensions and the extent of asymmetry on the flow phenomena in a Step channel will also be studied. Finally, to visualize the impact of this geometric modification on flow phenomena, Volume-of-Fluid (VOF) simulations will be performed on both Step and Standard Designs to compare the flow fields and pressure plots.

5.1. Methods and Materials

5.1.1. PDMS Microfluidic Chip Fabrication

The chips are fabricated similarly to the procedure described in Chapter 4. As it is important to modify the geometry of the chips, polydimethylsiloxane (PDMS) is used because the chips can be easily manufactured. PDMS is an organosilicon polymer that stays in liquid form upon mixing the elastomers with the curing agent. As a result, the mixture can be poured into a petri dish with a patterned mould master, where it takes the shape of the pattern printed on the mould master. The petri dish can be set in an oven to speed up the hardening process.

To fabricate microfluidic chips, we first fabricated the mould master using the soft lithography technique. On top of a cleaned 4 inch silicon wafer, we spin-coated a negative photoresist (SU8-2050, micro resist technology GmbH) at 2000 rpm for 30 s to obtain a layer of 50 µm thickness. The wafer was then baked at 100°C for 15 min and loaded onto LaserWriter (Heidelberg, 1 µm laser beam at 365 nm). In the LaserWriter, we converted a bottom pattern (Y-Y shape, width from 250 - 1000 µm, Figure 5.1a), designed using Autocad 2019 (Autodesk). The pattern was then written on the wafer. Afterwards, the wafer was soft-baked at 100°C for 5 min.

To deposit another layer, we spin-coated another negative photoresist. To obtain an additional 25 µm and 50 µm we used SU8-2025 and SU8-2050 accordingly, with similar spin-coating parameters. After the second spin-coating, the wafer was baked at 100°C for 15 min and reloaded onto the LaserWriter where a top pattern

(half-channel, refer to Figure 5.1b) was converted, aligned, and written. The wafer was soft-baked again at 100°C for 5 min. Thereafter, the wafer was developed using Propylene glycol methyl ether acetate (> 99.5%, Merck Sigma) for 10 min, and post-baked at 200°C for 30 min.

The PDMS microfluidic chips were fabricated by mixing the elastomer (Sylgard 184 Elastomer Kit, Dow Corning Comp.) and the curing agent with a mass ratio of 10:1. The mixture was then degassed, poured over the patterned master mould on a petri dish, and cured at 70°C for 10 h. The hardened PDMS chips were gently removed from the mould master and cut to size. The inlets and outlets were punched using a 1.5 mm biopsy puncher, before being cleaned using ethanol. On the other hand, a glass slide was spin-coated with 20 µm PDMS (2000 rpm for 2 min, Laurell WS-650-23B). Both the chips and the coated glass slides were bonded together using oxygen plasma treatment (Harrick PDC-002) at 0.2-0.4 mbar for 140 s. The preparation of the mould master and fabrication of the chips was done by Albert Santoso, while the chips were cut from the mould master by the author himself.

5.1.2. Fluid properties and Flow Setup

To conduct the flow experiments, we used two syringe pumps (Pump 11 Pico Plus Elite). On each of the syringe pumps, a 10 mL syringe (Beckton-Dickinson, Discardit II) was mounted. One of the syringes contained demineralized water with 10 mg/L brilliant blue dye while the other syringe contained an immiscible fluorinated oil (HydroFluoroEther, HFE, 3M™ Novec™ 7500 Engineered Fluid). The syringes were connected with PEEK tubes (0.5 mm ID, 1.59 mm OD, 300 mm in length) to the inlets of the microfluidic chips. The outlets were connected to other PEEK tubes, leading to a disposal container.

The fluid properties are given in Table 5.1. The contact angle corresponds to the angle made by the Novec-Water interface on the PDMS chip, and in our case, PDMS was observed to be hydrophobic.

Table 5.1: Fluid Properties

Fluid	**Density** (kg/m^3)	**Viscosity** (mPas)	**Surface Tension** (mN/m)	**Contact Angle** (°)
Water	997	1.01	43.8	-
HFE/Novec™ 7500	1614	1.24	-	39.7

5.1.3. Channel Geometry and Dimensions

Each of the channels in the experiments has a Y-Y geometry as shown in Figure 5.1a. In the case of the standard design, the depth remains uniform throughout,

whereas, in the step design, half of the channel has one depth and the other half has another depth as shown in Figure 5.1b.

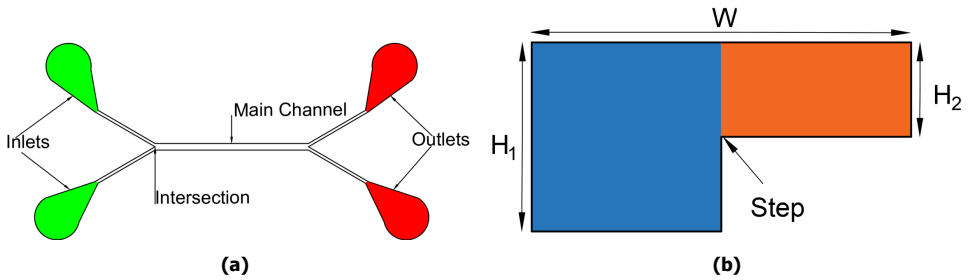

Figure 5.1: Channel geometry. a) Y-Y, with two inlets and outlets b)Step design with two depths for each half of the channel

Five different channels are used here - one standard and four step channels. Two geometrical dimensions are varied in the case of the step channel - the width (W) and the step ratio $\lambda = \frac{H_1}{H_2}$. The dimensions of the channels are described in Table 5.2.

Table 5.2: Channel dimensions used throughout this work. The height of the shallower section is fixed at 50 μm as the height of the deeper section is varied.

Number	**Length** (cm)	W (μm)	H_1 (μm)	λ
1 (Standard)	1.2	500	50	1
2	1.2	500	100	2
3	1.2	250	100	2
4	1.2	1000	100	2
5	1.2	500	75	1.5

5.1.4. Flow Initialization

Since the flow phenomena in the microscale are very sensitive to air bubbles, care must be taken to ensure proper initialization [15]. In the case of the standard channel, initializing with parallel flow will make it harder to achieve slug flow at lower flow rates. To ensure repeatable results for all the flow regimes and to prevent air bubbles from entering, we initialize the experiments by filling the channel with the more wettable fluid, in this case, Novec, at a high flow rate of 100-150 μL/min. In case any air bubbles enter, they are flushed out first before allowing water to enter. Then, the flow rates of Novec and water are adjusted to the desired Capillary number and then the experiments are performed.

For the step channel, the initialization procedure is different. Here, the fluid

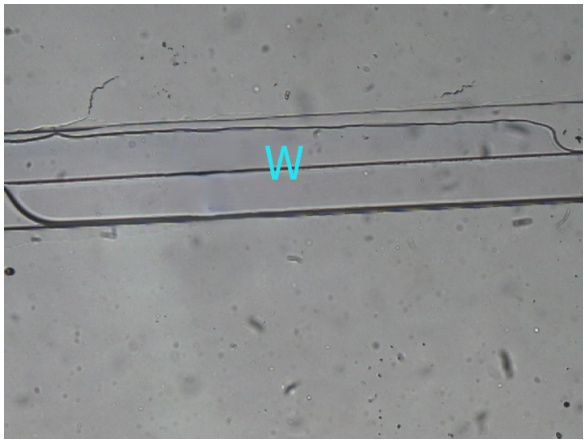

Figure 5.2: A mixed regime is observed in a step channel when initialized at a high flow rate. The dyed fluid is water (the regions corresponding to the letter W within the interface) and the colourless fluid is Novec.

with lower viscosity has to occupy the shallower channel, otherwise, viscous instabilities occur which make it difficult to obtain reproducible flow maps. Large flow rate ratios are then necessary to obtain stable parallel flow [3]. As the channel has an asymmetric cross-section, any air bubbles or liquid droplets can hinder the flow and cause some instabilities, making it difficult to obtain stable parallel flow.

Therefore, we initialize in such a way that water occupies the shallow section and Novec the deep section, and then vary the flow rates to create a flow map. Initializing at a high flow rate will lead to water wetting the entire channel, both the shallow and deep parts. Repeatable and reproducible results cannot be obtained once this happens. The problems associated with high flow rate initialization can be seen in Figure 5.2. Water occupies the entire channel at first, but because it is the non-wetting fluid, Novec occupies the regions near the channel walls. This leads to a mixed regime where both fluids occupy both sections regardless of the flow rate. Thus, no repeatable flow map can be obtained.

To ensure repeatable results, we first introduce water into the shallow section at a low flow rate(1-10 μL/min) and then introduce Novec into the deeper section at a similar flow rate. Once we observe stable parallel flow, we then proceed to vary the flow rates according to the desired regimes.

5.1.5. VOF Simulations

VOF simulations are run on Ansys Fluent and the equations are described in Chapter 3.

5.2. Experimental Results

The experiments are performed on five different channels as discussed in Table 5.2. First, we focus on the differences between the step and standard channel for the same dimensions. The observed flow regimes are elucidated and compared for both channels, followed by the flow maps showing the differences in flow regimes. A similar procedure is followed for the other step channels with variable geometric dimensions, and finally, a generalized flow map is proposed for all the regimes in the step design.

5.2.1. Step vs Standard

Flow Regimes

In this section, we characterize the experimentally observed flow regimes in both the standard and step channels of width 500 μm. The regimes are classified based on their behaviour across the entire channel - inlet, main channel and outlet. This is slightly different from other papers which only consider the inlet and main channel [16, 14, 8]. Including the outlet provides a rounded description of all the flow phenomena occurring in the channel, and it's especially useful when we consider LLE applications where leakage plays a significant role. For the standard channel, the following regimes are observed for various Capillary numbers and shown in Figure 5.3:

1. *Slug Flow:* This flow regime generally occurs at low Capillary numbers ($Ca = 10^{-6} - 10^{-5}$), where interfacial forces are dominant [14, 16]. In this regime, the dispersed phase occupies the entire channel and obstructs the flow of the continuous phase. Eventually, the pressure of the continuous phase builds up and leads to the shearing of the dispersed phase in the form of slugs as shown in Figure 5.3a [17].

2. *Parallel Breakup Flow:* Here, the two fluids flow alongside each other in the main channel (Figure 5.1a), but the inertial forces are not strong enough to maintain this configuration for the rest of the channel [18] (Figure 5.3b). This regime occurs at Ca number larger than those for slug flow (Ca of O(10^{-5}), where the flow rates of the two fluids are roughly comparable, although it is observed in some cases that the flow rate of the continuous phase is considerably larger than the dispersed phase. The inertial forces of the continuous phase seem to play a larger role in this regime, and this was also observed to be the case in the T-channel experiments of Zhao *et al* [19].

3. *Parallel Flow with Leakage and Pinching:* This regime generally occurs at Ca number larger than that observed in Parallel Breakup Flow at comparable flow ($Ca = 10^{-5} - 8\times10^{-4}$). The exceptions to the rule are when the dispersed flow rates are much lower than the continuous flow rates. The two phases flow alongside each other for the whole length of the channel, but the continuous phase "pinches" the dispersed phase at the entrance of the main channel as shown in Figure 5.3c, i.e, the dispersed phase is pushed slightly upwards by

the continuous phase, after which the dispersed phase restores the original interface position. The interface position keeps varying near the inlet, which is why this phenomenon is classified separately. At the end of the rectangular channel, either the continuous or dispersed phase leaks into the outlet of the other as in Figure 5.3d.

4. *Wavy Parallel Flow:* In this case, the two phases move alongside each other but the interface is not straight as in the previous two cases but wavy and unstable as the position of the interface changes with time (Figure 5.3e). This regime occurs at Ca number larger than Parallel Flow with Pinching but smaller than Parallel Flow with Leakage (Ca of O(10^{-3})). It is only observed for a small range of Ca number, with the flow rates of the two phases being comparable.

5. *Parallel Flow with Leakage:* This is similar to the previous regime, except that it occurs at a higher Ca number ($Ca > 10^{-3}$) without any pinching. The position of the interface remains more or less the same throughout the channel as the inertial forces are now large enough to sustain this regime [16, 19, 18, 14]. The flow rates of the two phases are comparable here and leakage is observed here as well.

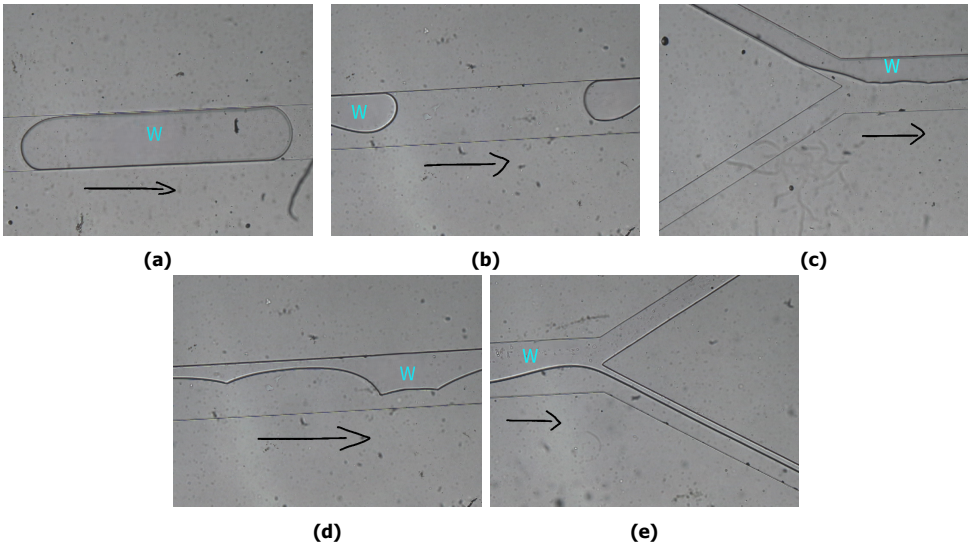

Figure 5.3: Flow regimes observed in a standard channel for a Novec-Water mixture. The colourless fluid is Novec and the dyed fluid is water (the regions corresponding to the letter W within the interface). a) Slug Flow, b) Parallel Breakup Flow, c) Parallel Flow with Leakage and Pinching, d) Wavy Parallel Flow, e) Parallel Flow with Leakage.

When it comes to the step channel, the flow regimes have not been previously classified in the literature to the author's knowledge. Thus, the results presented

in this research might be useful for further studies on step channels. The observed flow regimes in the step channel are shown in Figure 5.4 and classified as follows:

1. *Stable Parallel Flow*: As shown in Figure 5.4a, the two fluids move alongside each other in parallel, but unlike the standard design, the interface is located exactly in the middle of the channel without any leakage, and this is the key reason why this kind of channel is employed in radioisotope extraction [3, 20]. Surprisingly, this regime is observed at low Ca numbers in contrast to the standard channel ($Ca < 5 \times 10^{-5}$).

2. *Parallel Flow with Leakage and Pinching*: Similar phenomenon to that described for the standard channel. This phenomenon is observed for large Ca numbers at comparable flow rates. (Figure 5.4b, $Ca > 10^{-4}$)

3. *Parallel Flow with Leakage*: This regime isn't observed frequently, and thus it's difficult to describe a trend for this regime (Figure 5.4c).

4. *Parallel Breakup Flow*: As with the standard channel, parallel flow breaks down to form droplets, but these droplets only occupy the shallow section and do not penetrate the deeper section (Figure 5.4d). This regime generally occurs for larger continuous phase Ca numbers (Ca_{n}) and dispersed phase Ca numbers (Ca_{w}) as compared to stable parallel flow ($Ca_{\mathrm{n}}/Ca_{\mathrm{w}} \approx 10$).

5. *Complete Wetting*: When the flow rate of the continuous or dispersed phase is much larger compared to the other fluid (O(100) larger), one fluid completely wets the channel, and the other fluid only pinches the interface from time to time (Figure 5.4e).

Flow Maps

From the flow regimes discussed in the above section, we can clearly spot some differences between the regimes observed in the standard and step channels. To visualize these differences, we plot all the flow regimes on flow maps for the two channels based on the Capillary number in Figure 5.5.

The clearest indication of the influence of geometry can be seen in the onset of parallel flow for either of the channels. At low Ca numbers where interfacial forces are dominant, stable parallel flow occurs in the step channel, whereas slug or parallel breakup flow is observed in the standard channel at the same Capillary number. Additionally, no leakage is also observed in the step channel, which points to the role of geometry and interfacial forces in stabilizing parallel flow. Slug flow is also never observed in the step channel for this width. At higher Ca numbers, the step channel gives similar results to the standard channel with parallel flow and leakage being the dominant regime, although pinching is more common in the step channel.

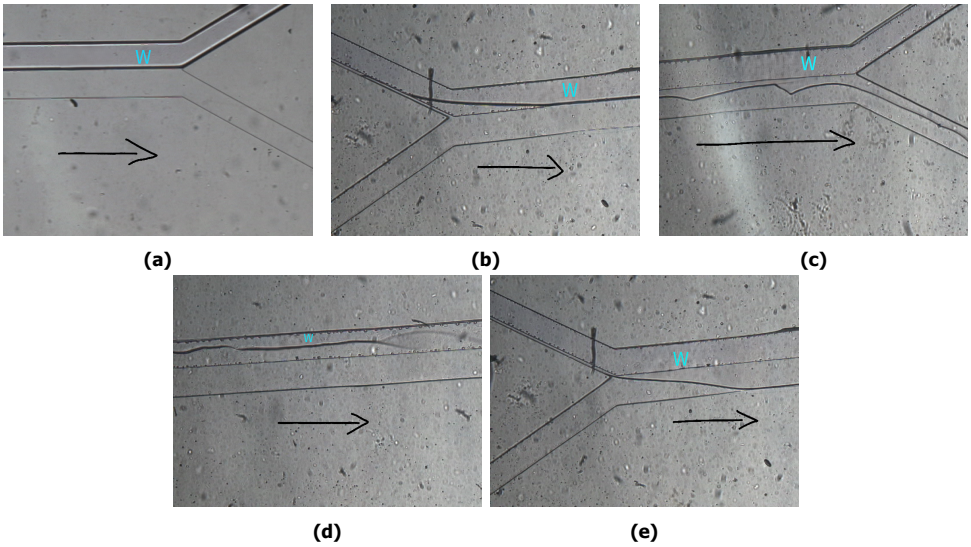

Figure 5.4: Flow regimes observed in a step channel for an Novec-Water mixture. The colourless fluid is Novec and the dyed fluid is water (the regions corresponding to the letter W within the interface). Water is located in the top and shallower section. a) Parallel Flow, b) Parallel Flow with Leakage and Pinching c) Parallel Flow with Leakage d) Parallel Breakup Flow e) Complete Wetting

5.2.2. Influence of Geometric Dimensions in the Step Channel

To further understand the behaviour of fluids in a step design, we work with step channels with different dimensions. Many studies have been conducted on the effect of aspect ratio (channel width to depth) on the formation of droplets and the subsequent transition from droplet/slug flow to other regimes in standard channels[21, 22, 23, 24]. The aspect ratio (Ψ) was found to affect the development of droplets, droplet frequency and onset of jetting or parallel flow. Some papers have also looked into the effect of the hydraulic diameter on the overall flow map [16, 5]. All these studies have been conducted only on channels with symmetric cross-sections (λ=1).

A clearer comprehension of fluid behaviour in the step design is only possible when we look into the impact of Ψ and the degree of asymmetry (λ) on the flow patterns. $\lambda = 1$ corresponds to the standard channel, and we have already observed the differences in Figure 5.5 when the channel is more asymmetric (λ>1). Therefore, we study the effect of ψ on the flow map for the step channel by varying the width along with λ - a parameter unique to this step channel.

Flow Regimes

In addition to the regimes that can be found in channels #1 and #2 (Table 5.2), the following regimes are observed in channels #3, #4 and #5 (Figure 5.6):

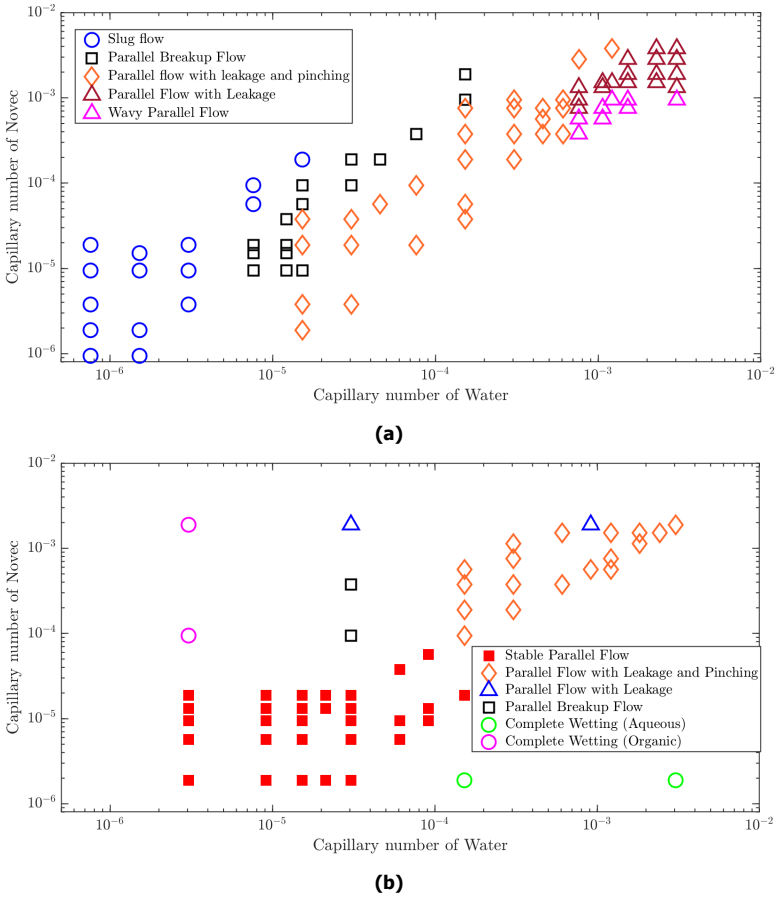

Figure 5.5: Flow map for a) Standard channel #1, b) Step channel #2

1. *Unstable Parallel Flow*: This regime starts with fluids flowing alongside each other, but the interface position is never stable, and the dispersed phase even detaches sometimes, after which it forms a wavy parallel flow-like pattern as shown in Figure 5.6a. Channel #4 shows this regime which normally occurs when the flow rate of the continuous phase is much larger than the dispersed phase ($Ca_{\mathrm{n}}/Ca_{\mathrm{w}} \approx 10$).

2. *Parallel Breakup Flow with Pinching*: The pinching phenomenon accompanies the parallel breakup flow regime described in Section 5.2.1. This occurs in Channel #3 at a high Ca number (O(10^{-3}))with the flow rates of the continuous and dispersed phases being similar.

3. *Slug/Droplet Flow*: Like the regime observed in the standard channel in Section 5.2.1, the dispersed phase detaches in the form of slugs/droplets. The key difference observed in a step channel is that the slug only occupies half

the width of the entire channel and never penetrates the deep channel as shown in Figure 5.6b. This regime occurs in Channels #3 and #5 at lower Ca_{w} and much larger Ca_{n} ($Ca_{\mathrm{n}}/Ca_{\mathrm{w}} \approx 20,\ Ca = 10^{-6} - 10^{-5}$).

4. *Intermittently Stable Parallel Flow*: As the name suggests, the flow regime alternates between stable parallel flow with complete separation and pinching with leakage at the outlet as shown in Figure 5.6c. This regime occurs only in channel #5 at low Ca numbers (O(10^{-5})) with similar flow rates.

5. *Wavy Parallel Flow*: Similar to the regime described for the standard channel in Section 5.2.1, the interface is wavy and its position keeps shifting (Figure 5.6d). The regime is only observed in channel #5 for a few values of the Ca number ($Ca = 3 \times 10^{-4} - 10^{-3}$).

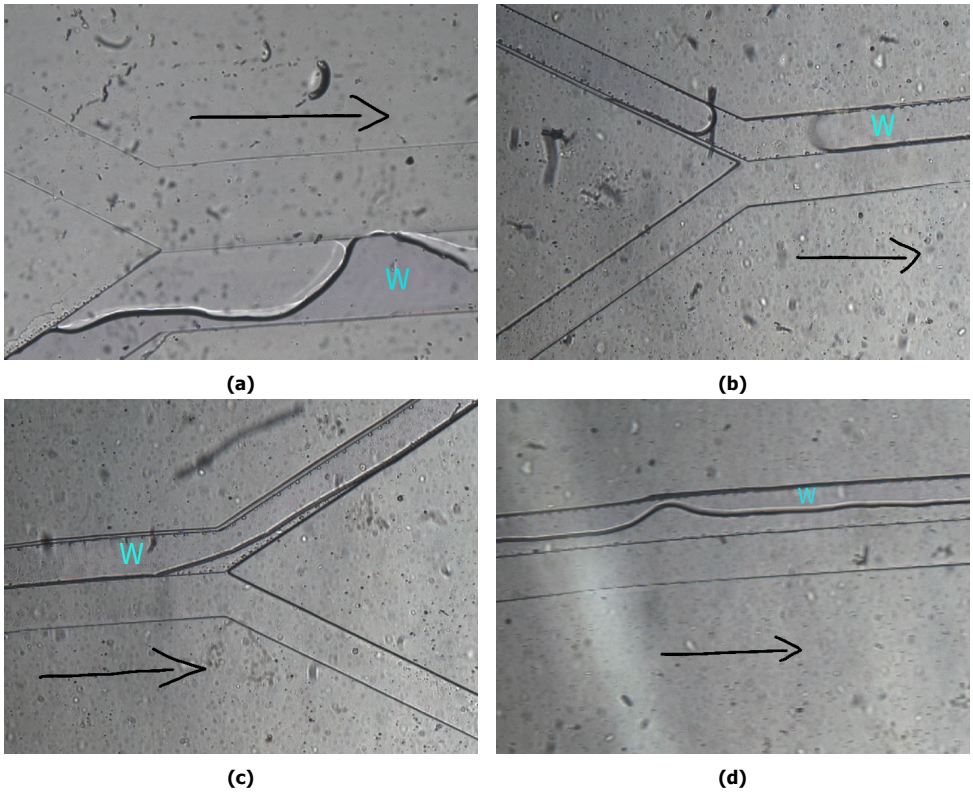

Figure 5.6: Flow regimes observed in a step channel for a Novec-Water mixture. The colourless fluid is Novec and the dyed fluid is water (the regions corresponding to the letter W within the interface). a) Unstable Parallel Flow, b) Slug Flow c) Intermittently Stable Parallel Flow d) Wavy Parallel Flow

Flow Maps

The flow regimes for channels #3, #4 and #5 are visualized using flow maps based on the Capillary number of both phases in Figure 5.7. As hinted by the regimes

discussed in the previous section, the width and λ clearly impact the nature of flow phenomena. In addition to the new regimes, the width also seems to have an influence on leakage, with the channel#4 flow map showing stable parallel flow for a broader range of Ca numbers as compared to channels #2 and #3 (Figures 5.7a, 5.7b, 5.7c). Neither channels #2 nor #3 show any slug or droplet flow, but channel #4 does.

In the case of channel #5, the reduction in λ results in a flow map that is much more scattered than the other step channel flow maps. Channel #5 still favours parallel flow because of its asymmetric nature as can be seen in Figure 5.7c, but leakage and slug flow are also more commonly observed compared to other step channels. Thus, it is imperative to have a considerable height difference for stable parallel flow across a broad range of Ca numbers.

5.2.3. Generalized Flow Maps

In order to visualize the influence of the step channel dimensions more clearly, we plot the regions where stable parallel flow is observed for all the channels in Figure 5.8. For the purpose of comparison, we also include the region where non-wavy parallel flow with leakage is observed in the standard channel just to visualize the stark contrast between the step and standard channel in terms of parallel flow. The figure shows a general pattern of stable parallel flow in step channels at low Ca numbers, which is in stark contrast to the results observed in standard channels. Aspect ratio and λ govern the range of Ca at which stable parallel flow is observed.

channels #2 and #3 show the broadest range of stable parallel flow . Stable parallel flow is observed even for higher Ca numbers in channel #3, whereas channel #2 shows stable parallel flow for lower Ca_{n} than that observed in channel #3. Decreasing the aspect ratio reduces leakage at higher Ca numbers, but the reduced width also results in more pinching at some lower Ca_{n} in channel #3.

A larger channel width in the case of channel #4 significantly reduces the region where stable parallel flow is observed. This might be related to the fact that the interfacial forces have to act over an increased surface area. Channel #5 shows the smallest region where stable parallel flow is observed, whereas the region for Channel #2 is much larger. This points to the role of λ on stable parallel flow, where the regimes were observed to be more scattered in Channel #5 as shown in Figure 5.7c

To obtain an overall picture of the flow regimes and regions observed in the step channel, we plot a generalized flow map similar to the one described by Asadi-Sanghadi *et al* [14] for all the step channels. Many papers have dedicated efforts to plotting such maps with numerous dimensionless number combinations [7, 11, 25], but Asadi-Sanghadi *et al* found that their combination ($Ca^{0.31}We^{0.07}$) was applicable for a broader range of fluids when it comes to generalized flow maps. We plot the flow regimes of all the step channels using their combination in Figure 5.9a.

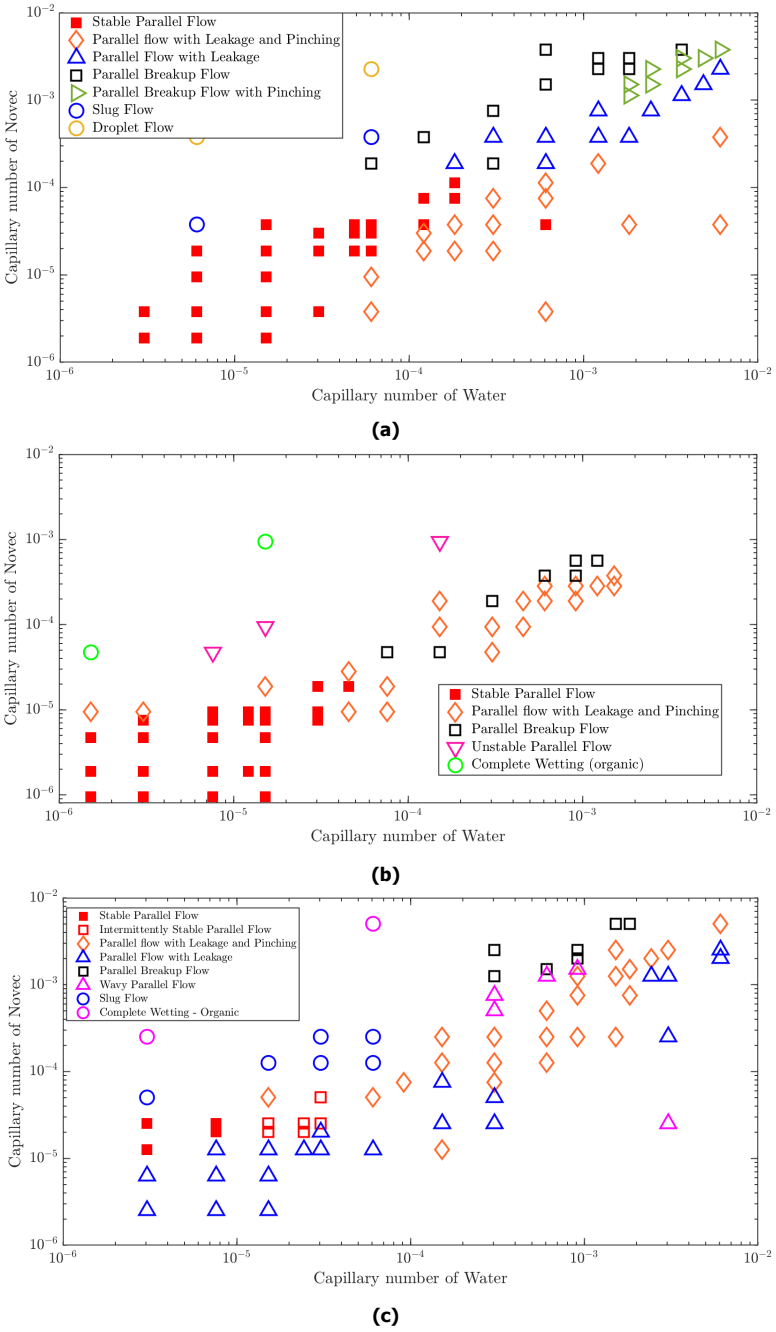

Figure 5.7: Flow map for a) Channel #3, b) Channel #4 c) Channel #5

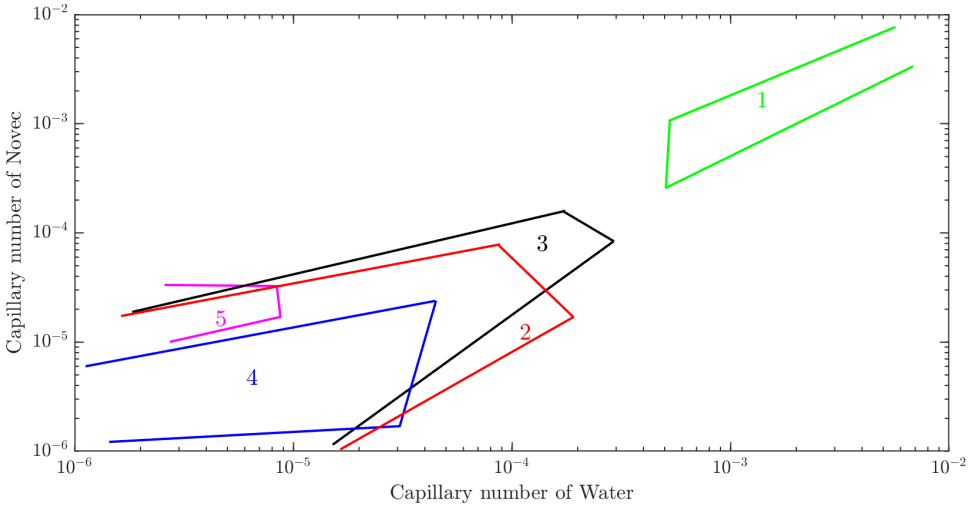

Figure 5.8: Stable Parallel Flow regions for all step channels along with the region of 'Parallel Flow with Leakage' for the standard channel

Based on the data, we propose to divide the generalized flow map into three regions: parallel, droplet/wetting, and transition. The parallel region includes all possible configurations of parallel flow - leakage or no leakage. The droplet/wetting region includes both the complete wetting and slug/droplet regimes. Parallel breakup flow and wavy parallel flow - the intermediate regimes - form a part of the transition regimes. There are some outliers in the flow map which do not fall into their respective regions, but broadly, this is a good division of the regions observed in the step channels.

From Figure 5.9a, we can see that the dominant region corresponds to parallel flow. At lower $Ca^{0.31}We^{0.07}$, stable parallel flow is observed and leakage is observed at higher $Ca^{0.31}We^{0.07}$ with or without pinching. A lower Ca and We number correspond to a greater influence of interfacial tension, and the prominence of stable parallel flow at low $Ca^{0.31}We^{0.07}$ reflects that.

When the $Ca^{0.31}We^{0.07}$ of both fluids are high, we move towards the transition region in the flow map. Higher Ca numbers correspond to larger viscous forces and higher We numbers correspond to larger inertial forces. The boundary separating the parallel and transition regions might indicate the greater importance of inertial forces, especially at higher $Ca_n^{0.31}We_n^{0.07}$. Figures 5.5b, 5.7a,5.7b and 5.7c all show transition regimes at higher Ca_n, which is in contrast to a standard channel (Figure 5.5), where transition regimes are observed intermediate to parallel and slug flow. More studies are needed on these transition regimes in step channels to see if the step induces more instabilities at higher $Ca^{0.31}We^{0.07}$, leading to the breaking of

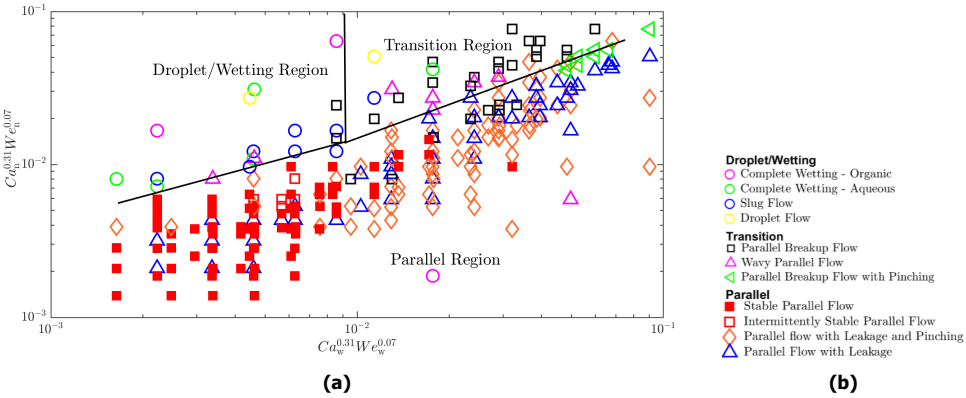

Figure 5.9: Generalized flow map for the step channels using the dimensionless number combination from Asadi-Saghandi *et al* [14]. The map is divided into Parallel, Droplet/Wetting and Transition regions.

the interface.

When the $Ca_n^{0.31}We_n^{0.07}$ is at least 10 times larger than that of the dispersed phase and the $Ca_w^{0.31}We_w^{0.07}$ smaller than 10^{-2}, droplets are observed, or one fluid completely wets the main channel. Droplets appear to be generated by a combination of interfacial forces (surface tension, wettability) and larger viscous forces of the continuous phase.

5.3. VOF Simulations

The experiments showed that fluids in a step channel behave differently than in a standard channel, with the step design favouring stable parallel flow and parallel flow in general as opposed to the standard design. To further understand how the channel design influences flow phenomena, we conduct VOF simulations to be able to visualize fluid behaviour in such channels better. To this author's knowledge, such simulations have not been performed in step channels before.

We compare slug flow in a standard channel with stable parallel flow in a step channel in order to shed some light on the role of interfacial tension in obtaining stable parallel flow in the step channel. Next, we turn our attention to how the fluids behave at a higher Ca number (10^{-3}) in a step channel and compare those flow profiles to the one observed at a low Ca number (10^{-5}).

VOF is chosen because we can obtain pressure plots from it, unlike the RK model where the pressure is coupled with the density. One problem associated with VOF is the large spurious velocities that are generated at low Ca numbers (Ca<10^{-3}) [26] as discussed in Chapter 3. The flow maps in Figures 5.5a and 5.5b clearly

show many possible flow regimes at lower Capillary numbers. Therefore, we first check whether VOF is able to capture stable parallel flow in a step channel before we compare the regimes in a step and standard channel.

5.3.1. Comparison with Experiments

First, we run simulations on Channel #2 at $(Ca_{\mathrm{n}}, Ca_{\mathrm{w}}) = (1.5 \times 10^{-5}, 3 \times 10^{-5})$, where stable parallel flow is expected (Figure 5.5b). Novec is always located in the deeper section of the channel, similar to the experiments. The subscripts n and w correspond to Novec and water respectively. A reduced length of 2 mm is used in the simulations for the main channel to save computational time. A reduced length has been used in many simulations involving Y-Y and T-T channels as it was found to have little impact on the simulation results [27, 28, 29, 30]. This was found to be true even in our simulations of the step channel, where the same flow regimes were obtained at lengths of 1.2 cm and 2 mm. Grid convergence was obtained at 5 μm, similar to the value obtained in Chapter 3. The properties of the fluids are the same as that described in Table 5.1.

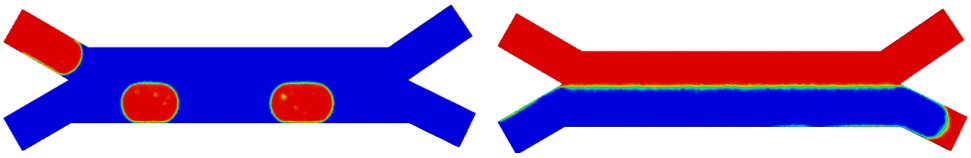

Figure 5.10: VOF simulations for Water-Novec mixture in channel 2 at $Ca_{\mathrm{n}} = 1.5 \times 10^{-5}, Ca_{\mathrm{w}} = 3 \times 10^{-5}$ with a a) Hydrophobic surface.b) Hydrophilic surface. The blue fluid is Novec and the red fluid is water, with Novec being located in the deeper section at the bottom half of the channel.

At $(Ca_{\mathrm{n}}, Ca_{\mathrm{w}}) = (1.5 \times 10^{-5}, 3 \times 10^{-5})$, however, droplets are surprisingly seen instead of stable parallel flow as in the experiments (Figure 5.10a), even though parallel flow is observed at such Capillary numbers, similar to the regime shown in Figure 5.5b).

When a hydrophilic channel is used, though, stable parallel flow is observed as shown in Figure 5.10b. The Capillary numbers and flow rates are the same as those used in the hydrophobic channel. Unfortunately, no experimental data is available for a hydrophilic channel, so this simulation result can't be confirmed. Nevertheless, since we wish to study the fluid behaviour in step channels, we apply the hydrophilic channel and compare the results at a low Capillary number with those observed in a standard hydrophilic channel. This study helps to characterize the flow development in both channels and observe how the variations in pressure influence the flow regime's nature.

5.3.2. Standard vs Step

In this section, we compare a standard and step channel at low Capillary numbers. From Figures 5.5a and 5.5b, we can see that two different regimes of slug and stable parallel flow are obtained in the standard and step channels respectively at low Ca numbers. VOF simulations are performed to study this contrast in greater detail through velocity contours and pressure plots.

As can be seen from Figure 5.5, the Ca numbers for parallel flow in a step channel are very low, resulting in large spurious velocities. In addition to the problem of spurious velocities, there is also the problem of long simulation times because of the low flow rates. Therefore, we work with a channel of a similar geometry but with smaller dimensions for both the step and standard designs as described in Table 5.3. Water occupies the shallower section and Novec occupies the deeper section, with the velocities of both fluids being equal.

Table 5.3: Channel Dimensions. The depth of the shallow channel is fixed at 20 μm.

Type	**Length** (mm)	**Width** (μm)	**Depth of Deeper Channel** (μm/ l.u)	λ
Standard	1	200	20	1
Step	1	200	40	2

In Section 5.1.4, we mentioned that the standard channel was initialized with the continuous phase occupying the entire domain and the dispersed phase introduced into one inlet. The simulations here are initialized similarly, with Novec being introduced from the deeper (bottom) inlet and water occupying the entire domain. Since we wish to compare the flow development in both the step and standard channels, the step channel is also initialized similarly. This initialization was found to have no impact on the simulated flow regime.

First, we discuss the simulation results for a standard channel. According to Figure 5.5a, slug flow is observed at Capillary numbers ranging from $10^{-6} - 10^{-5}$. However, even at such low Ca numbers, VOF could not capture slug flow in a standard channel. Instead, the dispersed phase fills the main channel and assumes a shape similar to blocking in slug flow [17] (Figure 5.12e), but is later pushed to form the regime shown in Figure 5.11a, where the dispersed phase splits to form two droplets at the outlet junction.

The dispersed phase in both channels follows the filling and blocking stages described in Lei *et al* [17] (Figure 5.12), but doesn't detach to form a slug. Such a result was also observed in the VOF simulations Jahromi *et al* [28], where the width of their main channel was twice the width of their inlets, similar to the channel used in our simulations. To see if the channel length is an issue, we ran simulations for a longer length of 2 mm and no slugs were observed even then. In the

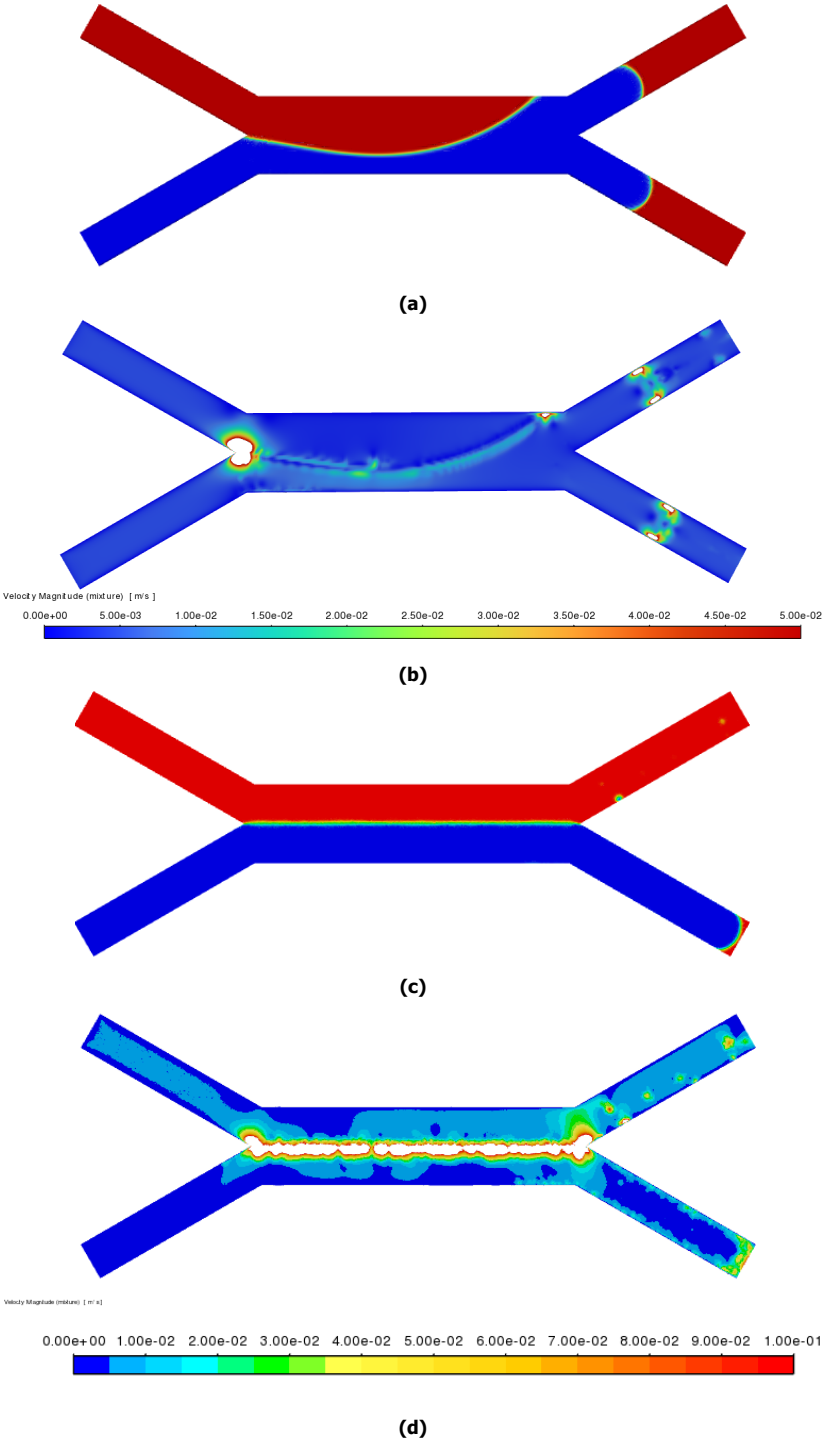

Figure 5.11: Flow regimes obtained for the standard channel and step channel described in Table 5.3 from VOF simulations at $Ca_w = 8 \times 10^{-5}$. a) Phase contour for the standard channel, the blue fluid is Novec and the red fluid is water at z=10 μm. b) Velocity contour with large velocity regions removed from the contour for clarity c) Phase contour for the step channel z=10 μm, with the deeper section located at the bottom half of the channel. d) Velocity contour for the step channel. The white spaces correspond to the spurious velocities.

experiments (Figure 5.5a), slugs of lengths around 500 μm are observed, and our channel lengths are chosen to be longer than that. Besides, Jahromi *et al* [28] did not observe slugs even for a channel with a length of 2 cm.

The regime shown in Figure 5.11a in a standard channel is compared with stable parallel flow in a step channel at $(Ca_{\mathrm{w}},\ Ca_{\mathrm{n}}) = (8 \times 10^{-5},\ 9.9 \times 10^{-5})$ as shown in Figure 5.4a. The inlet velocity of Novec is kept the same as that of water for both channels. First, we visualize the flow field through the velocity contours for both the channels in Figures 5.11b and 5.11d. The contours are plotted on the XY plane at z= 10 μm. As the spurious velocities at these Capillary numbers are quite high, we set an upper limit to the maximum velocity when we plot the velocity contours for the purposes of clarity. This is why white spaces are observed in Figures 5.11b and 5.11d.

The velocities in the main channel are similar to those at the inlets in the case of the step design. Even though the prescribed velocities at both the channel inlets are equal, the velocity at the top inlet is larger than that at the bottom inlet. This is related to the reduced area at the top half of the channel, which correspondingly results in a larger velocity. As for the standard channel, the velocities in the main channel are similar to the inlet velocities.

To further understand how the geometry influences the flow phenomena, we plot the flow development in both channels along with the variations in pressure as the flow develops. The various stages of flow development for each channel are shown in Figures 5.12 and 5.13. We measure the pressures of the aqueous and organic phases at two nodes located near the channel intersections (Figure 5.1a) on either side of the interface respectively. The evolution of pressure across the time period is plotted for both channels in Figure 5.14.

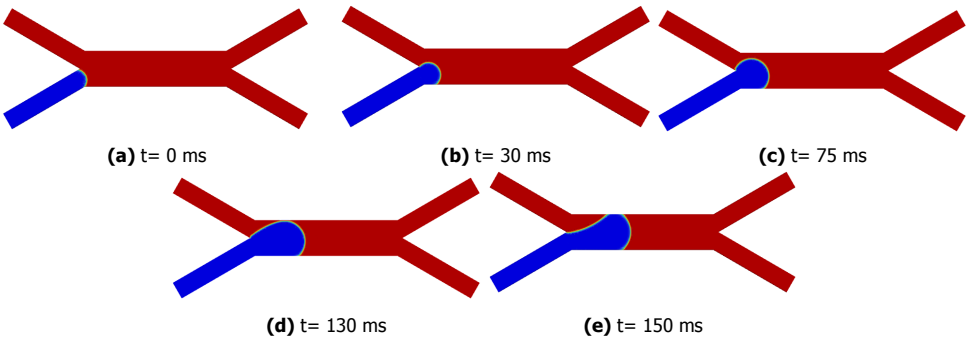

Figure 5.12: Flow development in a standard channel at $Ca_{\mathrm{w}} = 8 \times 10^{-5}$. The blue fluid is Novec and the red fluid is water.

In the case of the standard channel, we can see that the aqueous (continuous) pressure keeps increasing over time, though the degree of increase varies. The

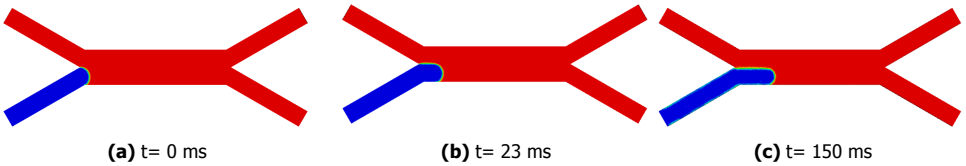

(a) t= 0 ms **(b)** t= 23 ms **(c)** t= 150 ms

Figure 5.13: Flow development in a step channel at $Ca_w = 8 \times 10^{-5}$. The blue fluid is Novec and the red fluid is water, with the deeper section located at the bottom half of the channel. The velocities of the two fluids are equal.

aqueous pressure gradually increases as the organic (dispersed) phase enters and fills the main channel (Figure 5.12b), after which a steep increase is observed as the organic phase blocks the flow of the aqueous phase (Figures 5.12c, 5.12d). A steep increase in the aqueous pressure was also observed in the blocking phase in the results of Lei *et al* [17], after which the aqueous pressure drops due to the shearing of the organic phase by the aqueous phase to form a slug. Slug formation, however, is not observed in our case, so we still observe an increase in pressure, though the slope is less steep. The interface is deformed to form a more convex shape (Figure 5.12e) as the aqueous phase pushes the organic phase towards the outlet.

The Novec pressure decreases until the period where the aqueous pressure sharply increases (Figure 5.12c), after which it roughly remains constant, similar to the expected trend for the blocking stage [17]. If a slug was formed, a slight increase in the organic pressure would be observed.

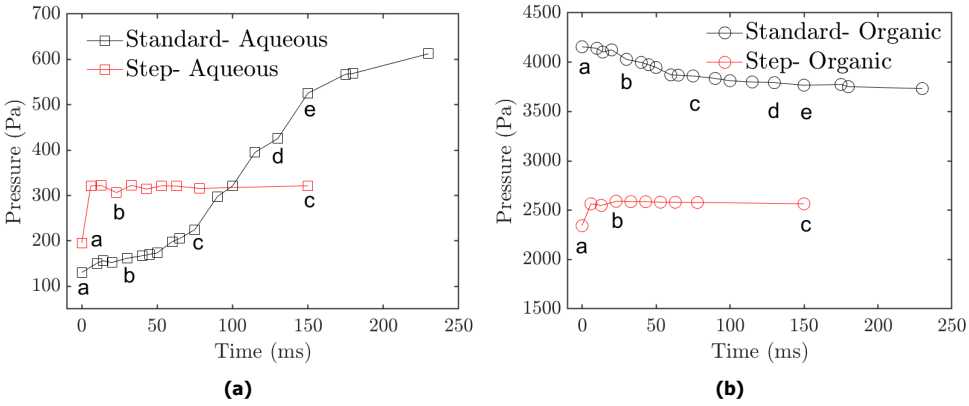

(a) **(b)**

Figure 5.14: Evolution of the pressure in the a)Aqueous phase b)Organic phase in both the channels. The letters in the plot correspond to the times shown in Figures 5.12 and 5.13.

In the case of the step channel, Novec enters the deeper section (Figure 5.13a) and moves parallelly to water. Parallel flow is constantly maintained as Novec progresses through the channel without any changes in the position of the interface

(Figures 5.13b, 5.13c). This is reflected in the pressure plot, with the aqueous and organic pressure remaining constant with time after the initial increase once Novec enters the main channel. The pressure is lower in magnitude than in the standard channel due to reasons related to the different flow regimes. In the case of parallel flow, both the aqueous and organic phases occupy half the channel area, whereas, for slug flow, both phases occupy the entire channel area. The larger pressure for slug flow is related to the increased area.

A constant pressure corresponds to a stable interface, as fluctuations in the fluid pressure result in the waviness of the interface. As discussed during the experimental results, the interfacial tension aids in stabilizing parallel flow at such low Capillary numbers. Since the inertial and viscous forces are very small, the interfacial tension guides the fluids into their respective channels. A strong interfacial force ensures that the fluid interface remains unperturbed for the entire duration of the flow in a step channel as the Laplace pressure balances the pressure drop due to viscous forces [31].

To summarize, the pressure development in a standard and step channel corresponds to the contrasting regimes observed at low Ca numbers. While the pressure keeps varying in a standard channel to correspond to slug formation, constant pressure in the step channel corresponds to stable parallel flow.

5.3.3. Leakage at higher Capillary numbers

In this section, we focus on understanding the fluid behaviour in a step channel at higher Ca numbers. At these Ca numbers, interfacial forces don't play as important a role in the flow phenomena, so studying this region will shed some light on how inertial and viscous forces behave in a step channel. We simulate fluid flow in the same step channel described in Table 5.3 at $(Ca_{\mathrm{w}},\ Ca_{\mathrm{n}}) = (3\times10^{-3},\ 1.86\times10^{-3})$. The flow velocities at this Ca number are larger than the spurious velocities, so the flow profile can be more clearly visualized. Novec flows at a velocity half that of water. The flow regime obtained from this simulation is plotted in Figure 5.15a.

At such a high Ca number, we obtain parallel flow with leakage to the organic outlet, as in Figure 5.5b. Pinching is also observed near the intersection, similar to the regimes observed in the experiments at high Ca numbers (Figure 5.5b). The velocity contour for this regime is plotted in Figure 5.15b at z=10μm. Immediately, we can visualize a stark contrast between the velocities at the inlet and the main channel. Even though the velocity of water is twice that of Novec, the fluids in the deeper section have a higher velocity than those in the shallower section once they enter the main channel. To check if this is indeed the case, we plot the velocity contours along the Y-Z plane at a point near the channel intersection (x=400μm, Figure 5.16b) and at a point in the middle of the channel (x= 800 μm, Figure 5.16c).

At the intersection (Figure 5.1a), we can see that the water velocity is higher

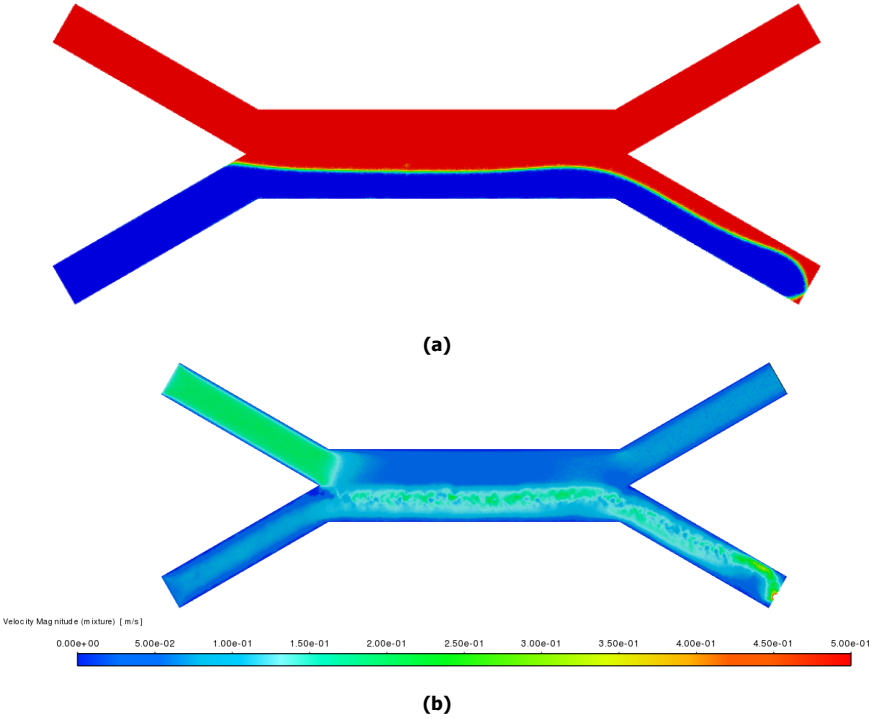

Figure 5.15: a) Flow regime obtained at $Ca_w = 3 \times 10^{-3}$ at z=10μm. The blue fluid is Novec and the red fluid is water, with the velocity of Novec being half of that of water. Novec is located in the deeper section at the bottom half of the channel b) Velocity contour

than that of Novec's, which corresponds to the larger inlet water velocity. However, in the middle of the channel, the largest velocities are observed in the deeper channel, particularly at the region near the step. This transfer of velocity is necessary for water to enter the deeper channel. This was not the case for stable parallel flow in Figure 5.11d, so this change in velocity profile is clearly related to leakage, as the Novec now occupies less area in the bottom section compared to the inlet. The water enters the deeper section with a larger velocity from the top (Figure 5.16a), and this is reflected in the velocity contour.

Though VOF was unable to capture the accurate flow phenomena as observed in the experiments for the Water-Novec mixture in a PDMS step channel, they clearly show how the inclusion of the step leads to changes in fluid behaviour, thereby influencing the flow phenomena. To further understand the intricacies of fluid behaviour in a step design, experimental techniques like micro-Particle Image Velocimetry (micro-PIV) can be used to study the flow profile better.

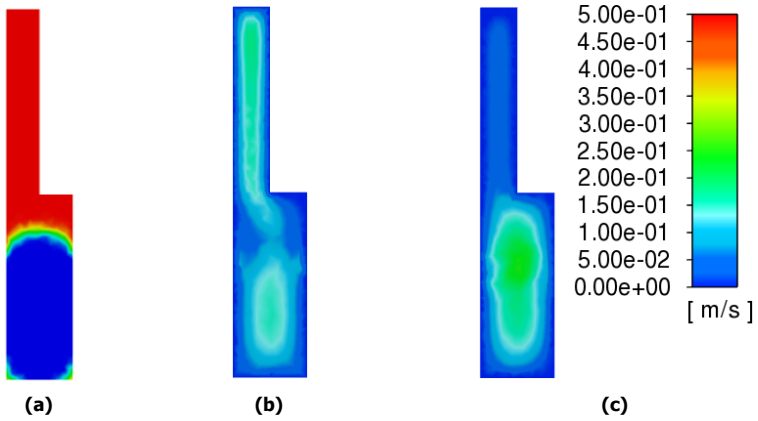

Figure 5.16: a) Cross-sectional view of leakage in a step channel at $Ca_w = 3 \times 10^{-3}$ at x= 800 μm. The blue fluid is Novec and the red fluid is water, with the Novec velocity being half of the water velocity. Novec is located in the deeper section at the bottom half of the channel b) Cross-sectional velocity contour at the channel intersection at x=400μm c) Cross-sectional velocity contour in the middle of the channel at x= 800 μm

5.4. Conclusion

In this chapter, the step channel previously used in mass transfer applications has been studied in detail. This step channel is marked by a difference in depth across its two halves, i.e., one section is shallow and the other is deep. To understand the influence such a design might have on the flow phenomena, experiments were conducted on both the step channel and a standard channel - channel with uniform depth - and the various flow regimes were compared and plotted. It was found that the stable parallel flow was obtained at low Capillary numbers in the step channel, whereas slug and parallel breakup flow was obtained in the standard channel for the same set of Capillary numbers. Additionally, the interface was located exactly in the middle of the step channel with no leakage, and this could not be observed in the standard channel.

The step channel was further studied experimentally by varying the channel dimensions such as the width and step ratio, with flow maps being plotted for these channels as well. Reducing the step ratio resulted in a more scattered flow map, with stable parallel flow occurring less frequently and leakage being more common. A smaller width increased the range of Capillary numbers for which stable parallel flow was observed, while a larger width correspondingly reduced this range. Changing the dimensions also led to different regimes previously not observed in the first step channel such as slug flow or intermittently stable parallel flow. Plotting a generalized flow map for all these step channels revealed that the step design tends to favour parallel flow significantly more than other regimes.

Finally, the flow phenomena observed in the step channel were compared and contrasted with those in the standard channel using VOF simulations. The pressure evolution at low Capillary numbers showed the variation of both aqueous and organic pressures in the standard channel as the organic phase enters into the filling and blocking stages. In contrast, the pressure of both the aqueous and organic phases was constant in the case of the step channel at the same Capillary number. The interfacial tension played a key role in maintaining the interface position and stable parallel flow along with the nature of the step design at such low Capillary numbers.

At higher Capillary numbers, however, the velocity in the deeper section was found to be larger than that in the shallow section even if the velocity at the shallow inlet was larger than that in the deeper inlet. This suggests that there is a transfer of water velocity from the shallower to the deeper channel, though more studies with more accurate simulation/experimental techniques are needed to fully grasp the flow phenomena in a step channel.

Bibliography

[1] Adelina Smirnova, Kazuma Mawatari, Akihide Hibara, Mikhail A. Proskurnin, and Takehiko Kitamori. Micro-multiphase laminar flows for the extraction and detection of carbaryl derivative. *Analytica Chimica Acta*, 558(1-2):69–74, February 2006. ISSN 00032670. doi: 10.1016/j.aca.2005.10.073. URL https://linkinghub.elsevier.com/retrieve/pii/S0003267005018519.

[2] Akihide Hibara, Shinobu Iwayama, Shinya Matsuoka, Masaharu Ueno, Yoshikuni Kikutani, Manabu Tokeshi, and Takehiko Kitamori. Surface Modification Method of Microchannels for Gas−Liquid Two-Phase Flow in Microchips. *Analytical Chemistry*, 77(3):943–947, February 2005. ISSN 0003-2700, 1520-6882. doi: 10.1021/ac0490088. URL https://pubs.acs.org/doi/10.1021/ac0490088.

[3] Gwendolyne Hellé, Sean Roberston, Siméon Cavadias, Clarisse Mariet, and Gérard Cote. Toward numerical prototyping of labs-on-chip: modeling for liquid–liquid microfluidic devices for radionuclide extraction. *Microfluidics and Nanofluidics*, 19(5):1245–1257, November 2015. ISSN 1613-4982, 1613-4990. doi: 10.1007/s10404-015-1643-8. URL http://link.springer.com/10.1007/s10404-015-1643-8.

[4] Yasutoshi Ban, Yoshikuni Kikutani, Manabu Tokeshi, and Yasuji Morita. Extraction of Am(III) at the Interface of Organic-Aqueous Two-Layer Flow in a Microchannel. *Journal of Nuclear Science and Technology*, 48(10):1313–1318, October 2011. ISSN 0022-3131, 1881-1248. doi: 10.1080/18811248.2011.9711821. URL http://www.tandfonline.com/doi/abs/10.1080/18811248.2011.9711821.

[5] Mayur Darekar, Krishna Kumar Singh, Sulekha Mukhopadhyay, and Kalsanka Trivikram Shenoy. Liquid–Liquid Two-Phase Flow Patterns in Y-Junction Microchannels. *Industrial & Engineering Chemistry Research*, 56(42):12215–12226, October 2017. ISSN 0888-5885, 1520-5045. doi: 10.1021/acs.iecr.7b03164. URL https://pubs.acs.org/doi/10.1021/acs.iecr.7b03164.

[6] Amin Farahani, Ahmad Rahbar-Kelishami, and Hadi Shayesteh. Microfluidic solvent extraction of Cd(II) in parallel flow pattern: Optimization, ion exchange, and mass transfer study. *Separation and Purification Technology*, 258:118031, March 2021. ISSN 13835866. doi: 10.1016/j.seppur.2020.118031. URL https://linkinghub.elsevier.com/retrieve/pii/S1383586620325041.

[7] Madhvanand Kashid and Lioubov Kiwi-Minsker. Quantitative prediction of flow patterns in liquid–liquid flow in micro-capillaries. *Chemical Engineering and Processing: Process Intensification*, 50(10):972–978, October 2011. ISSN 02552701. doi: 10.1016/j.cep.2011.07.003. URL https://linkinghub.elsevier.com/retrieve/pii/S0255270111001553.

[8] Anne-Laure Dessimoz, Laurent Cavin, Albert Renken, and Lioubov Kiwi-Minsker. Liquid–liquid two-phase flow patterns and mass transfer characteristics in rectangular glass microreactors. *Chemical Engineering Science*, 63 (16):4035–4044, August 2008. ISSN 00092509. doi: 10.1016/j.ces.2008.05.005. URL https://linkinghub.elsevier.com/retrieve/pii/S000925090800256X.

[9] YuMei Yong, Chao Yang, Yi Jiang, Ameya Joshi, YouChun Shi, and XiaoLong Yin. Numerical simulation of immiscible liquid-liquid flow in microchannels using lattice Boltzmann method. *Science China Chemistry*, 54 (1):244–256, January 2011. ISSN 1674-7291, 1869-1870. doi: 10.1007/s11426-010-4164-z. URL http://link.springer.com/10.1007/s11426-010-4164-z.

[10] Abdelkader Salim, Mostafa Fourar, Jacques Pironon, and Judith Sausse. Oil-water two-phase flow in microchannels: Flow patterns and pressure drop measurements. *The Canadian Journal of Chemical Engineering*, 86(6):978–988, December 2008. ISSN 00084034, 1939019X. doi: 10.1002/cjce.20108. URL https://onlinelibrary.wiley.com/doi/10.1002/cjce.20108.

[11] Zhen Cao, Zan Wu, and Bengt Sundén. Dimensionless analysis on liquid-liquid flow patterns and scaling law on slug hydrodynamics in cross-junction microchannels. *Chemical Engineering Journal*, 344:604–615, July 2018. ISSN 13858947. doi: 10.1016/j.cej.2018.03.119. URL https://linkinghub.elsevier.com/retrieve/pii/S1385894718304789.

[12] Zan Wu, Zhen Cao, and Bengt Sundén. Liquid-liquid flow patterns and slug hydrodynamics in square microchannels of cross-shaped junctions. *Chemical Engineering Science*, 174:56–66, 2017.

[13] Ich-Long Ngo, Sang Woo Joo, and Chan Byon. Effects of Junction Angle and Viscosity Ratio on Droplet Formation in Microfluidic Cross-Junction. *Journal of Fluids Engineering*, 138(5):051202, May 2016. ISSN 0098-2202, 1528-901X. doi: 10.1115/1.4031881. URL https://asmedigitalcollection.asme.org/fluidsengineering/article/doi/10.1115/1.4031881/372200/Effects-of-Junction-Angle-and-Viscosity-Ratio-on.

[14] Hamid Asadi-Saghandi, Javad Karimi-Sabet, Sohrabali Ghorbanian, and Seyed Mohammad Ali Moosavian. Dimensionless analysis on liquid–liquid two-phase flow patterns in a numbered-up microfluidic device. *Chemical Engineering Journal*, 429:132428, February 2022. ISSN 13858947. doi: 10.1016/j.cej.

2021.132428. URL https://linkinghub.elsevier.com/retrieve/pii/S1385894721040067.

[15] Can Huang, Jose A Wippold, Dimitra Stratis-Cullum, and Arum Han. Eliminating air bubble in microfluidic systems utilizing integrated in-line sloped microstructures. *Biomedical Microdevices*, 22:1–9, 2020.

[16] Madhvanand N. Kashid and David W. Agar. Hydrodynamics of liquid–liquid slug flow capillary microreactor: Flow regimes, slug size and pressure drop. *Chemical Engineering Journal*, 131(1-3):1–13, July 2007. ISSN 13858947. doi: 10.1016/j.cej.2006.11.020. URL https://linkinghub.elsevier.com/retrieve/pii/S1385894706005092.

[17] Li Lei, Yuting Zhao, Xinyu Wang, Gongming Xin, and Jingzhi Zhang. Experimental and numerical studies of liquid-liquid slug flows in micro channels with Y-junction inlets. *Chemical Engineering Science*, 252:117289, April 2022. ISSN 00092509. doi: 10.1016/j.ces.2021.117289. URL https://linkinghub.elsevier.com/retrieve/pii/S000925092100854X.

[18] Z. Liu. *Purifying Radionuclides with Microfluidic Technology for Medical Purpose: Simulating multiphase flows inside a microfluidic channel with the phase field method*. PhD thesis, Delft University of Technology, 2022. URL http://resolver.tudelft.nl/uuid:e1bebcdd-185a-4515-b352-76d68f65ace8.

[19] Yuchao Zhao, Guangwen Chen, and Quan Yuan. Liquid-liquid two-phase flow patterns in a rectangular microchannel. *AIChE Journal*, 52(12):4052–4060, December 2006. ISSN 00011541, 15475905. doi: 10.1002/aic.11029. URL https://onlinelibrary.wiley.com/doi/10.1002/aic.11029.

[20] H. Karim, C. Castel, A. Lélias, A. Magnaldo, and P. Sarrat. Kinetic study of uranium (VI) extraction with tributyl-phosphate in a stratified flow microchannel. *Separation and Purification Technology*, 314:123489, June 2023. ISSN 13835866. doi: 10.1016/j.seppur.2023.123489. URL https://linkinghub.elsevier.com/retrieve/pii/S1383586623003970.

[21] Jonathan D. Wehking, Michael Gabany, Larry Chew, and Ranganathan Kumar. Effects of viscosity, interfacial tension, and flow geometry on droplet formation in a microfluidic T-junction. *Microfluidics and Nanofluidics*, 16 (3):441–453, March 2014. ISSN 1613-4982, 1613-4990. doi: 10.1007/s10404-013-1239-0. URL http://link.springer.com/10.1007/s10404-013-1239-0.

[22] Piotr Garstecki, Michael J. Fuerstman, Howard A. Stone, and George M. Whitesides. Formation of droplets and bubbles in a microfluidic T-junction—scaling and mechanism of break-up. *Lab on a Chip*, 6(3):437, 2006. ISSN 1473-0197, 1473-0189. doi: 10.1039/b510841a. URL http://xlink.rsc.org/?DOI=b510841a.

[23] Santosh Kumar Jena, Tushar Srivastava, Supreet Singh Bahga, and Sasidhar Kondaraju. Effect of channel width on droplet generation inside t-junction microchannel. *Physics of Fluids*, 35(2), 2023.

[24] Kui He, Zhiling Zhang, Liangzhen Zhang, Wuzhi Yuan, and Si-Min Huang. Effects of geometrical confinement on the generation of droplets at microfluidics t-junctions with rectangle channels. *Microfluidics and Nanofluidics*, 27(10):67, 2023.

[25] Anna A. Yagodnitsyna, Alexander V. Kovalev, and Artur V. Bilsky. Flow patterns of immiscible liquid-liquid flow in a rectangular microchannel with T-junction. *Chemical Engineering Journal*, 303:547–554, November 2016. ISSN 13858947. doi: 10.1016/j.cej.2016.06.023. URL https://linkinghub.elsevier.com/retrieve/pii/S1385894716308300.

[26] Stéphane Popinet. Numerical Models of Surface Tension. *Annual Review of Fluid Mechanics*, 50(1):49–75, January 2018. ISSN 0066-4189, 1545-4479. doi: 10.1146/annurev-fluid-122316-045034. URL https://www.annualreviews.org/doi/10.1146/annurev-fluid-122316-045034.

[27] Piyush Kumar and Manabendra Pathak. Dynamic wetting characteristics during droplet formation in a microfluidic T-junction. *International Journal of Multiphase Flow*, 156:104203, November 2022. ISSN 03019322. doi: 10.1016/j.ijmultiphaseflow.2022.104203. URL https://linkinghub.elsevier.com/retrieve/pii/S0301932222001823.

[28] Peyman Foroozan Jahromi, Javad Karimi-Sabet, Younes Amini, and Hooman Fadaei. Pressure-driven liquid-liquid separation in y-shaped microfluidic junctions. *Chemical Engineering Journal*, 328:1075–1086, 2017.

[29] Jovan Jovanović, Evgeny V. Rebrov, T. A. (Xander) Nijhuis, M. T. Kreutzer, Volker Hessel, and Jaap C. Schouten. Liquid–Liquid Flow in a Capillary Microreactor: Hydrodynamic Flow Patterns and Extraction Performance. *Industrial & Engineering Chemistry Research*, 51(2):1015–1026, January 2012. ISSN 0888-5885, 1520-5045. doi: 10.1021/ie200715m. URL https://pubs.acs.org/doi/10.1021/ie200715m.

[30] Z Liu. Purifying radionuclides with microfluidic technology for medical purpose: Simulating multiphase flows inside a microfluidic channel with the phase field method. 2022.

[31] Arata Aota, Kazuma Mawatari, and Takehiko Kitamori. Parallel multiphase microflows: fundamental physics, stabilization methods and applications. *Lab on a Chip*, 9(17):2470, 2009. ISSN 1473-0197, 1473-0189. doi: 10.1039/b904430m. URL http://xlink.rsc.org/?DOI=b904430m.

6

Interfacial Mass Transfer in a Microchannel

Chapter 1 detailed the applications of LLE and the advantages of operating in the microscale. The previous chapters have looked at the flow regimes involved and the conditions necessary for achieving stable parallel flow. Stable parallel flow is very important for radioisotope extractions to avoid the separation step [1], but the mass transfer mechanisms for such a regime also need to be understood if microfluidic LLE is to be applied in different applications.

In the case of multiphase flow, the mass transfer can be influenced solely by diffusion, a chemical reaction, or a combination of both [2, 3, 4]. Generally, binding agents or chelators are added to the extracting fluid to enhance mass transfer through a chemical reaction [5, 6, 7]. These chemical reactions can either take place across the whole extracting fluid [8, 7] or be just restricted to the region around the liquid-liquid interface [5, 3]. The former is normally restricted to slug flow as the flow circulation near the slug boundaries transports the solute and ions across the entire slug [8].

However, for parallel flow, such circulating flows are generally not observed near the interface. Therefore, the reaction normally occurs in the interface region after which it gradually diffuses to the rest of the extracting fluid [5, 4]. Considering the prevalence of such a reaction mechanism in microfluidic LLE [4, 3, 6], it is important to understand the forces and factors which influence such a mass transfer.

Dimensionless numbers are very useful in providing an understanding of the transport phenomena as they show the competing forces involved. Zhang *et al* [8] numerically studied the extraction mechanism of Lanthanum for slug flow using the Damkohler (Da) and Graetz (Gz)numbers. In this way, they could better understand how the reaction takes place inside the slug and how the flow velocity

subsequently influences the reaction, thereby the mass transfer. To this author's knowledge, similar studies for reactions taking place close to the interface have not included dimensionless numbers in their analysis. This limits the understanding and applicability of the results as they are restricted to a particular set of fluids and solutes, and do not provide insight into the forces that influence the mass transfer mechanisms. Karim *et al* [4] mentioned the important dimensionless numbers for interfacial mass transfer, but did not use them in their study.

This chapter seeks to understand the factors which influence interfacial mass transfer. For this purpose, numerical simulations are first conducted for the set of fluids used by Helle *et al* [9]. Once the model is validated, dimensionless numbers are varied to understand the effect of the competing forces on the mass transfer for the same fluids used by Helle *et al* [9]. Finally, the simulations are used in combination with experiments to study the extraction kinetics of a Gallium isotope in water and chloroform, thereby extending the applicability of the model.

6.1. Interfacial Mass Transfer Theory

The simplified Convection-Diffusion equation (CDE) described in Equations 2.38 and 2.37 is once again used. However, there are dimensionless numbers and boundary conditions specific to interfacial mass transfer. This section looks at the interfacial boundary conditions and dimensionless numbers.

6.1.1. Interfacial Boundary Condition

In this chapter, both diffusion and reaction kinetics are considered when simulating mass transfer. Therefore, the interfacial boundary condition described in Equation 2.41 cannot be applied. As mentioned earlier, the reaction takes place in the region around the interface, therefore, a reaction boundary condition is applied at the interface while Equations 2.37 or 2.38 are solved for the rest of the channel.

First, numerical simulations are conducted using the fluids and kinetics of Helle *et al* [9]. Their extraction kinetics involved the transfer of Uranium from the aqueous to the organic phase. The chemical reaction describing the formation of Uranium is given by:

$$UO_2(Cl)_4^{2-} + 2\,R_4N^+, Cl^- \rightleftharpoons (R_4N^+)_2UO_2(Cl)_4^{2-} + 2\,Cl^-$$

Uranium is extracted from the aqueous HCl phase to the organic (dodecane) phase using Aliquat ($2\,R_4N^+, Cl^-$) to form a new Uranium complex that can only dissolve in the organic phase. R corresponds to an alkyl group here. It is assumed that the aqueous chloro-Uranium complex does not diffuse into the organic phase and the Aliquat does not diffuse to the aqueous phase. The concentrations of Aliquat and Cl^- are also much larger than the Uranium concentrations, therefore they

can be considered constant during the reaction. The interfacial BC for the Uranium species is given by [3, 9]:

$$-D_{j,i}\left.\frac{\partial c_j}{\partial y}\right|_{y=h} = (-1)^i J_{\mathrm{U(VI)}} \tag{6.1}$$

where j corresponds to the species, which is just Uranium (VI) in this case, i is the phase, with $i = 1$ being the aqueous phase and $i = 2$ being the organic phase, $D_{j,i}$ is the diffusion coefficient of species j in phase i, h is the position of the interface as shown in Figure 2.8 and $J_{\mathrm{U(VI)}}$ is the local mass flux (mol/(m^{2}s)) of Uranium (VI) generated at the interface because of the chemical reaction. For this first-order reaction with the above assumptions, the local flux at the fluid-fluid interface is given by:

$$J_{\mathrm{U(VI)}} = K_1\left[\mathrm{UO_2(Cl)_4}^{2-}\right] - K_{-1}\left[2\,\mathrm{R_4N^+}, \mathrm{Cl^-}\right] \tag{6.2}$$

where K_1 and K_{-1} (m/s) are the forward and reverse reaction kinetic constants respectively. The above equation can be rewritten as:

$$J_{\mathrm{U(VI)}} = K_1\left(\left[\mathrm{UO_2(Cl)_4}^{2-}\right] - \frac{1}{K_{\mathrm{eq}}}\left[2\,\mathrm{R_4N^+}, \mathrm{Cl^-}\right]\right) \tag{6.3}$$

where K_{eq} is the equilibrium kinetic constant, which is nothing but the ratio of the forward and reverse kinetic constants [3].

$$K_{\mathrm{eq}} = \frac{K_1}{K_2} \tag{6.4}$$

6.1.2. Dimensionless numbers

For this case of diffusion with a reaction at the interface, two dimensionless numbers can be used to describe the transport phenomena [4]. One is the Peclet number, which describes the ratio of the convective transport to the diffusive transport rate [10]. The formula for this number along the axial or x direction was given in Equation 2.36. For a microfluidic channel, the Peclet number along the transverse direction is given by:

$$Pe = \frac{Q}{DL} \tag{6.5}$$

where Q is the flow rate, L is the length of the channel and D is the diffusion coefficient. This equation can be further simplified for the 2D case [4]:

$$Pe_{2\mathrm{D}} = \frac{uH^2}{DL} \tag{6.6}$$

where u is the velocity of the fluid and H is the width of the channel. To quantify the competing influences of the interfacial reaction and diffusion, the Biot number

is used [4]. This number is given by:

$$Bi = \frac{K_1 H}{D} \tag{6.7}$$

The equilibrium kinetic constant (Equation 6.4) is also an important dimensionless number for mass transfer by reaction as it indicates the propensity of the reactants to form the products. In addition to these three dimensionless numbers, we define a new dimensionless number that looks at the influences of the interfacial reaction and convection. The Damkohler number is defined as the ratio of residence time to the reaction time scale [11]. For our case, the residence time is nothing but a convection time scale, so the convective Damkohler number (Da_c) is nothing but the ratio of the Biot and Peclet numbers.

$$Da_c = \frac{Bi}{Pe} = \frac{K_1 H L}{Q} \tag{6.8}$$

In the case of 2D, this equation simplifies to:

$$Da_c = \frac{K_1 L}{uH} \tag{6.9}$$

6.2. Experimental Methodology

The extraction efficiency of Gallium in a Zinc Nitrate-Chloroform mixture is studied both experimentally and numerically. Simulations are first used to validate the Finite Difference model and to study the experimentally observed transport phenomena. The 'step' design described in Chapter 5 is used here and the chips are manufactured using the same procedure described in that chapter. Before the mass transfer simulations are run, some data such as the diffusion coefficient and K_{eq} are required. Thus, this section describes the procedure for determining diffusion coefficients and K_{eq}, along with the experimental procedure for Gallium extraction. All the experiments described in this section were performed by Svenja Trapp.

6.2.1. Determination of Equilibrium Constant

K_{eq} is determined similarly to the procedure used in Ciceri *et al* [3]. In this case, the experiments were performed in batch and the concentrations were obtained. To illustrate how this method works, let us consider the reaction of Ga with N-benzoyl-N-phenylhydroxylamine (BPHA). It normally takes the form as shown below [12]:

$$Ga^{3+} + n(HL-) \longleftrightarrow GaL_3 + nH^+$$

L corresponds to the ligand (BPHA) which binds with the Gallium isotope to extract it to the organic phase and n corresponds to the stoichiometric number of BPHA. n is generally 3, but there is a possibility of multiple products being formed. To determine the dominant reaction and the value of n, we utilize the method adopted by Ciceri *et al* [3]. For the above reaction, K_{eq} is defined as:

$$K_{eq} = \frac{[GaL_3]_{eq}\left[H^+\right]^n_{eq}}{\left[Ga^{3+}\right]_{eq}[HL^-]^n_{eq}} \tag{6.10}$$

By plotting the ratio of $[GaL_3]_{eq} / \left[Ga^{3+}\right]_{eq}$ against $[HL^-]^n_{eq} / \left[H^+\right]]^n_{eq}$, K_{eq} can be obtained from the slope of the graph. But first, n has to be determined. Taking the log of equation 6.10 and rearranging, we obtain :

$$\log\frac{[GaL_3]_{eq}}{\left[Ga^{3+}\right]_{eq}} = n\log\,[HL^-]_{eq} + \log K_{eq} - n\log\,[H^+]_{eq} \tag{6.11}$$

Therefore, by plotting the ratio of the Gallium concentration in the organic and aqueous phases, and BPHA concentrations on the log scale, we can obtain the value of n from the slope.

For the batch experiments, a solution was first prepared consisting of 2 M $Zn(NO_3)_2$ (ACROS ORGANICS) and 1 µM $Ga(NO_3)_2$ in 0.01 M HNO_3 (Merck Sigma). A Ga-68 radiotracer (eluted from an Eckert Ziegler IGG100 GMP Ge-68/Ga-68-generator, supplied by Erasmus MC) was added at a concentration of 30 kBq/mL to the solutions. The organic solution consisted of BPHA (CAS: 304-88-1; ACROS ORGANICS) with varying concentrations between 1 and 200 mM in chloroform (Merck Sigma).

Aqueous and organic solutions were pipetted at equal volumes into Eppendorf vials and shaken on a Vortex mixer (Vortex-Genie 2; Scientific Industries) for 1 h to reach equilibrium. Afterwards, the aqueous and organic solution were pipetted into separate vials and measured separately for their Ga-68 radioactivity (representative of the total Ga concentration) with a Wallac Wizard 2 3" 2480 Automatic Gamma Counter (Perkin Elmer) and the results corrected for decay. Experiments were performed in triplicate and errors are given as one standard deviation of the mean.

6.2.2. Determination of Diffusion Coefficient

The method proposed by Milozic *et al* [13] is used to determine the diffusion coefficients. Here, a combination of experiments and simulations are used. Experiments are performed at different flow rates in a Y-Y microfluidic channel of dimensions 1.2cm x 1mm x 50 µm. Two solutions were prepared, one solution only containing 2 M Zn(NO3)2 in 0.01M HNO3 and one including 1 µM Ga(NO3)2 and a Ga-68 radiotracer at 100 kBq/mL. Both solutions were loaded into syringes and introduced to the microfluidic chip with AL-1000 Programmable Syringe Pumps (941-371-1003; World Precision Instruments Inc). The two solutions were pushed through the microfluidic chip with varying flow rates of 5 – 30 µL/min. At the outlets, the solutions were collected and next, measured with the Wallac Wizard2 3" 2480 Automatic

Gamma Counter (Perkin Elmer). The results were corrected for decay and the concentrations at the outlets were obtained. These experiments were done in triplicate and errors were given as one standard deviation of the mean.

The obtained experimental concentrations were then fed to the Finite Difference Code described in Chapter 2 and Equation 2.38 is solved. The flow profile is directly obtained from the analytical Poiseuille solution [14] for single-phase flow. The diffusion coefficient is unknown, but the outlet concentrations are known. Thus, the diffusion coefficient is varied in the code until converged results that match the experiments are obtained. This procedure is repeated for the other flow rates and the diffusion coefficient is then determined by averaging the values obtained from all the simulations.

6.2.3. Ga-68 Extraction

Microfluidic extractions of Ga-68 were performed in a Y-Y microfluidic channel with a step (Chapter 5) and nano-layer coating as described in Trapp et al. (2024). The dimensions of the channel are 1.2 cm * 1 mm * 50 µM/100 µM. The aqueous phase was prepared by adding 100 kBq/mL Ga-68 to a 2 M $Zn(NO_3)_2$ in 0.01M HNO_3 solution, and the organic extracting phase consisted of 0.2 M BPHA in chloroform. Both solutions were loaded into separate syringes and introduced to the chip with syringe pumps at varying flow rates. The aqueous ($C_{\mathrm{aq,o}}$) and organic phase ($C_{\mathrm{or,o}}$) were collected at the outlets, subsequently measured for their Ga-68 content with the Wallac gamma counter and corrected for decay. The extraction efficiency is calculated as follows:

$$\mathrm{EE} = \frac{C_{\mathrm{or,o}}}{(C_{\mathrm{or,o}} + C_{\mathrm{aq,o}})} \times 100 \tag{6.12}$$

For the simulations, the convection-diffusion equation described by Equation 2.37 is solved and the interfacial reaction condition described in Section 6.1 is applied for the Gallium reaction at the interface.

6.3. Fluid Properties for simulations

The simulations use the same fluids of Helle *et al* [9], where Uranium isotope was extracted from an aqueous HCl solution to n-dodecane solution. The properties of the fluids along with the diffusion coefficient of Uranium are described in Table 6.1. Since the contact angle is unknown, it is assumed to be 90 °.

6.4. Numerical Simulations

Numerical simulations are performed to understand the influence of the dimensionless number described in Section 6.1.2 on the transport phenomena. The Finite Difference Method is used for simulating mass transfer as described in Chapter 2.

Table 6.1: Flow, Diffusion and Kinetic properties used in the simulations

Property	Aqueous Phase	Organic Phase
Density (kg/m^3)	1081	750
Viscosity (mPas)	1.27	1.48
Surface Tension (mN/m)	29.83	-
Diffusion Coefficient (m^2/s)	10^{-8}	10^{-9}
K_1 (m/s)	1.6×10^{-5}	-
K_{eq}	-	5.91

The simplified Convection-Diffusion equation (CDE) described in Equations 2.38 and 2.37 is used once again. The flow profile is obtained from the modified RK model. The mass transfer simulations are performed in the rectangular channel shown in Figure 2.8, with the dimensions of the channel being 8 cm $\times$ 100 μm $\times$ 40 μm.

First, the model needs to be validated by comparing it with the results of Helle *et al* [5]. Helle *et al* also simulated mass transfer using a Finite Difference model and compared the extraction efficiencies with their experiments. Our simulations are compared with their simulation data. RK simulations are run for Q_{aq} = 1.56 μL/min and Q_{org} = 1.38 μL/min, where Q is the flow rate and the subscripts aq and org correspond to aqueous and organic phases respectively. After obtaining the flow profile, mass transfer simulations are run for the kinetic and diffusion parameters described in Table 6.1.

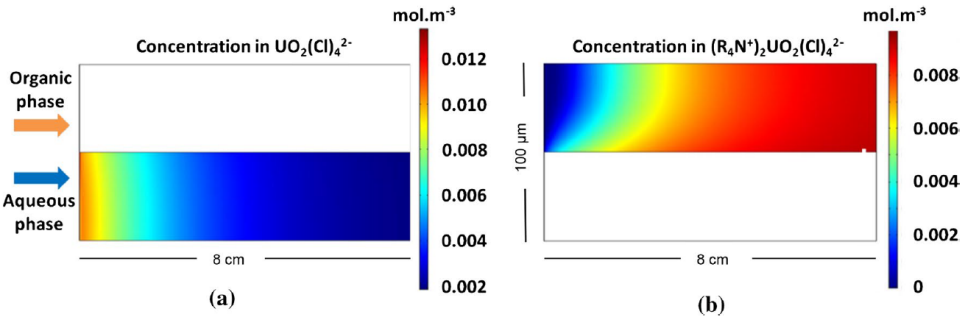

Figure 6.1: Concentration profile in the aqueous and organic phases as obtained by Helle *et al* [9] at Q_{aq}= 1.56 μL/min and Q_{org} = 1.38 μL/min. a)Aqueous Concentration Profile b)Organic Concentration Profile

The concentration profiles obtained from Helle *et al* [9] and our simulations are shown in Figures 6.1 and 6.2. In the case of Helle *et al*, the interface is exactly at the centre of the channel while ours is slightly shifted downwards. One reason for this is that the contact angle used in Helle *et al*'s experiments is unknown, so we ran simulations at a contact angle of 90 ° and determined the extraction efficiency

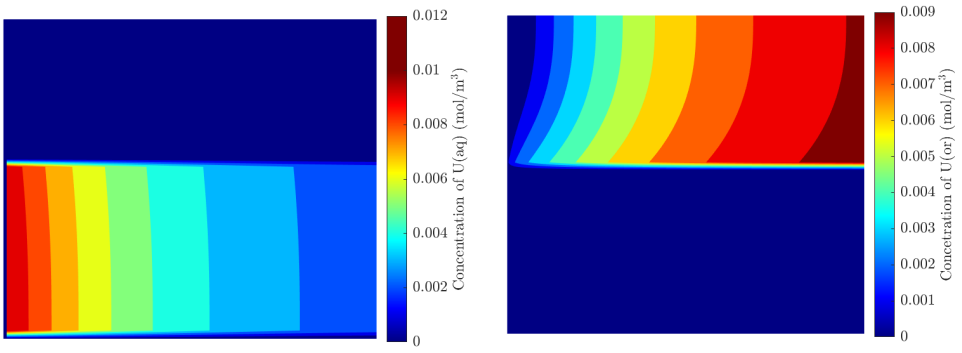

Figure 6.2: Simulated concentration profiles using the data from Helle *et al* [9] at Q_{aq}= 1.56 μL/min and Q_{org} = 1.38 μL/min. a)Aqueous Concentration Profile b)Organic Concentration Profile

using the same formula described in Equation 6.12. The extraction efficiency from our simulation is 76.95 % while the extraction efficiency obtained by Helle *et al* is 76.3 %. As the extraction efficiencies are very close, we can conclude that the model has been validated.

6

For the following simulations on the influence of dimensionless numbers, we use the analytical Poiseuille solution for the velocity [14] in 2D instead of using the RK model to determine the flow profile. An advantage of using the analytical solution is that we can fix the position of the interface to lie exactly at the centre of the channel, instead of adjusting the contact angle in the RK simulations to determine the appropriate contact angle that matches Helle *et al*'s experiments. The velocity profiles of the two fluids in 2D are given by [15]:

$$\begin{cases} v_{\text{aq}} = -\frac{y(h^2(\mu_{\text{org}}-\mu_{\text{aq}})-yH\mu_{\text{aq}}+H^2\mu_{\text{aq}}-yh(\mu_{\text{org}}-\mu_{\text{aq}}))}{2(h(\mu_{\text{org}}-\mu_{\text{aq}})+H\mu_{\text{aq}})\mu_{\text{aq}}}\nabla P \quad \text{for } 0 < y < h, \\ v_{\text{or}} = -\frac{(H-y)(Hh(\mu_{\text{org}}-\mu_{\text{aq}})+yH\mu_{\text{aq}}-h^2(\mu_{\text{org}}-\mu_{\text{aq}})+yh(\mu_{\text{org}}-\mu_{\text{aq}}))}{2(h(\mu_{\text{org}}-\mu_{\text{aq}})+H\mu_{\text{aq}})\mu_{\text{aq}}}\nabla P \quad \text{for } h < y < H \end{cases} \tag{6.13}$$

where v is the velocity of the fluid with the subscripts aq and org corresponding to aqueous and organic phases respectively, h is the position of the interface, H is the width of the channel, μ is the viscosity, and ∇P is the imposed pressure gradient which remains constant across the channel. The influence of surface tension and contact angle is absent from these equations, and as both these quantities have a role to play in the position of the interface, the analytical flow profile is an approximation. Despite this, it can be useful in studying the effect of the dimensionless numbers on the transport phenomena as the interface position can be fixed. If the flow rate of one fluid per unit depth and the position of the interface is fixed, the pressure gradient and the flow rate of the other fluid per unit depth can be determined using the following formulae [15]:

$$\begin{cases} Q_{\text{aq}} = \int_0^h v_{\text{aq}} dy \; = -\frac{h^2(h^2\mu_{\text{org}} - h^2\mu_{\text{aq}} - 2Hh\mu_{\text{aq}} + 3H^2\mu_{\text{aq}})}{12(\mu_{\text{org}}h - \mu_{\text{aq}}h + \mu_{\text{aq}}H)\mu_{\text{aq}}} \nabla P \\ Q_{\text{org}} = \int_h^H v_{\text{org}} dy \\ = -\frac{(4\mu_{\text{org}}hH^3 - \mu_{\text{org}}h^4 - 4\mu_{\text{aq}}hH^3 + \mu_{\text{aq}}h^4 + \mu_{\text{aq}}H^4 - 4\mu_{\text{aq}}Hh^3 - 9\mu_{\text{org}}h^2H^2 + 6\mu_{\text{aq}}h^2H^2 + 6\mu_{\text{org}}Hh^3)}{12\mu_{\text{org}}(\mu_{\text{org}}h - \mu_{\text{aq}}h + \mu_{\text{aq}}H)} \nabla P \end{cases} \tag{6.14}$$

where Q is the 2D flow rate. We test this analytical profile using the data of Helle *et al*[9] for the profiles shown in Figure 6.1. Q_{aq} is fixed at 1.56 μL/min, but instead of fixing Q_{org}, we fix $h = H/2$. Since the influence of surface tension and contact angle is neglected, the analytical formula should give a different value of Q_{org} than the experiments. This is indeed the case, as we obtain Q_{org} of 1.5 μL/min, as opposed to Q_{org} = 1.38 μL/min used in Helle *et al's* [9] experiments. For this flow configuration, we plot the concentration profiles in Figure 6.3 as there is only a slight difference in the flow rates. An extraction efficiency of 76.3 % was obtained, which is very close to the value of 76.1 % obtained by Helle *et al* in their experiments.

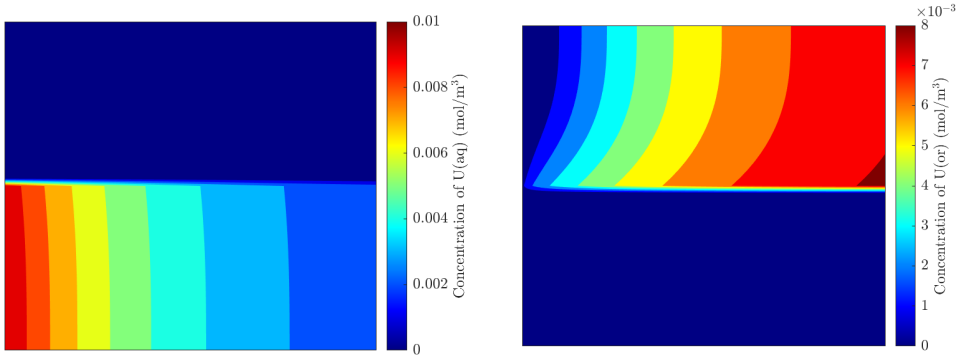

Figure 6.3: Simulated concentration profiles using the data from Helle *et al* [9] and the analytical flow profile defined in Equation 6.13. Q_{aq}= 1.56 μL/min , $h = H/2$, Bi_{aq}=0.16,Bi_{or}=1.6, Pe_{aq}=0.081, Pe_{or}=0.78. a)Aqueous Concentration Profile b)Organic Concentration Profile

6.4.1. Effect of Bi,Pe and K_{eq}

The influence of the Biot and Peclet numbers on extraction efficiency is studied in this subsection. The microfluidic channel used by Helle *et al* [9] is used here, with the parameters the same as that described in Table 6.1 unless otherwise stated. We vary the Bi by varying K_1 (Equation 6.7) as changing D or H also influences the Peclet number (Equation 6.6). K_{eq} remains the same for all Bi (K_{eq}=5.9). The flow rate of the aqueous phase is the same as the one used in Figures 6.2 and 6.1 (Q_{aq} = 1.56 μL/min), with the position of the interface fixed at the middle of the channel.

Similarly, we vary the Pe number by varying either the velocity or length of the channel to ensure that only the Pe, and not the Bi number, is changed. The interface position is fixed at the middle of the channel regardless of the flow rate. The extraction efficiencies are determined and the results are plotted for varying Pe and Bi in Figure 6.4a.

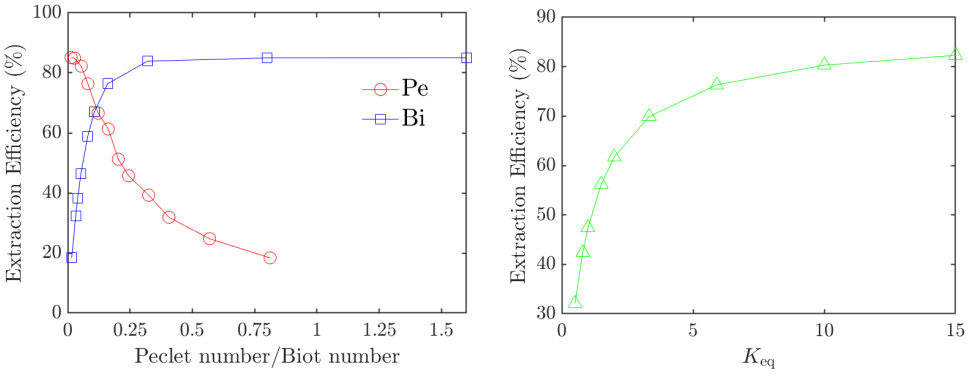

Figure 6.4: Influence of a) Peclet and Biot numbers, and b) K_{eq} on the extraction efficiency in the microfluidic channel used by Helle *et al* [9]. Bi is varied by changing K_1, Pe by changing the flow rate/velocity and K_{eq} is varied by changing K_2. The Peclet and Biot number of the aqueous phase is shown here.

As expected, a larger Bi and a smaller Pe number leads to large extraction efficiencies. A fast reaction ensures that the Uranium product forms quickly, and a lower velocity allows for more time for Uranium to diffuse towards the reactive interface [4, 16]. At high Pe numbers, Uranium does not have enough time to diffuse to the interface.

From Figure 6.4a, we can see that saturation in extraction efficiency is observed after Bi_{aq} =0.32. At such Bi numbers, the system is now diffusion-limited, and a higher extraction efficiency can be obtained only when we operate at smaller Pe numbers. Similarly, at low Pe numbers, saturation is observed as the system is now reaction-limited [16].

Finally, the influence of K_{eq} on the extraction efficiency is plotted in Figure 6.4b. K_{eq} is varied by only changing K_2, thereby ensuring that the Biot number remains the same (Bi_{aq}=0.16 and Pe_{aq}=0.081). As expected, a higher K_{eq} results in a higher extraction efficiency, and this is because there is a greater propensity for the formation of the Uranium complex in the organic phase.

6.4.2. Effect of Da_c

Influence of Diffusion Coefficient

A higher Da_c is preferred for efficient mass transfer because this corresponds to a higher Bi or/and lower Pe. From Equation 6.8, we can see that Da_c increases as we increase K_1 and decreases with increase in velocity. These two parameters affect both Bi and Pe as well (Equations 6.7 and 6.6), therefore, to understand the influence of Da_c, the diffusion coefficient and width of the channel are varied. The diffusion coefficient affects both Pe and Bi, but Da_c remains the same. The influence of the diffusion coefficient on the extraction efficiency is tabulated in Table 6.2, along with the various dimensionless numbers.

Table 6.2: Influence of diffusion coefficient of aqueous and organic on extraction efficiency

D_{aq} (m^2/s)	D_{org} (m^2/s)	Pe_{aq}	Pe_{org}	Bi_{aq}	Bi_{org}	$Da_{c,aq}$	$Da_{c,org}$	EE(%)
10^{-7}	10^{-8}	0.0081	0.078	0.016	0.16	1.98	2.05	77.27
10^{-7}	10^{-9}	0.0081	0.780	0.016	1.60	1.98	2.05	76.71
10^{-8}	10^{-9}	0.0810	0.780	0.160	1.60	1.98	2.05	76.31
10^{-8}	10^{-8}	0.0810	0.078	0.160	0.16	1.98	2.05	76.94
10^{-8}	10^{-10}	0.0810	7.800	0.160	16.0	1.98	2.05	70.87
10^{-9}	10^{-9}	0.8100	0.780	1.600	1.60	1.98	2.05	72.95
10^{-9}	10^{-8}	0.8100	0.078	1.600	0.16	1.98	2.05	73.51
10^{-9}	10^{-10}	0.8100	7.800	1.600	16.0	1.98	2.05	67.87
10^{-9}	10^{-8}	0.8100	0.078	1.600	0.16	1.98	2.05	73.52

It appears that the diffusion coefficient has little impact on the extraction efficiency, as the obtained values in Table 6.2 are very close to each other. In Figure 6.4a, we observed that a low Pe or high Bi number results in a higher extraction efficiency. When the diffusion coefficient is high, the Pe number is lower but so is the Bi number. The table covers the regions of low Pe and low Bi number, high Pe and high Bi number, and regions where the Pe and Bi numbers are neither high nor low. This is why Da_c is a useful dimensionless number for understanding transport phenomena. From Table 6.2, it can be seen that Da_c remains constant even though Bi and Pe keep changing, and this is because Da_c is independent of the diffusion coefficient (Equation 6.9).

The above results could be very useful in extraction studies for parallel flow when the diffusion coefficient is unknown. However, the obtained results do not mean that the diffusion coefficient has no influence altogether. The impact of the diffusion coefficient is more clearly observed in the concentration profiles. Figure 6.5 shows the concentration profiles of the fluids when D_{aq}= 10^{-7} m^2/s, D_{aq}= 10^{-8} m^2/s and D_{aq}= 10^{-9} m^2/s, D_{aq}= 10^{-10} m^2/s, and these can be compared with Figure 6.3, where the actual experimental diffusion coefficients were used. When the diffusion coefficient is higher, the concentration gradients are less steep and more evenly dispersed. On the other hand, for lower diffusion coefficients, Uranium is

concentrated near the interface in the organic fluid. Therefore, the diffusion coefficient influences the absolute distribution of Uranium, but has a low influence on the overall extraction efficiency in parallel flow-based mass transfer.

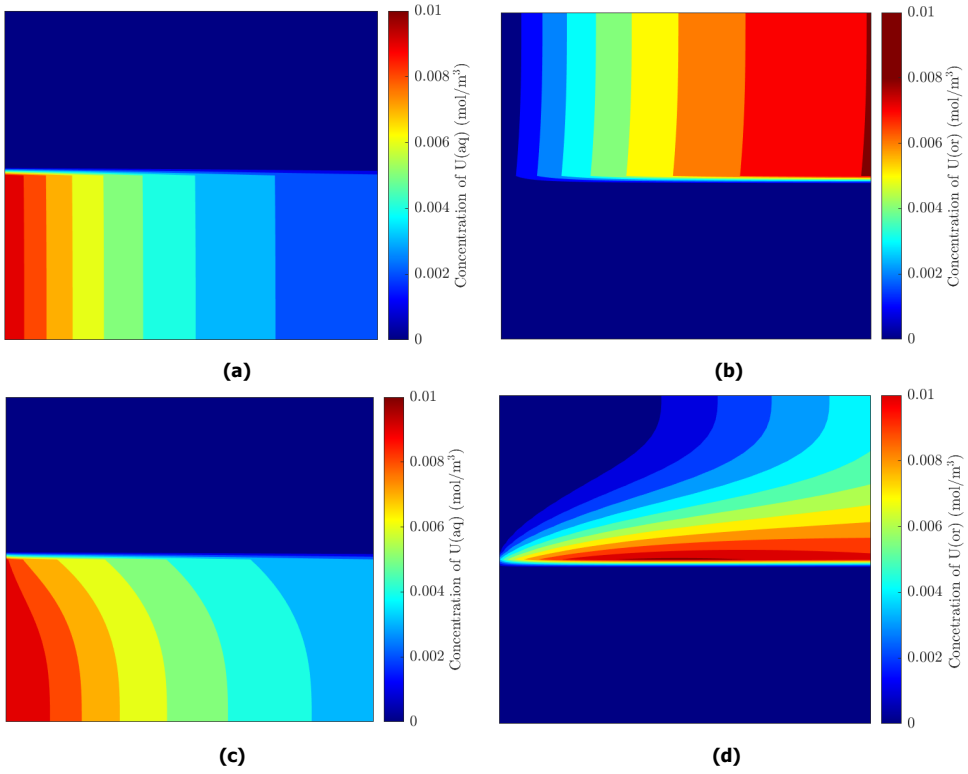

Figure 6.5: Simulated concentration profiles using the data from Helle *et al* [9] but altering the diffusion coefficient such that a),b) D_{aq}= 10^{-7} m^2/s, D_{aq}= 10^{-8} m^2/s and c),d) D_{aq}= 10^{-9} m^2/s, D_{aq}= 10^{-10} m^2/s.

Table 6.2 showed that the diffusion coefficient has little impact on the extraction efficiency. To check if Da_c has the maximum influence on extraction efficiency, we vary the channel width H in the next section.

Influence of the Channel Width

Numerous papers have studied the influence of the channel width on extraction efficiency for parallel flow [17, 18, 19], and the overall conclusion of all these papers is that the extraction efficiency decreases with an increase in width. The larger interfacial area resulting from the larger width has been attributed as the main reason for this observation as this increases the diffusion time (The channel width is along the y direction as shown in Figure 2.8). While this reason is indicative of what happens in channels with larger widths, it doesn't provide the full picture as

the dimensionless numbers are not included in the discussion. From Equations 6.6 and 6.7, we can see that both the Peclet and Biot number are influenced by the width, though Pe ∝ H^2 while Bi ∝ H. This means that if the average velocity remains constant in channels of different widths, the extraction efficiency should decrease with an increase in width, as the Pe number increases quicker than the Bi number.

Table 6.3: Influence of channel width on the extraction efficiency when average velocity is kept constant at v_{aq}=0.0138 m/s and v_{org}=0.011 m/s

Width(μm)	**Pe_{aq}**	**Pe_{org}**	**Bi_{aq}**	**Bi_{org}**	**$Da_{c,aq}$**	**$Da_{c,org}$**	**EE(%)**
50	0.0202	0.195	0.08	0.8	3.950	4.100	84.38
100	0.0810	0.780	0.16	1.6	1.980	2.050	76.31
200	0.3240	3.120	0.32	3.2	0.990	1.025	56.41
300	0.7290	7.090	0.48	4.8	0.660	0.680	42.31
400	1.2960	12.48	0.64	6.4	0.495	0.512	33.72
500	2.0250	19.50	0.80	8.0	0.395	0.410	27.79
600	2.9160	28.08	0.96	9.6	0.333	0.343	23.65

Table 6.3 confirms our expectations of the extraction efficiency reducing with increasing width, as long as the average velocity remains the same. It also shows how the extraction efficiency changes with Da_c, as a higher Da_c corresponds to a higher extraction efficiency. So we run simulations in channels of different widths with the flow rates of the fluids per unit depth (uH) being constant, thus changing the average velocity accordingly and keeping Da_c constant.

Table 6.4: Influence of channel width on the extraction efficiency when the flow rate is kept constant, and thus Da_c is also constant

Width (μm)	**Pe_{aq}**	**Pe_{org}**	**Bi_{aq}**	**Bi_{org}**	**$Da_{c,aq}$**	**$Da_{c,org}$**	**EE(%)**
50	0.0405	0.39	0.08	0.8	1.98	2.05	76.88
100	0.0810	0.78	0.16	1.6	1.98	2.05	76.31
200	0.1620	1.56	0.32	3.2	1.98	2.05	74.91
300	0.2430	2.34	0.48	4.8	1.98	2.05	73.27
400	0.3240	3.12	0.64	6.4	1.98	2.05	72.64
500	0.4050	3.90	0.80	8.0	1.98	2.05	71.56
600	0.4860	4.68	0.96	9.6	1.98	2.05	70.51

Extraction Efficiency Correlation

Using dimensionless analysis, the extraction efficiency for interfacial mass transfer in a Y-Y microfluidic channel can be expressed as follows:

$$EE = f(Pe, Bi, Gz) = c_2 Pe^{\alpha} Bi^{\beta} Gz^{\gamma} \tag{6.15}$$

where c_2 is a constant and Gz is the Graetz number shows the lateral penetration of the isotope across the width of the channel H[16]. Tables 6.2 and 6.4 showed that the extraction efficiency remains approximately the same even though the diffusion coefficient and, channel height and u are changed. This implies that $\alpha = -\beta$, therefore Equation 6.15 can be simplified to:

$$EE = c_2 Gz^{\gamma} Da_c^{\beta} \tag{6.16}$$

Since Gz is not observed to have an impact on the the extraction efficiency (Tables 6.2 and 6.4), Equation 6.16 can therefore be simplified to the following form:

$$EE = cDa_c^{\beta} \tag{6.17}$$

We now plot the extraction efficiency against Da_c to observe if it follows the above relation. From Figure 6.6, we can see that Equation 6.17 is followed for all the Da_c, but the values of c and β are different for different regions. For Da_c>1, the extraction efficiency increases significantly with the Da_c. The increase in extraction efficiency is reduced for 2<Da_c<5, which appears to be a transition region, and then a saturation in the extraction efficiency is observed for Da_c>5. At low Da_c, not all the reactants have reacted as either the reaction rates are low, or they leave the chip early because of a high flow rate. As Da_c increases, more reactants react quickly at the interface and therefore, more of the isotope is transferred to the organic phase. At a large Da_c, most of the reactants have already reacted, so much so that even a low flow rate has a minimal impact. It must be stressed that these results are only valid for this standard channel.

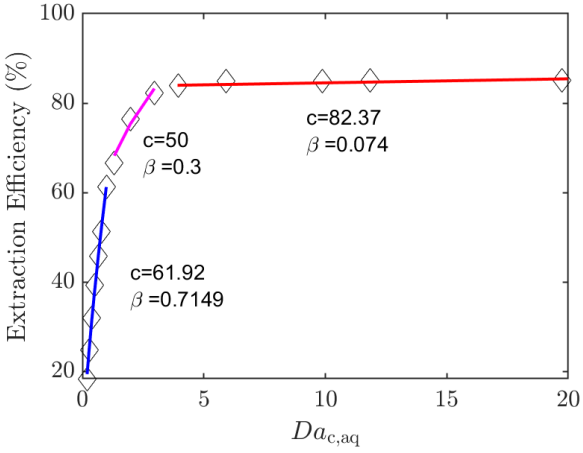

Figure 6.6: Influence of Da_c on the extraction efficiency. The aqueous Da_c is shown in the x-axis and the data is fitted using curves to observe the trend.

To summarize, Tables 6.2, 6.3 and 6.4 show the influence of Da_c on the extraction efficiency. A higher extraction efficiency is obtained at a higher Da_c, and if Da_c

does not change, the extraction efficiency is less affected regardless of whether the Pe or Bi number changes.

6.5. Ga Extraction - Experiments and Simulations

The previous simulations were conducted in a standard channel only. Considering the utility of the step channel studied in Chapter 5, it is important to understand the mass transfer phenomena in a step channel as well. This section thus looks at the results from the Gallium extraction experiments and the factors that govern the mass transport phenomena using simulations. The basic idea is to extend the results we have discussed in our simulations to a larger channel and a different radioisotope, while also testing the capability of the simulation technique to capture the mass transfer phenomena in a step channel. Additionally, mass transfer in a step channel has only been studied experimentally, and though Helle *et al* [9] performed mass transfer simulations on a step channel, they did not compare their results with experiments. Running simulations using the finite difference method will also examine the capability of the technique to be extended to different channels.

As discussed in Section 6.2, Gallium was extracted from 2 M $Zn(NO_3)_2 \cdot 6\,H_2O$ to chloroform solution in a step channel with dimensions 1.2cm × 1000 μm × 100/50 μm. First, K_{eq} and the diffusion coefficient of Gallium in water is determined. The analytical solution shown in Equation 6.13 is no longer valid for the step channel, so RK simulations are run to obtain the flow profile. The flow profile is then fed to the Finite Difference code for mass transfer and the extraction efficiencies are determined. The extraction efficiencies are compared with the experiments, followed by an understanding of the transport mechanisms of Gallium.

6.5.1. Determination of K_{eq}

Before we determine the value of K_{eq}, the dominant reaction and stoichiometric ratio of Gallium and BPHA need to be determined first. Using the procedure described in Section 6.2.1, we first plot the ratio of Gallium concentrations in the organic and aqueous phases, and the BPHA concentration on the log scale in Figure 6.7.

From Figure 6.7 and Equation 6.11, we can see that the best fit is observed for n=2.5. However, a stoichiometric ratio of 1:2.5 has not been observed in literature. The common reactions for Ga with BPHA generally have a stoichiometric ratio of 1:3 or 1:1 [12]. Since n=2.5 is closer to n=3, we take the reaction to have a stoichiometric ratio of 1:3. Ga also exists in the form of Ga^{3+}, so this stoichiometric ratio is also the most logical option (Equation 6.11). Using n=3, we plot the concentrations of all the compounds involved and use the slope of the graph to determine K_{eq} according to Equation 6.10.

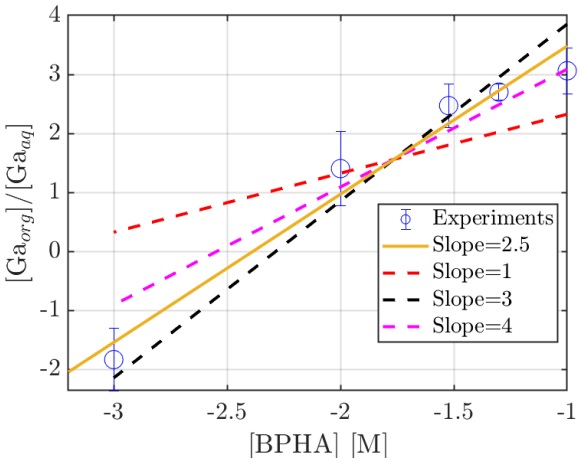

Figure 6.7: Determination of stoichiometric ratio by fitting lines of slopes 1,2,2.5 and 3.

Figure 6.8 shows that most of the points lie on a straight line with a line equation as described in the figure, which justifies our assumption of using n=3. The obtained equilibrium constant is 6.46 $\pm$ 0.72.

6

6.5.2. Determination of Diffusion Coefficient

Single-phase diffusion experiments of Gallium in 2 M $Zn(NO_3)_2 \cdot 6\,H_2O$ (aqueous phase) are performed and the diffusion coefficient is determined from the outlet concentrations using the same procedure described in Section 6.2.2. The diffusion coefficients are obtained for varying flow rates and plotted in Figure 6.9.

The diffusion coefficient is expected to be constant regardless of the flow rate and only varies with temperature [20]. However, in Figure 6.9, the diffusion coefficient varies considerably with the flow rate. This variation in diffusion coefficient with flow rate was also observed by Binda *et al* [21], who used the same microfluidics technique to estimate the diffusion coefficient. A possible reason for this is the fluctuating flow rates and pressure differences observed in syringe pumps [22, 23]. While the average flow rate remains the same as the value used in the analytical solution, these fluctuations might result in discrepancies in local concentration gradients and mass transfer.

Table 6.2 indicated that the diffusion coefficient hardly has any influence on the extraction efficiency. Therefore, for our purposes, we determine the average of the diffusion coefficients from Figure 6.9 (9.61 $\pm$ 0.39 $\times$ 10^{-10} m^2/s) and use it in our simulations. The diffusion coefficient of Ga in chloroform is difficult to determine as chloroform evaporates when collected at the outlets. Mass transfer simulations are, therefore, performed only for the 2 M $Zn(NO_3)_2$ solution, and the extraction efficiency is calculated based on the amount of Gallium lost from the 2 M $Zn(NO_3)_2$

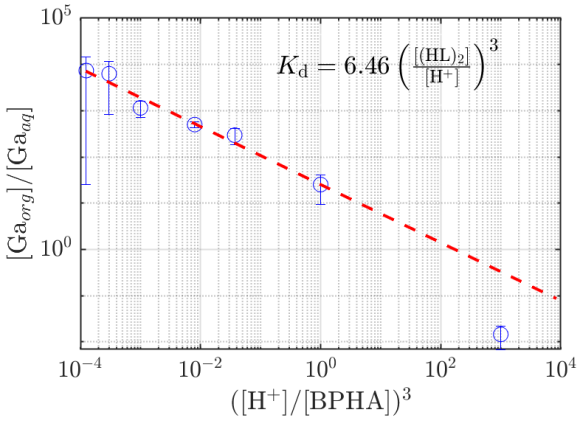

Figure 6.8: Determination of K_{eq} using Equation 6.10. K_d is the ratio of Gallium concentration in the organic and aqueous phases respectively.

solution according to the following formula:

$$EE = \frac{C_{\text{aq,inlet}} - C_{\text{aq,outlet}}}{C_{\text{aq,inlet}}} \tag{6.18}$$

To test if this methodology is valid and to observe if the diffusion coefficient of the organic phase has any influence, we performed simulations only for the aqueous phase using the data of Helle *et al* [9] (Table 6.1) shown in Figures 6.1 and 6.2 for the Uranium isotope. Extraction efficiency is calculated using Equation 6.18 and diffusion in the organic phase is not considered. An extraction efficiency of 76.95 % was obtained, which is the exact value that was obtained even when diffusion in the organic phase was considered. This is because the reaction does not occur in either the aqueous or organic phases, but at the fluid interface. The diffusion coefficient of the organic phase is needed only to visualize the concentration profile. Therefore, we only perform simulations in the aqueous phase for the gallium extraction experiments in the step channel.

6.5.3. Transport Properties

The fluid properties, along with the diffusion coefficient and K_{eq}, used in the Gallium extraction experiments and simulations are listed in Table 6.5. K_1 is unknown, and it is determined using a similar procedure used by Helle *et al* [9] as described in Section 6.5.4. A step channel of dimensions 1.2 cm × 1 mm × 100/50 μm is used in the simulations and experiments, with chloroform occupying the shallower channel as it is less viscous than the aqueous phase.

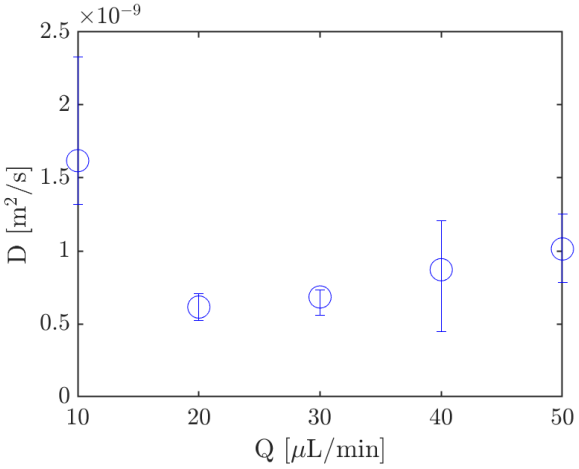

Figure 6.9: Diffusion coefficient of Gallium in 2 M $Zn(NO_3)_2 \cdot 6\,H_2O$ for various flow rates

Table 6.5: Flow, diffusion and kinetic properties used in the Ga extraction experiments and simulations

Property	Aqueous Phase	Organic Phase
Density (kg/m^3)	1400	1500
Viscosity (mPas)	1.9	0.6
Surface Tension (mN/m)	16.52	-
Diffusion Coefficient (m^2/s)	9.602×10^{-10}	-
K_1 (m/s)	3×10^{-5}	-
K_{eq}	-	6.46

6.5.4. Ga Extraction

Ga extraction experiments were conducted for different flow rates using the procedure described in Section 6.2.3. The flow rates of the aqueous and organic phases were kept the same. First, RK simulations were run for the step channel and the fluids described in Table 6.5. Both the phase contour and velocity profile in the main channel are plotted in Figure 6.10 at a flow rate $Q = 15\mu$L/min.

Since the extraction efficiencies are known from the experiments, and K_{eq} and the diffusion coefficient are known, K_1 is varied until the simulated extraction efficiency matches the experimental extraction efficiency for a particular flow rate. To check if the determined K_1 is correct, simulations are run with this K_1 at different flow rates and compared with the experimental data.

From Figure 6.10, we can see that the interface is diffuse. To determine the exact position of the interface, the mass transfer simulations based on the FD scheme

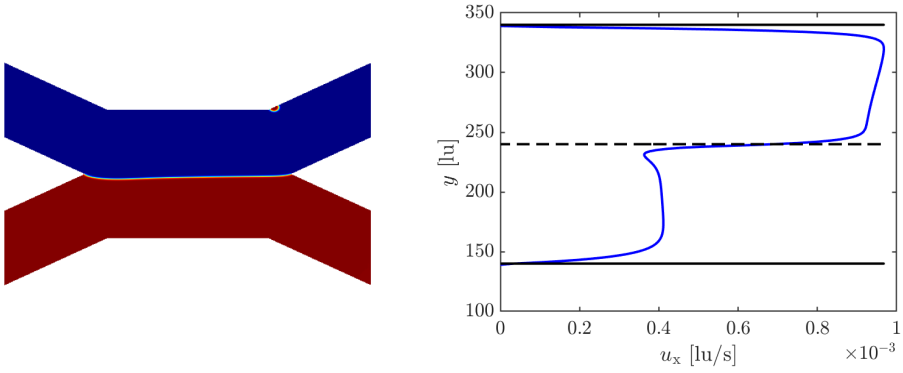

(a) (b)

Figure 6.10: RK simulations of the Zinc Nitrate solution and chloroform in a step channel at $Q = 15\mu$ L/min. a) Phase Contour, with the red fluid being Zinc Nitrate solution and the blue fluid being chloroform. b) Velocity profile in the main channel at a height of 25 μm.

are performed on a finer grid with a resolution of 2.5 μm, as opposed to the RK simulations which were performed on a grid with a resolution of 5 μm. Based on the value of ρ_N (Equation 2.17), the position of the interface is determined on the new grid for mass transfer. Basically, the fluid at each node is given by:

$$\rho_N \begin{cases} > 0, & \text{Zinc Nitrate Solution} \\ < 0, & \text{Chloroform} \end{cases} \tag{6.19}$$

In the RK simulations, there is no node where ρ_N=0, which would correspond to the position of the interface. Therefore, if we conduct mass transfer simulations on a finer grid, we could find the position of the interface based on interpolation. This means that the interface is located at the grid point in the finer grid based on the following condition:

$$\text{If} \begin{cases} \rho_N > 0 & \text{at } x = x_i \\ \rho_N < 0 & \text{at } x = x_{i+1} \end{cases} \text{ then } \rho_N = 0 \text{ at } x = x_{i+\frac{1}{2}} \tag{6.20}$$

The velocities at these intermediate nodes are also determined by interpolation.

Once the experimental extraction efficiencies were obtained, simulations were run for $Q = 10\mu$L/min to determine the value of K_1 such that the simulated and experimental extraction efficiencies are within 10 % of each other. After this, simulations were run for the remaining flow rates at $K_1 = 3 \times 10^{-5}$ m/s and compared with the experiments in Figure 6.11.

Since the error associated with the diffusion coefficient is high, we also conduct simulations at the upper and lower limits of the measured diffusion coefficient. Like the results observed in Table 6.2, the diffusion coefficient appears to have little im-

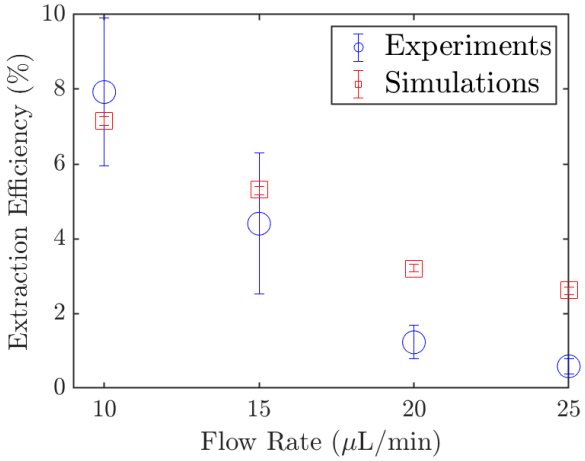

Figure 6.11: Comparison of Gallium extraction experiments (circles) and simulations (squares) for a Zinc Nitrate - Chloroform mixture at different flow rates. The error bars for the experiments correspond to the standard deviation of the mean. In the case of simulations, the error bars represent the errors in extraction efficiency corresponding to the errors in diffusion coefficient measurements.

pact on the extraction efficiency (Figure 6.11). This confirms our observations on the importance of Da_c as it remains constant.

The simulation results are well within the bounds of the experimental extraction efficiencies for $Q = 10$ and 15 μL/min. However, the simulations appear to overestimate the extraction efficiencies at higher flow rates. One reason is the fluctuations in the flow rate in the pump [22, 23]. A secondary reaction could also be taking place as our estimations showed n to be 2.5 instead of 3 (Figure 6.4). Additionally, at higher flow rates, waves are introduced in the interface (Figures 6.12) than that observed at lower flow rates (Figure 6.10). Figure 6.12 even shows periodic leakage at $Q = 20\mu$L/min in the form of droplets. We don't know if this periodic leakage was observed in the experiments, as no cameras were used to visualize the flow. The purity of the liquids collected at the outlet was measured and these measurements didn't show any contamination or leakage. Even if no leakage is observed in the experiments, the simulations clearly show that the interface position keeps oscillating over time, therefore the assumption of a straight interface is not valid for higher flow rates.

Finally, most papers have compared their simulations for interfacial mass transfer with experiments in a standard channel [3, 4, 24, 9]. Few simulations in literature are available for the step channel, so we do not know if flow phenomena such as the stability of the interface have been adequately captured by the simulations. Even though Helle *et al* [9] used a step channel in their simulations for Europium, they didn't compare these results with experiments. The velocity profile along the main channel doesn't follow a Poiseuille flow profile like that in a standard channel

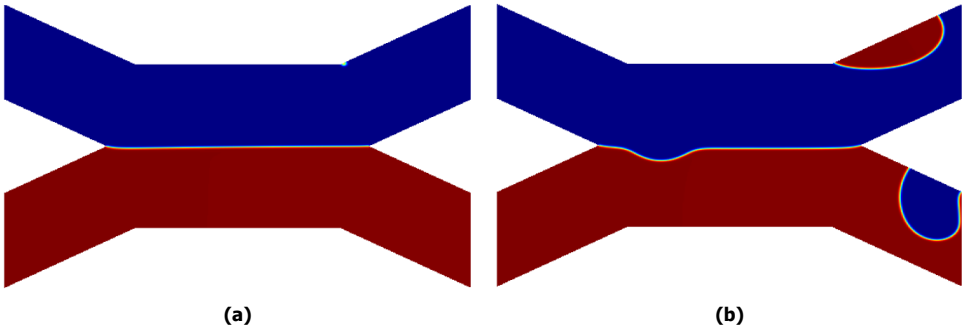

Figure 6.12: RK simulations of Zinc Nitrate solution and chloroform in a step channel at $Q = 20\mu$L/min. a) Phase Contour at t=3.7 ms. b) t= 0.26 s

(as discussed in Chapter 5), so discrepancies in the velocity profile are expected. Despite these differences, the simulated extraction efficiencies are of the same order as the experimental results, which shows that the simulations are capable of capturing the transport phenomena.

To understand if the Gallium extraction is diffusion or reaction-limited, the Biot and Peclet numbers are varied and their effect on the extraction efficiency is studied. First, the Biot number is varied by varying K_1, along with the Da_c at a flow rate of 10 μL/min and the extraction efficiencies are plotted in Figure 6.13.

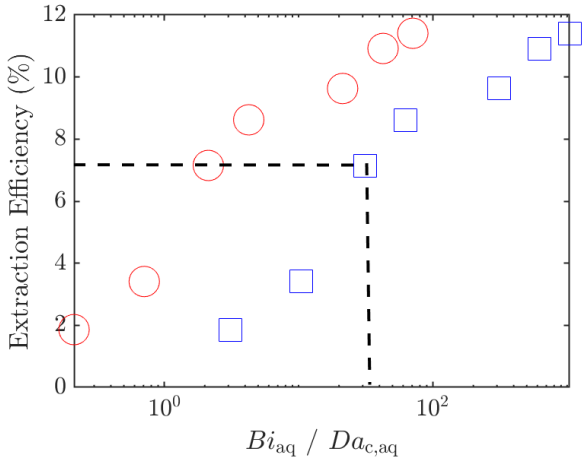

Figure 6.13: Influence of the Biot number (blue squares) on the Gallium extraction efficiency in the step channel. The Biot number is varied by changing K_1 (ranging from 3×10^{-6} to 10^{-3} m/s) at a flow rate of 10 μL/min. The Da_c (red circles) is also plotted for the same Biot numbers.

Even at a high Biot number of 1000 ($K_1 = 10^{-3}$ m/s), the extraction efficiency is still only around 12 %. For this kind of system with a first-order reaction, the

mass transfer, therefore, appears to be limited by the reaction. To confirm if this is indeed the case, the Peclet number is varied by changing the flow rate. At flow rates greater than 25 μL/min, leakage is observed. Therefore, we use the velocity profile at 10 μL/min to determine the flow profile at higher flow rates. For such flow rates (Q), the velocity profile is obtained by multiplying the velocity profile at 10 μL/min by a uniform factor of Q/10 (the 10 in the denominator corresponds to the flow rate of 10 μL/min) to account for the change in velocity. We thus assume that the shape of the flow profile remains constant as that observed at 10 μL/min. This may lead to a deviation from the real situation, but a numerical approximation is performed to understand the influence of the Peclet number.

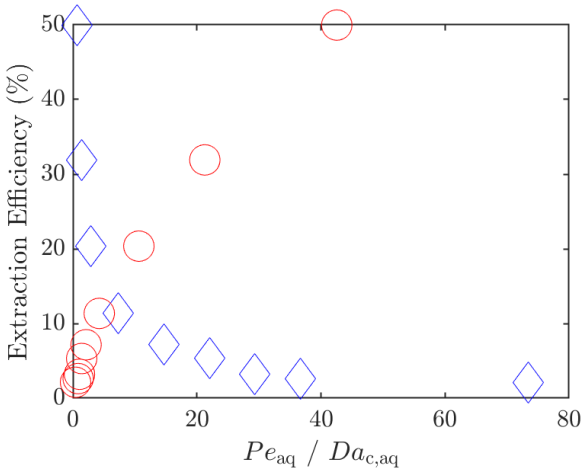

Figure 6.14: Influence of the Peclet number (blue diamonds) on the Gallium extraction efficiency in the step channel at $K_1 = 3 \times 10^{-5}$ m/s. The Peclet number is varied by changing the flow rate. The Da_c (red circles) is also plotted for the same Peclet number.

Figure 6.14 clearly shows the importance of the Peclet number on Gallium extraction. At low Pe, extraction efficiencies as high as 70 % are obtained because of the large residence time due to the lower flow rate. From Figures 6.13 and 6.14, we can see that even though the values of the Da_c are comparable, the extraction efficiency is a lot higher for a lower Peclet number. This implies that the Peclet number has more influence in the step channel than the Da_c, though this was not the case for the results of Helle *et al* [9], where the Da_c was found to have a greater influence. The width of the step channel is 10 times larger than that used by Helle *et al* [9], which implies that the diffusion time is much longer ($t_d \propto D_h^2$, where D_h is the hydraulic diameter [16]). This also means that less Gallium is available for reaction to take place at the interface. Table 6.3 also showed reduced extraction efficiencies at large widths when the average velocity was kept the same. The Peclet number, thus, emerges as the most influential dimensionless number in step channels of larger widths, and the Da_c is more influential in standard channels. More studies are required in step channels of different dimensions to see if a trend

similar to that observed in Figure 6.6 can be described for a step channel as well.

6.6. Conclusion

Mass transfer with diffusion and a first-order reaction at the interface was studied for two fluids flowing parallel to each other. First, simulations were performed and validated using the data of Helle *et al* [9]. After validation, the influence of three dimensionless numbers - the Biot, Peclet and Da_c - was studied on the mass transfer. In general, a higher Biot number and a lower Peclet number are preferred. However, when both numbers are changed in such a way that the Da_c is constant, the extraction efficiency remains approximately the same. A considerable increase in the extraction efficiency is observed only when the Da_c is increased.

Gallium extraction from 2 M $Zn(NO_3)_2 \cdot 6\,H_2O$ solution to chloroform in a step channel of large width is also studied. Extraction experiments are performed for different flow rates and compared with the simulations. The simulated extraction efficiencies were more accurate at lower flow rates than at higher flow rates. Both the Biot and Peclet numbers were varied for this system and it was observed that this system is diffusion-limited. The Peclet number appears to have the greatest influence on such channels with large widths.

Bibliography

[1] Sachit Goyal, Amit V. Desai, Robert W. Lewis, David R. Ranganathan, Hairong Li, Dexing Zeng, David E. Reichert, and Paul J.A. Kenis. Thiolene and SIFEL-based microfluidic platforms for liquid-liquid extraction. *Sensors and Actuators, B: Chemical*, 190:634–644, 2014. ISSN 09254005. doi: 10.1016/j.snb.2013.09.065.

[2] B. Malengier, J.L. Tamalapakula, and S. Pushpavanam. Comparison of laminar and plug flow-fields on extraction performance in micro-channels. *Chemical Engineering Science*, 83:2–11, December 2012. ISSN 00092509. doi: 10.1016/j.ces.2012.03.027. URL https://linkinghub.elsevier.com/retrieve/pii/S0009250912001972.

[3] Davide Ciceri, Lachlan R. Mason, Dalton J.E. Harvie, Jilska M. Perera, and Geoffrey W. Stevens. Extraction kinetics of Fe(III) by di-(2-ethylhexyl) phosphoric acid using a Y–Y shaped microfluidic device. *Chemical Engineering Research and Design*, 92(3):571–580, March 2014. ISSN 02638762. doi: 10.1016/j.cherd.2013.08.033. URL https://linkinghub.elsevier.com/retrieve/pii/S0263876213003626.

[4] H. Karim, C. Castel, A. Lélias, A. Magnaldo, and P. Sarrat. Kinetic study of uranium (VI) extraction with tributyl-phosphate in a stratified flow microchannel. *Separation and Purification Technology*, 314:123489, June 2023. ISSN 13835866. doi: 10.1016/j.seppur.2023.123489. URL https://linkinghub.elsevier.com/retrieve/pii/S1383586623003970.

[5] Gwendolyne Hellé, Clarisse Mariet, and Gérard Cote. Liquid–liquid microflow patterns and mass transfer of radionuclides in the systems Eu(III)/HNO3/DMDBTDMA and U(VI)/HCl/Aliquat® 336. *Microfluidics and Nanofluidics*, 17(6):1113–1128, December 2014. ISSN 1613-4982, 1613-4990. doi: 10.1007/s10404-014-1403-1. URL http://link.springer.com/10.1007/s10404-014-1403-1.

[6] Davide Ciceri, Lachlan R. Mason, Dalton J. E. Harvie, Jilska M. Perera, and Geoffrey W. Stevens. Modelling of interfacial mass transfer in microfluidic solvent extraction: part II. Heterogeneous transport with chemical reaction. *Microfluidics and Nanofluidics*, 14(1-2):213–224, January 2013. ISSN 1613-4982, 1613-4990. doi: 10.1007/s10404-012-1039-y. URL http://link.springer.com/10.1007/s10404-012-1039-y.

[7] Y. Haroun, D. Legendre, and L. Raynal. Volume of fluid method for interfacial reactive mass transfer: Application to stable liquid film. *Chemical Engineering*

Science, 65(10):2896–2909, May 2010. ISSN 00092509. doi: 10.1016/j.ces.2010.01.012. URL https://linkinghub.elsevier.com/retrieve/pii/S0009250910000291.

[8] Qi Zhang, Hongchen Liu, Shuainan Zhao, Chaoqun Yao, and Guangwen Chen. Hydrodynamics and mass transfer characteristics of liquid–liquid slug flow in microchannels: The effects of temperature, fluid properties and channel size. *Chemical Engineering Journal*, 358:794–805, February 2019. ISSN 13858947. doi: 10.1016/j.cej.2018.10.056. URL https://linkinghub.elsevier.com/retrieve/pii/S1385894718319958.

[9] Gwendolyne Hellé, Sean Roberston, Siméon Cavadias, Clarisse Mariet, and Gérard Cote. Toward numerical prototyping of labs-on-chip: modeling for liquid–liquid microfluidic devices for radionuclide extraction. *Microfluidics and Nanofluidics*, 19(5):1245–1257, November 2015. ISSN 1613-4982, 1613-4990. doi: 10.1007/s10404-015-1643-8. URL http://link.springer.com/10.1007/s10404-015-1643-8.

[10] Junior D Seader, Ernest J Henley, and D Keith Roper. Separation process principles. 2006.

[11] H Scott Fogler. *Essentials of chemical reaction engineering: essenti chemica reactio engi*. Pearson education, 2010.

[12] Lauretta Morroni, Fernando Secco, Marcella Venturini, Begoña Garcia, and José Maria Leal. Kinetics and Equilibria of the Interactions of Hydroxamic Acids with Gallium(III) and Indium(III). *Inorganic Chemistry*, 43(9):3005–3012, May 2004. ISSN 0020-1669, 1520-510X. doi: 10.1021/ic034781r. URL https://pubs.acs.org/doi/10.1021/ic034781r.

[13] N. Miložič, M. Lubej, U. Novak, P. Žnidaršič Plazl, and I. Plazl. Evaluation of Diffusion Coefficient Determination using a Microfluidic Device. *Chemical and Biochemical Engineering Quarterly Journal*, 28(2):215–223, 2014. ISSN 03529568, 18465153. doi: 10.15255/CABEQ.2014.1938. URL http://pierre.fkit.hr/hdki/cabeq/pdf/28_2_2014/Cabeq%202014-2%20Chapter%204.pdf.

[14] Bastian E Rapp. *Microfluidics: modeling, mechanics and mathematics*. Elsevier, 2022.

[15] B. Malengier, S. Pushpavanam, and S. D'Haeyer. Optimizing performance of liquid-liquid extraction in stratified flow in micro-channels. *Journal of Micromechanics and Microengineering*, 21(11), 2011. ISSN 09601317. doi: 10.1088/0960-1317/21/11/115030.

[16] Thomas Gervais and Klavs F Jensen. Mass transport and surface reactions in microfluidic systems. *Chemical engineering science*, 61(4):1102–1121, 2006.

[17] Amin Farahani, Ahmad Rahbar-Kelishami, and Hadi Shayesteh. Microfluidic solvent extraction of Cd(II) in parallel flow pattern: Optimization, ion exchange, and mass transfer study. *Separation and Purification Technology*, 258 (P2):118031, 2021. ISSN 18733794. doi: 10.1016/j.seppur.2020.118031. URL https://doi.org/10.1016/j.seppur.2020.118031.

[18] Donata Maria Fries, Tobias Voitl, and Philipp Rudolf von Rohr. Liquid extraction of vanillin in rectangular microreactors. *Chemical Engineering and Technology*, 31(8):1182–1187, 2008. ISSN 09307516. doi: 10.1002/ceat.200800169.

[19] Jovan Jovanović, Evgeny V. Rebrov, T. A. (Xander) Nijhuis, M. T. Kreutzer, Volker Hessel, and Jaap C. Schouten. Liquid–Liquid Flow in a Capillary Microreactor: Hydrodynamic Flow Patterns and Extraction Performance. *Industrial & Engineering Chemistry Research*, 51(2):1015–1026, January 2012. ISSN 0888-5885, 1520-5045. doi: 10.1021/ie200715m. URL https://pubs.acs.org/doi/10.1021/ie200715m.

[20] Junior D Seader, Ernest J Henley, and D Keith Roper. *Separation process principles*, volume 25. wiley New York, 1998.

[21] L. Binda, M. Bolado, A. D'Onofrio, and V. M. Freytes. Analysis of a microfluidic device for diffusion coefficient determination of high molecular weight solutes detectable in the visible spectrum. *The European Physical Journal E*, 45(6):56, June 2022. ISSN 1292-8941, 1292-895X. doi: 10.1140/epje/s10189-022-00211-4. URL https://link.springer.com/10.1140/epje/s10189-022-00211-4.

[22] Zida Li, Sze Yi Mak, Alban Sauret, and Ho Cheung Shum. Syringe-pump-induced fluctuation in all-aqueous microfluidic system implications for flow rate accuracy. *Lab on a Chip*, 14(4):744–749, 2014.

[23] Martina Baeckert, Martin Batliner, Beate Grass, Philipp K Buehler, Marianne Schmid Daners, Mirko Meboldt, and Markus Weiss. Performance of modern syringe infusion pump assemblies at low infusion rates in the perioperative setting. *British journal of anaesthesia*, 124(2):173–182, 2020.

[24] Davide Ciceri, Lachlan R. Mason, Dalton J.E. Harvie, Jilska M. Perera, and Geoffrey W. Stevens. Modelling of interfacial mass transfer in microfluidic solvent extraction: Part II. Heterogeneous transport with chemical reaction. *Microfluidics and Nanofluidics*, 14(1-2):213–224, 2013. ISSN 16134990. doi: 10.1007/s10404-012-1039-y.

7

Conclusions and Recommendations

The potential of parallel flow for radioisotope transfer at the microscale is immense, especially considering that it eliminates the need to separate the two fluids. This allows for faster extraction of radioisotopes while maintaining high purity [1]. However, stable parallel flow with complete separation of the fluids at the outlets is difficult to obtain as it is contingent on several factors such as fluid properties, channel geometry, contact angle and flow rates [2, 3]. Therefore, this thesis studied the various transport phenomena observed in the parallel flow regime in a microfluidic channel. The transport phenomena includes a broader study of the conditions which influence the leakage of the fluids, with a special focus on the role played by the channel geometry, and the mass transport in such channels.

To study the transport phenomena, the Lattice Boltzmann Method (LBM), specifically the Rothman-Keller (RK) model was used [4], along with experiments, Finite-Difference (FD) and Volume-of-Fluid (VOF). First, the thesis investigated the capability of the RK model to capture parallel flow and leakage. Then, the influence of the outlet geometry on leakage was studied and new designs were proposed. The overall channel geometry was modified such that the two sections of the channel had varying depths in the form of a step. Finally, the mass transfer in a parallel flow regime was studied for a standard Y-Y channel and the modified asymmetric channel. Section 7.1 describes the conclusions associated with each of the chapters and Section 7.2 provides recommendations for the future.

7.1. Conclusions

This thesis focuses on the transport phenomena observed in microfluidic channels, specifically parallel flow. In such channels, the choice of the simulation technique

is very important as different techniques are better or worse at capturing different flow regimes. The transport phenomena are dependent on various factors such as fluid properties, flow rates and channel geometry. Among these, this thesis zooms in on the role played by the channel geometry - both the outlet and overall geometry. While modifying the outlet only influences the leakage, changing the entire geometry can result in a different flow map altogether. These changes to the flow phenomena naturally affect the mass transfer as well. More microfluidic studies are necessary, both numerically and experimentally, to characterize the influence of geometry better.

In Chapter 3, a modified RK model was developed and its effectiveness was studied by comparing the simulation results with the experiments of Liu [3]. The RK model uses the Continuum Surface Force (CSF) model proposed by Brackbill *et al* [5] to implement the surface tension. Unfortunately, this method introduces spurious velocities at low Capillary numbers as the Young-Laplace equation is not completely satisfied [6, 7]. Since many of the experimental results involve flows at low Capillary numbers, a modification was proposed as shown in Equation 3.1, where the impact of the CSF term on the lattice velocity was set to 0. This modified model was compared to both experiments and other simulation techniques in a Y-Y microfluidic channel. The main findings of this chapter are:

1. The modified RK model resulted in a significant reduction in spurious velocities, converging much faster than the traditional RK model and capturing the flow regimes more accurately. In terms of grid convergence, the modified RK model converges faster than VOF as well, while showing reduced spurious velocities.

2. The slug lengths from the modified RK model simulations decreased with increasing Capillary numbers. This trend could not be captured by both VOF and the traditional model. However, the obtained slug lengths from the modified RK model were not accurate. The phase field method was better in this aspect.

3. The modified RK model proved to be the most successful method in capturing leakage. Unlike the phase-field method or the VOF, leakage was obtained for all the Capillary numbers as observed in the experiments. The leakage regimes matched the experiments for most of the Capillary numbers, except for a small set of Capillary numbers.

Chapter 4 covered the influence of the outlet geometry on leakage. Four different outlet designs were proposed for a T-T microfluidic channel. The first design was a modification of the design proposed by Lu *et al* [8], where a third outlet was added at the centre of the channel. A circular head was added at the entrance of the third outlet to minimize the loss of the organic fluid to the third outlet. The second design involved the addition of a closed circular head without the third outlet.

The third and fourth designs involved placing a large circular reservoir between the two outlets. The upper outlet was displaced from the lower outlet by the radius of the reservoir. The third design included a circular and rectangular pillar inside the reservoir, while the fourth design included a circular pillar concentric to the reservoir. The main findings of this chapter are:

1. The modified triple outlet design was very successful in ensuring the complete separation of the fluids. The loss of fluid at the third outlet can be controlled by either changing the measures of the circular head or the flow rate ratio ϕ.
2. No fluid entered the circular head in the case of the second design. The fluid velocities are significantly reduced in the head as it is fully closed.
3. Circular pillars were found to be more effective in preventing leakage as compared to the design with two pillars. The organic fluid is pinned inside the reservoir as the pillar exerts a capillary (burst) pressure on the organic fluid [9]. Leakage was found to depend on the diameter of the pillar and the Weber number of the fluids.

The channel with asymmetric cross-section (step) was studied in Chapter 5. Such a channel has been used before in extraction studies [10, 11, 12], but its influence on fluid phenomena has not been studied before. Therefore, experiments are performed to compare Y-Y microfluidic channels of symmetric cross-section (standard) with step channels. Additionally, the influence of the channel dimensions on the step channel is also studied. To further understand the role played by the step, VOF simulations are run to compare step and standard channels. The main findings of this chapter are:

1. Stable parallel flow without any leakage was obtained at low Capillary numbers for the step, in stark contrast to the standard channel, where parallel flow was only observed at high Capillary numbers, and that too with leakage.
2. Reducing the step ratio (ratio of the depths in the step channel) resulted in a more scattered flow map. Stable parallel flow occurred less frequently for channels with lower step ratios, with intermediate regimes such as parallel flow with leakage and pinching more commonly observed.
3. A larger channel width reduced the range of Capillary numbers for which stable parallel flow was observed, while a smaller width increased the range. Changing the width also led to different regimes previously not observed such as droplet flow.
4. Pressure plots of the fluids in a step and standard channel at low capillary numbers revealed that the interfacial tension aided the formation of stable parallel flow in a step channel while it aided the formation of slug flow in a standard channel. The pressure of the aqueous and organic phases kept

increasing the standard channel as the organic phase occupied the entire channel (blocking) when forming a slug. In contrast, the pressure of both phases in a step channel remained constant after the initial increase.

Finally, Chapter 6 studies the mass transfer for parallel flow in a Y-Y microfluidic step and standard channel. A finite difference code was developed for solving mass transfer and validated using the results of Helle *et al*. The mass transfer mechanism involves both diffusion and reaction taking place only at the interface. To understand the competing forces involved in such a transfer, the influence of three dimensionless numbers - Peclet, Biot and Damkohler (Da_c, where c corresponds to the role played by convection) numbers - was studied numerically in a standard channel. Next, extraction studies were conducted in a step channel for a different radioisotope (Gallium). Experiments were performed and simulations were compared with the experimental results. The main findings of this chapter are:

1. A higher Biot number and a lower Peclet number are generally preferred for higher extraction efficiency. However, when both these numbers are changed such that Da_c is constant, the extraction efficiency remains approximately the same. Da_c appears to have the greatest influence on extraction efficiency in channels with small widths.
2. In the case of mass transfer in a step channel, the simulations were found to be more accurate at lower flow rates than at higher flow rates.
3. The Peclet number was found to have the biggest impact on the extraction efficiency in such step channels with large widths.

In general, this thesis confirms the potential of microfluidic channels for radioisotope transfer, particularly parallel flow. Problems associated with leakage can be overcome by modifying the geometry of microfluidic channels. This method is more effective than using coatings as it can be applied to different combinations of fluids. However, effective radioisotope transfer cannot be accomplished through stable parallel flow alone. The conditions for efficient mass transfer are, as discussed in Chapter 6, governed by different parameters and phenomena, and these need to be understood in greater detail if microfluidic LLE is to be used for different applications and industries. Dimensionless numbers are very useful in this regard to study both the fluid mechanics and mass transfer in microfluidic channels, and this thesis sheds some light on the possible directions microfluidic LLE studies should take . Once we have a good grasp of the competing phenomena in a single microfluidic channel, we can then extend our analysis to study microfluidic LLE when microfluidic channels are connected in parallel.

7.2. Recommendations

Based on the results from the chapters, the following are recommendations for future research.

1. Though the spurious velocities were reduced using the modified RK model, they weren't eliminated. For studies involving Capillary numbers $< 10^{-4}$, spurious velocities could still pose a problem. Ierardi *et al* [13] and Raeini *et al* [7] have developed methods to limit the spurious velocities based on the application of filters. Such modifications have not been tried for channel flows and they might provide better results at low Capillary numbers.

2. Liu *et al* [14] implemented contact angle hysteresis in a channel with straight boundaries based on the determination of the interface normal using advancing and receding angles. Though such an approach could be difficult in a curved channel, the interface normals could be determined in a Y-Y channel. The role of hysteresis in leakage could therefore be studied.

3. Micro-Particle Image Velocimetry (Micro-PIV) experiments can be performed on the circular reservoir design with the circular pillars to reveal the flow field inside the reservoir. Also, pressure contours should be plotted using the experimental results to reveal the interaction of various forces inside the reservoir. These experiments could confirm the insights observed in the simulations and also enhance the theory discussed in Section 4.3.5.

4. The influence of step ratio and the channel depth could be studied in greater detail for the step channel with more experiments. In Chapter 5, only two step ratios were considered, and it is not known how higher step ratios increase the range of Capillary numbers for which stable parallel flow is observed.

5. Micro-PIV experiments could also be performed on the step channel to further understand the influence of the step on the fluids. These experiments could shed light on the flow profiles, streamlines and pressure development in such channels, especially in the regions around the step. The simulations discussed in Section 5.3 could also be validated using these experiments.

6. The type of channel inlet (Y, T or cross junction) has been found to have an impact on the regimes observed in standard channels [15]. Experiments on the step channel with different inlet designs could help to generalize the results observed in a step channel and confirm if parallel flow is indeed observed at Low Capillary numbers. Also, these experiments could also shed some light on the role played by the inlet on the flow regimes.

7. Radioisotope extraction can also be studied for slug flow because of the circulation that takes place inside the slug [16]. The time required for separation can also be quantified in order to understand if slug or parallel flow is more beneficial for radioisotope transfer.

8. More precise pressure pumps can be used for the experiments to minimize the fluctuations in flow rate, thereby increasing the accuracy of the experimental results. This can be especially useful in removing the uncertainty associated with the flow rates and contribute to our understanding of how changes in the flow rate affect interface position and subsequently, mass transfer.

9. Extraction experiments have to be conducted in step channels of varying widths, heights and step ratios to understand the influence of geometry on mass transfer. Chapter 6 showed how important Peclet number was for a step channel with a larger width, and the Damkohler number was observed to be more important in a standard channel. More experiments on step channels of different dimensions can illuminate the role of these dimensionless numbers in step channels.

10. Microfluidic channels connected in parallel for larger extraction efficiencies should be studied in greater detail using the dimensionless numbers discussed in the previous chapters. Additionally, the role of the connecting outlet to the inlet of the next channel in the transport phenomena in such parallel channels should be understood and elucidated as bubble formation and backflow can hinder isotope transfer.

Bibliography

[1] Sachit Goyal, Amit V. Desai, Robert W. Lewis, David R. Ranganathan, Hairong Li, Dexing Zeng, David E. Reichert, and Paul J.A. Kenis. Thiolene and SIFEL-based microfluidic platforms for liquid-liquid extraction. *Sensors and Actuators, B: Chemical*, 190:634–644, 2014. ISSN 09254005. doi: 10.1016/j.snb.2013.09.065.

[2] Madhvanand Kashid and Lioubov Kiwi-Minsker. Quantitative prediction of flow patterns in liquid-liquid flow in micro-capillaries. *Chemical Engineering and Processing: Process Intensification*, 50(10):972–978, 2011. ISSN 02552701. doi: 10.1016/j.cep.2011.07.003. URL http://dx.doi.org/10.1016/j.cep.2011.07.003.

[3] Z. Liu. *Purifying Radionuclides with Microfluidic Technology for Medical Purpose: Simulating multiphase flows inside a microfluidic channel with the phase field method*. PhD thesis, Delft University of Technology, 2022. URL http://resolver.tudelft.nl/uuid:e1bebcdd-185a-4515-b352-76d68f65ace8.

[4] Haibo Huang, Michael Sukop, and Xiyun Lu. Multiphase lattice boltzmann methods: Theory and application. 2015.

[5] Jeremiah U Brackbill, Douglas B Kothe, and Charles Zemach. A continuum method for modeling surface tension. *Journal of computational physics*, 100 (2):335–354, 1992.

[6] Stéphane Popinet. Numerical Models of Surface Tension. *Annual Review of Fluid Mechanics*, 50(1):49–75, January 2018. ISSN 0066-4189, 1545-4479. doi: 10.1146/annurev-fluid-122316-045034. URL https://www.annualreviews.org/doi/10.1146/annurev-fluid-122316-045034.

[7] Ali Q. Raeini, Martin J. Blunt, and Branko Bijeljic. Modelling two-phase flow in porous media at the pore scale using the volume-of-fluid method. *Journal of Computational Physics*, 231(17):5653–5668, July 2012. ISSN 00219991. doi: 10.1016/j.jcp.2012.04.011. URL https://linkinghub.elsevier.com/retrieve/pii/S0021999112001830.

[8] Yangcheng Lu, Yang Xia, and Guangsheng Luo. Phase separation of parallel laminar flow for aqueous two phase systems in branched microchannel. *Microfluidics and Nanofluidics*, 10(5):1079–1086, May 2011. ISSN 1613-4982, 1613-4990. doi: 10.1007/s10404-010-0736-7. URL http://link.springer.com/10.1007/s10404-010-0736-7.

[9] Francesca Garbarino, Kasper Kistrup, Giovanni Rizzi, and Mikkel Fougt Hansen. Burst pressure of phaseguide structures of different heights in all-polymer microfluidic channels. *Journal of Micromechanics and Microengineering*, 27 (12):125015, December 2017. ISSN 0960-1317, 1361-6439. doi: 10.1088/1361-6439/aa97b7. URL https://iopscience.iop.org/article/10.1088/1361-6439/aa97b7.

[10] Gwendolyne Hellé, Sean Roberston, Siméon Cavadias, Clarisse Mariet, and Gérard Cote. Toward numerical prototyping of labs-on-chip: modeling for liquid–liquid microfluidic devices for radionuclide extraction. *Microfluidics and Nanofluidics*, 19(5):1245–1257, November 2015. ISSN 1613-4982, 1613-4990. doi: 10.1007/s10404-015-1643-8. URL http://link.springer.com/10.1007/s10404-015-1643-8.

[11] Adelina Smirnova, Kazuma Mawatari, Akihide Hibara, Mikhail A. Proskurnin, and Takehiko Kitamori. Micro-multiphase laminar flows for the extraction and detection of carbaryl derivative. *Analytica Chimica Acta*, 558(1-2):69–74, February 2006. ISSN 00032670. doi: 10.1016/j.aca.2005.10.073. URL https://linkinghub.elsevier.com/retrieve/pii/S0003267005018519.

[12] Yasutoshi Ban, Yoshikuni Kikutani, Manabu Tokeshi, and Yasuji Morita. Extraction of Am(III) at the Interface of Organic-Aqueous Two-Layer Flow in a Microchannel. *Journal of Nuclear Science and Technology*, 48(10): 1313–1318, October 2011. ISSN 0022-3131, 1881-1248. doi: 10.1080/18811248.2011.9711821. URL http://www.tandfonline.com/doi/abs/10.1080/18811248.2011.9711821.

[13] C. Ierardi, A. Della Torre, G. Montenegro, A. Onorati, F. Radaelli, L. Visconti, and M. Miarelli. Modeling of two-phase flows at low Capillary number with VoF method. *Computers & Fluids*, 252:105772, February 2023. ISSN 00457930. doi: 10.1016/j.compfluid.2022.105772. URL https://linkinghub.elsevier.com/retrieve/pii/S0045793022003644.

[14] Haihu Liu, Yaping Ju, Ningning Wang, Guang Xi, and Yonghao Zhang. Lattice Boltzmann modeling of contact angle and its hysteresis in two-phase flow with large viscosity difference. *Physical Review E - Statistical, Nonlinear, and Soft Matter Physics*, 92(3), 2015. ISSN 15502376. doi: 10.1103/PhysRevE.92.033306.

[15] Madhvanand N. Kashid and David W. Agar. Hydrodynamics of liquid–liquid slug flow capillary microreactor: Flow regimes, slug size and pressure drop. *Chemical Engineering Journal*, 131(1-3):1–13, July 2007. ISSN 13858947. doi: 10.1016/j.cej.2006.11.020. URL https://linkinghub.elsevier.com/retrieve/pii/S1385894706005092.

[16] M.N. Kashid, A. Renken, and L. Kiwi-Minsker. CFD modelling of liquid–liquid multiphase microstructured reactor: Slug flow generation. *Chemical Engineering Research and Design*, 88(3):362–368, March 2010. ISSN 02638762. doi:

10.1016/j.cherd.2009.11.017. URL https://linkinghub.elsevier.com/retrieve/pii/S0263876209003104.

Acknowledgements

This dissertation would have been more difficult without the invaluable support I had obtained in these four years. First, I would like to thank my promoter, Martin, for not only giving me the opportunity to work on an interesting project, but also for his inspiring guidance which helped me grow as a researcher. Our vibrant discussions were very enjoyable primarily because you put me on an equal footing, giving me the space even to disagree. Your keen eye for detail and sharp acumen only improved my results, while instilling in me a critical and analytical way of thinking fundamentally about the physics. You were not only relaxed, but very understanding of my concerns, ensuring that I never felt stressed during the PhD and I finished my work on time. Working with you was an experience I cherish and one that I will dearly miss. I also wish to thank Jan-Leen Kloosterman for his time during the meetings and for the speedy approval of my thesis.

Though I was part of a larger, collaborative project, I was never made to feel awkward as all my collaborators were easily approachable. Albert and Svenja, my fellow PhDs in this endeavour, were not only easy to work with, but also lovely sounding boards for my problems. Our discussions were enlivened by a healthy mix of relevant research, intriguing questions and general PhD struggles that put my mind at ease. I would also like to thank their supervisors, Robin, Volkert and Ruud, all of whom took a keen interest in my project and also shared their guidance when needed.

I was very happy to be a part of such a convivial research group, whose silly jokes and jovial atmosphere provided a much-needed respite from the frustrations of research life. I doubt I could ever find a workplace as spirited as ours, where ping-pong and volleyball were always available at our beck and call whenever research seemed too much. All my colleagues - Jaen, Oscar, Marc, Tiberiu, Celebrity, Andries, Dennis, Ruben, Jelte, Alessandro, Anish, Bouke, Mikolaj, Daphne, Ana, Nick, Lukasz, Aron, Niccolo, Laurent and more - were friendly to talk and made this journey a lot breezier.

My friends always knew how to lift my spirits, be it through vacations, cricket matches or casual get-togethers. I would like to express my thanks to friends - Juntha, Poogles, Abe, Onkhar, Kuthacks, Kisaan, Mahaprabhu, Amogh, Agniveer Aryan, Ajay, Nilay, Alan, Mandyam, Punnybaku, Yuyuen (mostly nicknames) and more - both in NL and across the world for their constant presence and silly repartees.

Finally, I would like to thank my family - my mother, aunt and grandmother -

without whose unwavering support and encouragement I could never have gone this far. This thesis was written in memory of my grandfather, who was the keenest in my family to see me do a PhD. I am glad I could fulfil his expectations even if he isn't there to see it.

Curriculum Vitæ

Anand Sudha

31-08-1995 Born in Chennai, India.

Education

2013-2017 B.E in Mechanical Engineering
SSN College of Engineering
Chennai, India

2017-2019 M.S. in Mechanical Engineering
TU Delft
Delft, Netherlands

2020-2025 PhD in Applied Physics
TU Delft
Thesis: Study of Transport Phenomena for Parallel Flow in Microfluidic Channels
Promotor: Dr. ir. M. Rohde
Prof. dr. ir. J. L. Kloosterman

List of Publications

3. **A. Sudha**, M. Rohde, *Using Dimensionless Numbers to Understand Interfacial Mass Transfer for Parallel Flow in a Microchannel*, **Submitted**.

2. **A. Sudha**, A. Santoso, M. Rohde, *Influence of a 'Step' on the Liquid-Liquid Flow Patterns and Flow Phenomena in a Microfluidic Y-Y channe*, **Submitted**.

1. **A. Sudha**, M. Rohde *A modified forcing approach in the Rothman–Keller method for simulations of flow phenomena at low capillary numbers*, International Journal of Numerical Methods in Fluids, Volume 96, Issue 8 (2024).

Conferences

- **A. Sudha**, M. Rohde, *Investigation of Liquid-Liquid Flow Patterns in a Y-Y channel using the Lattice Boltzmann Method*, International Conference for Mesoscopic Methods in Engineering and Science - 2022